

Development of selective coating systems for solar-thermal flat-plate collectors

Von der Fakultät für Mathematik und Physik
der Gottfried Wilhelm Leibniz Universität Hannover

zur Erlangung des Grades
Doktorin der Naturwissenschaften
- Dr. rer. nat -
genehmigte Dissertation

von
Dipl. Phys. Nicole Ehrmann
geboren am 08.12.1982 in Kassel

2012

Referent: Prof. Dr. Rolf Brendel
Korreferent: Prof. Dr. Gunther Seckmeyer
Tag der Promotion: 16. Mai 2012

Development of selective coating systems for solar-thermal flat-plate collectors

With regard to future applications of solar-thermal energy, such as solar heating with high solar fractions, solar cooling, or the generation of industrial process heat, cost-efficient and robust collectors are needed that provide high efficiencies at temperatures above 100°C as well as with low solar irradiation. Up to now, evacuated tube collectors have to be used for these applications since the efficiency of conventional flat-plate collectors is too low due to high heat losses through the transparent covering. However, evacuated tube collectors are expensive and less robust in comparison to flat-plate collectors. For this reason, the Institute of Solar Energy Research (ISFH) works on the development of highly efficient flat-plate collectors by improving the insulation of the transparent covering. For this purpose, the principle of thermal protection glazing is transferred to flat-plate collectors by implementing an argon filled double-glazing with a low emitting coating on the inner glass pane to reduce radiative and convective heat losses. In contrast to thermal protection glazing, the collector application requires higher solar transmittance and thermal stability.

The aim of this thesis is, therefore, the development of a selective coating system, which provides a high solar transmittance and at the same time, a sufficient low infrared emissivity with a high thermal stability. Transparent conducting oxides (TCOs) are particularly suitable due to their selectivity. This thesis focuses on the deposition, characterization, and optimization of aluminum-doped zinc oxide (ZnO:Al) thin films. The thin films are deposited with varying process parameters and doping concentrations by DC magnetron sputtering on glass substrate sizes manageable in the laboratory. However, sputtering is an industrially applicable process, which can be scaled to larger substrates. Special attention is paid to the optical analysis of the films by simultaneous modeling of ellipsometric and photometric data with an appropriate model dielectric function in the relevant wavelength range for solar-thermal applications from 0.3 to 50 μm . To verify the modeling results, independent thin film characterization methods are used, such as Hall measurements, atomic force microscopy, scanning and transmission electron microscopy, X-ray diffraction and secondary-neutral-mass spectroscopy. In order to raise the solar transmittance of the glazing, low-iron glass and additional antireflective (AR) coatings are necessary. The implementation of two additional dielectric films below and above the ZnO:Al film raises the solar transmittance to 85% while the infrared emissivity remains at 31%. The AR layers are deposited by reactive pulsed DC magnetron sputtering from silicon targets by varying the reactive gas composition of nitrogen and oxygen to reach SiO_xN_y with middle refractive index and SiO_2 with low refractive index. The AR layers act additionally as efficient protection layers as durability tests with heat and condensation loads, each of 540 h, have shown. To evaluate the influence of the coating properties on the collector performance, a collector model is developed, which is balancing the radiative, conductive, and convective heat losses of the collector components. The radiation-balance model of Rubin [Energy Research, 6:341, 1982] is extended to spectral data and takes account of the multiple reflections inside the system even if infrared transparent media are assumed. The calculated collector efficiency of the three-layer system yields 52% at a temperature difference between fluid and ambient of 100 K while a conventional single-glazed collector reaches only 35%.

Keywords: Transparent conducting oxides, spectroscopic ellipsometry, solar-thermal flat-plate collectors.

Entwicklung selektiver Schichtsysteme für solarthermische Flachkollektoren

Im Hinblick auf zukünftige Anwendungen der Solarthermie, wie solares Heizen mit hohen solaren Deckungsgraden, solares Kühlen oder der Erzeugung von industrieller Prozesswärme, werden kostengünstige und robuste Kollektoren benötigt, die eine hohe Effizienz bei Temperaturen über 100°C, sowie bei niedriger solarer Einstrahlung aufweisen. Bisher mussten Vakuumröhrenkollektoren für solche Anwendungen eingesetzt werden, da die Effizienz konventioneller Flachkollektoren aufgrund hoher Wärmeverluste durch die transparente Abdeckung zu gering ist. Vakuumröhrenkollektoren sind jedoch teuer und weniger robust im Vergleich zu Flachkollektoren. Aus diesem Grund entwickelt das Institut für Solarenergieforschung (ISFH) hocheffiziente Flachkollektoren durch Verbesserung der Wärmedämmung der transparenten Abdeckung. Hierfür wird das Prinzip der Wärmeschutzverglasung auf Flachkollektoren durch den Einsatz einer Argon-gefüllten Doppelverglasung mit einer niedrig emittierenden Schicht auf der inneren Glasscheibe übertragen, um Wärmeverluste durch Strahlung und Konvektion zu reduzieren. Im Gegensatz zu Wärmeschutzverglasungen erfordert die Kollektoranwendung eine höhere solare Transmission und thermische Stabilität.

Das Ziel dieser Dissertation ist daher die Entwicklung eines selektiven Schichtsystems, welches eine hohe solare Transmission bei gleichzeitig ausreichender Infrarot-Emissivität und thermischer Stabilität bietet. Transparent leitfähige Oxide sind aufgrund ihrer Selektivität besonders geeignet. Die Dissertation beschäftigt sich mit der Abscheidung, Charakterisierung und Optimierung von dünnen Aluminium dotierten Zinkoxid (ZnO:Al) Schichten. Die dünnen Schichten werden mit variierenden Prozessparametern und Dotierkonzentrationen mittels DC-Magnetron-Sputtern auf laborrelevanten Glassubstratgrößen abgeschieden. Sputtern ist jedoch ein industrierelevanter Prozess, der auf große Substrate skaliert werden kann. Besondere Aufmerksamkeit ist auf die optische Analyse der Schichten mittels simultaner Modellierung der ellipsometrischen und photometrischen Daten mit einer geeigneten dielektrischen Modell-Funktion für den für solarthermische Anwendungen relevanten Wellenlängenbereich von 0.3 bis 50 μm gerichtet. Zur Überprüfung der Modellergebnisse wurden unabhängige Dünnschicht-Charakterisierungsmethoden genutzt, wie Hall Messungen, Rasterkraft-Mikroskopie, Raster- und Transmissions-Elektronen-Mikroskopie, Röntgenbeugung und Sekundär-Neutronenteilchen-Massen-Spektroskopie. Gläser mit niedrigem Eisengehalt und zusätzliche Antireflexschichten (AR) sind nötig, um die solare Transmission der Verglasung zu steigern. Der Einsatz von zwei zusätzlichen dielektrischen Schichten unter und über der ZnO:Al Schicht erhöht die solare Transmission auf 85%, während die Infrarot-Emissivität bei 31% erhalten bleibt. Die AR-Schichten werden mittels reaktiven gepulsten DC Magnetron Sputtern von Siliziumtargets durch Variation der Reaktivgaszusammensetzung von Stickstoff und Sauerstoff abgeschieden, um SiO_xN_y mit mittlerem und SiO_2 mit niedrigem Brechungsindex zu erhalten. Die AR-Schichten wirken zusätzlich als effiziente Schutzschichten, wie Beständigkeitstests mit Temperatur- und Kondensat-Belastung, jeweils für 540 h, ergeben haben. Um den Einfluss der Schichteigenschaften auf die Kollektoreffizienz beurteilen zu können, wird ein Kollektormodell entwickelt, welches die Strahlungs-, Leitungs- und Konvektions-Wärmeverluste bilanziert. Das Strahlungsbilanz-Modell von Rubin [Energy Research, 6:341, 1982] wird für spektrale Daten erweitert und berücksichtigt die Mehrfachreflexionen innerhalb des Systems, auch wenn infrarot transparente Medien betrachtet werden. Der berechnete Kollektorstufigwirkungsgrad von dem Dreischichtsystem ergibt 52% bei einer Temperaturdifferenz zwischen Fluid und Umgebung von 100 K, während ein konventioneller einfachverglaster Kollektor nur 35% erreicht.

Schlagwörter: Transparent leitfähige Oxide, Spektral-Ellipsometrie, solarthermische Flachkollektoren.

Contents

1	Introduction	1
2	Basics	7
2.1	Selective coatings and surfaces for solar-thermal applications	7
2.2	Solar-thermal flat-plate collectors	9
2.3	Transparent conducting oxides	13
2.3.1	Structural properties of ZnO:Al thin films	14
2.3.2	Electronic properties of ZnO:Al thin films	15
2.3.3	Optical properties of ZnO:Al thin films	20
2.4	Antireflective coating systems	23
2.5	Film deposition	29
2.5.1	DC magnetron sputtering	29
2.5.2	RF magnetron sputtering	30
2.5.3	Reactive mid-frequency sputtering	31
2.5.4	Film growth	34
3	Analysis of ZnO:Al thin films	37
3.1	Experimental details	37
3.1.1	Film deposition	37
3.1.2	Film analysis	39
3.2	Model dielectric function (MDF) of sputtered ZnO:Al thin films	48
3.2.1	Modeling of the surface roughness layer	49
3.2.2	Modeling of the ZnO:Al bulk layer	50
3.2.3	Modeling of the interface layer	57
3.3	Results and discussion	59
3.3.1	Comparison of the MDF results with independent thin film characterization methods	60
3.3.2	Discussion of the MDF and thin film characterization results	63
3.3.3	Results of the deposition parameter studies	68
3.3.4	Discussion of the results of the deposition parameter studies	71
3.3.5	Results of the doping-concentration variation	73
3.3.6	Discussion of the results of the doping series	82
3.4	Summary	87

4	Investigations of AR coating systems for collector covers	89
4.1	Simulations of AR coating systems	89
4.2	Experimental details	91
4.2.1	Film deposition	91
4.2.2	Film analysis and durability investigations	93
4.3	Results and Discussion	93
4.3.1	Results of the AR coating deposition	94
4.3.2	Discussion of the AR coating deposition	94
4.3.3	Results of the AR coating system	97
4.3.4	Discussion of the AR coating system	99
4.3.5	Results of the durability investigations	100
4.3.6	Discussion of the durability investigations	101
4.4	Summary	102
5	Modeling of collector efficiency	103
5.1	Collector model	103
5.1.1	Calculation of radiative transfer	103
5.1.2	Calculation of conductive and convective interchange	108
5.1.3	Calculation of collector efficiency	110
5.2	Decision criterion for applicability of coating systems for collector covers	113
5.3	Simulation of collector efficiencies for different coating configurations .	116
5.3.1	Collector simulation results of the deposition parameter studies	116
5.3.2	Collector simulation results of single ZnO:Al and AR-ZnO:Al coating systems	117
5.3.3	Collector simulation results of coating systems with different doping concentration	119
5.3.4	Collector simulation results of coating systems with different ZnO:Al film thickness values	119
5.3.5	Discussion of the simulation results	120
5.4	Comparison with commercially available low-e glass	122
5.5	Summary	123
6	Summary and outlook	125
	Appendix	129
1	Fit parameters of ZnO:Al thin films on different substrates	129
2	Electronic properties of ZnO:Al thin films with varying film thickness determined by SE and Hall analysis	130
3	Fit parameters of ZnO:Al thin films with varying doping concentration	130
4	Parameters for collector simulation	135
	Acronyms and symbols	137

Bibliography	142
List of Publications	159
Danksagung	161
Lebenslauf	163

1 Introduction

One way of utilization of solar energy is the conversion into heat by solar-thermal collectors. There exist many different collector designs that are intended for different applications and temperature regimes, such as unglazed swimming pool collectors as well as flat-plate collectors and vacuum tube collectors, which are usually applied to family houses for warm water generation and heater assistance.

With regard to the future applications of solar-thermal energy, such as solar heating with high solar fractions, solar cooling, or the generation of industrial process heat [1], cost-efficient and robust collectors are needed, which provide high efficiencies at temperatures above 100 °C as well as with low solar irradiation. In Germany, today's flat-plate collectors are market leaders [1], since they are cost-efficient, robust, and effective even with diffuse solar irradiation. However, the efficiency of standard flat-plate collectors is too low for the above-mentioned applications in comparison to vacuum-tube collectors. The low efficiency at high temperatures or low solar irradiation is caused by considerably high heat losses through the transparent covering of the flat-plate collector. There are many efforts to reduce the radiative and convective heat losses, such as the use of selective absorber coatings, the introduction of a second glass pane or a foil as well as the hermetic sealing and inert gas filling or evacuating of gaps in the collector. Today, selective absorber coatings, which provide high solar absorptances of approximately 95% and low infrared emissivities of 5%, are state of the art [2]. The company BBT Thermotechnik-Buderus introduced a hermetic sealing and argon filling between the absorber and glass pane of their flat-plate collector [3]. Schüco developed a double-glazed collector where the glass panes provide antireflective (AR) coatings and the glazing gap is filled with argon to reduce convective heat losses [4]. Another concept was pursued by Ökotech and also by the Bavarian Center for Applied Energy Research with the introduction of a foil instead of a second glass pane, which has the advantage of lower weight [5, 6]. Centrosolar develops an evacuated flat-plate collector with the absorber sandwiched between two glass panes in an ongoing project [7]. However, the long-term stability of vacuum components is often critical.

Another approach is pursued by the Institute for Solar Energy Research Hamelin (ISFH) in the project “Solarthermie2000plus - Principles for selectively coated high-efficiency glazing to be applied in flat-plate collectors (HGlas),” which is funded by the German Federal Ministry for the Environment, Nature Conservation and Nuclear Safety (BMU). In this project, the flat-plate collector efficiency is increased by improving the insulation of the transparent covering [8]. For this purpose, a double glazing with a low-emitting (low-e) coating on the inner glass pane is used to reduce the exchange of thermal radiation, as shown in Fig. 1.1. Convective heat losses are reduced by filling the gap in the glazing unit with argon. In order to raise the solar trans-

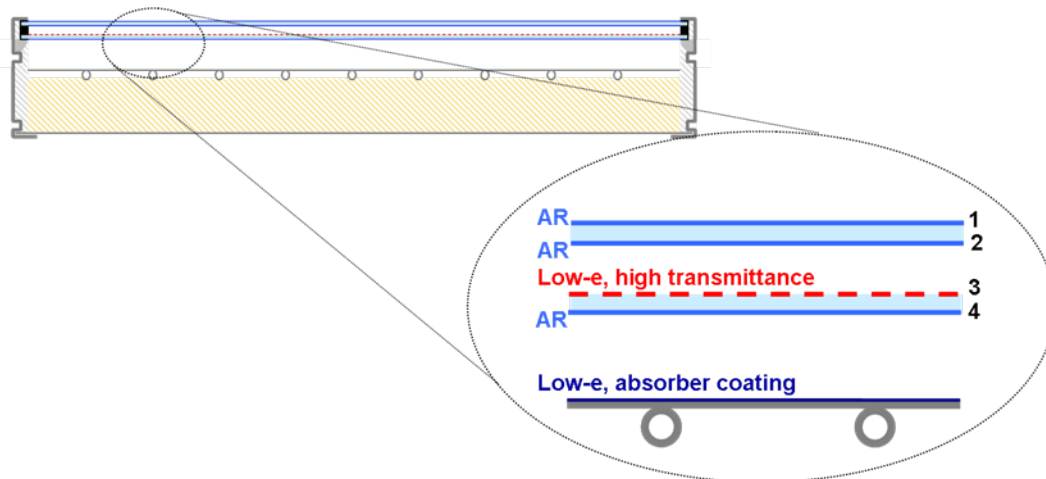


Figure 1.1: Schematic representation of the HGlas collector [8].

mittance of the glazing, low-iron glass and additional AR coatings are necessary. As AR-coatings at positions 1, 2, and 4 of Fig. 1.1, commercially available glass with porous SiO_2 sol-gel coatings (e.g. from Centrosolar Glas [9]) can be used. The concept of a low-e coated, argon-filled double glazing is also used for window applications for many years to reduce the heat losses of buildings [10]. Commercially available low-e coatings for window applications usually consist of a series of layers containing an approximately 12-nm-thick layer of silver [10], which provides transmittance mainly in the visible part of the solar spectrum. Since the application as a covering for flat-plate collectors requires high solar transmittance, thermal protection glazing for buildings is not suitable.

In contrast, transparent conductive oxides (TCOs) are particularly suitable for application as a covering for flat-plate collectors due to their optical selectivity. TCOs provide high solar transmittance due to their wide band gap and at the same time, low thermal emissivity. The emissivity of the TCOs can be controlled by n-type doping [10, 11] while the choice of the dopant depends on the TCO material. TCOs are used in many applications such as optoelectronic devices as well as for architectural and automotive glazing. Usually, indium tin oxide (ITO) is used as standard material for photovoltaic devices and flat panel displays since it provides favorable electronic properties. However, due to the toxicity and scarcity of ITO, which results in high cost [12], ITO is hardly suitable for large-area applications. For window and automotive glazing applications, fluorine doped tin oxide (FTO) is also an appropriate TCO due to its high stability against oxygen and humidity [13]. Fluorine-doped tin oxide is usually deposited by chemical vapor deposition directly after the glass fabrication [10] and requires high deposition temperatures. However, commercially available products (e.g. KGlassTM from Pilkington [14]) provide only a poor transmittance over the whole solar spectral range due to high iron contents in the glass substrates, missing AR coatings as well as the optimization of the FTO with respect to low emissivity.

Another promising TCO is aluminum-doped zinc oxide (ZnO:Al) due to its good electronic and optical properties as well as low cost, heat stability, and non-toxicity [12, 15]. Therefore, there are many efforts to study and to optimize the properties of ZnO:Al thin films with the aim to use it as an alternative material for ITO [16]. Especially for photovoltaic applications, ZnO:Al seems to be a promising candidate as transparent conducting front contact [17]. The requirements on the ZnO:Al layers are a high transmittance in the visible and near infrared wavelength range as well as a high conductivity. Amorphous silicon (a-Si) based thin film photovoltaic cells require in addition rough surfaces of the TCO layer, which exhibit optimized light trapping properties to raise the near infrared absorption of the thin silicon layers [18, 19]. There are two different ways to yield rough ZnO:Al layers. One way is the choice and optimization of the appropriate deposition technique to grow rough films, such as low-pressure chemical vapor deposition [20] and the other way is a wet-chemical etching of the films after deposition with appropriate acids [18, 19]. Although the research investigations on ZnO:Al lasts for some time, there are still many effects not understood and still subject of the ongoing research [16, 21]. This is the reason why commercial ZnO:Al coated glass with suitable electronic and optical properties is still not available or is too expensive [22].

In contrast to photovoltaic and window applications, the solar-thermal application requires a considerable high transmittance over the whole solar spectral range. Therefore, the low-e coating of the double-glazed collector should be optimized with regard to the optical and electronic properties. In addition, the low-e coating should provide smooth surfaces since rough surfaces, which are used for light trapping effects in photovoltaic cells, could lead to total reflection at the double glazing and lower the transmittance of the glazing unit. Rommel et al. [23] showed that a collector glazing with prismatic surfaces exhibits a much lower solar transmittance which causes a decrease of the collector efficiency, especially for larger angles of incidence ($\theta > 30^\circ$), in comparison to a collector glazing with smooth surfaces. Since the refractive index of the ZnO:Al thin films is high in comparison to the ambient atmosphere and the glass substrate, additional AR coatings would be necessary to yield a suitable solar transmittance.

A variety of physical and chemical deposition methods for ZnO:Al thin films are known today [12, 15, 16, 24–29], which influence the structural, electronic, and optical properties. Sputtering is a promising deposition technique for large area applications since it is an industrially applicable process with relatively high deposition rates and moderate substrate temperatures. The films presented in this thesis are deposited by reactive and non-reactive magnetron sputtering on substrate sizes manageable in the laboratory. However, sputtering processes can be scaled to larger substrate for industrial applications.

In the case of stagnation of the collector, which means that the collector fluid is evaporated and the heat is not dissipated any more, the coated glass can reach high temper-

atures due to the free-carrier absorption of the TCO and a higher heat performance of the absorber. The temperature range of the coated glass is much higher in comparison to window applications. If the edge bond of the double glazing leaks, the gap of the glazing unit will be filled with air and the coating system will be in contact with ambient oxygen and humidity. As a consequence, the application as selective coating of a collector cover makes high demands on the heat, humidity, and condensation stability of the low-e coating.

One aim of this thesis is, therefore, the development of a sputter-deposited AR low-e coating system for the application as selective coating of a collector glazing that provides a high solar transmittance, a sufficient infrared emissivity as well as long-term heat and humidity stability. Since the structural, electronic, and optical properties of the ZnO:Al thin films depend strongly on the growth technique, on the process parameters, on the substrate, and the kind and amount of doping, the films have to be characterized and optimized for every application itself.

The application as low-e coating of a collector glazing requires the knowledge of the optical properties of the thin films over a wide wavelength range of 0.3 to 50 μm . Spectroscopic ellipsometry is a powerful tool for non-destructive characterization of thin films if reliable models for calculating the dielectric function exist. There are many different ways of modeling the dielectric function of intrinsic and doped ZnO [30–36]. However, depending on the film properties, some of the models fail in describing the measured data or produce unreliable results. Therefore, the development of a reliable dielectric function model of sputtered ZnO:Al thin films is one central part of this thesis.

It is a common practice that the optical properties of solar-thermal flat-plate collectors are described in two different ways with respect to different wavelength regimes such as the solar spectral range (0.3 to 2.5 μm) and the infrared spectral range (2.5 to 50 μm) [37, 38]. In the solar spectral range, multiple reflections of the incident light in the whole collector system are taken into account. However, for both spectral ranges, only the wavelength-averaged solar transmittance and reflectance of the collector components are considered, and the spectral behavior is neglected to save calculation time. Since glass is opaque for long wavelengths, the radiative heat exchange is calculated in each case only between two collector components, for instance between the absorber and the inner glass pane and between the outer and inner glass pane. However, glass is transparent for wavelengths between 2.5 and 4.5 μm and multiple reflections should be taken into account also in this wavelength range. Since all the commonly used assumptions may lead to errors, especially when selective coatings are used, another aim of this thesis is to calculate the propagation of the light in the collector by taking into account the spectral behavior as well as multiple reflections of the collector components that are independent of the light source and wavelength regime. The influence of the film properties of the low-e coatings on the optical collector performance is also

evaluated.

The thesis is organized as follows: In Chapter 2, the physical and technological basics of solar-thermal flat-plate collectors, of ZnO:Al thin films, of selective and AR coatings, as well as of reactive and non-reactive sputtering techniques are introduced. Chapter 3 addresses to the deposition, characterization, and optimization of ZnO:Al thin films with varying process parameters and doping concentrations. Special attention is paid to the development of a model dielectric function of sputtered ZnO:Al thin films and necessary modifications of existing models. In Chapter 4, the simulations of AR coating systems as well as the deposition details and the structural and optical properties of the realized AR coating systems are shown. In this context, also durability tests on the coating systems are presented. Chapter 5 focuses on modeling the optical collector performance in dependence of the spectral behavior and multiple reflections of the collector components with respect to the low-e coatings presented in the previous chapters. Chapter 6 summarizes the main results of this thesis and gives an outlook.

2 Basics

2.1 Selective coatings and surfaces for solar-thermal applications

For solar-thermal applications, selective coatings are usually used as absorber coatings [2]. These coatings provide a high absorptance in the solar spectral range and a high reflectance in the infrared spectral range, as shown in Fig 2.1.

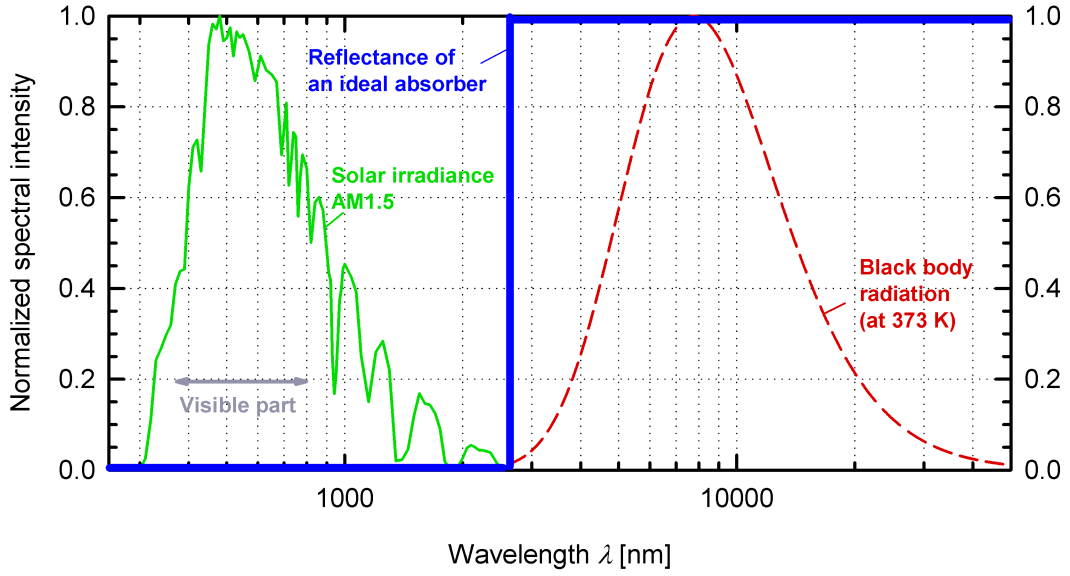


Figure 2.1: Reflectance spectra of an ideal absorber coating in comparison to the normalized solar irradiance of air mass (AM) 1.5 and the black body radiation for 373 K.

Kirchhoff's law [39] states for opaque materials

$$\alpha(\lambda, \theta) = 1 - \rho(\lambda, \theta) \quad (2.1)$$

$$\alpha(\lambda, \theta) = \epsilon(\lambda, \theta), \quad (2.2)$$

where α is the absorptance at wavelength λ and angle of incidence θ , ρ denotes the total reflectance (diffuse and specular reflectance), and ϵ is the emissivity. Usually, the spectral reflectance is measured, and the wavelength-averaged solar absorptance is given by

$$\alpha_{\text{sol}} = \frac{\int_{300 \text{ nm}}^{2500 \text{ nm}} (1 - \rho(\lambda)) S_{\text{sol}}(\lambda) d\lambda}{\int_{300 \text{ nm}}^{2500 \text{ nm}} S_{\text{sol}}(\lambda) d\lambda}, \quad (2.3)$$

where S_{sol} denotes the solar irradiance. S_{sol} differs for different air mass indices and is tabulated in several engineer standards [40, 41]. The solar reflectance is calculated in an analogous way. For the determination of the emissivity, the reflectance in the

infrared spectral range is usually measured at room temperature and the wavelength-averaged infrared emissivity for a desired surface temperature T_{surf} is given by the following formula [2, 42]:

$$\epsilon_{\text{IR},T} = \frac{\int_{2.5 \mu\text{m}}^{50 \mu\text{m}} (1 - \rho(\lambda)) S_{P,T}(\lambda) d\lambda}{\int_{2.5 \mu\text{m}}^{50 \mu\text{m}} S_{P,T}(\lambda) d\lambda}, \quad (2.4)$$

where $S_{P,T}$ is Planck's blackbody radiation [39]. This means that the temperature dependence of ϵ derives only from the spectral power distribution of the blackbody radiation. Therefore, the actual performance of an absorber at high temperatures may not agree with the calculated performance since the emissivity of some materials may change with temperature. Another problem for the determination of the emissivity is that small relative errors in ρ lead to large relative errors in $\epsilon_{\text{IR},T}$ [2].

It is a common practice to use these wavelength-averaged data for the determination of the performance of solar-thermal flat-plate collectors, which means that the spectral behavior is not taken into account. However, by using coatings with a highly selective spectral behavior for the absorber or even for the glazing, errors may be produced. Therefore, the discrepancy between wavelength-averaged and spectral calculation is analyzed and presented in Sec. 5.1.3.

Different types of selective absorber coatings are on the market [2, 37]. The type of coating used depends on the desired application and temperature range. Good selective coatings exhibit a solar absorptance as high as 95% and an infrared emissivity lower than 5% [2].

Glass that is used as transparent cover for solar-thermal flat-plate collectors is highly transparent in the solar spectral range and highly absorbing in the infrared spectral range, so the emissivity of glass is very high, approximately 84%. In the case of transparent materials with transmittance τ , Eq. 2.1 changes to

$$\alpha(\lambda, \theta) = 1 - \rho(\lambda, \theta) - \tau(\lambda, \theta). \quad (2.5)$$

The solar transmittance is calculated according to Eq. 2.3. There exist also transparent selective coatings that are transparent in the solar spectral range and provide a low emissivity in the infrared spectral range and are, therefore, used for insulating windows. These coatings are called low-e coatings. For window applications, usually, coating systems with very thin silver films from 10 to 20 nm are used since they provide a high visible transmittance and a very low emissivity, which is lower than 10% [10]. Other selective coatings are transparent conductive oxides which will be discussed in detail in Sec. 2.3.

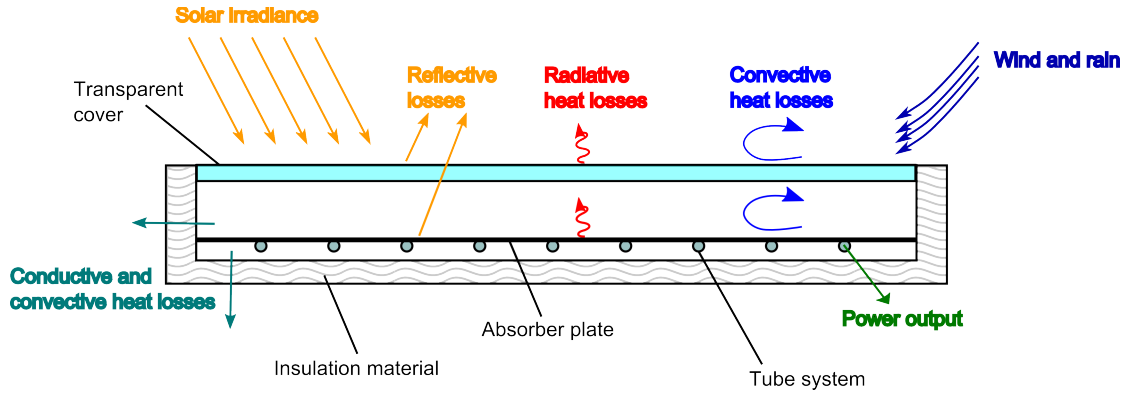


Figure 2.2: Schematic representation of a solar-thermal flat-plate collector (according to Ref. [43]).

2.2 Solar-thermal flat-plate collectors

Figure 2.2 shows a typical representation of a solar-thermal flat-plate collector [43]. This type of collector consists of an absorber plate with a selective coating, which absorbs the solar light and converts this energy into heat. The selective coating has a high absorptance in the solar spectral range and a high reflectance in the infrared spectral range, so that radiative heat losses are reduced. The tubes behind the absorber are filled with a frost-resistant heat-transfer medium of an ethylene or glycol water mixture, which transfers the useful heat to a storage tank. For a good heat transfer, the tubes have to be in good contact with the absorber plate. The enclosure of the collector contains insulation wool, which reduces the conductive heat losses of the absorber plate and tubes to the ambient. Radiative heat losses could be reduced by a reflecting foil behind the absorber plate and tubes. The transparent cover of the collector reduces convective and radiative heat losses and consists usually of one or two sheets of glass or plastic.

The efficiency of a thermal collector is the ratio of the useful power to the incident global irradiance G . Efficiency losses are distinguished into losses of optical and thermal origin. Optical losses in the solar spectral range result from reflective and absorptive losses at the transparent cover as well as incomplete absorptance at the absorber. Thermal losses are distinguished in terms of their transfer mechanism, such as heat conduction, convection, and radiation and are caused by the temperature difference between the collector components and the ambient. For experimental purposes, the temperature difference between the mean fluid temperature \bar{T}_{fluid} and the ambient temperature T_{amb} is used as reference magnitude [44]. In this case, the efficiency of a flat-plate collector is defined by

$$\eta_{\text{col}} \equiv \eta_0 - k_1 \frac{\bar{T}_{\text{fluid}} - T_{\text{amb}}}{G} - k_2 \frac{(\bar{T}_{\text{fluid}} - T_{\text{amb}})^2}{G}. \quad (2.6)$$

Here, η_0 denotes the conversion factor, which depends mainly on the optical properties of the transparent cover and the absorber. The heat loss coefficients k_1 and k_2 describe

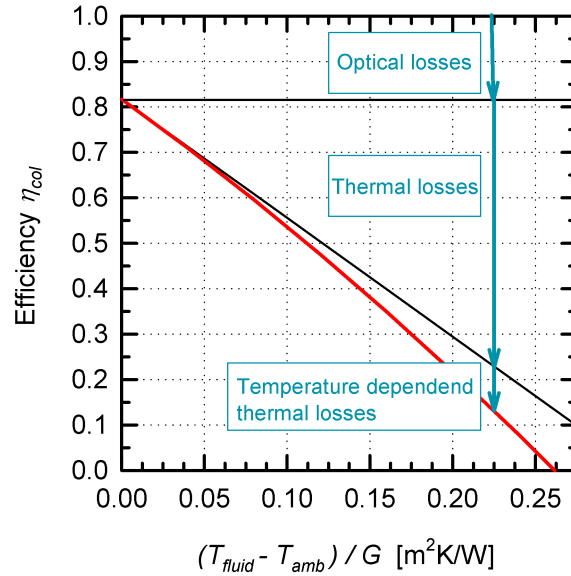


Figure 2.3: Efficiency of an AR coated, single-glazed solar-thermal flat-plate collector for an inclination angle 45° , a solar irradiance of 800 W/m^2 and an ambient temperature of 20°C .

the thermal losses, which are approximately linearly and quadratically dependent on the temperature difference. The equation for radiative losses will be shown later in this section. The calculation of convective and conductive heat losses will be presented in Sec. 5.1.2 and are also described in detail elsewhere [37]. Figure 2.3 shows a typical efficiency curve as a function of temperature difference between fluid and ambient weighted by the global irradiance $(\bar{T}_{\text{fluid}} - T_{\text{amb}}) / G$.

The central part of this thesis will be on the improvement of the transparent cover to further reduce thermal losses through the glazing. As already shown in Fig. 1.1, convective and conductive heat losses are reduced by using a second glass pane and filling the glazing gap with inert gas such as argon or krypton. Since the transmittance of the collector cover limits the fraction of light which reaches the absorber, it is necessary that the glazing is highly transparent over the whole solar spectral range. Therefore, it is necessary to use low-iron glass with a low absorptance and AR coatings that reduce the reflective losses. Radiative heat losses are reduced by using a low-e coating on the inner glass pane with a high solar transmittance and a low emissivity in the infrared spectral range. The radiative heat transfer between two parallel infinite surfaces, 1 and 2, as shown in Fig. 2.4, is given by [45]

$$\dot{q} = \frac{1}{\frac{1}{\epsilon_1} + \frac{1}{\epsilon_2} - 1} \sigma (T_1^4 - T_2^4). \quad (2.7)$$

If both surfaces, 1 and 2, behave as ideal blackbodies $\epsilon_1 = \epsilon_2 = 1$, the fraction of Eq. 2.7 becomes unity. If one of the surfaces has a low-e coating with $\epsilon_1 = 0.05$, the fraction of Eq. 2.7 decreases by about a factor of 20 [8]. However, if both of the surfaces have a

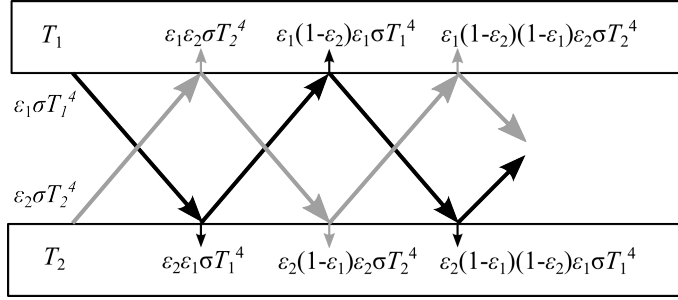


Figure 2.4: Radiative heat transfer between two parallel infinite surfaces 1 and 2.

low-e coating with $\epsilon_i = 0.05$, the additional improvement is only of a factor of 2. Since additional low-e coatings would decrease the solar transmittance, it is favorable to use only one low-e coating for each gap of the glazing unit.

The application of a low-e coated glass pane in a solar-thermal flat-plate collector exhibits special requirements for the optical properties of the low-e coating. The following figures show simulated efficiency curves of a double-glazed collector for various optical parameters of the low-e coating [46]. The efficiency curves were calculated for an inclination angle of 45° , an ambient temperature of 20°C and low solar irradiance of 600 Wm^{-2} . The collector consists of a low-iron, AR coated outer glass pane ($\tau_{\text{sol}} = 91\%$, $\rho_{\text{sol}} = 8\%$, and $\epsilon_{\text{IR}} = 84\%$), a low-e coating on the inner glass pane at position 3 of Fig. 1.1 (parameters varied), and a selective absorber ($\alpha_{\text{sol}} = 94\%$, $\epsilon_{\text{IR}} = 6\%$). One out of the optical parameters of the low-e coating such as the solar absorptance and the reflectance, as well as the infrared emissivity is varied while the other two parameters are kept constant at their standard values (black lines in Fig. 2.5). The standard values refer to a commercially available TCO coated glass (KGlassTM from Pilkington), which is used for first prototype collectors in the HGlas project. To evaluate the influence of the optical parameters, the collector efficiency is calculated as a linear function $f(\alpha, \rho, \epsilon)$ with four coefficients b_i ($i = 0, 1, 2, 3$) by using regression analysis

$$\eta_{\Delta T, 600\text{ W}} = b_0 + b_1\alpha_{\text{sol}} + b_2\rho_{\text{sol}} + b_3\epsilon_{\text{IR}}. \quad (2.8)$$

The coefficients represent a weighting of the optical parameters concerning the collector efficiency losses. Table 2.1 shows the coefficients for three different temperature differences between collector fluid and ambient.

Table 2.1: Loss coefficients of collector efficiency according to Eq. 2.8.

ΔT [K]	b_0	b_1	b_2	b_3
70	0.576	-0.355	-0.766	-0.156
90	0.486	-0.352	-0.764	-0.200
105	0.415	-0.370	-0.764	-0.235

The influence of the reflectance on the collector losses is about a factor two higher than the influence of the absorptance. Both parameters exhibit no significant temperature

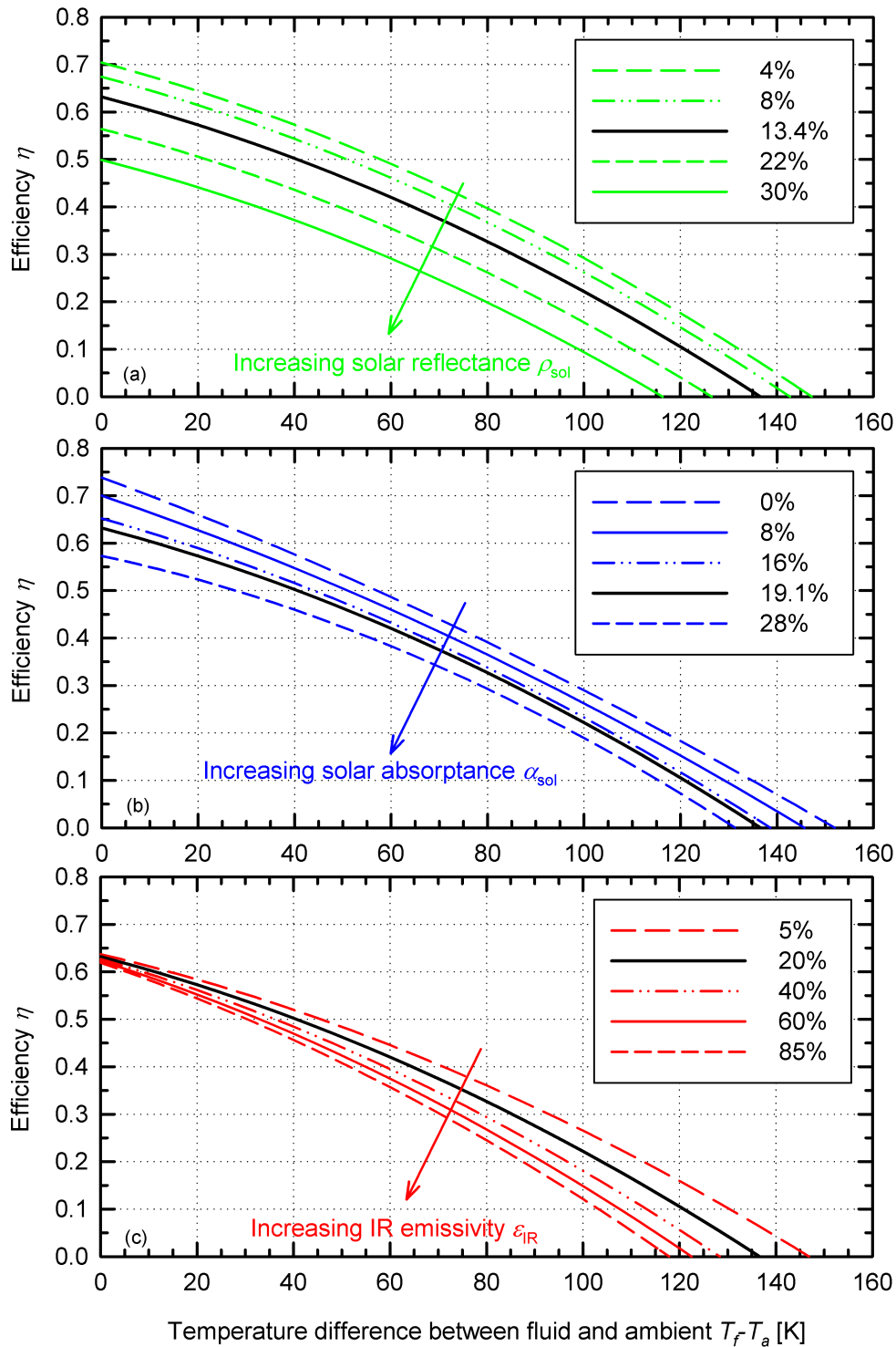


Figure 2.5: Simulated efficiency curves of a double-glazed collector with low-e coating on the inner glass pane with varying optical constants such as (a) solar reflectance, (b) solar absorptance, and (c) infrared emissivity. The simulations are performed for an inclination angle of 45° , an ambient temperature of 20°C , and low solar irradiance of 600 Wm^{-2} . Standard values are represented by black lines.

dependence. In contrast to the reflectance and absorptance, the influence of the emissivity on the collector efficiency is strongly influenced by the temperature difference. If the reflectance of the low-e coating is high, the light leaves the collector before it can reach the absorber. Therefore, η_0 decreased with an increase in reflectance. However, this has no direct influence on the thermal losses of the collector, which becomes obvious from the parallel efficiency curves shown in Fig. 2.5(a). With increasing absorptance, η_0 decreases and the inner glass pane gets hot and acts as a radiative heater for the absorber. The thermal losses are, therefore, influenced by the absorptance of the low-e coating (see Fig. 2.5(b)). The emissivity has an influence on the thermal losses since the thermal radiation of a surface depends strongly on the emissivity and temperature of the surface. In contrast, η_0 is only marginally influenced (see Fig. 2.5(c)). However, concerning the whole thermal losses of a collector, the radiative heat losses play only a minor role in comparison to the convective and conductive heat losses since the radiative exchange is small due to the low-e coatings on the inner glass pane and the absorber. This means that the solar transmittance is of more importance for the development of a low-e coating for the glazing of a flat-plate collector than the infrared emissivity.

2.3 Transparent conducting oxides

Silver coatings are commonly used as selective coatings for insulation of windows since these coatings provide a high visible transmittance and a very low infrared emissivity [10]. The spectral transmittance of a film $\tau(\lambda) = \exp(-4\pi kd\lambda^{-1})$ is limited by the material's extinction coefficient k , the film thickness d and the wavelength of light λ [39]. Due to the high extinction coefficient of silver ($k = 4.15$ at $\lambda = 653$ nm, from Ref. [47]), the film thickness has to be smaller than 20 nm. By reducing the film thickness, the transmittance is further increased. However, if the films are too thin, the film properties degrade. The reason is that metal film growth starts with single nuclei and continues with the formation of small islands due to the low interface energy between the glass surface and the metal. Stable film properties are only reached if the percolation threshold is exceeded [10]. However, over the whole solar spectral range, the transmittance of silver coatings is too low for solar-thermal applications. The only way to raise the solar transmittance would be, therefore, the use of grid-like metal films whose holes are big enough to transmit short wavelengths and small enough to reflect long wavelengths [48]. The practical realization of such structures is yet difficult. Another possibility to realize a higher solar transmittance is the use of transparent conducting oxides (TCOs). TCOs are wide band gap semiconductors. Therefore, TCOs are transparent over a wide wavelength range [11]. Figure 2.6 shows typical transmittance spectra of commercially available silver and TCO coating systems [49]. TCO coatings are used in architectural and automotive glazing as low-e coatings

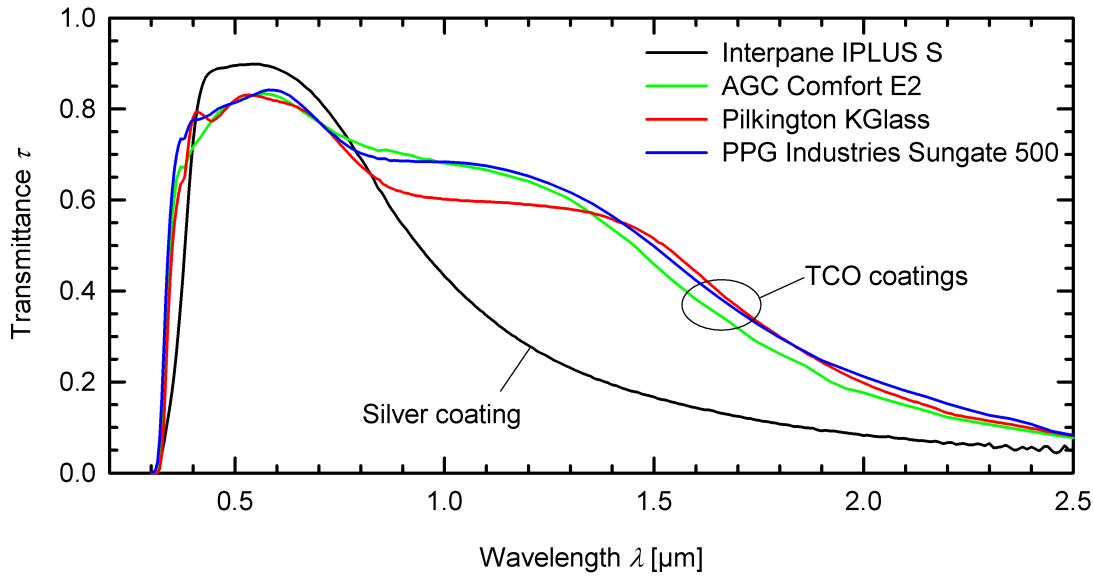


Figure 2.6: Transmittance spectra of commercially available low-e coated glass based on silver and transparent conductive oxides (TCOs) (from Ref. [49]).

[10, 50, 51] as well as in optoelectronic devices such as flat panel displays [30, 50, 52, 53] or photovoltaic devices as transparent electrodes [17, 50, 54–57]. The standard TCO material for optoelectronic devices is indium tin oxide (ITO) due to its favorable electronic properties. However, indium has some disadvantages such as toxicity and high cost because of its scarcity [12]. Therefore, ITO is hardly suitable for large-area applications such as solar-thermal collectors or glazing. In search for alternative low-cost materials, aluminum-doped zinc oxide (ZnO:Al) has attracted much attention due to its good electronic and optical properties as well as low cost, heat stability, and non-toxicity [12, 15]. Therefore, ZnO:Al is probably an appropriate TCO for the application as low-e coating of a collector glazing. In the following, the fundamental structural, electronic, and optical properties are described.

2.3.1 Structural properties of ZnO:Al thin films

Zinc oxide belongs to the II-VI semiconductors and exhibits a direct band gap of 3.2 eV to 3.4 eV [20]. The ZnO crystal is of hexagonal wurtzite structure with the c -axis as symmetry axis, as shown in Fig. 2.7. The structure is made up of two interpenetrated lattices with one lattice of zinc atoms and one lattice of oxygen atoms. The oxygen atoms surround the zinc atoms in a nearly tetrahedral position. The lattice parameters are $a_0 = 0.325$ nm and $c_0 = 0.521$ nm and the density is 5.67 g/cm³ at room temperature. Film growth depends extremely on the deposition technique, the process parameters [50], the element and amount of doping [58, 59], and the substrates used [60, 61]. In the case of sputtering on glass substrates, the growth of ZnO:Al thin films is usually polycrystalline with a columnar structure perpendicular to the substrate [61].

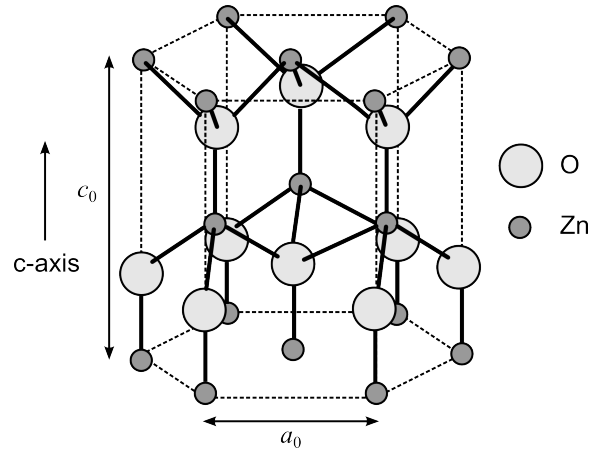


Figure 2.7: Crystal structure of ZnO with the c-axis as symmetry axis.

For sputtering on other substrates such as sapphire, single crystalline film growth was reported [34, 60]. Raising the substrate temperature causes an increase of grain size and crystalline quality [24].

2.3.2 Electronic properties of ZnO:Al thin films

Stoichiometric and intrinsic ZnO exhibits only a low free-carrier concentration of approximately 10^{15} cm^{-3} and a high resistivity [62]. The Fermi level lies inside the band gap while doping generates states near the valence or conduction bands. The energy required for the excitation of free carriers is reduced. ZnO films usually exhibit n-type conductivity while successful p-type doping is also reported [63, 64]. However, p-type ZnO shows lower conductivity and is, therefore, not applicable as low-e coating. For n-type doping, intrinsic and extrinsic doping are distinguished.

Intrinsic doping

Intrinsic doping is caused by the non-stoichiometry of the films [11, 20]. An under-stoichiometric film growth with interstitial zinc ions or oxygen vacancies causes the occupation of states below the bottom of the conduction band with weak bounded valence electrons of the zinc atoms which results in n-type conductivity. Atomic hydrogen is also known to be always embedded into the ZnO crystal as interstitial atom during film growth [20]. There, hydrogen binds to oxygen forming an O-H group and causes n-type conductivity. The hydrogen concentration depends on the film growth and reaches $5 \cdot 10^{16} \text{ cm}^{-3}$ in single crystals or $1 \cdot 10^{20} \text{ cm}^{-3}$ in sputtered films [65]. For intrinsic doping, free-carrier concentrations up to $3 \cdot 10^{20} \text{ cm}^{-3}$ were reported [66]. However, the conductivity of intrinsically doped ZnO films shows no sufficient thermal stability [67, 68] since oxygen vacancies are filled by ambient oxygen and hydrogen is removed by annealing in oxidic atmosphere [69]. For the application as low-e coating in a solar-thermal flat-plate collector, it is necessary that the films provide long-term

heat stability. Therefore, intrinsically doped ZnO films are not applicable.

Extrinsic n-type doping

The conductivity of ZnO is increased by orders of magnitude in comparison to undoped films by extrinsic doping with trivalent atoms such as aluminum, boron, gallium, or indium [11]. These atoms are embedded on zinc lattice sites. Heptavalent fluorine and chlorine atoms are also known to be extrinsic dopants on oxygen lattice sites [20]. The electrons of the dopant atoms, which are not involved for the bonding, cause the raise of conductivity. The amount of doping is limited by the solubility of the dopant atoms in ZnO. Free-carrier concentrations up to $1.5 \cdot 10^{21} \text{ cm}^{-3}$ are possible [62]. At higher dopant concentrations, a segregation of the dopant occurs in the form of dopant-oxide clusters at the grain boundaries. These clusters build an amorphous and non-conducting phase and lower the conductivity of the films [70].

The structure and morphology of the films are strongly influenced by the element and amount of doping. The physical and chemical properties of the dopant atoms should, therefore, fit to those of the zinc atoms [71, 72]. Gallium is known to be an excellent dopant since the ion radius is very similar to zinc, and gallium cause no significant lattice defects [17]. Also, aluminum is often used as a dopant due to its good electronic and optical properties. During film growth, it is necessary to avoid the oxidization of the dopants [73]. Since the standard enthalpy of formation is much more negative for Al_2O_3 ($\Delta_f H_{\text{solid}}^\circ = -1675.7 \text{ kJ/mol}$) than that for ZnO ($\Delta_f H_{\text{solid}}^\circ = -350.5 \text{ kJ/mol}$) [74], reactive film-growth processes have to be controlled carefully. The thermal stability of extrinsically doped ZnO is much higher than that of intrinsically doped ZnO, but oxidization of the dopant atoms near the grain boundaries and a decrease of conductivity may also occur because of annealing at high temperatures in oxidizing atmosphere [71, 75, 76].

Band structure

The band structure of undoped ZnO exhibits three doubly degenerated valence bands due to spin-orbit and crystal-field interaction [31]. The valence bands are completely filled with electrons and the Fermi level lies inside the gap, so that the conduction band is empty. The excitation energy required for a valence electron to reach the conduction band is E_{g0} (see Fig. 2.8 (a)). N-type doping generates states near the bottom of the conduction band, which build an own donator band at high doping concentrations. The Fermi level lies inside this band. By increasing the doping concentration, the donator band and the Fermi level are shifted up towards the conduction band. If a critical free-carrier concentration N_{crit} is reached, the donator band merges with the conduction band [77, 78]. Then, the TCO becomes a degenerated semiconductor. The conductivity of degenerated semiconductors is almost as high as that of metals. The

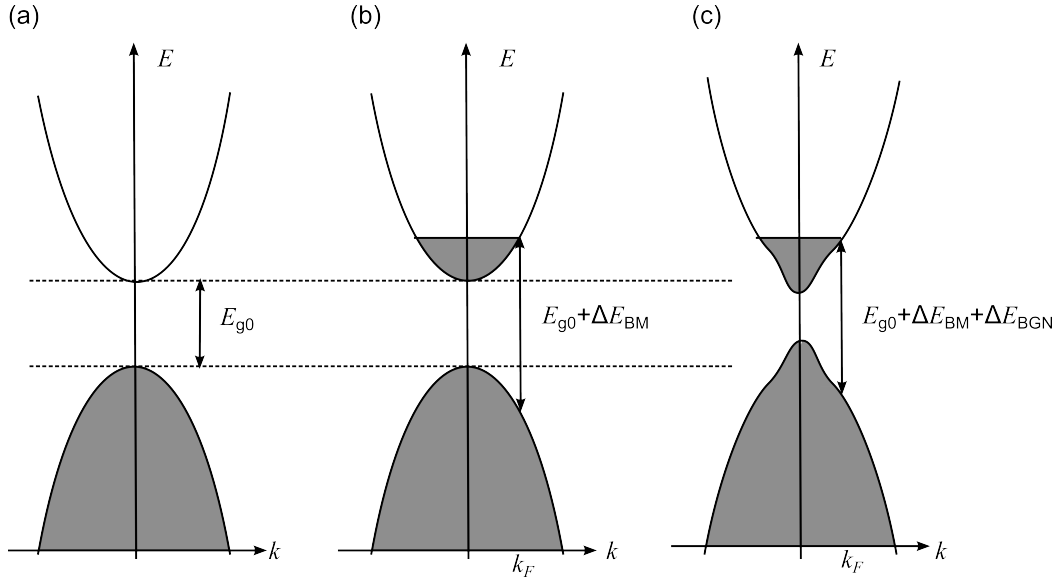


Figure 2.8: Schematic representation of the band structure of (a) undoped ZnO as well as of degenerately doped ZnO considering (b) the Burstein-Moss (BM) shift and (c) additionally a band-gap narrowing (BGN) (according to Sernelius et al. [77]).

critical free-carrier concentration is defined by the Mott criterion [79]

$$(N_{\text{crit}})^{1/3} a_B^* \approx 0.2, \quad (2.9)$$

where $a_B^* = (4\pi\hbar^2\epsilon_0\epsilon_s) / (e^2m_e^*)$ denotes the effective Bohr radius with the static dielectric constant ϵ_s , the permittivity of vacuum ϵ_0 , and the effective mass of the electrons in the conduction band m_e^* . The critical free-carrier concentration of zinc oxide depends on the values used for the static dielectric constant and the effective mass and is $N_{\text{crit}} \approx 1.1 \cdot 10^{18} \text{ cm}^{-3}$ if $\epsilon_s = 8.75$ [80] and $m_e^* = 0.24m_0$ [81, 82] with m_0 as the free-electron mass are assumed. This represents a relatively low value for doped ZnO thin films. Therefore, most of the films show a degenerated behavior. If the semiconductor is degenerated, many states in the conduction band are filled and due to the Pauli principle, valence electrons have to be excited into free states of the conduction band. For optical transitions, the wave vector k has to be conserved. Therefore, the transition occurs at the Fermi wave vector $k_F = (3\pi^2N_e)^{1/3}$ and not at the Γ point ($k = 0$) of the Brillouin zone (Fig. 2.8 (b))[77]. As a consequence, the energy required for the valence electrons to reach free states in the conduction band is [83, 84]

$$E_g = E_{g0} + \Delta E_{BM} \quad (2.10)$$

$$\Delta E_{BM} = \frac{\hbar^2 k_F^2}{2} \left(\frac{1}{m_h^*} + \frac{1}{m_e^*} \right), \quad (2.11)$$

with the so called Burstein-Moss (BM) shift ΔE_{BM} and the effective mass of the valence holes m_h^* and conduction band electrons m_e^* . The increase of the band gap depends on the curvature of the conduction and valence band. With the effective mass approxima-

tion, the band structure information is substituted in the effective mass value, which allows the description of the crystal electrons as quasi-free electrons [85]. Usually, one has to distinguish between the conductivity effective mass m_c^* and the density of states effective mass m_{DOS}^* [86]. However, for ZnO, it is reported that both masses are equal to each other since ZnO exhibits a single-valley minimum in the conduction band at the center of the Brillouin zone and the constant-energy Fermi surface is of spherical nature [21, 86]. In the following, the effective mass of the electrons is represented again by m_e^* and a differentiation of both types of effective masses is not necessary.

Due to high doping, the curvature of the conduction band is of a non-parabolic nature [35, 51, 78]. In order to take account of the non-parabolicity of the conduction band, the effective-mass model of Pisarkiewicz et al. [87] is often used, which describes the dependence of the electron-effective mass on the free-carrier concentration in a degenerated semiconductor [35, 78, 82, 88]. Pisarkiewicz et al. used the following approach to take account of an energy-dependent effective mass value:

$$\frac{\hbar^2 k^2}{2m_0^*} = E + CE^2, \quad (2.12)$$

with the effective mass m_0^* at the bottom of the conduction band and a constant non-parabolicity factor C . According to this approach, the electron effective mass at the Fermi level is

$$m_e^* = m_0^* \left[1 + 2C \frac{\hbar^2}{m_0^*} \left(3\pi^2 N_e \right)^{2/3} \right]^{1/2}. \quad (2.13)$$

Besides the band-gap widening due to conduction band filling, a band-gap narrowing (BGN) occurs, which is caused by many-body effects such as exchange and correlation interaction due to spin statistics and Coulomb repulsion [51, 77, 78, 89]. This results in a downward shift of the conduction band. An additional downward shift occurs due to a relaxation of the electron density around the positive charged dopant impurities. As a consequence, the band structure is distorted and additional band tailing occurs, which lowers the band gap (Fig. 2.8 (c)). There are different theoretical analyses on band-gap renormalization [78, 89, 90]. Inkson [90] assumed that the impurity ions build a uniform neutralizing background and the electrons filled the conduction band. Inkson derived the self-energy correction for the conduction band electrons due to electron-electron and electron-ion interaction by the use of a plasmon-pole approximation and Thomas-Fermi expression for the dielectric function. The following equations in SI-units describe the contribution to the band-gap shift of the electron-electron interaction

$$\Delta E_c^{ee} = -\frac{e^2 k_F}{2\pi^2 \epsilon_s \epsilon_0} - \frac{e^2 k_{\text{TF}}}{8\pi \epsilon_s \epsilon_0} \left[1 - \frac{4}{\pi} \arctan \left(\frac{k_F}{k_{\text{TF}}} \right) \right], \quad (2.14)$$

and the electron-impurity interaction

$$\Delta E_c^{ei} = -\frac{e^2 N_e}{\epsilon_s \epsilon_0 a_B^* k_{\text{TF}}^3}, \quad (2.15)$$

with the Thomas-Fermi screening wave vector $k_{\text{TF}} = (4k_F/\pi a_B^*)^{(1/2)}$. The entire shift of the absorption edge is $\Delta E = \Delta E_{\text{BM}} + \Delta E_{\text{BGN}}$, with $\Delta E_{\text{BGN}} = \Delta E_c^{ee} + \Delta E_c^{ei}$. At low free-carrier concentrations, band-gap narrowing has only a minor effect, but becomes more important at higher free-carrier concentrations. However, for ZnO:Al thin films, the Burstein-Moss shift outweighs the band-gap narrowing. As a consequence, the band-gap energy increases with increasing free-carrier concentration, as will be shown in Sec. 3.3.5.

Free-carrier transport

One simple model for the free-carrier transport in conducting materials is the theory of Drude [91], which describes the free carriers as electron gas. Electron-electron interactions are not taken into account. However, the diffusion motion of the free carriers is influenced by scattering at for instance ions, defects, or impurities. Scattering is described by a mean scattering time

$$\langle \tau_e \rangle = \frac{m_e^* \mu_e}{e}, \quad (2.16)$$

which corresponds to the time between two collisions and depends on the elementary charge e , the effective mass m_e^* , and free-carrier mobility μ_e . The simple Drude model does not differentiate between different scattering phenomena and their dependence on temperature, free-carrier, or defect concentration. Therefore, the Drude model often fails in describing TCO materials [11, 36, 92–94]. In the following, the different scattering phenomena will be discussed.

- **Ionized impurity scattering:** Ionized impurities are caused by zinc interstitials or oxygen vacancies (intrinsic doping) as well as by extrinsic doping with foreign atoms on lattice sites [11, 15, 92, 93]. Due to the exchange of electrons of the dopants with the valence or conduction band of ZnO, the dopants get charged and their electrostatic field is not screened completely by the free carriers. The interaction of the free carriers with the remaining electrostatic field causes the scattering. Brooks and Herring [95, 96] published a method for calculating the mobility in dependence of ionized impurity scattering which is valid for carrier concentrations up to $5 \cdot 10^{18} \text{ cm}^{-3}$ [20]. The agreement of the model with experimental data can be improved by taking into account the degeneracy [97, 98] and the non-parabolicity of the conduction band [20, 98]. Ionized impurity scattering is usually the dominant scattering phenomenon at free-carrier concentrations of $N_e > 1 \cdot 10^{20} \text{ cm}^{-3}$. For degenerated thin films, Johnson and Lark-Horovitz [99]

showed that the ionized impurity scattering is independent of temperature. However, at lower carrier-concentrations or higher temperatures also other scattering phenomena become important.

- **Grain boundary scattering:** This scattering phenomenon plays a dominant role for polycrystalline ZnO films [11, 15, 100, 101] with free-carrier concentrations of $N_e < 1 \cdot 10^{20} \text{ cm}^{-3}$. The boundaries show a crystal disorder with defects and high interface-state concentrations, which are able to trap and scatter free carriers of the bulk of the grain. Grain boundaries have also the tendency to adsorb oxygen and water molecules. Due to the interface states, a space charge region is built in the grain boundaries, which causes band bending and potential barriers. These potential barriers lower the electronic transport since only tunneling or thermal excitation of electrons is the possible overcoming of the barriers. With increasing carrier concentration, the width of the barriers decreases, which is the reason why grain boundary scattering is not significant for degenerated films. Grain boundary scattering is described by a model developed by Seto [102].

Besides ionized impurity and grain boundary scattering other types of scattering of the free carriers such as lattice scattering, neutral impurity or electron-electron scattering occur. However, the electronic transport in degenerated TCOs is dominated by ionized impurity and grain boundary scattering [98]. Intrinsic ZnO single crystals exhibit free-carrier mobilities up to $200 \text{ cm}^2/\text{Vs}$ and resistivities of $1 \text{ }\Omega\text{cm}$ to $10 \text{ }\Omega\text{cm}$ [62]. The mobility is limited by phonon scattering. For extrinsic-doped, polycrystalline ZnO, free-carrier mobilities of $\leq 60 \text{ cm}^2/\text{Vs}$ at $N_e \approx 1 \cdot 10^{20} \text{ cm}^{-3}$ are reported [62]. At higher free-carrier concentrations, the mobility is limited by ionized impurity scattering and reaches mobilities of $5 \text{ cm}^2/\text{Vs}$ to $40 \text{ cm}^2/\text{Vs}$ [52, 62].

2.3.3 Optical properties of ZnO:Al thin films

The optical properties of ZnO:Al thin films, taking into account all absorption mechanism, are characterized by the dielectric function of ZnO:Al. Many different ways of modeling the dielectric function are reported [30–36]. However, some of the dielectric function models failed in describing the measured spectra of this thesis. Therefore, the development of an appropriate dielectric function model is the central part of this thesis and will be presented in detail in Sec. 3.2. Here, only the fundamental optical properties of ZnO:Al thin films are shown.

As a result of the wide band gap, ZnO exhibits a high transmittance in the visible and near infrared spectral range. Doped ZnO also has a high conductivity wherefore ZnO is an interesting material for optoelectronic devices [30, 50, 52]. The free carriers cause a high reflectance in the infrared spectral range and therefore a low emissivity. The optical properties are strongly influenced by the electronic properties, the band structure, and morphology of the films. The transmittance and reflectance spectra of Fig. 2.9

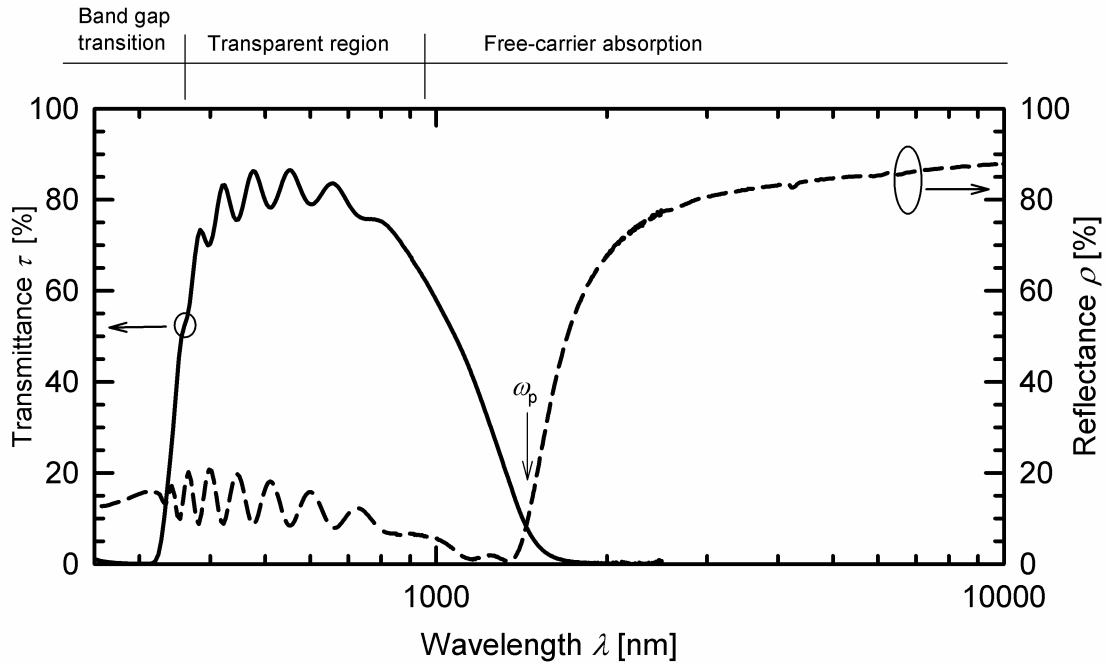


Figure 2.9: Transmittance (solid line) and reflectance (dashed line) spectra of a ZnO:Al thin film on glass.

make obvious that there are three characteristic ranges on the wavelength scale. High energetic photons as from the UV region are needed to excite valence electrons into empty states of the conduction band. The optical gap depends also on the free-carrier concentration due to occurring band-gap shifts and conduction band filling as discussed already in Sec. 2.3.2. Therefore, the UV absorption depends on the band structure and the amount of doping [78]. In addition to the fundamental absorption, ZnO shows a strong excitonic interaction, which causes excitonic absorption peaks near the absorption threshold [31–34, 103]. The excitons are also influenced by the temperature and screening due to the free-carrier concentration [33, 104]. In the visible and near infrared wavelength scale, ZnO and ZnO:Al thin films are transparent since the energy of the photons is too low to excite valence electrons into empty states of the conduction band. The transmittance and reflectance spectra show interference oscillations due to coherent multiple reflections at the air-film and film-substrate interfaces, which depend on the refractive index and film thickness. As a result of doping, free-carrier absorption in the near-infrared spectral range takes place. At these photon energies, the electrons in the conduction band can follow the light field. At high free-carrier densities, the electrons in the conduction band behave as a free-electron gas similar to metals. If the free-electron gas is displaced against the background of the positive charged ions of the solid, an electric field is build which carries a restoring force on the electrons and causes a collective longitudinal oscillation of the free-electron gas [105]. The equation of motion of the electron gas equals the equation of a harmonic oscillator. Transversal natural oscillations of the electron gas do not occur due to the missing restoring force in transversal direction. The longitudinal resonance frequency of the free-electron gas

is called plasma frequency and the quanta of the plasma oscillation are called plasmons since the electrons and the ions of the material build a plasma. If the frequency of the incident light equals the resonance frequency of the electron gas, plasmons are excited and intra-band absorption inside the conduction band occurs. At lower light frequencies, the oscillating electrons reflect the incident light waves and cause low emissivity in the infrared spectral range. The resonance frequency of the electron gas is defined by the Drude theory as [11, 106]

$$\omega_D = \left(\frac{e^2 N_e}{\epsilon_0 m_e^*} \right)^{1/2}, \quad (2.17)$$

where N_e is the free-carrier concentration and ϵ_0 denotes the permittivity of vacuum. If also scattering of the free electrons is taken into account, a damping $\gamma_D = 1 / \langle \tau_e \rangle$ of the oscillating electron gas occurs and the longitudinal plasma frequency $\omega_p = \sqrt{\omega_D^2 / \epsilon_\infty - \gamma_D^2}$ differs from the Drude frequency ω_D [94], with ϵ_∞ as the high-frequency dielectric constant, which describes the contribution of the background of the positive charged ions. At high free-carrier densities, the plasma edge shifts to higher frequencies. The infrared reflectance and emissivity is influenced by the conductivity of the films and therefore by the free-carrier concentration and the mobility. Figure 2.10 shows simulated transmittance and reflectance spectra where the free-carrier concentration and mobility are varied independently from each other to study the influence of both parameters (band-gap shifts are not taken into account for this simulation). The free-carrier concentration determines the plasma edge as well as the maximum achievable infrared reflectance [11]. The absorption peak, which results from $\alpha(\lambda) = 1 - \tau(\lambda) - \rho(\lambda)$, shifts with increasing carrier concentration to smaller wavelengths and gets narrower. In contrast, the mobility affects the gradient of the transmittance and reflectance spectra as well as the maximum achievable infrared reflectance. With increasing mobility, the absorption peak gets smaller and narrower but stays at the same wavelength position. In degenerated films, the mobility is not independent but strongly influenced by the free-carrier concentration due to scattering at ionized dopants. Therefore, the optimization potential of the electronic parameters is limited [100, 107].

The application in a solar-thermal flat-plate collector requires a high solar transmittance and at the same time, a sufficient infrared reflectance, which is determined by the conductivity of the film. Usually, one has to compromise between a high solar transmittance and a high conductivity since both requirements are conflicting [21]. The sheet resistance of the films $R_{\text{sheet}} = (N_e \mu_e e d)^{-1}$ depends on the free-carrier concentration N_e and mobility μ_e as well as on the film thickness d [11]. Increasing film thickness would lower the solar transmittance because of absorption, as stated by the Lambert-Beer law [39]. As shown in Fig. 2.10, a low free-carrier concentration would be favorable to reach a high solar transmittance since the plasma edge shifts to the infrared region with decreasing free-carrier concentration. However, decreasing the free-carrier con-

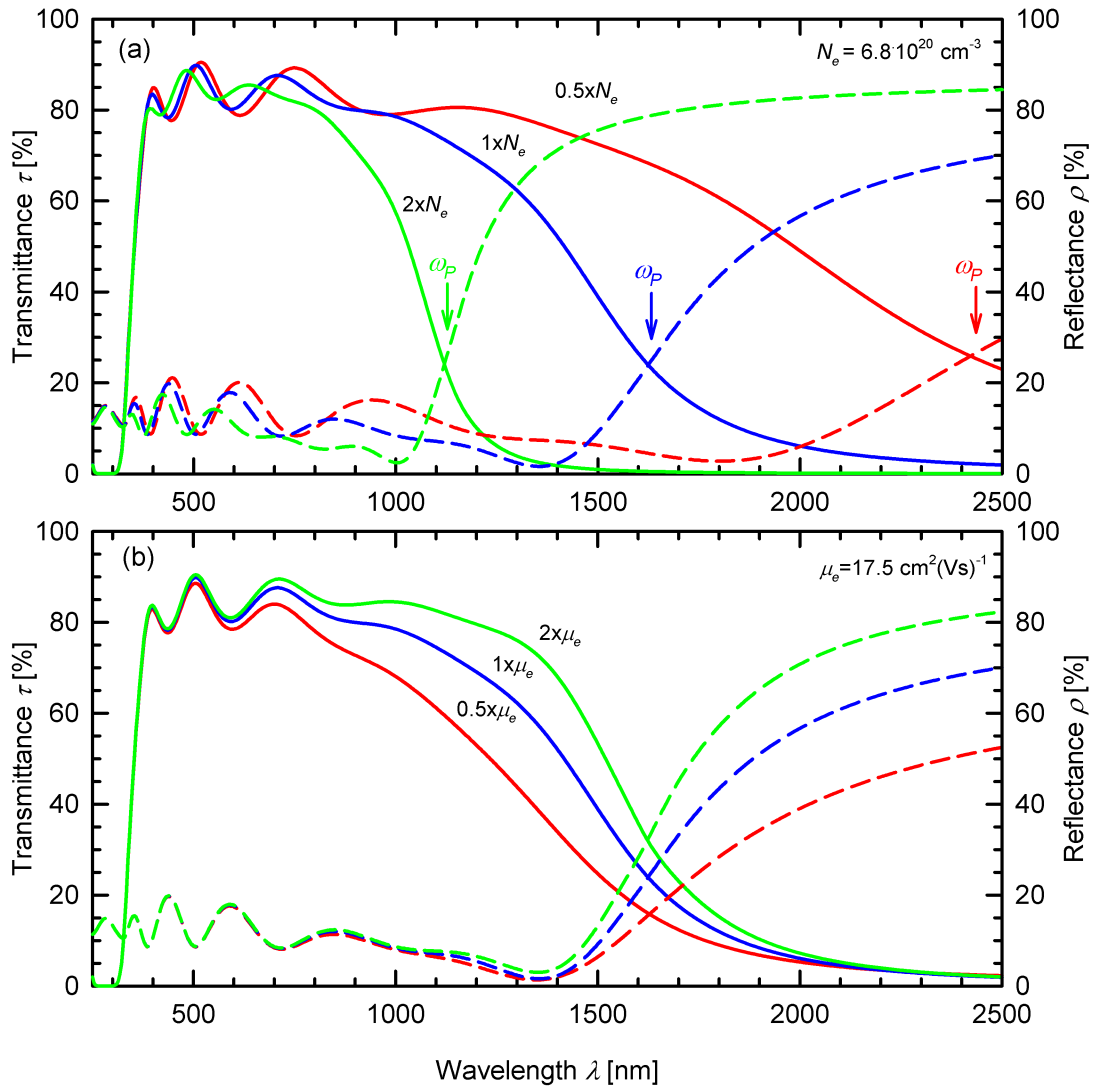


Figure 2.10: Simulated transmittance (solid lines) and reflectance (dashed lines) spectra for varying free-carrier concentration and mobility.

centration results in a decrease of conductivity. The only way to realize a sufficient conductivity and keep a high solar transmittance is to increase the free-carrier mobility [21]. Decreasing the free-carrier concentration may reduce ionized-impurity scattering and cause an increase in mobility [15, 50, 52]. However, other scattering sources also have to be limited. Therefore, an optimization of the process and film growth parameters as well as a compromise concerning the film thickness, free-carrier concentration, and transmittance are required.

2.4 Antireflective coating systems

The behavior of light in vacuum as well as in matter is explained by the Maxwell equations [39]. The Maxwell equations for an isotropic, linear, homogeneous, and not

ferroelectric or ferromagnetic medium are

$$\nabla \cdot \vec{E} = \frac{\sigma}{\epsilon_m} \quad (2.18)$$

$$\nabla \cdot \vec{B} = 0 \quad (2.19)$$

$$\nabla \times \vec{E} = -\frac{\partial \vec{B}}{\partial t} \quad (2.20)$$

$$\nabla \times \vec{B} = \mu_m \sigma \vec{E} + \mu_m \epsilon_m \frac{\partial \vec{E}}{\partial t}, \quad (2.21)$$

with the electric \vec{E} and magnetic \vec{B} field vectors, the electric conductivity σ , the permittivity ϵ_m , and the permeability μ_m of the material, and the time t . Equation 2.18 represents Gauss's law and Eq. 2.19 denotes that magnetic monopoles do not exist. Faraday's induction law and Ampère's law modified by Maxwell are given by Eqs. 2.20 and 2.21, respectively. For the propagation of light in vacuum, σ is zero and the permittivity ϵ_0 and permeability μ_0 of vacuum have to be used instead of $\epsilon_m = \epsilon_0 \epsilon$ and $\mu_m = \mu_0 \mu$, with the relative permittivity ϵ and permeability μ . The Maxwell equations are spatial and temporal coupled equations. Based on the Maxwell equations, the homogeneous wave equations for an electromagnetic wave inside an isotropic, linear and homogeneous medium are given by [106]

$$\nabla^2 \vec{E} - \mu_m \epsilon_m \frac{\partial^2 \vec{E}}{\partial t^2} - \mu_m \sigma \frac{\partial \vec{E}}{\partial t} = 0 \quad (2.22)$$

$$\nabla^2 \vec{B} - \mu_m \epsilon_m \frac{\partial^2 \vec{B}}{\partial t^2} - \mu_m \sigma \frac{\partial \vec{B}}{\partial t} = 0. \quad (2.23)$$

If a non-conducting medium is assumed with $\sigma = 0$, Eqs. 2.22 and 2.23 are further simplified. The solutions of the wave equations and the Maxwell equations are plane transversal waves with

$$\vec{E} = \vec{E}_0 \exp [i (\vec{k} \cdot \vec{r} - \omega \cdot t)] \quad (2.24)$$

$$\vec{B} = \vec{B}_0 \exp [i (\vec{k} \cdot \vec{r} - \omega \cdot t)], \quad (2.25)$$

with the wave vector $\vec{k} = \vec{E} \times \vec{B}$. Due to the interaction of the light with the medium, a phase shift occurs and the phase velocity of the light inside the medium is $v = 1/\sqrt{\mu_m \epsilon_m} = c/N$ with the velocity of light in vacuum $c = 1/\sqrt{\mu_0 \epsilon_0}$ and the complex refractive index $N = \sqrt{\mu \epsilon}$.

Incident light on an interface between two media is partly reflected according to the law of reflection and partly refracted according to the law of refraction of Snellius. The fraction of light that is reflected and transmitted at an interface depends on the angle of incidence θ_i and the complex refractive indices $N = n + ik$ of the neighboring media, with the real refractive index n and the extinction coefficient k . The light waves have to fulfill the boundary conditions of the electromagnetism, which require that the

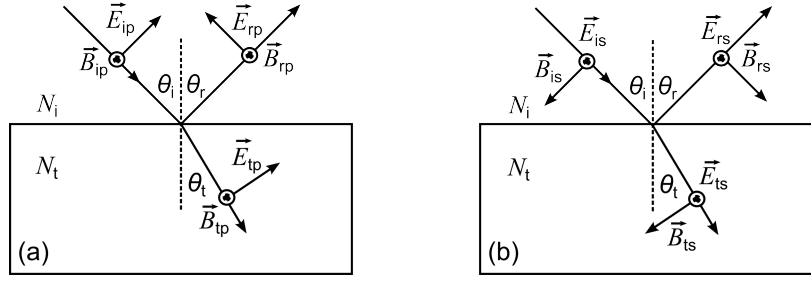


Figure 2.11: Electric \vec{E} and magnetic \vec{B} field vectors for parallel (a) and perpendicular (b) polarized light at an interface of two media. The magnetic field vector \vec{B} in (a) and the electric field vector \vec{E} in (b) are perpendicular to the plane of the paper and are pointing to the reader (according to Ref. [106]).

components of the electric and magnetic fields of the wave which are parallel to an interface between two media are continuous at the interface if non-magnetic media are assumed. The Fresnel equations describe the amplitude reflection $r_{p,s}$ and transmission coefficients $t_{p,s}$ of parallel (subscript p) and perpendicular (subscript s) polarized light according to the plane of incidence at the interface of the two media. The Fresnel equations are

$$r_s \equiv \left(\frac{E_{0r}}{E_{0i}} \right)_s = \frac{N_i \cos \theta_i - N_t \cos \theta_t}{N_i \cos \theta_i + N_t \cos \theta_t} \quad (2.26)$$

$$t_s \equiv \left(\frac{E_{0t}}{E_{0i}} \right)_s = \frac{2N_i \cos \theta_i}{N_i \cos \theta_i + N_t \cos \theta_t} \quad (2.27)$$

$$r_p \equiv \left(\frac{E_{0r}}{E_{0i}} \right)_p = \frac{N_t \cos \theta_i - N_i \cos \theta_t}{N_i \cos \theta_t + N_t \cos \theta_i} \quad (2.28)$$

$$t_p \equiv \left(\frac{E_{0t}}{E_{0i}} \right)_p = \frac{2N_i \cos \theta_i}{N_i \cos \theta_t + N_t \cos \theta_i}, \quad (2.29)$$

where the subscripts i , r and t denote the case of incidence, reflection and transmission, as shown in Fig. 2.11. Using the Fresnel equations, the reflectance ρ and transmittance τ for polarized light are defined by

$$\rho_{p,s} = r_{p,s}^2 \quad (2.30)$$

$$\tau_{p,s} = \frac{N_t \cos \theta_t}{N_i \cos \theta_i} t_{p,s}^2. \quad (2.31)$$

If natural or unpolarized light is considered, the reflectance and transmittance are given by $\rho = (\rho_p + \rho_s)/2$ and $\tau = (\tau_p + \tau_s)/2$. If the difference between the refractive indices of both media is large, the fraction of light, which is reflected, increased. Since reflection and transmission at each interface of an optical system occur, there are multiple reflections inside the system [108]. Figure 2.12 shows a schematic representation of a thin film on a thick substrate. If the film thickness is in the same order of magnitude as the coherence length (spatial and temporal) of the incident light, the reflected light waves of both interfaces of the film can interfere, as shown in Fig. 2.12.

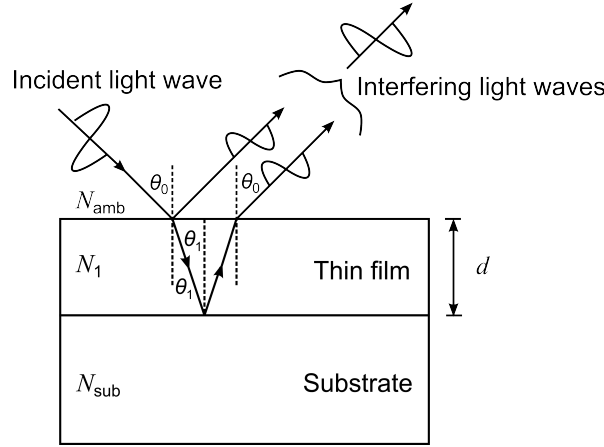


Figure 2.12: Schematic representation of the interaction of light with an optical system consisting of a thin film on a thick substrate (according to Ref. [106]).

Usually, the substrate thickness is thick enough with regard to the coherence length of the incident light (depending on the light source) that the reflected light waves of the substrate show no interference. The transfer-matrix method is a common method to calculate the optical performance of coating systems and can be found in several text books [39, 109] or publications of for instance Rubin [110], Harbecke [111], and Katsidis [112]. The transfer-matrix method treats the propagation of light coherent inside the system of thin layers and takes account of interreflections inside the system and interference effects. The propagation of light through an interface of neighboring media $m - 1$ and m and the propagation through a layer of medium m are described by the matrices

$$D_{m-1}^{-1}D_m = \frac{1}{t_{m-1,m}} \begin{bmatrix} 1 & r_{m-1,m} \\ r_{m-1,m} & 1 \end{bmatrix} \quad (2.32)$$

$$P_m = \begin{bmatrix} \exp(i\delta_m) & 0 \\ 0 & \exp(-i\delta_m) \end{bmatrix} \quad (2.33)$$

with the amplitude transmission $t_{m-1,m}$ and reflection $r_{m-1,m}$ coefficients determined by the Fresnel equations (Eqs. 2.26 – 2.29) for p or s polarized light and the phase thickness $\delta_m = 2\pi d_m N_m / \lambda$. The whole system of M layers is then described by

$$\begin{pmatrix} E_0^+ \\ E_0^- \end{pmatrix} = D_0^{-1} \left[\prod_{m=1}^M D_m P_m D_m^{-1} \right] D_{M+1} \begin{pmatrix} E_{M+1}^+ \\ E_{M+1}^- \end{pmatrix} \quad (2.34)$$

$$= \begin{bmatrix} T_{11} & T_{12} \\ T_{21} & T_{22} \end{bmatrix} \begin{pmatrix} E_{M+1}^+ \\ E_{M+1}^- \end{pmatrix} \quad (2.35)$$

with the field amplitudes of the waves propagating in the right (+) and the left (–) direction. The complex reflection and transmission coefficients of the front and the rear side of the multilayer are obtained by the ratios of the transmitted and reflected

field amplitudes to the incident field amplitude in accordance to the Fresnel equations and the corresponding elements of the transfer matrix T_{ij} . The reflectance $\rho^{+,-}$ and transmittance $\tau^{+,-}$ of each side are given by the square of the corresponding complex coefficients:

$$\rho^+ = (r^+)^2 = \left(\frac{E_0^-}{E_0^+} \right)^2 \Big|_{E_{M+1}^- = 0} = \left(\frac{T_{21}}{T_{11}} \right)^2 \quad (2.36)$$

$$\rho^- = (r^-)^2 = \left(\frac{E_{M+1}^+}{E_{M+1}^-} \right)^2 \Big|_{E_0^+ = 0} = \left(-\frac{T_{12}}{T_{11}} \right)^2 \quad (2.37)$$

$$\tau^+ = (t^+)^2 = \left(\frac{E_{M+1}^+}{E_0^+} \right)^2 \Big|_{E_{M+1}^- = 0} = \left(\frac{1}{T_{11}} \right)^2 \quad (2.38)$$

$$\tau^- = (t^-)^2 = \left(\frac{E_0^-}{E_{M+1}^-} \right)^2 \Big|_{E_0^+ = 0} = \left(\frac{T_{11}T_{22} - T_{12}T_{21}}{T_{11}} \right)^2. \quad (2.39)$$

Harbecke [111] published a formalism to take account of incoherent light propagation in thick layers such as the substrate. With this formalism, the system of thin layers is treated coherently and the transfer matrix is calculated up to the thick layer. In the following, the complex coefficients in the remaining matrices are replaced by their square amplitudes.

To reduce the level of reflection, different methods are possible. Usually, they are based on a better alignment of the refractive indices between the neighboring media [10, 113]. For instance, thin porous SiO_2 layers are effective AR coatings for glass substrates. Due to the voids of the porous layer, the effective refractive index is lower than that for SiO_2 , and its value lies in between the refractive index of air and the glass substrate. The voids have to be small enough otherwise scattering or absorption may occur. Another possibility for the alignment of the refractive indices is gradient coatings [10]. A gradient coating consists of a number of very thin layers, which change their refractive indices only slightly from a value similar to the substrate to a value similar to the ambient. Another method is the use of one or more layers whose thicknesses and refractive indices are aligned in a way that the reflected waves eliminate each other due to destructive interference [10, 113, 114]. The required number of coatings, their thicknesses d_i , and refractive indices N_i depend on the wavelength range where the reflectance should be reduced. The materials which are suitable as AR coatings provide a very low absorption ($k \rightarrow 0$). Therefore, only the real refractive indices are considered in the following. The amplitude and phase requirements for destructive interference of the reflected light waves at one AR coating on a substrate (see Fig. 2.12) are $n_1 = \sqrt{n_{\text{amb}}n_{\text{sub}}}$ and $n_1d_1 \cos \theta_1 = (2m - 1)(\lambda/4)$ (for $m = 1, 2, 3, \dots$), respectively [114]. λ denotes the wavelength for which the AR coating is optimized, and θ_1 is the angle between the light beam inside the medium and the elongated axis of incidence.

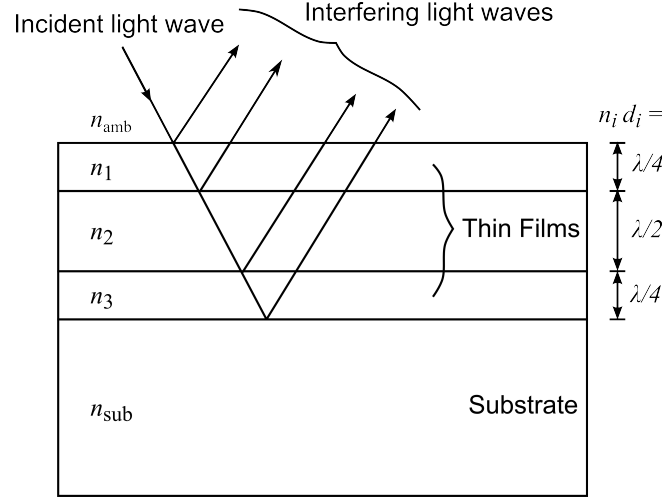


Figure 2.13: Schematic representation of an antireflective (AR) coating system consisting of three thin films on a thick substrate.

For one AR coating on a glass substrate, the refractive index of the coating should be $n_1 = 1.23$. However, there is no coating with such a low refractive index and low absorption available and therefore usually MgF_2 is used since its refractive index is very low, $n = 1.38$ [10]. A system of two AR coatings enables only the reduction of the reflectance in a small wavelength region. For an AR effect in a wider wavelength range, more coatings are necessary. A typical broadband AR coating system consists of a repetition of a two layer stack of two materials with high and low refractive index. These materials are, for example, TiO_2 ($n = 2.1$) and SiO_2 ($n = 1.46$) [10]. In this thesis, the reflectance of the ZnO:Al coating should be reduced in the whole solar spectral range. ZnO:Al , with $n = 1.9$, exhibits a high refractive index and therefore the reflectance is very high. To reach a high transmittance also the interference oscillations have to be eliminated. A coating system with repeated layer stacks of ZnO:Al and another material is not suitable for the application in a flat-plate collector since ZnO:Al has a considerable high free-carrier absorption and the transmittance would be lowered if there would be more than one ZnO:Al layer. A three-layer system with one ZnO:Al layer is more suitable. The amplitude and phase requirements of a three-layer system (see Fig. 2.13) at normal incidence of light are [114]

$$n_1^2 n_{\text{sub}} = n_3^2 n_{\text{amb}} \quad (2.40)$$

$$n_i d_i = \begin{cases} \lambda/4 & \text{for } i = 1, 3 \\ \lambda/2 & \text{for } i = 2 \end{cases} \quad (2.41)$$

The refractive index of the second layer, in this case, the refractive index of the ZnO:Al thin film, is not important for the reduction of the reflectance at the wavelength λ . However, this value influences the reflectance in the neighboring wavelength regions and is therefore not arbitrary. The refractive indices of the first and third layers should

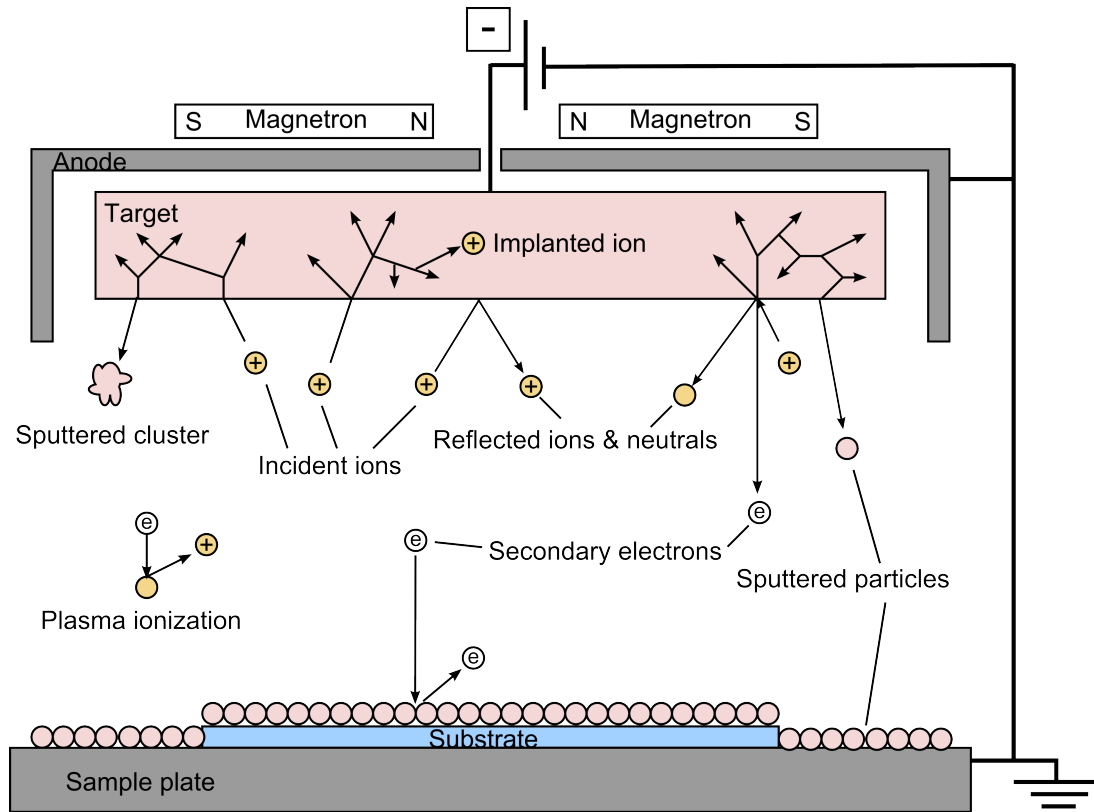


Figure 2.14: Schematic representation of the sputtering process (according to Ref. [116]).

be in the low ($n_1 < 1.5$) and in the middle ($1.6 < n_3 < 1.8$) range in relation to the refractive index of glass $n = 1.5$ and TCO $n = 1.8$ to 2.2 [115]. For the development of the coating system, the knowledge of the optical constants over the whole wavelength range is essential.

2.5 Film deposition

There are a variety of physical and chemical deposition methods for ZnO:Al thin films, such as DC or RF sputtering [12, 15, 24, 25], sol-gel techniques [26], spray pyrolysis [27], plasma-enhanced chemical vapor deposition [28], or pulsed laser deposition [29]. Sputtering of ZnO:Al is the most promising deposition technique for large-area applications since it provides high-quality films with a relatively high deposition rate at moderate substrate temperatures [12]. Flat-plate collector covers have sizes of up to 3 m^2 ; therefore, sputtering is used in this thesis. In the following, the different kinds of sputtering techniques will be introduced.

2.5.1 DC magnetron sputtering

Figure 2.14 represents a schematic sputtering configuration. A vacuum chamber contains two capacitor plates where a target with the coating material is arranged on the cathode and the substrate on the anode. The capacitor plates are, usually, operating

with a DC voltage of several hundreds of volts and the gap of the capacitor is filled with gas. Commonly, inert gas such as argon is used. Due to the electric field in the capacitor, a gas discharge ignites at a sufficient argon pressure and sufficient high field intensity. The ions and electrons are accelerated by the electric field and due to collisions with neutral gas atoms, ionization takes place. A plasma is built where argon atoms, ions, and electrons coexist. The accelerated ions impinge to the target surface and due to a momentum transfer, target atoms or clusters can leave the target. Their kinetic energy of some eV is enough to reach the substrate or the chamber walls. There, the atoms and clusters condensate and build a film. The growing film may be bombard by high-energetic species from the sputtering target and from the plasma, such as oxygen ions and neutral argon atoms, which are repelled from the target surface [25, 117]. The kinetic energy of these species may reach ≈ 100 eV and therefore disturb the film growth.

Sputtered atoms and clusters may collide with plasma particles on their way to the substrate. As a consequence, they lose energy and may not reach the substrate, which lowers the deposition rate. Therefore, small process pressures are favorable. However, at low pressures the plasma may disappear. To keep the plasma glowing, usually magnetic fields are introduced to the plasma in such a way that the plasma electrons are deflected on cyclotron pathways near the target surface [20]. The collisions of the electrons with argon atoms and the ionization are increased since the path of the electrons in the plasma is longer and the plasma stays stable at lower pressures. One disadvantage of so called “magnetrons” is that due to the alignment of the magnetic fields, particles are sputtered only in a small region of the target. This causes an inhomogeneous film deposition [12, 24, 25] and only 20% to 50% of the target material is useable [114]. To overcome this problem, often movable magnetrons or rotatable, cylindrical targets are used [118–120]. Another possibility is to move the sample with respect to the target and deposit dynamically [121]. However, this may influence the film structure and morphology.

DC sputtering is only applicable for conducting targets since the impinging argon ions also transfer their charge to the target. A non-conducting target material such as undoped ZnO, Al₂O₃, or SiO₂ gets highly charged. As a consequence, arcing occurs which may destroy the growing film or even the target. The charged layer on the target surface build an electric field, which screens the outer field. If the electric fields of the charged surface layer and the capacitor cancel each other, the electrons and ions are not accelerated and ionization does not occur any longer which results in a plasma break-down. In this case, another discharge excitation is more applicable.

2.5.2 RF magnetron sputtering

By applying a high-frequency AC voltage with 13.56 MHz, the electrons can follow the AC field while the argon ions cannot, due to their mass inertia. As a consequence,

the target is periodically impinged and charged by the argon ions and the electrons. Due to the high frequency, the inert argon ions move only a short path and cannot neutralize the negative charge of the electrons. The target surface always provides a negative charge which still accelerates the argon ions and keeps the plasma glowing. This effect is called "self biasing" of the cathode.

There are several publications about RF sputtering of ZnO:Al thin films from ceramic ZnO:Al₂O₃ targets [12, 52, 122]. It is reported that RF sputtering provides films with higher free-carrier mobilities and better crystal quality since the bombardment of the growing film with high-energetic species is much lower than that by DC sputtering [117, 123]. However, RF processes with oxidic targets provide a smaller deposition rate of approximately one-half of the deposition rate of DC processes at the same discharge power [117]. The reason is that the acceleration voltage is much lower, and the discharge current is dominated by the electrons, which do not participate in the sputtering process. Therefore, DC sputtering is more applicable for industrial and large area applications and used in this thesis for the ZnO:Al deposition.

2.5.3 Reactive mid-frequency sputtering

Compound materials can be deposited by sputtering from ceramic targets in pure argon atmosphere or by reactive sputtering from metallic targets in a reactive atmosphere [10]. One advantage of using metallic targets is the low cost since the production of ceramic targets is very expensive [22]. Due to the choice of the gas composition, a variety of compounds such as oxides, nitrides, carbides, or mixtures of them are possible. The targets consist usually of pure metals or alloys and are highly conducting. The stoichiometry of the films is controlled by the composition and the amount of the reactive gas. The processes that take place during the sputtering are very complex since there are reactions between the reactive gas with the sputtered particles in the gas phase or of the growing film and with the target. Different sputtering modes are distinguished by varying the reactive gas content, as shown in Fig. 2.15 [10, 124, 125]. If the reactive gas flux is low, metallic particles are sputtered, and the reaction takes place mainly in the gas phase or at the growing film. All the reactive gas ions react with the sputtered particles. By increasing the reactive gas flux, reactions at the target surface occur. As long as the sputtering rate is high enough, the target surface is free of compound particles. If there are more reactive gas ions than required for the sputtered particles, a compound layer on the target surface is built. The discharge voltage is lowered since the sputtering yield has to divide into the sputtering yield of the metal and its reactant. Also the number of the electrons emitted from the target is lowered due to the compound layer. The lower metal-sputtering rate causes a less reactive gas consumption and the increase of the compound layer on the target. The sputtering conditions change only little if the reactive gas flux is further increased. This state is called compound mode. Decreasing of the reactive gas flux results in an hysteresis

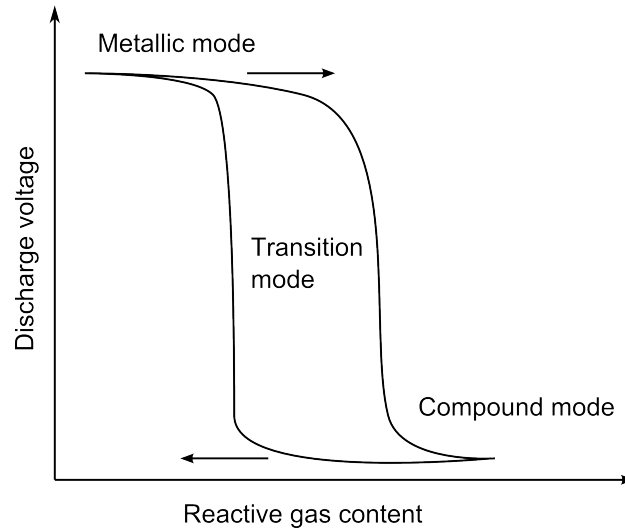


Figure 2.15: Schematic representation of the discharge voltage behavior with varying reactive gas content.

behavior. The target surface is freed of the compound layer at lower reactive gas fluxes because of the lower sputter rate. The transition between the compound and metallic mode is abruptly due to the additional change of the metallic sputtering rate.

This is a problem for materials that should be deposited with reactive gas fluxes within this transition mode, such as for ZnO:Al [22, 126]. Sputtering in the metallic mode yields under-stoichiometric films of high absorptance, and sputtering in the compound mode yields highly transparent films, which provide only a poor conductivity due to oxidation of the Al dopant. Reactive deposition of ZnO:Al is therefore difficult and requires a good process control [18, 22, 50, 126]. One possibility is to control the discharge power and sputter rate to keep a constant oxygen partial pressure, which is measured with a lambda sensor [126]. However, a lambda sensor provides only the possibility to control the oxygen partial pressure and is not applicable for other reactive gases. Another possibility is the usage of a plasma-emission-monitoring (PEM) system [18, 127]. With the PEM system, the plasma emission spectral line of the sputtered metal is detected, whose intensity depends on the metal sputtering rate. By varying the reactive gas flux, the sputtering rate is kept constant. This system is applicable for a variety of gases and metals since only the spectral line changes. However, the sputter configuration used in this thesis does not provide such a process control yet; therefore, the ZnO:Al samples are deposited by non-reactive DC sputtering from ceramic targets. In contrast, the AR coatings presented in this thesis are deposited by reactive sputtering since dielectric materials do not require the deposition in the transition mode. The deposition in the transition mode is, in that case, only favorable if higher deposition rates are required [128]. Sputtering in compound mode yields highly transparent films with low absorption. The advantage of reactive sputtering is the possibility to deposit materials with different optical properties by varying only the composition and amount of the reactive gas. The sputtering process becomes much more complex if two reactive

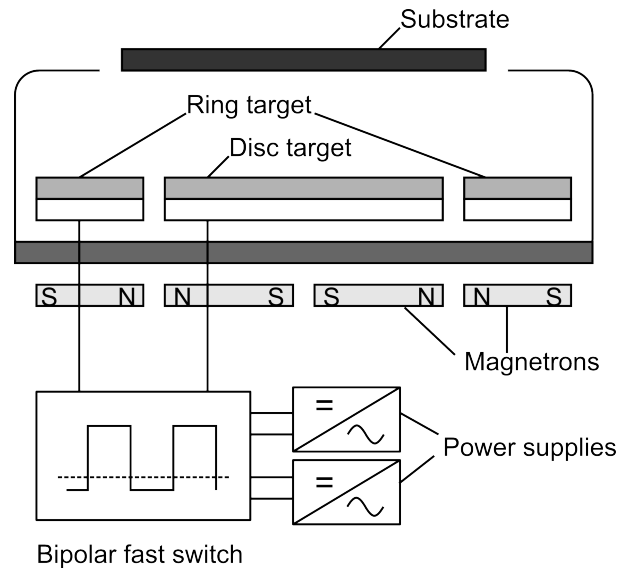


Figure 2.16: Double cathode system for pulsed DC sputtering consisting of a ring and disc target which are operated in bipolar mode (according to Ref. [130]).

gases are used [124]. These processes depend strongly on the reaction enthalpy of both elements with the metal. Usually, oxygen shows a more negative reaction enthalpy than nitrogen. The hysteresis also exhibits another shape than the one shown in Fig. 2.15 if two reactive gases are used.

Since the compound layer formed on the target surface during sputtering in compound mode is non-conducting, problems arise with the charging of the target. Then, arcing or plasma breakdown may occur [114]. Another problem is the so called disappearing anode [10]. The anode is built of the sample holder and the chamber walls. Due to the film deposition, these areas are also coated with non-conducting films, and a long-term stable deposition is not possible. To overcome these problems, another type of discharge is more applicable for reactive processes.

In this thesis, a double cathode system is used, which contains two targets [128–130], as shown in Fig. 2.16. Both are excited by a pulsed DC power in the mid-frequency range. In one half-cycle, one target acts as cathode and the other target acts as anode, and in the next half-cycle they are changed. This configuration is called bipolar mode. Both electrodes are usually electrically isolated from the rest of the chamber. Other configurations use other types of anodes and are explained elsewhere [129, 130]. The frequency is adjustable from 20 kHz to 70 kHz. At these frequencies, also the heavy argon ions can follow the AC field. Charged target regions are effectively discharged in every next half-cycle and arcing does not take place any more. The anode does not change since the targets only change at their erosion areas. Therefore, the processes are very stable over a long time.

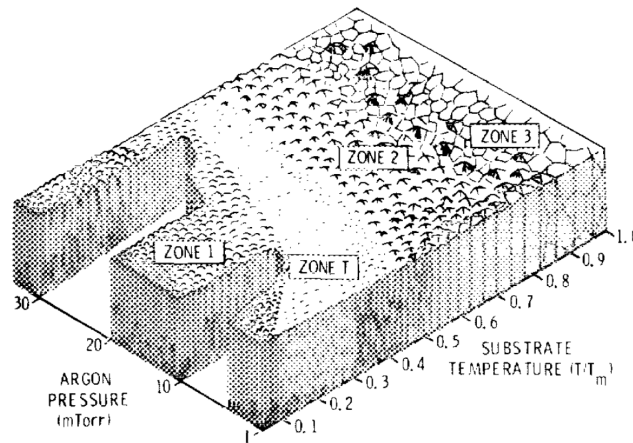


Figure 2.17: Structure zone model for sputtered metal films developed by Thornton (from Ref. [131, 132]).

2.5.4 Film growth

Film growth is influenced by many different physical effects in the plasma and on the substrate and film surface [131, 132]. Due to collisions of sputtered particles with plasma particles, they arrive on the substrate with a special angle and energy distribution, which depends on the process parameters [114]. The energy transfer of the kinetic energy of the sputtered particles to the surface of the substrate or the growing film results in the adsorption of these particles. Most of the sputtered particles are atoms that are able to diffuse on the surface. The only kind of movement of the atoms in the growing film is volume diffusion which requires high excitation energies. Diffusion processes depend on the remaining kinetic energy, the thermal energy of the substrate, and the interaction with other atoms of the surface. Desorption of surface atoms may also occur if the thermal energy of the substrate is high. The growing film may be distorted or resputtered due to a bombardment with highly energetic atoms and ions, which stem from the gas or are repelled and neutralized at the target. In contrast to sputtered atoms, sputtered clusters provide a low mobility and stay usually at the same position of their impact, which causes voids in the growing film. If the growing film exhibits a high surface roughness, shadowing effects become important.

Thornton developed a structure-zone model [131, 132] for the growth of sputtered metal films on the basis of the 3-zone model of Movchan and Demchishin for vapor deposited films [133] (see Fig. 2.17). The Thornton model describes the film structure and morphology as a function of sputter pressure and substrate temperature (normalized to the melting temperature of the metal). Three different zones and one transition zone are distinguished. The film growth in zone 1 shows a film structure with lots of voids because of shadowing effects and low surface diffusion of sputtered particles. The grains are very small. Higher surface diffusion results in dense films with columnar structure, smooth surfaces, and low shadowing effects at zone 2. At higher substrate temper-

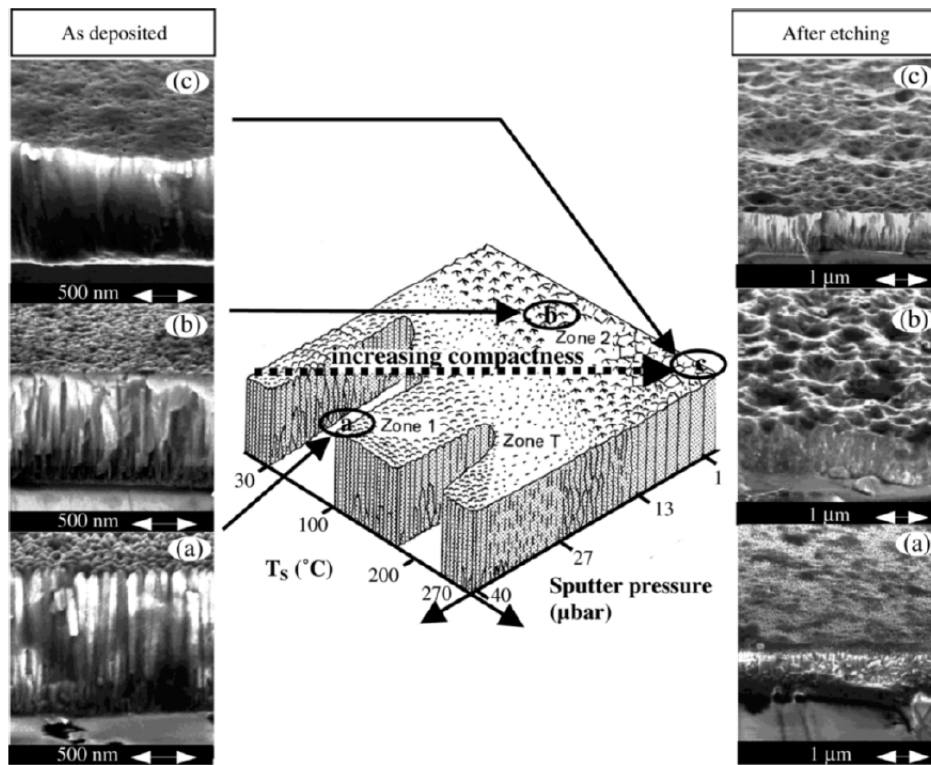


Figure 2.18: Structure zone model for sputtered ZnO:Al thin films and their etching behavior developed by Kluth et al. (from Ref. [19]).

atures the columns expand and defects are mostly at the grain barriers. Both zones are divided by the transition zone, which provides columnar structure with very thin filamentary columns. Due to higher substrate temperatures near the melting point in zone 3, volume diffusion and recrystallization occur, which result in very dense films with bulk properties. The Thornton model demonstrates that with increasing substrate temperature, the transition pressure of the different zones also increased. At higher temperatures, the influence of the pressure becomes less important since the thermal energy excites diffusion processes.

Kluth transferred the Thornton model to the film growth of RF sputtered ZnO:Al thin films and their etching behavior [19] (see Fig. 2.18). In contrast to the Thornton model, ZnO films exhibit a higher pressure dependence. Therefore, Kluth modified the model and changed both the axes. Due to the high melting temperature of 1975 °C of ZnO, the scaling of the temperature axis was also modified. Other differences to the Thornton model are the absence of the transition zone and that zone 3 is not reachable due to the low limit of the substrate temperature in comparison to the melting point. Dense film growth requires low sputter pressures and high substrate temperatures.

3 Analysis of ZnO:Al thin films

3.1 Experimental details

3.1.1 Film deposition

The ZnO:Al thin films are deposited by DC magnetron sputtering in an in-line coater from ceramic targets of ZnO:Al₂O₃ (from Avaluxe) with different Al₂O₃ contents. The target diameter is 200 mm. The in-line coater was developed by Antec GmbH and ISFH and produced by Pfeiffer Vacuum. Figure 3.1 shows a schematic representation of the in-line coater. The in-line coater consists of four vacuum chambers that are connected via vacuum valves. The chambers house different RF and DC sputter sources as well as vapor coating places, which are all on the bottom of the chambers. As a consequence, the deposition takes place from the bottom up to the substrate. In this thesis, only one of two DC magnetron sputter sources (PPS-A 200 from Von Ardenne Anlagentechnik) of chamber four is used, which is connected to a DC generator (PFG 5000 DC from Hüttinger Electronics). The substrates are handled with a graphite carrier on rolls through the in-line coater. Possible sizes of the substrates are 100 × 100 mm², 50 × 50 mm², and 25 × 25 mm². Below the cover of the chambers are the banks of lamps which heat the substrate to a maximum temperature of 400 °C. Several thermocouple elements measure the temperature inside the chamber near the lamps. The in-line coater contains a liquid cooling system inside the chamber walls, which prevents the sputter sources and the chamber outer face from overheating. The pressure before deposition is usually lower than 5 · 10⁻⁴ Pa. During deposition, a mass flow meter for pure argon controls the pressure in the chamber. The target substrate distance is 65 mm. As substrates, float glass (Optifloat from Pilkington) and boron-doped silicon wafers (100) (from Wacker, with polished fronts and lapped rears) are used. The glass substrates have a maximum size of 100 × 100 mm² and 2-inch silicon wafers are used. A typical process takes place as follows: After the inward transfer into chamber one and the pump down of this chamber, the carrier is transferred to the 2nd DC sputter source of chamber four, which is heated by the lamps. The choice of the preheating time of the samples depends on the vacuum quality due to outgassing of the components inside the chamber at high temperatures and may take several hours. To clean the target surface, the target has to be sputtered for some minutes before the deposition on the substrate takes place. This process is called presputtering. To prevent sputtered particles to reach the substrate surface, the carrier stays in a presputtering position. After presputtering, the carrier moves to the sputter position and now the substrate is coated. If a certain film thickness is reached, the process is stopped and the carrier is transferred to chamber one, where it has to cool down before venting the chamber with nitrogen.

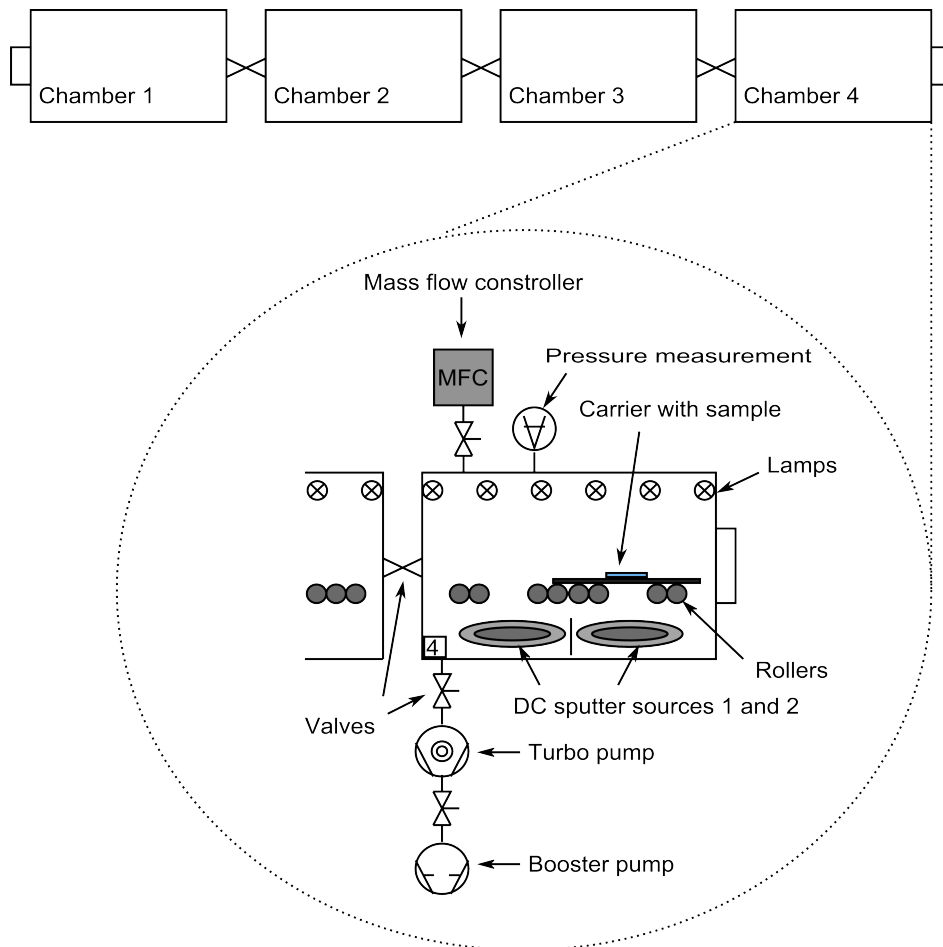


Figure 3.1: Schematic representation of the in-line coater. The sputter source used for the ZnO:Al deposition is arranged in vacuum chamber 4.

In order to optimize the film properties, several parameters such as the substrate temperature, the process pressure, the DC power, the film thickness, as well as the Al_2O_3 content of the targets are varied in this thesis. Table 3.1 shows the range of the varied process parameters of the analyzed sample series.

Table 3.1: Parameters for ZnO:Al deposition.

Parameter	Value
Al_2O_3 content	0.2 wt.%, 1.0 wt.%, and 2.0 wt.%
Substrate temperature	unheated, 150 °C to 400 °C at 50 °C steps
Preheating time	0.5 h to 6 h (depends on outgassing)
Pressure before deposition	$< 5 \cdot 10^{-4}$ Pa
Pressure during deposition	0.3 Pa to 0.6 Pa at 0.1 Pa steps
Discharge power	100 W to 600 W at 100 W steps
Film thickness	100 nm to 800 nm at 100 nm steps

3.1.2 Film analysis

The central part of this thesis is the optical characterization of the samples, which is carried out by spectroscopic ellipsometry and photometry. Simultaneous modeling of the measured spectra with an appropriate dielectric function model enables the determination of the optical constants, the optical band gap, the free-carrier properties as well as the film thickness and surface roughness. In order to verify the reliability of the dielectric function model developed in this thesis, several independent characterization methods for the determination of the electronic and structural properties of the films are used for comparison with the results of the optical modeling. In the following, the characterization methods applied in this thesis are introduced.

Optical characterization

Spectroscopic ellipsometry (SE)

Spectroscopic ellipsometry is a powerful tool for nondestructive characterization of thin films if reliable models for calculating the dielectric function exist. A rotating compensator ellipsometer (M-2000UI from J.A. Woollam, Inc.) records the ellipsometric spectra in the wavelength range from 240 nm to 1700 nm at various angles of incidence. In ellipsometry, the light waves of the light source (a mercury vapor lamp and a deuterium lamp for different spectral regions) pass through a polarizer so that parallel (p) and perpendicular (s) polarized light waves are irradiated onto a sample under different angles of incidence, as shown in Fig. 3.2. With an analyzer, the change in the polarization state by light reflection at the sample surface is measured. The measured ellipsometric values are Ψ and Δ , which are determined from the ratio of the amplitude reflection coefficients r_p and r_s (from Eqs. 2.26 and 2.28) for p - and s -polarizations

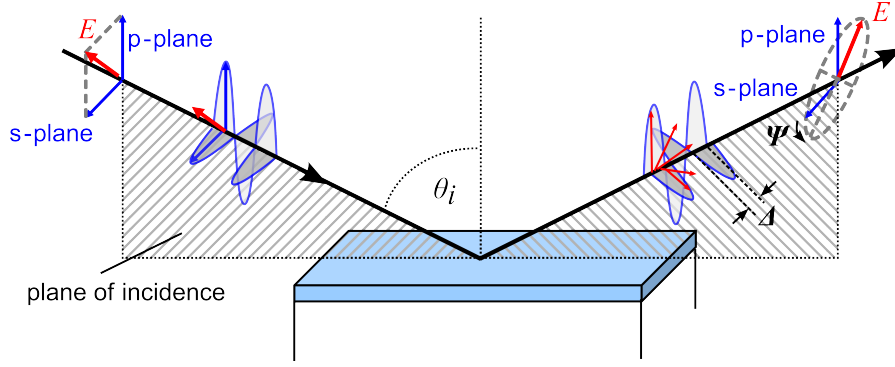


Figure 3.2: Schematic representation of the measurement principle of ellipsometry.

with the following relationship

$$\rho_{\text{ellips}} = \tan \Psi \cdot \exp(-i\Delta) = \frac{r_p}{r_s}, \quad (3.1)$$

where Ψ denotes the amplitude ratio, and Δ is the phase difference between p- and s-polarizations [106]. When light is irradiated onto a dielectric medium, the electric AC field of the light waves induces a dielectric polarization P inside the medium. Due to the polarization, the electric field inside the dielectric medium is reduced to $E = (D - P)/\epsilon_0$, where D is the electric displacement and ϵ_0 is the permittivity of vacuum. The relative permittivity ϵ , for simplification just called dielectric constant, is given by

$$\epsilon = 1 + \frac{P}{\epsilon_0 E} = 1 + \chi, \quad (3.2)$$

where χ denotes the dielectric susceptibility. The electric AC field of the light waves induces time-varying polarizations where the charges of the dipoles are accelerated. As a result, the accelerated dipoles also radiate electromagnetic waves, which are superimposed consistent with Huygens's principle to a propagating wave through the medium and a reflected wave. The propagation speed of light inside the medium changes and the relation between the dielectric constant and the complex refractive index $N = n + ik$ (n : refractive index, k : extinction coefficient) follows from Maxwells equations [106], as shown in Sec. 2.4:

$$N^2 = \epsilon = \epsilon_1 + i\epsilon_2. \quad (3.3)$$

Usually, ϵ is not a single complex number but a function of photon energy of the incident light [106]. Figure 3.3 shows a typical spectral distribution of the real ϵ_1 and imaginary ϵ_2 part of the dielectric function. The dielectric function at low photon energies is influenced by the atomic and electric polarization. For dielectric materials, ϵ_1 reaches a constant value at low photon energies, which is called static dielectric constant ϵ_s . In contrast, conducting materials exhibit free-carrier absorption which results in a decrease of ϵ_1 and an increase of ϵ_2 with decreasing photon energy, as shown by the dashed line in Fig. 3.3. The plasma energy $\hbar\omega_P$ is defined by the zero point of the real

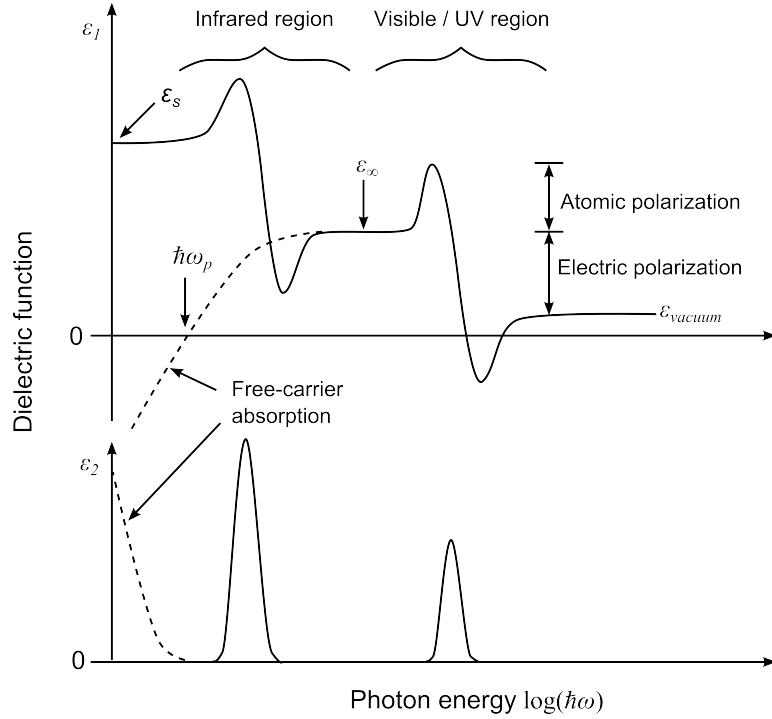


Figure 3.3: Real part ϵ_1 and imaginary part ϵ_2 of the complex dielectric function $\epsilon = \epsilon_1 + i\epsilon_2$ as a function of photon energy $\hbar\omega$ (according to Ref. [106]).

part of the dielectric function. Absorption occurs if the photon energy of the incident light coincides with the resonant energy of the medium. In the infrared region, the absorption is caused by the resonant oscillation of the atomic polarization. The resonant oscillation of the electric polarization takes place in the ultraviolet and visible region. The imaginary part of the dielectric function is proportional to the light absorption, which is described by the extinction coefficient k . As a result, ϵ_2 exhibits peaks, which are related to the resonant energies of the atomic and electronic polarizations. At photon energies higher than the resonant energy of the atomic polarization, the atomic polarization cannot follow the oscillation of the incident light and ϵ_1 reaches the value of the high frequency dielectric constant ϵ_∞ . If the photon energy of the incident light exceeds the resonant energy of the electric polarization, ϵ_1 reaches the value of vacuum ($\epsilon_1 = 1$).

The real and imaginary part of the dielectric function are not independent of each other. The relation between ϵ_1 and ϵ_2 is given by the Kramer-Kronig relation

$$\epsilon_1(E) = 1 + \frac{2}{\pi} P \int_0^\infty \frac{E' \epsilon_2(E')}{E'^2 - E^2} dE' \quad (3.4)$$

$$\epsilon_2(E) = -\frac{2E}{\pi} P \int_0^\infty \frac{\epsilon_1(E') - 1}{E'^2 - E^2} dE', \quad (3.5)$$

with the principal value of the integral P

$$P \int_0^{\infty} dE' = \lim_{\delta \rightarrow 0} \left(\int_0^{E-\delta} dE' + \int_{E+\delta}^{\infty} dE' \right). \quad (3.6)$$

The Kramer-Kronig relation describes the fact that light absorption in a medium takes place after the light reached the medium so that the causality is ensured. If a dielectric function model satisfies the Kramer-Kronig relation, the model is physically correct. The Kramer-Kronig relation is often used to determine ϵ_1 if only ϵ_2 is known. The Kramer-Kronig relation is in this case only applicable if $\epsilon_2(E)$ is known from $E = 0$ to ∞ and $\epsilon_2(E) = 0$ at $E \rightarrow \infty$.

For complex layer-substrate systems, data analysis is necessary to determine the optical constants and thicknesses of the layers since there are more unknown than measured variables and data inversion is no longer possible. The data analysis consists of the development of a dielectric function model, an iterative fit of the model parameters to the measured (Ψ , Δ) spectra, and a modification of the dielectric function model until a sufficient agreement with the measurement is reached [106]. The WVASE32-software (from J.A. Woollam, Inc.) is used for modeling the dielectric function. During the fitting, the WVASE32 software determines the mean squared error (MSE) as a sum of the squares of the differences between the measured and calculated data, with each difference weighted by the standard deviation of the data measured and minimizes the MSE by using a Levenberg-Marquardt algorithm [134].

Usually, problems occur in the SE analysis of transparent thin films on transparent substrates due to rear-side reflection of the substrate [35]. For that reason, a borosilicate wedge and turpentine oil with a refractive index similar to that of glass is used for minimizing rear-side reflection of the glass substrates. In order to avoid rear-side reflection of the silicon substrates, wafers with a rough rear surface are used. The SE analysis of the substrates is performed before film deposition to render the modeling of the ZnO:Al films more precisely.

For transparent thin films, ellipsometry is very sensitive to refractive indices, but not to small extinction coefficients ($k < 0.01$). It is, therefore, advisable to model the measured transmittance spectra simultaneously, which are sensitive even to slight absorption with extinction coefficients on the order of $k \approx 10^{-5}$ or less [135]. In this thesis, the ellipsometric data are modeled simultaneously with the transmittance and the reflectance spectra of the samples, where in the infrared wavelength range (> 1700 nm) only the photometric data are available.

Photometry

Photometric spectra in the solar spectral range from 250 nm to 2500 nm are measured with a double beam spectrometer (Cary 5000 from Agilent Technologies) using an integrating sphere. Figure 3.4 shows the measurement configuration for the transmittance and reflectance measurements. The two beams represent the sample beam and the

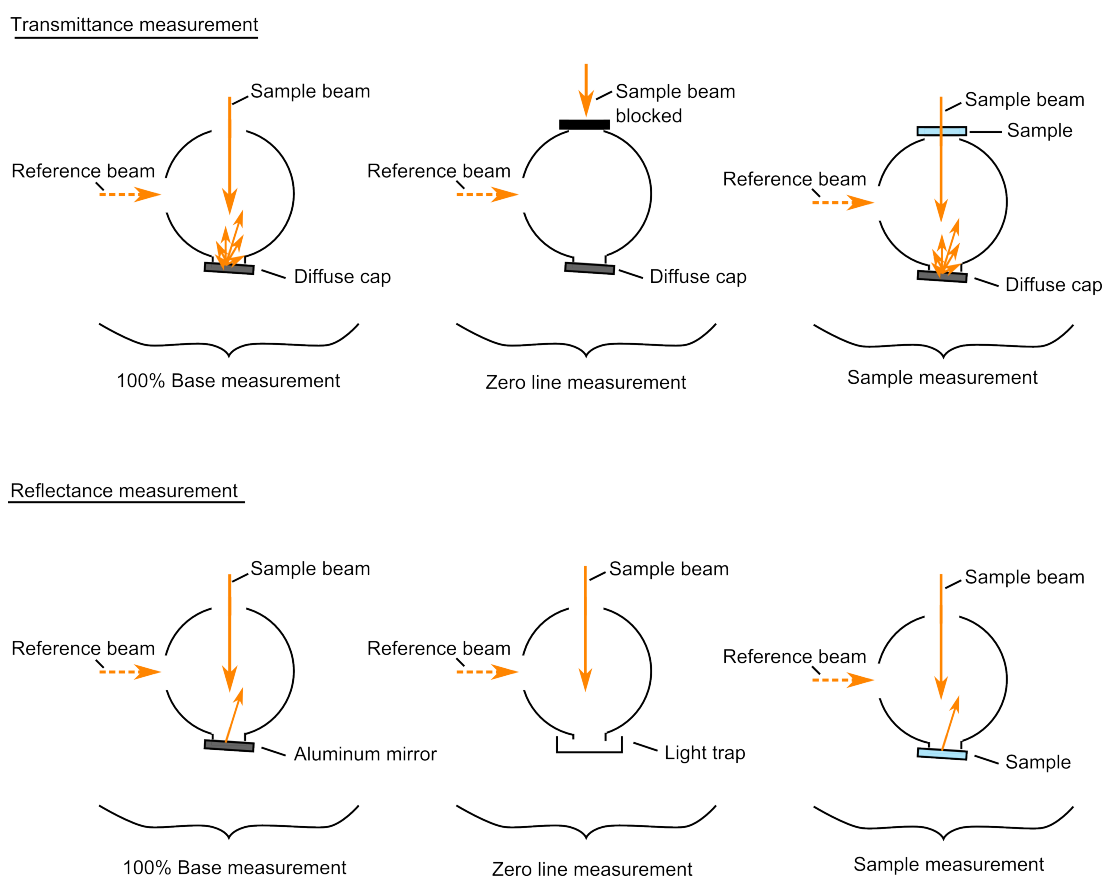


Figure 3.4: Schematic representation of the measurement configurations using an integrating sphere for the transmittance and reflectance measurements.

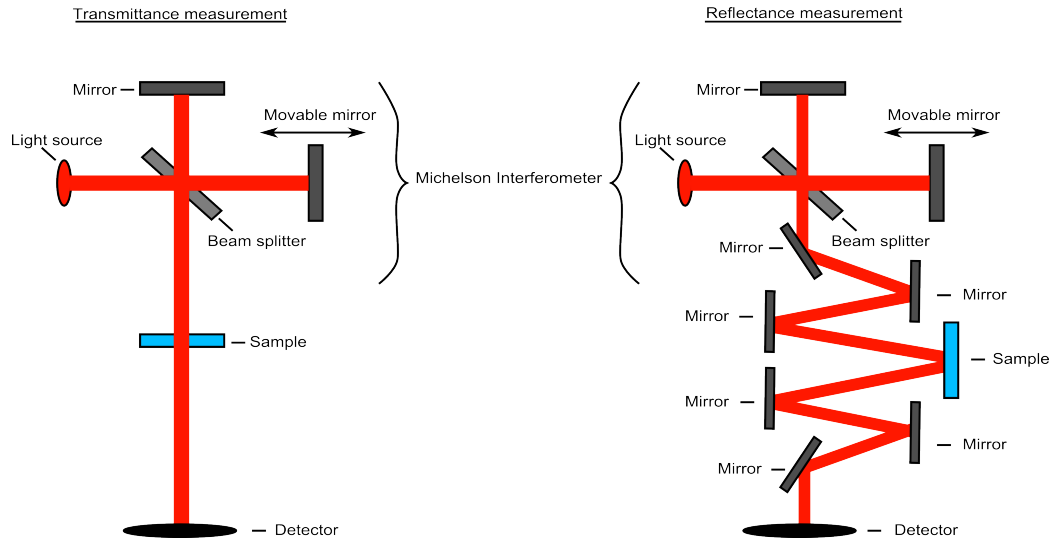


Figure 3.5: Schematic representation of the measurement configuration of the FTIR transmittance and reflectance measurements.

reference beam, respectively. The light of both beams is temporally separated by a chopper in such a way that the detected light of the reference beam is used to account for intensity instabilities of the light sources (a halogen lamp for the ultraviolet wavelength range and a deuterium lamp for the visible and near-infrared wavelength range) and changes of mean sphere reflectivity. The integrating sphere collects the whole specular and diffuse reflected and transmitted light of the sample. Since the films show only slight surface roughnesses of only some nanometers the diffused part is negligible. For each measured value, transmittance or reflectance, it is necessary to measure a 100%-base spectrum of a known standard and a zero line spectrum to take account of the spectral sensitivity of the detector as well as of stray light inside the measurement configuration, which may reach the detector. For the transmittance measurements, the 100%-base spectrum is that of an open sample port in front of the integrating sphere where the rear port is closed with a highly reflecting diffuse cap. The zero line spectrum is measured with the sample beam blocked before it could reach the integrating sphere. The transmittance of the sample is determined with the sample in front of the integrating sphere and a closed rear port with a diffuse cap. In the case of the reflectance measurements, the reflectance spectra of a calibrated aluminum mirror at the rear port of the integrating sphere is measured as 100%-base spectrum. The zero line spectrum is recorded with an open sample port in a dark room, which acts as an effective light trap. The reflectance measurements of the sample take place with the sample at the rear port of the integrating sphere.

Using a Fourier transform infrared (FTIR) spectrometer (Equinox 55 from Bruker), the measured reflectance and transmittance spectra of the samples involve the wavelength range from $2.5 \mu\text{m}$ to $50 \mu\text{m}$. These measurements take place without an integrating sphere, as shown in Fig. 3.5. The determination of the 100%-base spectra is also nec-

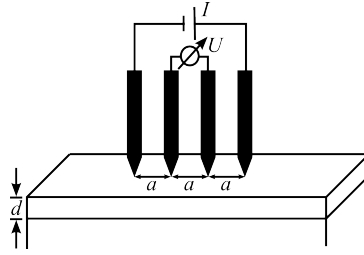


Figure 3.6: Schematic representation of the four-point probe measurement configuration.

essary. However, a zero line spectrum need not be recorded since in this measurement configuration there would be no stray light. The 100%-transmittance base spectrum is determined again with an open sample port and the 100%-reflectance base spectrum is measured with a calibrated gold mirror.

The uncertainty of the ellipsometric data is tabulated with $\Delta\psi = 0.02^\circ$ and $\Delta\Delta = 0.02^\circ$. The uncertainty of the photometric measurements is approximately $\pm 2\%$ for the measurements with the Cary5000 and the FTIR, respectively. Among other things, the uncertainty of the photometric measurements depends on the uncertainty of the calibrated standards as well as on the sensitivity of the detectors.

Electronic characterization

In order to determine the electronic properties of the films, two measurement techniques such as the four-point probe and the Hall measurement technique are applied in this thesis. Hall measurements with van der Pauw geometry were taken at the Helmholtz-Centre Berlin.

Four-point probe technique

The four-point probe technique is a fast and nearly non-destructive characterization method [11]. Four equidistant needles are pushed to the sample surface, as shown in Fig. 3.6. A constant electric current I flows from one of the outer needles through the film to the other outer needle. With the two inner needles, the voltage drop U is determined. The resistance of a conductor is $R = \rho_e \cdot l / (w \cdot d)$ with the resistivity ρ_e , the length l , width w , and thickness d . If the sample is square-cut ($l = w$), the resistance simplifies to $R_{\text{sheet}} = \rho_e / d$ and is now called sheet resistance. In the ideal case of an infinitely thin film whose thickness d is much smaller than the needle distance, the sheet resistance of the film is determined by

$$R_{\text{sheet}} = \frac{\rho_e}{d} = \frac{\pi}{\ln 2} \cdot \frac{U}{I}. \quad (3.7)$$

When the film thickness is known, the resistivity ρ_e of the films is given by Eq. 3.7. Since the resistivity is determined by $\rho_e = (eN_e\mu_e)^{-1}$, only the product of the free-carrier density N_e and mobility μ_e can be determined by the four-point probe measurement.

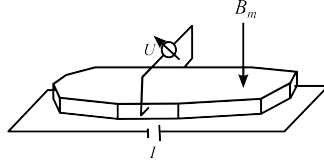


Figure 3.7: Schematic representation of the Hall measurement configuration in van der Pauw geometry.

The measurement errors of the sheet resistance are determined by repeated measurements and are smaller than 10%.

Hall measurements

Using the Hall measurement technique, the determination of the free-carrier density and the mobility are decoupled due to the dependence of the Hall voltage on the free-carrier density [86]. In contrast to the four-point probe technique, the four current- and voltage-carrying contacts are not arranged in one line. Hall measurements with van der Pauw geometry [136, 137] enable the arrangement of the contacts on the edges of a homogeneous, arbitrary formed sample. To determine the Hall coefficient, the current-carrying contacts and voltage-measuring contacts are arranged in a crosswise way, as shown in Fig. 3.7. An external magnetic field with field intensity B_m is applied to the sample with the field direction perpendicular to the film plane. Due to the magnetic field, the free carriers are deflected by the Lorentz force and the resistance R_m changes in comparison to a measurement without magnetic field. The Hall coefficient is determined using the relation $R_H = d/B_m \cdot \Delta R_m$. The free-carrier concentration depends on the Hall coefficient as follows

$$N_{\text{Hall}} = \frac{A_r}{eR_H}, \quad (3.8)$$

where A_r denotes a proportionality factor whose value depends on the scattering mechanism, temperature, band structure, and magnetic field density [86]. Usually, the value of A_r is set to unity for TCOs [21, 86] which is also done in this thesis. The mobility is calculated by

$$\mu_{\text{Hall}} = \frac{|R_H|}{\rho_e}. \quad (3.9)$$

Hall measurements were taken with van der Pauw geometry at room temperature at the Helmholtz-Centre Berlin. The precision of the Hall parameters is obtained by repeated measurements on the same sample and the measurement errors are $\leq 10\%$.

Structural characterization

Structural properties of the films deposited in this thesis such as morphology, crystalline structure, surface roughness, and interface structure are analyzed by scanning electron microscopy (SEM), X-ray diffraction (XRD), atomic force microscopy (AFM), and high-resolution transmission electron microscopy (HRTEM). Some of the mea-

measurements were taken at other research institutes as described below. Since these are established measurement techniques, the basics of these techniques are not specified here but can be found elsewhere [138–141]. In the following, only the relevant measurement configurations and parameters are described.

Scanning electron microscopy (SEM)

In this thesis, a scanning electron microscope (S-4800 from Hitachi) is used to analyze the film structure such as grain growth and size as well as the film thickness. Therefore, cross-sectional and top-view images of the films are taken with an accelerating voltage of 2.0 kV and a working distance of 4.0 mm. For image generation, two detectors are used, which detect the back scattered electrons and secondary electrons, respectively.

X-ray diffraction analysis (XRD)

XRD analysis is used to characterize the crystallinity of the films. The XRD analysis was performed at Solid State Analytics (Wietze, Germany) in Bragg-Brentano geometry (PW1800 from Philips) and subsequent Rietveld analysis [139]. The sample was irradiated under different angles of incidence θ with x-rays of a $\text{CuK}\alpha_{1/2}$ source with wavelengths $\lambda_{\alpha 1} = 154.060$ pm and $\lambda_{\alpha 2} = 154.439$ pm. The diffracted x-rays were detected under the angle 2θ concerning the incoming x-ray beam in the range of $2\theta \in [2^\circ - 100^\circ]$. Due to the interference of the x-rays after diffraction at the different lattice planes of a crystalline sample, only Bragg reflexes for discrete angles remain. Scherrer [142] showed that the width of the Bragg peaks depends on the size of the crystallites of a sample. If a crystallite is large there are many lattice planes which contribute to the coherent diffraction of the x-rays and the width of the Bragg peak becomes smaller in comparison to a Bragg peak which results from the diffraction at a small crystallite. This is the same principle as the diffraction of light at a grating where the width of the intensity peaks depends on the number of the gaps of the grating. With the full width of half maximum (FWHM) of the Bragg peaks, the grain size is given by the Scherrer equation [142]

$$g = \frac{k\lambda}{\cos(\theta_{\text{BR}}) \text{FWHM}(2\theta_{\text{BR}})}, \quad (3.10)$$

where k is a constant, which depends on the crystalline geometry of the samples [139]. For ZnO:Al thin films, $k = 0.94$ and $k = 1.05$ are reported [12, 22], while $k = 0.94$ is used in this thesis.

Atomic force microscopy (AFM)

In order to determine the surface roughness of the samples, atomic force microscopy (Autoprobe M5 from Park Scientific) was applied at the Institute for Solid State Physics at the Leibniz University Hanover. The surface of the sample was scanned with a small tip, lithographically made of silicon which was arranged at the end of a cantilever. The measurement was taken in dynamic mode (amplitude-modulation AFM), in which the

driving frequency of the cantilever was about 330 kHz during the scanning. The scan area was about $5 \times 5 \mu\text{m}^2$.

High-resolution transmission electron microscopy (HRTEM)

The interface region of the thin film and the glass substrate was studied by HRTEM (Type JEOL JEM-2100 F) at the Institute for Physical Chemistry and Electrochemistry at the Leibniz University Hanover. For TEM analysis, the samples have to be very thin so that the electrons are able to move through the sample. Therefore, the cross-sectional samples were prepared by gluing with a special epoxy resin such that mechanical thinning with polishing techniques was possible. This was followed by argon-ion milling to a thickness of 30 nm to 70 nm. The accelerating voltage of the electron beam in this analysis was adjusted to 200 kV.

Composition analysis

To clarify whether there are doping gradients inside the films or whether the interface between the films and the glass substrates has a chemical origin, composition-depth profiles of the samples were analyzed with secondary-neutral-mass spectroscopy (SNMS) (INA3 from Leybold) at the Technical University of Clausthal. In SNMS, the films were sputtered with krypton ions. The sputtered film particles are predominantly neutral. After sputtering, these particles are ionized by a low-pressure plasma with electrons and then analyzed by a mass spectrometer to quantify the mass and number of the film elements. The decoupling of the ablation and ionization processes in SNMS reduces matrix effects and mass interferences, which is advantageous compared to secondary-ion-mass spectroscopy (SIMS) [143]. The SNMS analysis results in composition-sputtering-time profiles, which can be converted to composition-depth profiles if the sputtering rate is known.

3.2 Model dielectric function (MDF) of sputtered ZnO:Al thin films

As stated already in Sec. 3.1.2, the ellipsometric analysis requires subsequent modeling of the measured spectra with an appropriate dielectric function model for the determination of the optical constants, the film thickness, and other film properties. There are many different ways of modeling the dielectric function of intrinsic and doped ZnO [30–36], which take account of fundamental band-gap transitions and free-carrier absorption. Zinc oxide is a direct band-gap semiconductor with wurtzite structure and a strong excitonic interaction [103]. Doped ZnO is usually a degenerated semiconductor and ionized impurity scattering is the dominant scattering phenomenon. Reported MDFs include surface roughness [34, 35] and uniaxial anisotropy [144, 145] of the films. However, some of the MDFs reported failed in describing the measured spectra of the

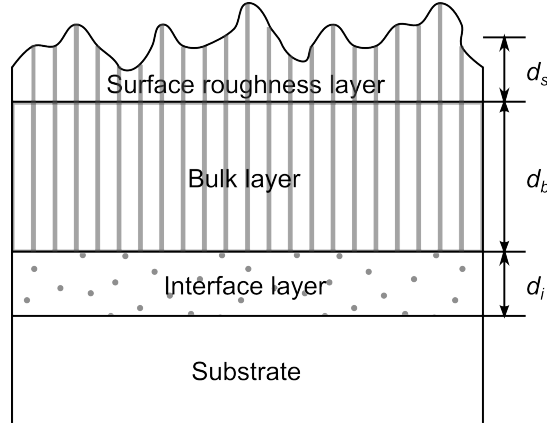


Figure 3.8: Schematic representation of the layer structure used for modeling the ellipsometric and photometric spectra of a ZnO:Al thin film on glass. The layer thicknesses are labeled d_s for the surface roughness layer, d_b for the ZnO:Al bulk layer, and d_i for the interface layer.

sputtered ZnO:Al thin films of this thesis. Therefore, special attention is paid in this section to the development of a reliable MDF and necessary modifications of existing models.

At first, the MDF is developed for films sputtered from a target with 2 wt.% Al_3O_3 . However, in Sec. 3.3.5, the model developed in this section is also applied to films with lower Al concentrations. For modeling the thin films, the films are divided into three model layers: the surface roughness layer, the ZnO:Al bulk layer and the interface layer, as shown in Fig. 3.8.

3.2.1 Modeling of the surface roughness layer

The morphology of thin films has a great influence on the spectroscopic ellipsometric data [134]. Therefore, it is necessary to take account of the surface roughness of the polycrystalline ZnO:Al films. The Bruggeman effective medium approximation (BEMA) [146] enables the determination of the effective optical constants of composite materials, the surface roughness or interface layers. The BEMA model describes a composite material consisting of two spherical constituents a and b embedded in a host material with the effective dielectric function ϵ

$$f_a \frac{\epsilon_a - \epsilon}{\epsilon_a + 2\epsilon} + (1 - f_a) \frac{\epsilon_b - \epsilon}{\epsilon_b + 2\epsilon} = 0, \quad (3.11)$$

with the volume fractions f_a and $f_b = 1 - f_a$ and the dielectric functions ϵ_a and ϵ_b of the phases a and b [106]. The volume fractions are related to the probabilities of finding phase a or b in a spherical space of the effective medium [106]. The surface roughness is modeled with a BEMA model of a 50/50 vol.% mixture of the bulk layer and voids, which is a commonly used method and agrees with AFM measurements [147, 148].

3.2.2 Modeling of the ZnO:Al bulk layer

The dielectric function of the ZnO:Al bulk layer is split up into three different constituents, which take account of the different absorption mechanisms

$$\epsilon(E) = \epsilon_{\infty} + \epsilon_{\text{high interband}}(E) + \epsilon_{\text{band gap}}(E) + \epsilon_{\text{free carrier}}(E). \quad (3.12)$$

In this thesis, the high frequency dielectric constant ϵ_{∞} is fixed to unity and describes the fact when the electronic polarization cannot follow the oscillation of the light field at high photon energies ($E \rightarrow \infty$). $\epsilon_{\text{high interband}}$ stands for interband transitions from the valence band to higher states in the conduction band, $\epsilon_{\text{band gap}}$ is the fundamental absorption of the semiconductor, and $\epsilon_{\text{free carrier}}$ stands for the free-carrier absorption process.

High interband transitions

In ZnO and ZnO:Al thin films, a few interband transitions occur at high energies above the measured spectral range and might involve conduction bands other than the one responsible for the band gap. Since these transitions are outside the measured spectral range, there is no need to take account of the details of the band structure. In the literature, different ways of modeling high interband transitions are presented, such as harmonic oscillator [30] or Sellmeier [34, 147] modeling. According to the literature, these high-energy absorption peaks are located between 10 and 12 eV. A pole oscillator is used to take account of high interband transitions. This is a zero-broadening oscillator, which only affects the real part of the dielectric function and describes absorptions that occur outside the measured spectral range. The pole oscillator is derived by the following formula:

$$\epsilon_{\text{high interband}}(E) = \frac{A_p}{E_p^2 - E^2} \quad (3.13)$$

with the pole magnitude A_p and the pole position E_p .

Band-gap modeling

Yoshikawa and Adachi [31], Jellison and Boatner [32], as well as Djurišić et al. [33] used three-dimensional critical points for modeling fundamental absorption and took account of bound and unbound excitonic states in their models for single-crystal ZnO. The model dielectric functions of Jellison and Boatner and Djurišić et al. are all based on the model of Holden et al. [149], but the fault in Holdens model is the incorrect introduction of broadening [33]. Djurišić et al. modified the Holden model by introducing correct broadening to band-to-band transitions, as well as discrete and continuum excitons. However, at room temperature the broadening of discrete and continuum excitons cannot be distinguished and broadening may be independent of the order of the excitons [33]. In this case, the Djurišić et al. model reduces to the Tanguy model [104].

Postava et al. [34] established the Tanguy model for single-crystal Ga- and Al-doped ZnO thin films on sapphire substrates. The Tanguy model is a compact analytical formula for the dielectric function of Wannier excitons, which includes the contribution of all bound and unbound states with correctly introduced Lorentzian broadening. The model even includes the screening of the excitonic interaction due to the Coulomb potential of high-carrier densities and is, therefore, suitable for modeling highly doped ZnO.

Since the optical properties of polycrystalline ZnO thin films may differ from single-crystal ZnO, the question arises which model for fundamental absorption is reliable in the case of sputtered polycrystalline ZnO thin films? Fujiwara and Kondo [35] used the Tauc-Lorentz model [150] for Ga-doped ZnO thin films on silicon substrates and Quiao et al. [30] applied the O'Leary-Johnson-Lim model [151] to Al-doped ZnO thin films on glass substrates; both models were primarily developed for modeling the dielectric function of amorphous semiconductors. However, sputtered polycrystalline ZnO thin films exhibit a columnar structure with grain diameters greater than 30 nm and lengths of several hundred nanometers according to film thickness. As a consequence, ZnO thin films have a dominant long-range order, and momentum conservation should be taken into account.

The models for single-crystal ZnO may, therefore, also be applicable to sputtered polycrystalline ZnO thin films. Since the measurement of the ellipsometric and transmittance spectra take place at room temperature, the discrete and continuum excitonic states cannot be distinguished [33]. In the case of highly doped ZnO thin films, excitonic interaction is screened due to high carrier densities. The Tanguy model [104] is used for modeling fundamental absorption and includes the contributions of all bound and unbound states as well as screening effects of the Coulomb potential due to high carrier densities. Screening is described by the Hulthén potential [152]. Equations 3.14– 3.16 illustrate Tanguy's formulae:

$$\epsilon_{\text{band gap}}(E) = \frac{A_g \sqrt{R}}{(E + i\gamma)^2} [\tilde{g}(\xi(E + i\gamma)) + \tilde{g}(\xi(-E - i\gamma)) - 2\tilde{g}(\xi(0))] \quad (3.14)$$

with

$$\tilde{g}(\xi) = -2\psi\left(\frac{s}{\xi}\right) - \frac{\xi}{s} - 2\psi(1 - \xi) - \frac{1}{\xi} \quad (3.15)$$

and

$$\xi(y) = \frac{2}{\sqrt{(E_g - y)/R} + \sqrt{(E_g - y)/R + 4/s}} \quad (3.16)$$

where A_g is the amplitude, R denotes the Rydberg energy of the unscreened exciton, γ is the broadening constant and E_g is the band-gap energy. Here $\psi(z) = d \ln \Gamma(z) / dz$ denotes the digamma function and s is a dimensionless screening parameter. If $s < 1$, no bound state exists for the Hulthén potential. The argument y in Eq. 3.16 acts as a

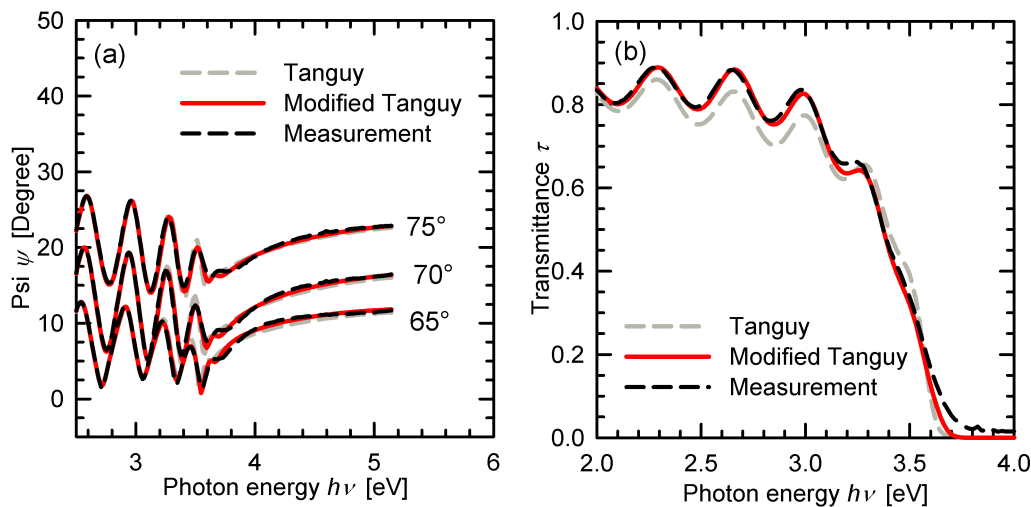


Figure 3.9: Measured and modeled Psi spectra (a) and transmittance spectra (b) of a ZnO:Al sample deposited at 250 °C substrate temperature near the fundamental absorption threshold. Only three angles are shown for clarity. Delta spectra are not shown. The spectra are modeled with Tanguy’s formula (dashed gray lines) as well as with the modified Tanguy model (solid red lines). The dashed black lines show the measured data.

complex auxiliary variable and is either $(E + i\gamma)$, $(-E - i\gamma)$ or 0, as given by Eq. 3.14. The argument z of the digamma function is then defined by Eqs. 3.15 and 3.16. Figure 3.9 (a) and (b) shows the measured and modeled ellipsometric and transmittance spectra of a ZnO:Al film on glass, grown at a substrate temperature of 250 °C. The Tanguy model agrees with the measured ellipsometric data, but Lorentzian broadening causes an extended absorption tail below the absorption threshold [33], which becomes obvious in the transmittance spectra. Lorentzian broadening is conventionally used because only then analytical expressions of the dielectric function exist, but due to various effects, the line-shape of the broadening in semiconductors can differ from a Lorentzian form. Impurities, crystal strain, and alloy composition variations are known to cause Gaussian broadening, whereas thermal broadening effects display Lorentzian broadening. Djurišić et al. [33] introduced an energy-dependent formula developed by Kim et al. [153] for the broadening term, which provides the possibility to distinguish between Lorentzian and Gaussian broadening or intermediate types. The energy-dependent broadening formula with the following form is used:

$$\gamma'(E) = \exp \left[-\kappa \left(\frac{E - E_g}{\gamma} \right)^2 \right], \quad (3.17)$$

where γ denotes the broadening constant of the Tanguy model and E_g is the band-gap energy. Lorentzian broadening is expressed with $\kappa = 0$ and Gaussian-like broadening with $\kappa \approx 0.3$. Values between $[0, 0.3]$ are intermediate types of broadening. The Kramer-Kronig consistency of Eqs. 3.14–3.17 is checked numerically in the measured spectral region with the WVASE32 software by calculating the ϵ_1 values using the Kramer-Kronig relation, according to Eq. 3.4:

$$\epsilon_1^{\text{KK}}(E) = \frac{2}{\pi} P \int_0^\infty \frac{E' \epsilon_{2,\text{mod}}(E')}{E'^2 - E^2} dE' + \epsilon_{\text{offset}} \quad (3.18)$$

with the ϵ_2 values of the model and comparing them to the ϵ_1 values of the model. P is the principal value and ϵ_{offset} is a constant offset which represents high-energy contributions. For small values of $\kappa \leq 0.3$, the model satisfies the Kramer-Kronig relation within the experimental error bars. However, for large values of κ the Kramer-Kronig consistency will be violated and users should be aware of this inconsistency [33, 154]. Figure 3.9 (b) demonstrates that the modification of the Tanguy model improves agreement with the measured ellipsometric and transmittance spectra.

Free-carrier absorption

Free-carrier absorption in the near infrared (NIR) and infrared (IR) spectral range is commonly modeled with a simple Drude formula [34, 35, 155] with two fit parameters A_D and Γ_D :

$$\epsilon_{\text{free carrier}}(E) = -\frac{A_D}{E^2 + i\Gamma_D E}, \quad (3.19)$$

where A_D depends on the free-carrier density N_e and the effective electron mass m_e^* in the conduction band

$$A_D = \epsilon_\infty (\hbar\omega_D)^2 = \hbar^2 \frac{e^2 N_e}{\epsilon_0 m_e^*} \quad (3.20)$$

and Γ_D denotes the damping term, which is in relation to the free-carrier mobility μ_e

$$\Gamma_D = \frac{\hbar}{\langle \tau_e \rangle} = \hbar \frac{e}{m_e^* \mu_e}. \quad (3.21)$$

Fitting the Drude model to the measured data yields the fit parameters A_D and Γ_D which enables the determination of the free-carrier density and mobility using Eqs. 3.20 and 3.21 if the effective mass of the free carriers is known. The determination of the effective mass of the free-carriers will be discussed later in Sec. 3.3.1.

The simple Drude model, however, has an inherent limitation because the damping formula is assumed as being independent of the photon energy of incident light [11]. As a consequence, the modeling and the fits over the whole spectral range are usually unsatisfactory because of the over-estimation of free-carrier absorption. In TCOs, many electron-scattering processes such as electron-defect scattering, electron-lattice scattering, or electron-electron scattering take place, which may be responsible for

an energy-dependent damping term [92]. In heavily doped TCOs, ionized impurity scattering is usually the dominant scattering phenomenon [51]. For that reason, it is important to use a modified Drude model, which takes account of the ionized impurity scattering of the free carriers with an energy-dependent damping term [30, 36, 51, 92–94]. In the model presented, a formula developed by Mergel et al. [94] is used, which is an empirical representation of the broadening term and is easily implemented with the WVASE32 software:

$$\Gamma_D(E) = \Gamma_{\text{low}} - \left(\frac{\Gamma_{\text{low}} - \Gamma_{\text{high}}}{\pi} \right) \left[\arctan \left(\frac{E - \Gamma_{\text{changeover}}}{\Gamma_{\text{width}}} \right) + \frac{\pi}{2} \right]. \quad (3.22)$$

The four fit parameters are Γ_{low} as low-energy ($E = 0$) and Γ_{high} as high-energy ($E = \infty$) damping term, $\Gamma_{\text{changeover}}$ is the changeover energy, and Γ_{width} denotes the width of the function. With the relation $\epsilon_{\text{free carrier}}(E) = i\hbar(\epsilon_0 E \rho_e(E))^{-1}$ [21] and Eq. 3.19, dynamic resistivity is determined by

$$\rho_e(E) = \frac{\hbar \Gamma_D(E)}{\epsilon_0 A_D} - i \frac{\hbar E}{\epsilon_0 A_D}. \quad (3.23)$$

The real part of Eq. 3.23 for low energies ($E \rightarrow 0$) is in accordance with the DC resistivity of Hall or four-point probe measurements [156], whereas the imaginary part is independent of scattering and represents the effect of the inertia of the electrons [51]. Figure 3.10 (a) plots the real part of the dynamic resistivity as a function of photon energy, determined by SE analysis. Here, $\hbar\omega_p$ indicates the plasma energy of the free carriers, at which the real part of the dielectric function is $\text{Re}(\epsilon_\infty + \epsilon_{\text{free carrier}}(\hbar\omega_p)) = 0$ [51, 94]. In the following, the mean free path of the free carriers is considered to estimate the influence of ionized impurity scattering in dependence of the photon energy of the incident light. The mean free path describes the mean path length that the free carriers are able to move without being scattered but it does not mean the real length of the movement. If the free carriers are accelerated by an electromagnetic wave with high frequency, the amplitude of the free carriers is small due to the inertia of the electrons and increases with decreasing light frequency. With an increasing amplitude, the free-carrier movement becomes longer and more scattering events take place which lowers the mean free path of the free carriers. Figure 3.11 shows a schematic representation of the free-carrier movement caused by an AC field of the incident light. The mean free path of the free carriers at the Fermi level is expressed by the equation [51]

$$l = v_{\text{Fermi}} \langle \tau_e \rangle, \quad (3.24)$$

with the velocity of the free carriers at the Fermi level $v_{\text{Fermi}} = \hbar k_F / m_e^*$, the Fermi wave vector $k_F = (3\pi^2 N_e)^{1/3}$ and the mean scattering time $\langle \tau_e \rangle$ which is given by Eq. 3.21. Inserting the energy dependent broadening term $\Gamma_D(E)$ of Eq. 3.22, the

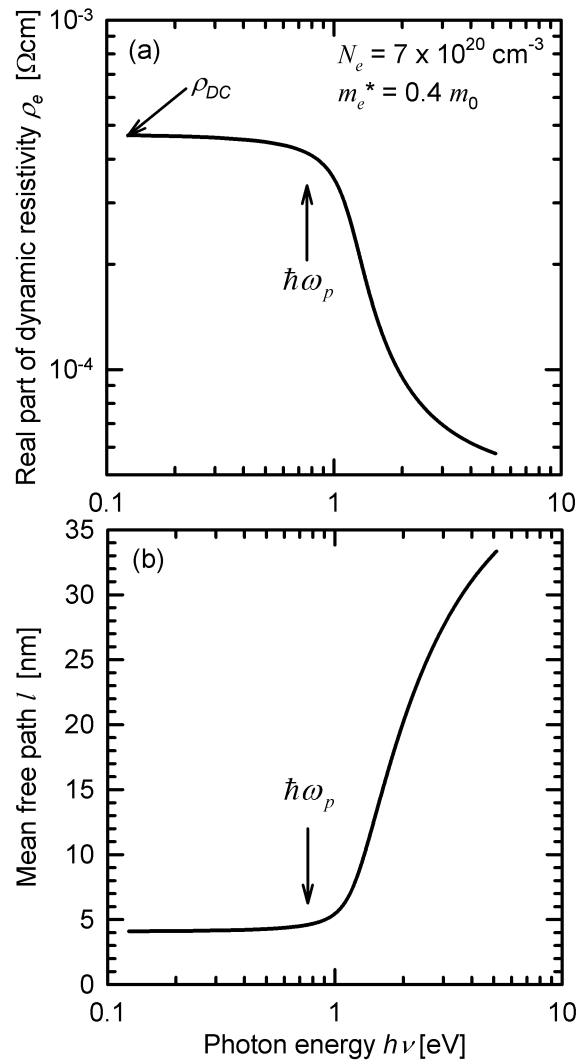


Figure 3.10: (a) Real part of the dynamic resistivity and (b) mean free path of the free carriers obtained from SE analysis of a ZnO:Al sample deposited at 250 °C substrate temperature. For small photon energies ($h\nu \rightarrow 0$), the dynamic resistivity converges to an upper limit. This value is compared to data obtained by DC measurements. $\hbar\omega_p$ denotes the plasma energy of the free carriers.

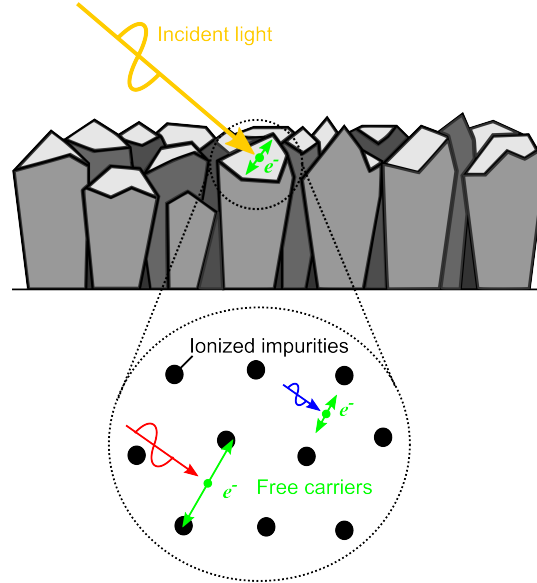


Figure 3.11: Schematic representation of the free-carrier movement in a polycrystalline ZnO:Al thin film caused by an AC field of the incident light.

mean free path is given by

$$l = \frac{\hbar^2 (3\pi^2 N_e)^{1/3}}{m_e^* \Gamma_D(E)}. \quad (3.25)$$

Figure 3.10 (b) shows the mean free path as a function of photon energy of the incident light, determined using a free-carrier concentration of $7 \cdot 10^{20} \text{ cm}^{-3}$ and an effective mass of the free carriers at the Fermi level of $m_e^* = 0.4m_0$ (see Sec. 3.3.1). In the case of $\hbar\omega < \hbar\omega_p$, we obtain $l < 5 \text{ nm}$. In contrast, the mean free path increases by an order of magnitude for $\hbar\omega > \hbar\omega_p$. For $\hbar\omega < \hbar\omega_p$, the electrons can follow the light field and ionized impurity scattering becomes dominant which lowers the mean free path and increases the resistivity. The distance between ionized impurities is $d \approx 1 \text{ nm}$ if $N_e = 7 \cdot 10^{20} \text{ cm}^{-3}$ is assumed. For $\hbar\omega > \hbar\omega_p$, the ionized scatterers become inefficient because at high light frequencies, the electron movement is shorter than the distances between the scatterers [51].

Phonon absorptions are negligible for modeling the infrared behavior of highly doped TCO thin films since the transverse optical phonon polaritons are effectively screened out by the free electrons [51]. However, for low-doped TCOs, phonon absorption has to be taken into account, as will be seen in Sec. 3.3.5. These absorptions can be modeled with simple Gaussian oscillators.

Modeling of anisotropy

As discussed in Sec. 3.3.1, SEM and XRD analysis show film crystallinity with a preferred c-axis orientation [001] that is perpendicular to the substrate. In the case of this alignment of the c-axis with the ellipsometer, no cross-polarization should occur,

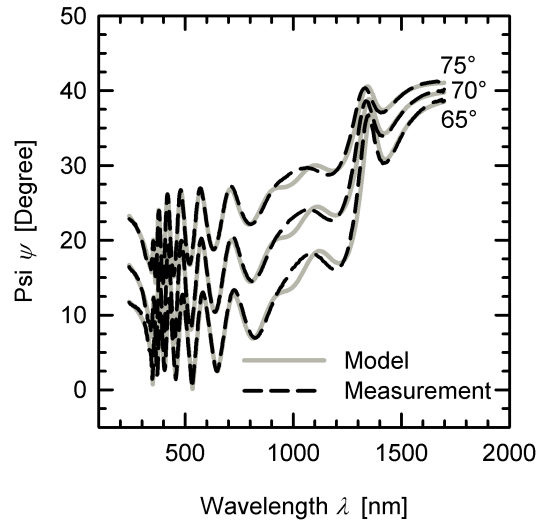


Figure 3.12: Measured (dashed black lines) and modeled (solid grey lines) Psi spectra of a ZnO:Al thin film on glass deposited at 250 °C substrate temperature. For clarity, only three angles are shown. The modeled data represent the fit result of a model without the interface layer.

the off-diagonal elements of the sample Jones matrix, which is used to describe the change of the polarization state of the light after interacting with the sample, should remain at zero and standard ellipsometry is applied [106]. In the model presented in this thesis, uniaxial anisotropy is taken into account by assuming a constant difference of the refractive index for the c-axis with respect to the refractive index in the film plane ($dn(\lambda) = n_{c\text{-axis}}(\lambda) - n_{\text{film plane}}(\lambda) = \text{const.}$).

3.2.3 Modeling of the interface layer

Figure 3.12 shows that the modeled Ψ spectrum of a ZnO:Al thin film on glass grown at a substrate temperature of 250 °C exhibits a misfit in the spectral region of 900 nm to 1200 nm if no interface layer is included into the model. Figure 3.13 shows that the measured and modeled ellipsometric and photometric spectra are improved due to the interface layer. The interface layer is associated with structural and electronic differences at the beginning of film growth as well as diffusion effects as will be shown by HRTEM analysis in Sec. 3.3.1 and is, therefore, modeled with a Bruggeman effective medium approximation (Eq. 3.11) of a 90/10-vol.% mixture of nonconducting ZnO and glass. In the case of silicon substrates, the interface layer is not necessary to obtain satisfying fit results in contrast to glass substrates, as shown in Fig. 3.14.

In Table 1 in Appendix 1, the fit results of characteristic ZnO:Al thin films deposited on different substrates such as glass and silicon are shown.

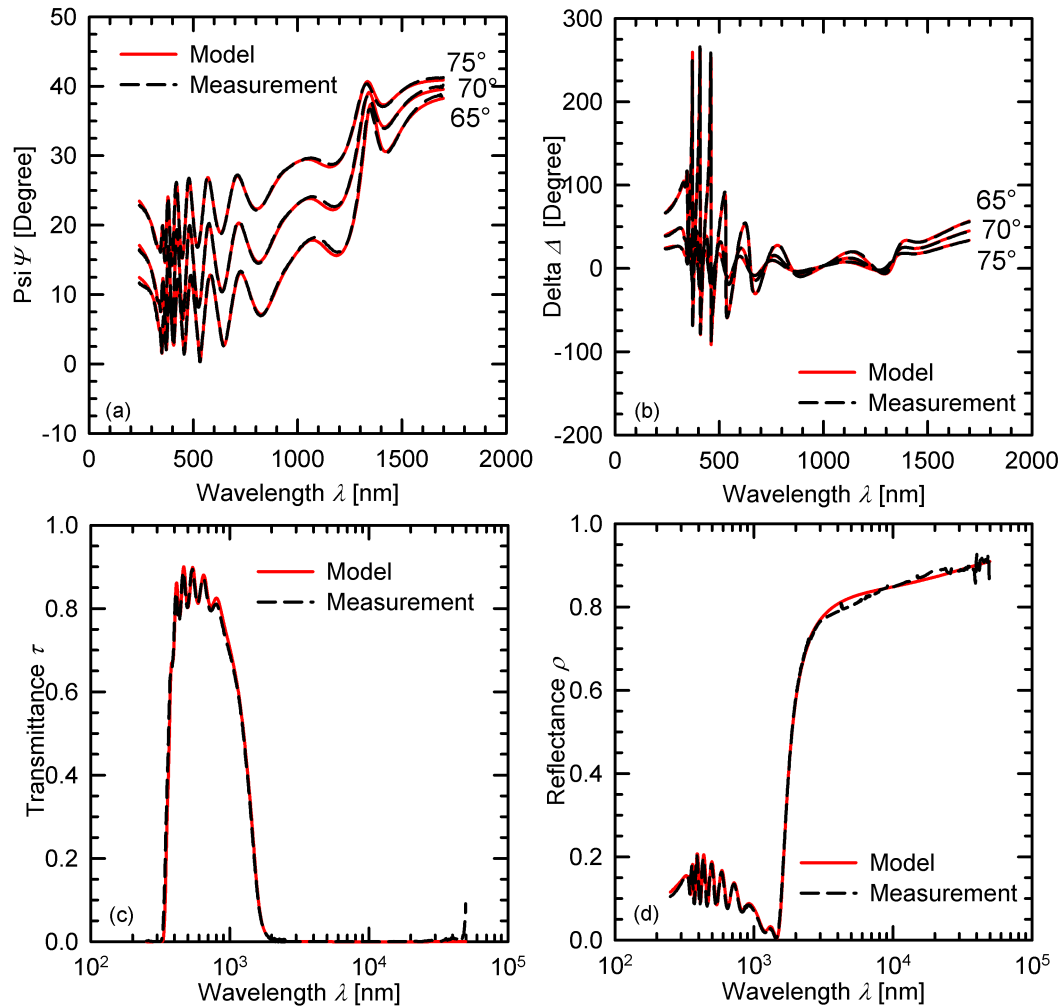


Figure 3.13: Measured and modeled Psi (a) and Delta (b) spectra as well as transmittance (c) and reflectance (d) spectra of a ZnO:Al thin film on glass deposited at 250 °C substrate temperature. Only three angles are displayed for clarity. Solid red lines and dashed black lines show the modeled and measured data, respectively. The model includes the interface layer.

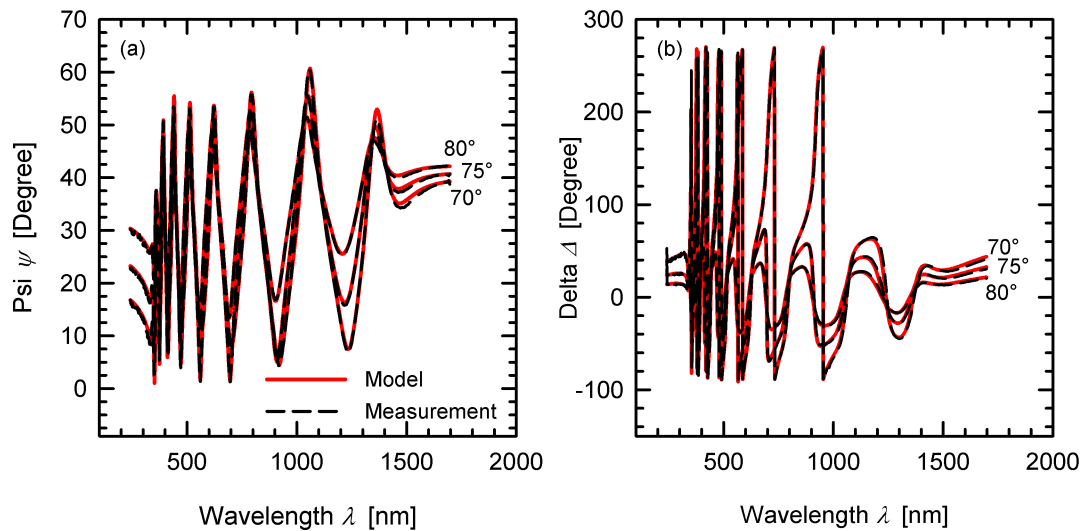


Figure 3.14: Measured and modeled Psi (a) and Delta (b) spectra of a ZnO:Al thin film on silicon deposited at 250 °C substrate temperature. Only three angles are displayed for clarity. Solid red lines and dashed black lines show the modeled and measured data, respectively. The model does not include any interface layer.

3.3 Results and discussion

The first part of this section examines the verification of the MDF developed in Sec. 3.2 with several independent thin film characterization methods in order to legitimate the further application of the MDF for the characterization of samples deposited at various parameters. As shown in Sec. 3.2 and Sec. 3.3.1, the MDF enables the determination of several optical and electronic film properties such as the optical constants and the band-gap energy, the free-carrier concentration, mobility and resistivity as well as the effective mass of the free carriers. In order to optimize the film properties of the ZnO:Al thin films for the solar-thermal application, the dependence of these properties on the deposition parameters such as the substrate temperature, the argon pressure, the DC power and the target doping concentration as well as the film thickness are analyzed in the second and third part of this section. Although many research investigations on the variation of deposition parameters of sputtered ZnO:Al thin films were already published [18, 19, 24, 52, 58, 66, 67, 71, 123, 157], the ubiquitous applicability of the results of these investigations is limited since the film properties depend strongly on the coater configuration, the type of plasma excitation and the target material. Additionally, in these publications, the films are usually intended for the application in optoelectronic devices or solar cells. Therefore, the film optimization criteria of these applications are quite different with respect to the transmittance, the resistivity and the etching behavior in comparison to the solar-thermal application. For this reason, own deposition parameter studies are done in this thesis which are relevant for the development of AR coating systems and for the improvement of the efficiency of the

double-glazed flat-plate collector, as will be shown in Chapter 4 and Chapter 5.

3.3.1 Comparison of the MDF results with independent thin film characterization methods

In order to evaluate the MDF results, several independent thin-film characterization methods are applied to samples with different film thicknesses grown at 200 °C substrate temperature from a target with 2 wt.% Al₂O₃.

Electronic properties:

Figure 3.15 shows the electronic properties of the films, such as the free-carrier concentration and mobility as well as the specific resistivity, obtained from Eqs. 3.19–3.23 using the best-fit parameters, in comparison to the results of the Hall measurements. The determination of the free-carrier concentration and mobility by the Drude equations Eqs 3.20 and 3.21 requires the knowledge of the effective mass of the free carriers. The electron effective mass values of the different samples are determined with Eq. 3.20 by the approximation of $N_e \approx N_{\text{Hall}}$ [35]. In the following, the mean value of the effective mass of the different samples $m_e^* = 0.4m_o$ is used to determine the electronic properties of the samples, which is the reason for the differences between the free-carrier concentration determined by the SE analysis and Hall measurements in Fig. 3.15 (a). Figure 3.15 (a) shows that the free-carrier concentration obtained by Hall measurement and SE analysis is nearly constant for film thickness values greater than 300 nm. For film thickness values less than 300 nm, the free-carrier concentration slightly decreases. The difference between the results of the Hall and SE analysis becomes obvious only for the 100 nm film. Figure 3.15 (b) demonstrates that Hall mobility is nearly constant for film thickness values greater than 400 nm and is much smaller for film thickness values below 400 nm. The SE analysis shows a slight, almost linear decrease of free-carrier mobility with decreasing film thickness. The resistivity in Fig. 3.15 (c) demonstrates a high dependence on film thickness for film thickness values less than 400 nm in the case of DC measurements and SE analysis. For film thickness values below 400 nm, the SE analysis produced mobility values greater than the Hall measurements and this effect is also reproduced in the values for resistivity. Table 2 in appendix 2 shows the related values of the SE and Hall parameters.

Morphology and crystalline structure:

The SEM image in Fig. 3.16 shows the cross-section of a 400-nm-thick sample, where the columnar structure of the ZnO:Al film perpendicular to the film plane can be observed. The diameter of the columns is in the range of 30 nm to 60 nm, one order of magnitude larger than the mean free path of the free carriers at low photon energies. Figure 3.17 demonstrates that the XRD analysis indicates a well-defined crystalline

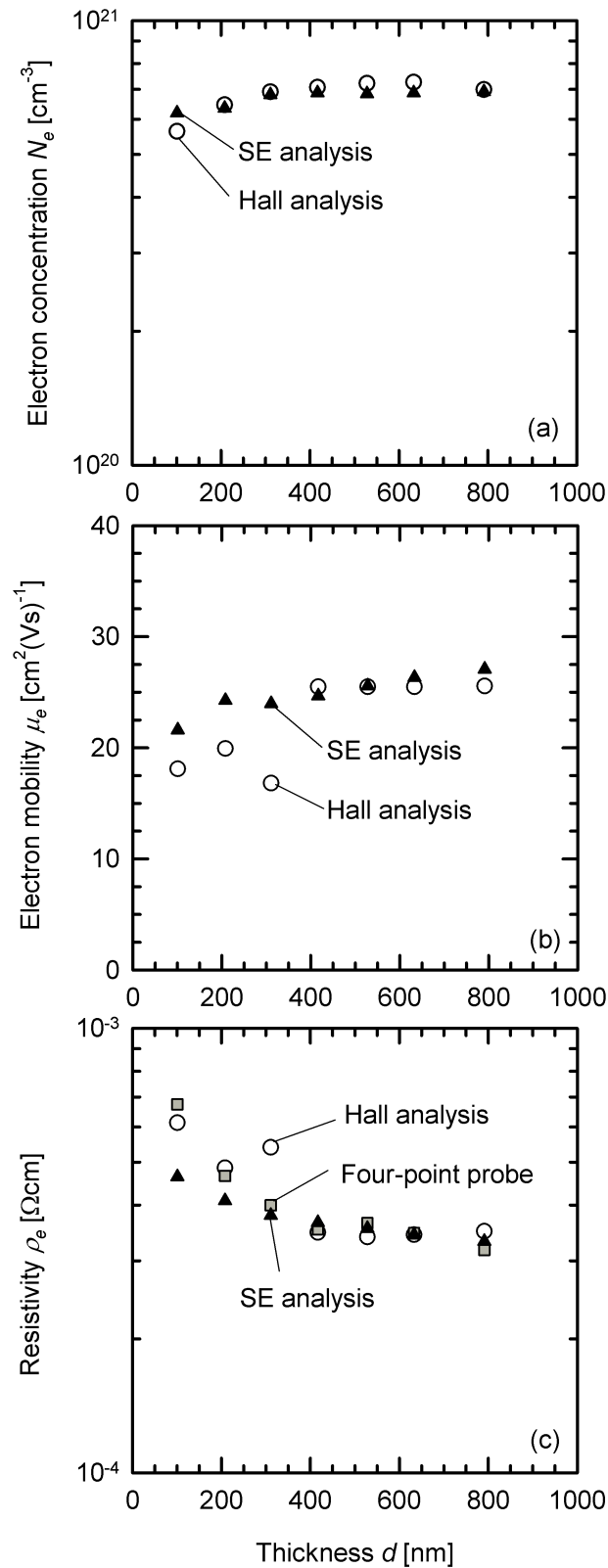


Figure 3.15: Comparison of the free-carrier concentration N_e (a) and mobility μ_e (b) determined from Hall measurements and SE analysis as well as the resistivity ρ_e (c) determined from Hall and four-point probe measurements and SE analysis against film thickness of ZnO:Al thin films on glass deposited at 200 °C substrate temperature. The error of the free-carrier properties determined by SE and Hall analysis is $\leq 10\%$, respectively.

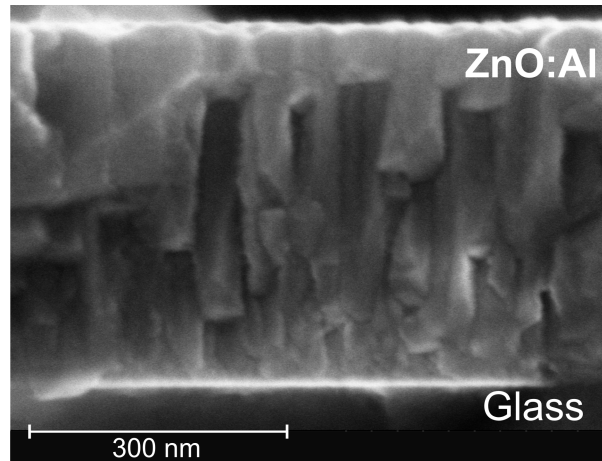


Figure 3.16: SEM image of a cross-section of a ZnO:Al thin film on glass deposited at 200 °C substrate temperature.

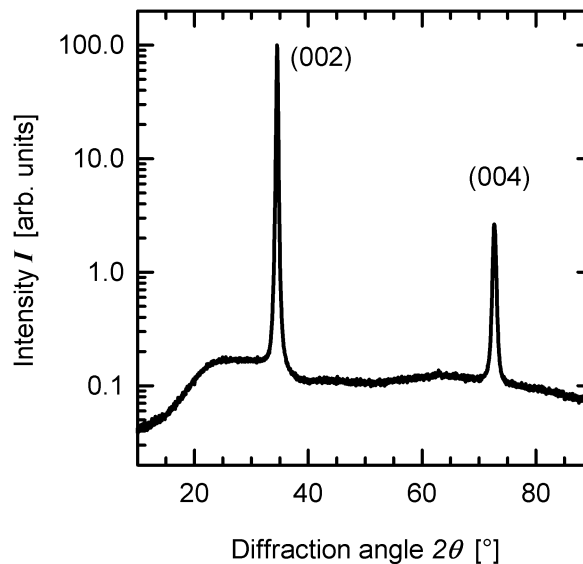


Figure 3.17: XRD pattern of a ZnO:Al thin film on glass deposited at 200 °C substrate temperature.

structure of the ZnO:Al film with a preferred c -axis orientation. The average grain size determined by the Scherrer formula (Eq. 3.10) using the FWHM of the (002) diffraction peak is 44.4 nm and in agreement with the SEM results.

The fit result of the MDF of the refractive-index difference between the c -axis and the film plane is $dn = 0.0166 (\pm 0.0003)$ and in agreement with the reported [158] uniaxial anisotropy of single-crystal bulk ZnO with a refractive-index difference of $dn = 0.016$ (at $\lambda = 632.8$ nm).

AFM measurements are taken on two samples deposited at 200 °C substrate temperature with film thickness values of 100 nm and 400 nm, respectively. The AFM measurements yield roughness values of 3.4 nm and 3.2 nm determined by the root-mean-squared (rms) method. The MDF results for the surface roughness of samples with different film thicknesses deposited at 200 °C substrate temperature range be-

tween 3 nm and 5 nm.

Composition results:

SNMS measurements should elucidate whether the interface layer required in the MDF has a physical or chemical origin. Figure 3.18 shows the corresponding depth profiles of the SNMS analysis of thin films on glass and silicon substrates deposited at 200 °C substrate temperature. Both depth profiles show very sharp transitions between substrate and film, but in the case of the glass sample, Fig. 3.18 (c) demonstrates that the transition region determined by the zinc profile is approximately 10 nm greater than that of the silicon sample. The aluminum depth profiles of both samples exhibit transition regions of the same size (not shown in detail).

Also, HRTEM analysis of the interface region was performed. To avoid a misinterpretation of the influence of tin of the float glass production, two samples were analyzed: one was deposited on the air side and the other on the bath side of the floated glass substrate. Figure 3.19 shows the HRTEM image of a 400-nm-thick ZnO:Al thin film on the air side of the glass. The HRTEM image shows that there is a 5-nm-thick layer at the interface region, which exhibits a morphology different than the bulk ZnO:Al layer. The sample deposited on the bath side exhibits a similar structure at the interface region and in addition isolated inclusions of tin compounds in the glass (not shown). The thickness of the interface layer determined by ellipsometric analysis is 8 nm for a sample deposited with the same sputter parameters.

Optical properties:

Very important results of the SE analysis for the development of coating systems are the optical constants. They are derived from the model dielectric function with Eq. 3.3. Figure 3.20 shows the optical constants of the film plane as a function of the wavelength for samples with different film thickness values. The spectra of the extinction coefficients depict the fundamental absorption region at short wavelengths and free-carrier absorption in the NIR spectral range. Figure 3.20 demonstrates that the optical constants of all samples are very similar in the band-gap region, but they differ in their behavior in the NIR spectral range. The reasons are smaller mobility values and smaller carrier concentration for samples with small film thickness values. Thus, the free-carrier extinction coefficient decreases with decreasing film thickness.

3.3.2 Discussion of the MDF and thin film characterization results

Electronic properties

The free-carrier concentrations determined by SE analysis and Hall measurements indicate that the ZnO:Al thin films are degenerate since the values exceed the critical

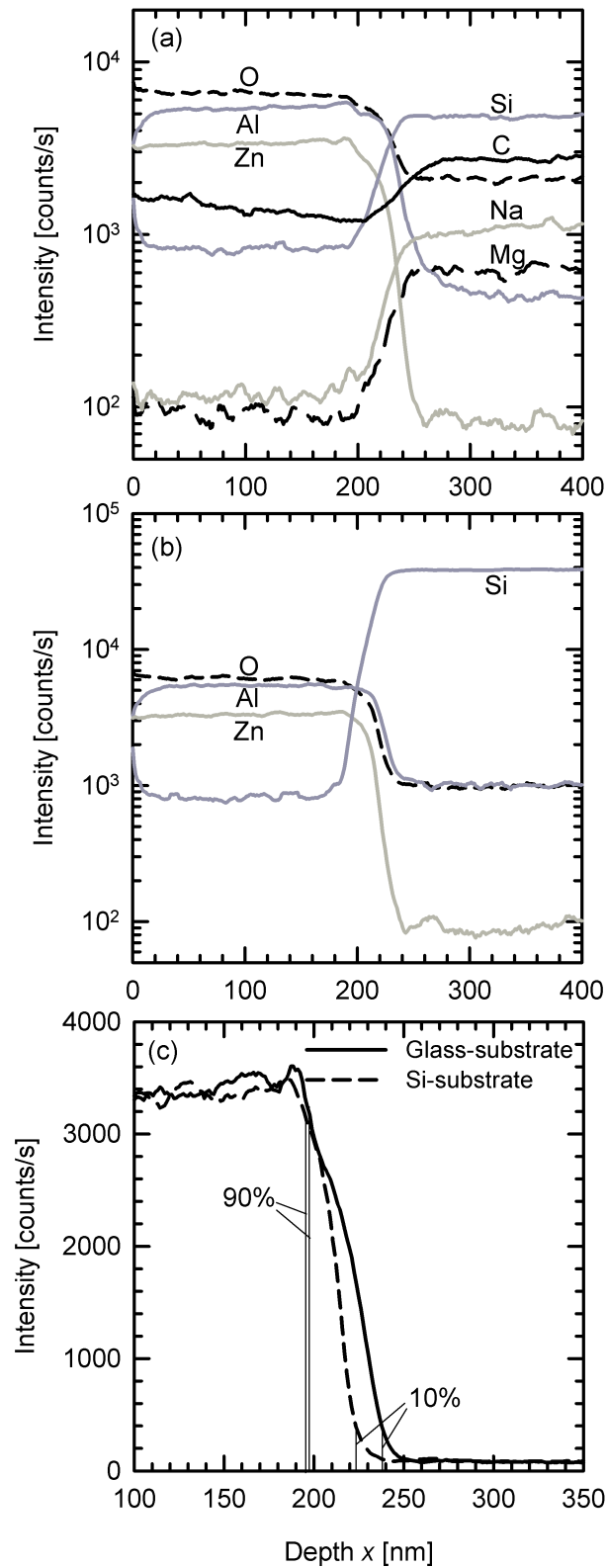


Figure 3.18: SNMS depth profiles of ZnO:Al films on glass (a) and silicon (b) deposited at 200 °C substrate temperature as well as the comparison (c) of the depth profiles of Zn for the two samples. The positions of the 10% and 90% full-scale signal levels are indicated.

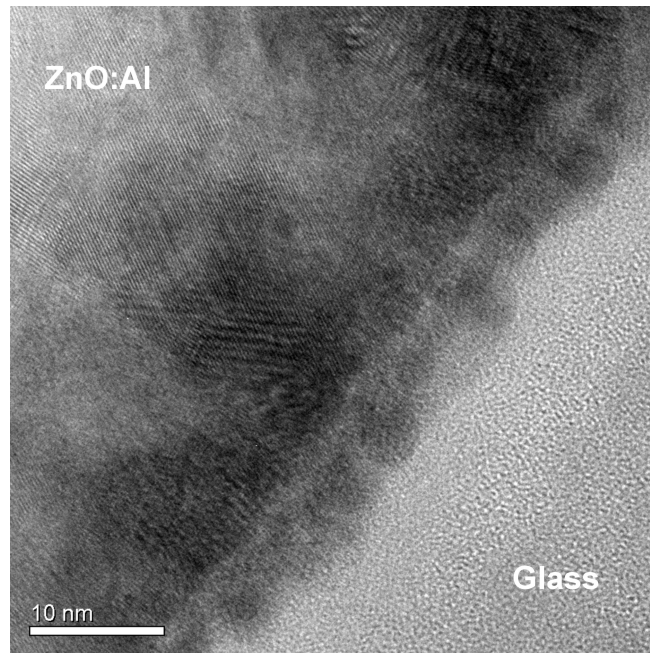


Figure 3.19: Cross-sectional HRTEM image of a 400-nm-thick ZnO:Al thin film on glass (air side of float glass) deposited at 200 °C substrate temperature. The interface is presented diagonally due to a metrologically caused image rotation.

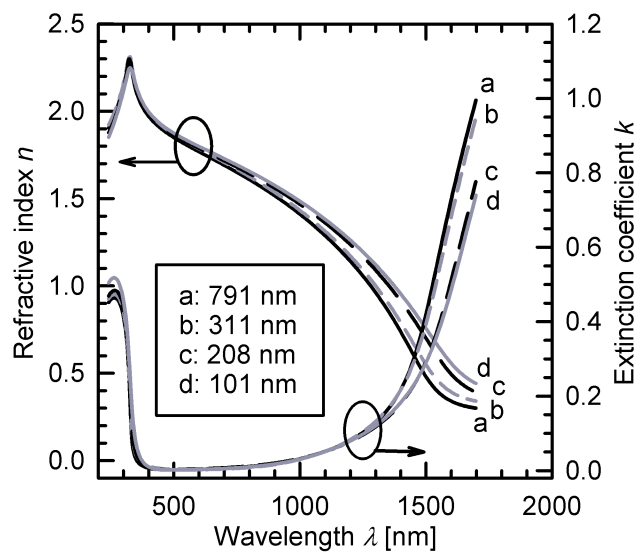


Figure 3.20: Optical constants of ZnO:Al thin films on glass with different film thicknesses deposited at 200 °C substrate temperature. Only the refractive index of the film plane $n_{\text{film plane}}$ is shown for clarity.

density of the Mott criterion (see Sec. 2.3.2). The SE results of the electronic properties of the samples agree with the results of the Hall analysis if an effective mass of $m_e^* = 0.4m_0$ is assumed. Taking into account the non-parabolic form and degeneracy of the conduction band [35, 62, 82, 87, 159], the model developed by Pisarkiewicz et al. (Eq. 2.13) describes the effective mass of the electrons in dependence of the free-carrier concentration in degenerated films. With an effective mass of undoped ZnO of $m_0^* = 0.24m_0$ [81, 82] and a non-parabolicity factor of $C = 0.39 \text{ eV}^{-1}$ (see Sec. 3.3.5), the Pisarkiewicz model gives an effective mass of the electrons at the Fermi level of $m_e^* = 0.405m_0$, which is in accordance with our assumption of $m_e^* = 0.4m_0$ in Sec. 3.3.1.

Figure 3.15 also shows a slight deviation between the results of the SE analysis and the Hall measurements for film thickness values lower than 400 nm. For ZnO:Al thin films, grain size increases with film thickness and the density of grain boundaries decreases due to an anisotropic film growth with different growth rates of the grains parallel and perpendicular to the film plane, as reported by Fenske et al. [160]. The difference between SE analysis and DC measurements for small film thicknesses may be caused by the greater dependence on grain boundary scattering of the DC measurements in contrast to optical measurements [94]. As discussed in Sec. 3.2.2, the amplitude of the free carriers is very short in comparison to the grain size if they are accelerated by an electromagnetic wave with frequencies in the solar and infrared spectral range. As a result, ionized impurity scattering is the dominant scattering process since the distances between the ionized scatterers are much shorter than the grain size; therefore, grain boundary scattering is negligible for the optical determination of the electronic parameters. For films with small free-carrier densities, the potential barriers of the grain boundaries increase, which may cause also an increase of the difference between optical and DC measurements.

Anisotropy

Standard SE measurements are only applicable if the optical axis is parallel or perpendicular to the plane of the incident light since only then the diagonal elements of the Jones matrix are zero. If this is not the case, generalized ellipsometry has to be applied [20, 106]. The result of the XRD analysis is an indication for a well defined crystalline structure of the sputtered films with a preferred *c*-axis orientation. Therefore, the application of standard SE measurements is justified. The XRD spectrum exhibits no Al_2O_3 phase, which is also an indication for the efficient incorporation of Al on Zn sites [50]. The fit result dn of the difference between the refractive indices parallel and perpendicular to the film plane is in agreement to literature data for single-crystal bulk ZnO. However, the assumption of a constant refractive-index offset between the refractive index parallel and perpendicular to the film plane is a rough approximation and only valid for the transparent spectral range [134]. In spectral regions where absorption

occurs, especially the band-gap region, the dispersion relations of the refractive index in the film plane and for the optical axis may differ from each other [144, 145]. In this case, there have to be different oscillator models for the film plane and the optical axis. However, this is out of the scope of this thesis.

Substrate-film interface

The transition regions determined by the SNMS analysis in Fig. 3.18 (c) may be caused by a greater roughness of the glass substrate in comparison to the silicon wafer or an indication of an interface layer because of a different morphology.

There are a few publications about the existence of an interface layer. Several authors [53, 59, 60, 72, 160] reported that the growth of sputtered ZnO and ZnO:Al is greatly influenced by the crystalline structure, the surface roughness, and the thermal expansion coefficients of the substrates. Yoshino et al. [60] observed that in the case of an amorphous substrate such as glass, a several-nanometers-thick amorphous layer of ZnO is formed at the interface followed by a second polycrystalline layer before the well-known c-axis-oriented layer grows. This is an indication of a considerable atomic interaction of ZnO with the substrate surface. Sieber et al. [59] determined the influence of Al-doping on film growth at the interface of a silicon substrate and the bulk. With increasing Al-content, an increasing nanocrystalline region between the interface and the columnar bulk became obvious. Phase analysis of the nanocrystalline region revealed many different phases with different conductivities, such as hexagonal ZnO, hexagonal $\text{Zn}_4\text{Al}_{22}\text{O}_{37}$ and tetragonal Al_2O_3 . Thus, the phase composition as well as the conductivity of this region were very inhomogeneous. Fenske et al. [160] showed that ZnO and ZnO:Al exhibit anisotropic grain growth with different growth rates parallel and perpendicular to the film plane and an increase of the growth rate and of preferred oriented crystalline structure with increasing film thickness. Li et al. [53] obtained an increase of the crystallite size with increasing film thickness, which was also indicated by an increase in electron mobility [73]. The results cited above were obtained for unheated substrates. For comparison, the HRTEM analysis in this thesis of films grown on heated substrates shows a formation of an interface region, which is assumed to be a result of the tendency of ZnO:Al to dilute into the glass substrate. As conclusion, the interface layer required in the MDF may be a consequence of structural modifications at the early stages of film growth, which also have a great influence on the conductivity of this region.

The model presented in this thesis yields good fit results for the measured ellipsometric and photometric data of sputtered ZnO:Al thin films over the whole measured spectral range of 240 nm to 50 μm , which is the relevant spectral range for solar-thermal applications and is in accordance to several independent thin film characterization methods. In the following, the MDF is used to characterize the optical and electronic properties of ZnO:Al thin films deposited by various deposition parameters.

3.3.3 Results of the deposition parameter studies

In order to optimize the film properties with respect to the solar-thermal application, this section addresses the influence of the deposition parameters on the optical and electronic properties of sputtered ZnO:Al thin films. There are many publications about deposition parameter studies. Here, only some of them are mentioned. Minami et al. published several studies [24, 66, 123] on the influence of the substrate temperature, the sputtering pressure, the power, and the target doping concentration on the properties of ZnO:Al thin films deposited either by RF or DC magnetron sputtering. Agashe et al. [52, 58] investigated the influence of the doping concentration, the substrate temperature, the sputtering pressure, as well as the film thickness on ZnO:Al thin films deposited by RF magnetron sputtering from ceramic targets. Song et al. [12] showed also the influence of the sputtering pressure and the RF power on the film properties. Kluth et al. [19] developed a modified Thornton model (see Sec. 2.5.4) of the ZnO:Al growth and etching behavior on the basis of parameter studies with varying substrate temperature, sputtering pressure and plasma excitations. Berginski [157] and Hüpkes [18] showed detailed parameter studies for solar cell applications in their theses concerning the dependence of the film properties on the substrate temperature, the pressure and the etching behavior of ZnO:Al thin films with different doping concentrations deposited by non-reactive RF and reactive MF magnetron sputtering, respectively. However, usually these parameter studies are aimed at the film optimization for optoelectronic and solar cell applications which have different optimization criteria in comparison to the solar-thermal application. In addition, the film properties depend strongly on the deposition conditions such as the coater geometry, the plasma excitation and the target material so that the application of these results is limited. For this reason, the parameter studies presented in this section are necessary for the development of AR coating systems and the improvement of the collector performance.

In the following, the optical and electronic properties of ZnO:Al thin films deposited by DC magnetron sputtering from a ceramic target with 2 wt.% Al₂O₃ are investigated as a function of the substrate temperature, the argon pressure and the DC power. The standard set of parameters at the beginning of this work were an argon pressure of 0.5 Pa, a DC power of 500 W, and no substrate heating. In the following, one out of these parameters is varied while the other two parameters are kept constant at their standard values. The substrate temperature is varied in the range from room temperature to 400 °C, which is the upper limit of the in-line coater. In contrast, there exists only a small range of suitable pressure values. The lower limit of the pressure range is 0.3 Pa since with lower pressures, the plasma was not stable. At pressures higher than 0.8 Pa, the films have poor transmittance due to high absorption. An increase in the number of arcing events with increasing argon pressure is also observed. The DC power is varied from 200 W to 600 W. At lower power levels, the deposition rate becomes

very small, 0.56 nm/s, which is not favorable for industrial processes. At higher power levels, the number of arcing events increases drastically and might become a problem. Figure 3.21 shows the electronic and optical properties such as the free-carrier density and mobility, the resistivity as well as the solar transmittance, reflectance, and infrared emissivity of samples deposited with varying parameters. The film properties are determined by simultaneous modeling of the ellipsometric and photometric spectra. The free-carrier properties of Fig. 3.21 (d)–(f) are obtained from Eqs. 3.19–3.23 from the fit parameters of the SE analysis.

Although the sputtering time is kept constant at 620 s for every process, the film thickness values range from 300 nm to 900 nm because of the dependence of the deposition rate on the process parameters, as shown in Fig. 3.21 (g)–(i). Since the transmittance of the films depends on the film thickness according to the Lambert-Beer law and the Fresnel equations, the comparison of the transmittance spectra of films with different thicknesses is not significant. The reflectance in the solar spectral range also changes with film thickness since the number and position of the interference maxima and minima depend on the film thickness. As already shown in Fig. 3.15, the resistivity of a very thin sample is high due to small grain sizes and poor crystalline quality at the beginning of film growth. To make the comparison of the samples reasonable, the optical constants of the samples are determined by simultaneous modeling of the ellipsometric and photometric spectra, and in the following, the transmittance, reflectance, and emissivity spectra are simulated for a normed film thickness of 500 nm. Figure 3.21 (a)–(c) shows the solar and infrared wavelength-averaged values of the simulated spectra obtained from Eqs. 2.3 and 2.4.

Substrate temperature variation

Varying of the substrate temperature (see Fig 3.21 (a) and (d)) shows that there exists a minimum of resistivity. The free-carrier concentration and mobility increase with increasing substrate temperature up to a temperature of 200 °C and 250 °C, respectively. At higher temperatures, both values decrease again. The infrared emissivity shows a behavior similar to the resistivity. The solar reflectance reaches a maximum when the resistivity and emissivity are minimal. In contrast, the solar transmittance increases almost linearly with increasing substrate temperature.

Argon pressure variation

Varying of the argon pressure (see Fig 3.21 (b) and (e)) causes no clear minimum of the resistivity and of the emissivity. Both values exhibit a rapid decrease from 0.3 Pa to 0.4 Pa, and at higher argon pressures the decrease becomes more flat. The free-carrier concentration is increased with increasing argon pressure and the mobility shows, after a short increase, an almost constant behavior at argon pressures higher than 0.4 Pa.

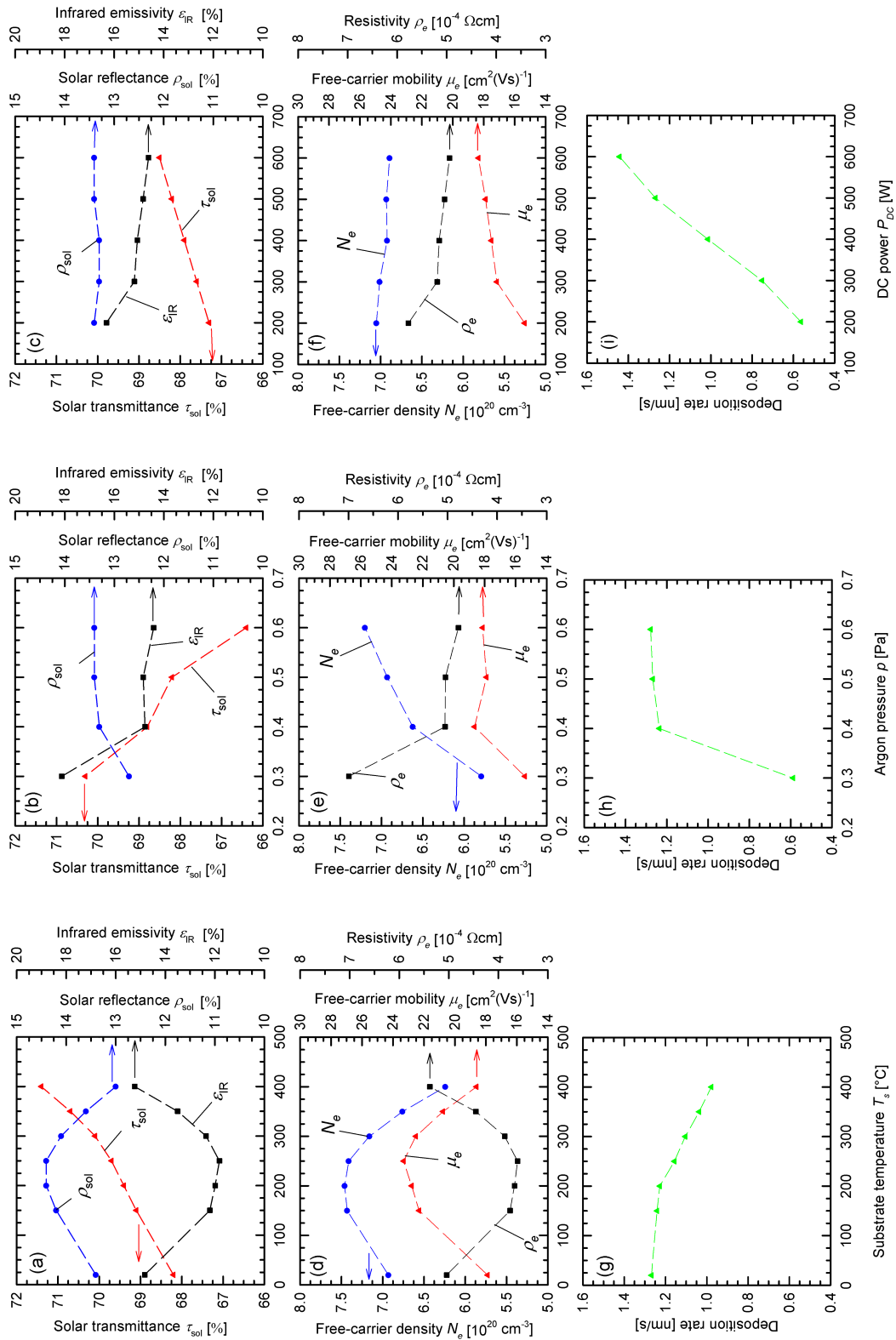


Figure 3.21: Film properties such as (a)–(c) solar transmittance, reflectance, and infrared emissivity as well as (d)–(f) free-carrier properties and (g)–(i) deposition rates as functions of substrate temperature, argon pressure, and DC power. The errors of the free-carrier properties determined by the optical analysis are $\Delta N_{\text{opt}} \leq 3\%$ for the electron concentration, $\Delta \mu_{\text{opt}} \leq 3\%$ for mobility, and $\Delta \rho_{\text{opt}} \leq 3\%$ for resistivity.

In contrast, the solar transmittance is strongly reduced with increasing argon pressure. The solar reflectance is nearly constant at argon pressures higher than 0.4 Pa.

DC power variation

Varying of the DC power (see Fig 3.21 (c) and (f)) shows slightly decrease in resistivity and emissivity with increasing DC power. The free-carrier concentration is almost constant while the mobility increases with increasing DC power. The solar reflectance shows also a nearly constant behavior while the solar transmittance exhibits an almost linear increase with increasing DC power.

3.3.4 Discussion of the results of the deposition parameter studies

In Fig. 3.21 (a)–(f), it becomes obvious that the optical and electronic properties are strongly correlated with each other. The graphs of the emissivity always show the same characteristic slope in comparison to the resistivity of the films. The solar reflectance is influenced by the free-carrier concentration since the plasma wavelength, at which the reflectance starts to increase, is shifted to shorter wavelengths with increasing free-carrier concentration. If the plasma wavelength is shifted to shorter wavelengths of the solar spectral range, the solar reflectance increases due to the weighting of the reflectance spectrum with the solar spectrum (see Eq. 2.3). The solar transmittance is influenced by both free-carrier properties and crystalline quality. The free-carrier absorption peak is shifted to smaller wavelengths with increasing free-carrier concentration, which decreases the transmittance (see Fig. 2.10). An increasing mobility reduces the free-carrier absorption peak and causes an increase in the solar transmittance. Whether the solar transmittance is increased or decreased depends on which effect is more dominant as well as on the crystalline quality of the films.

Substrate temperature variation

The electronic and optical properties of films deposited on heated substrates show a strong temperature dependence, as shown in Fig. 3.21 (a) and (d). The increase of solar transmittance may be connected with an improvement of crystalline quality. On heated substrates, the thermal energy enables a better migration of incoming sputtered particles and therefore, a better crystal growth with less defects. However, at temperatures higher than 250 °C, the conductivity of the films decreased. The decrease in conductivity at higher substrate temperatures may be related to adsorbed atoms of the residual gas, which is emitted from the hot walls of the vacuum chamber, or to a diffusion of alkali atoms of the glass substrate into the growing film [10]. Vinnichenko et al. [161] showed that there exists a critical substrate temperature for reactively sputtered ZnO:Al thin films from Zn-Al alloyed targets, which is related to a desorption of Zn due

to its high vapor pressure and the formation of an insulating metastable homologous $(\text{ZnO})_3\text{Al}_2\text{O}_3$ phase.

Argon pressure variation

The sample deposited with an argon pressure of 0.3 Pa shows a much higher resistivity and emissivity in comparison to the other samples of the pressure series (see Fig. 3.21 (b) and (e)). The reason may be the small film thickness of the film since thin ZnO:Al films have only a poor conductivity due to small grain sizes and poor crystalline quality. The other samples of the pressure series do not vary much in their electronic and optical properties in comparison to the temperature series (Fig. 3.21 (a) and (d)) except for the solar transmittance (compare Fig. 3.21 (a) and (b)). The reason for the decrease of the solar transmittance may be connected with a poor crystalline quality. On the one hand, much argon ions are accelerated to the target and the sputter yield is high at high argon pressures. On the other hand, the sputtered particles incur lots of collisions with the plasma particles and their energy is reduced. Therefore, the incoming sputtered particles on the substrate surface have low energy and the crystal growth will be less dense and with defects [19]. At argon pressures higher than 0.6 Pa, the films become more and more opaque with a black color, which may be related to the non-stoichiometry of the films [20]. Oxygen vacancies may be attributed to cause an increase in free-carrier concentration.

DC power variation

The high resistivity and high emissivity of the sample deposited at 200 W DC power (see Fig. 3.21 (c) and (f)) may be caused by the small film thickness for the same reason as mentioned for the sample deposited with an argon pressure of 0.3 Pa. The power series exhibits only slight changes of the resistivity and emissivity, as well as the free-carrier concentration and solar reflectance for DC power values higher than 300 W. With increasing DC power, the free-carrier mobility increases, which may be caused by an improvement in crystalline quality. The energy of the sputtered particles increases with increasing DC power, which enables the migration of the incoming sputtered particles on the substrate surface and improves the crystal growth. An increase in crystalline quality also causes an increase of the solar transmittance since the free-carrier absorption is reduced. However, with increasing DC power, the number of arcing events also increases, which may damage the target.

The parameter studies show that in most cases one has to compromise between high solar transmittance and low resistivity as well as infrared emissivity. For the application in a solar-thermal flat-plate collector, a high solar transmittance and a sufficient low emissivity are required. To analyze the influence of the film properties on the collector efficiency, one has to calculate the radiative interchange inside the collector

system and to take account of conductive and convective thermal losses, which will be shown in Chapter 5. At this point of this thesis, the deposition parameters used for the following samples are chosen with respect to the lowest infrared emissivity since the solar transmittance can be increased by adjusting the film thickness and adding AR coatings, as will be shown in Chapter 4.

Substrate heating up to 250 °C is advantageous for improving the solar transmittance and infrared emissivity. However, for industrial sputtering on large substrates, it is difficult to reach a homogeneous temperature distribution over the whole substrate area at high substrate temperatures. Especially for industrial processes on glass substrates (typical sizes are 3.21 m × 6.00 m), it is difficult to use high temperatures [10]. In this case, it is a great challenge to reach a good vacuum in an in-line coater in a sufficient short time. Another problem may be the stability of the glass substrates under temperature gradients. If high temperatures are needed, only smaller substrate sizes such as 2.5 m² can be used [10]. Therefore, the substrate temperature should be as low as possible. Since the difference of the infrared emissivity for 200 °C substrate temperature is only marginal higher than the infrared emissivity for 250 °C (see Fig. 3.21 (a)), the lower substrate temperature is chosen. The optical properties are favorable using an argon pressure of 0.4 Pa (see Fig. 3.21 (b)), however, by reason of plasma stability 0.5 Pa is chosen in the following. The best properties of the power series are reached at a DC power of 600 W (see Fig. 3.21 (c)). However, since the number of arcing events is very high for 600 W, the following samples are sputtered with a DC power of 500 W.

3.3.5 Results of the doping-concentration variation

In the following, the results of ZnO:Al films sputtered from targets with varying Al₂O₃ content (0.2 wt.%, 1.0 wt.% and 2.0 wt.%) are shown for studying the influence of the doping concentration on various film properties such as the morphology, the electronic, and the optical properties. Special attention is paid here to the influence of the free-carrier concentration on the optical band gap and the effective mass of the free carriers. For this purpose, the results of the optical analysis using the MDF presented in Sec. 3.2 are compared to theoretical investigations of the band-gap shifts and the effective mass given in Sec. 2.3.2. Other studies on varying doping concentrations of ZnO:Al thin films can be found in for instance publications of Minami et al. [66, 71], of Agashe et al. [52, 58], as well as of Hüpkes [18] and of Berginski [157]. All the films presented in this section are sputtered with 0.5 Pa argon pressure and 500 W DC power, but with varying substrate temperature and film thickness.

Morphology

Figure 3.22 shows SEM top-view images of films with varying doping concentration and substrate temperature. Cross-sectional images are not shown since the difference between the samples becomes more obvious with the top-view images. All the films

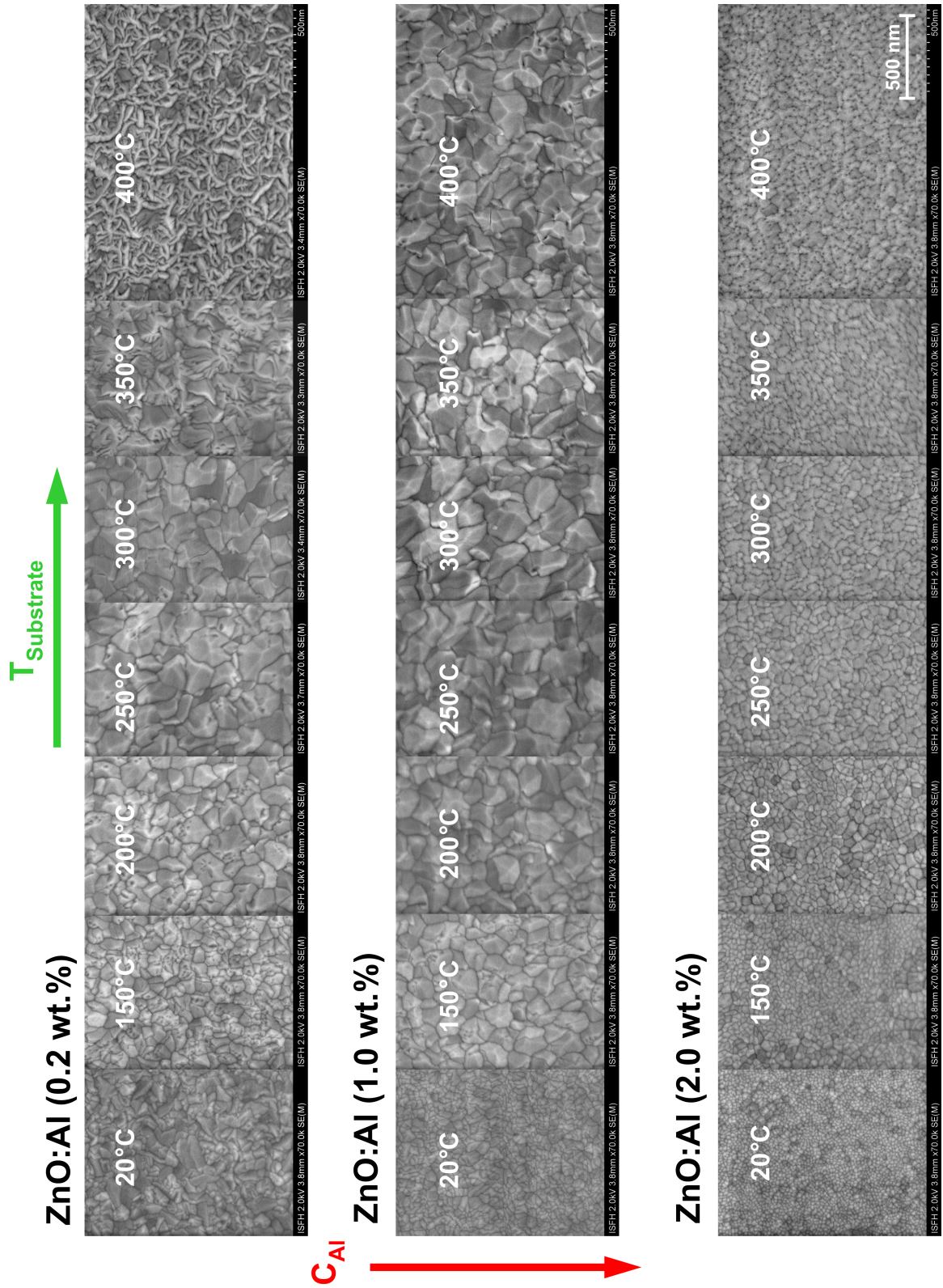


Figure 3.22: SEM top-view images of ZnO:Al thin films with varying doping concentrations deposited with different substrate temperatures on glass substrates.

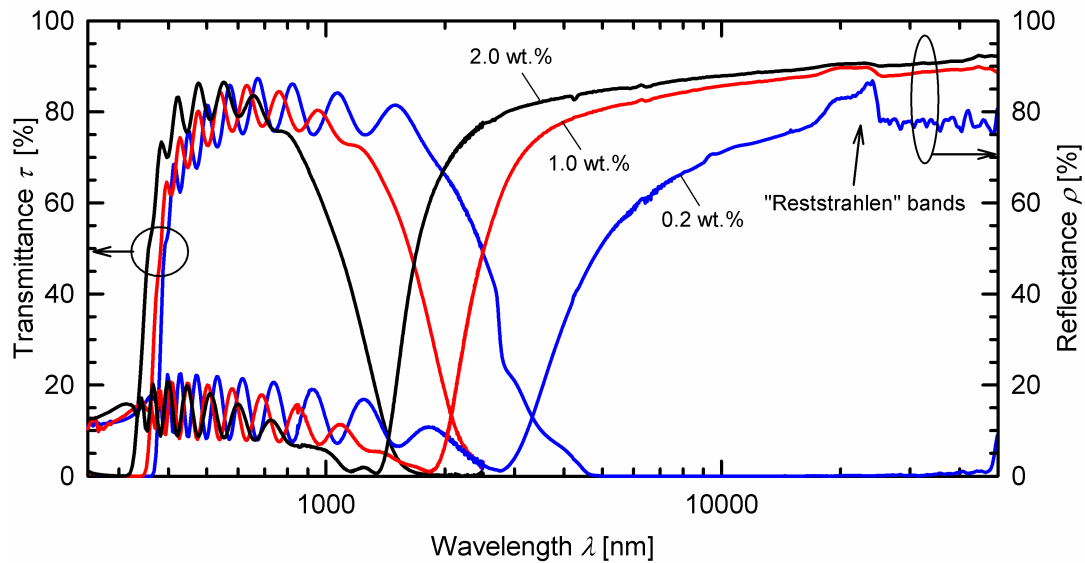


Figure 3.23: Measured transmittance and reflectance spectra of ZnO:Al thin films with varying doping concentration deposited at 150 °C substrate temperatures on glass substrates.

exhibit a columnar film growth but with varying grain sizes. The increase of the substrate temperature provides an increase of the grain size up to a temperature of 300 °C, independent of the doping concentration. At higher substrate temperatures, the grains change their structure. This effect becomes especially obvious for the films sputtered from the target with 0.2 wt.% Al_2O_3 . The films sputtered from a target with 2.0 wt.% Al_2O_3 have small grain sizes, less than 100 nm. In contrast, the grain sizes of the films sputtered of the targets with lower Al_2O_3 contents exhibit grain sizes up to 300 nm.

Optical properties

Figure 3.23 depicts the transmittance and reflectance spectra of films with varying doping concentration sputtered for 620 s at 150 °C substrate temperature. With increasing doping concentration, the fundamental absorption edge as well as the plasma wavelength are shifted to lower wavelengths. The film sputtered from the target with 2.0 wt.% Al_2O_3 reaches the highest infrared reflectance out of the three samples. A feature in the reflectance spectra of the films with low doping concentration becomes also obvious at about 20000 nm (see Fig. 3.23), which looks like a shouldered peak. The peaks are related to the coupling of transversal optical phonons with photons and are called “reststrahlen” bands [105], as will be discussed in Sec. 3.3.6.

In order to determine the optical and electronic properties of the samples, ellipsometric and photometric data are analyzed simultaneously with the model presented in Sec. 3.2. The model is also applicable for films sputtered from the targets with 0.2 wt.% and 1.0 wt.% Al_2O_3 . However, the insertion of the interface layer does not improve the fit result of samples sputtered from the targets with 0.2 wt.% and 1.0 wt.% Al_2O_3

further more in contrast to the highly doped films. In addition, a unique determination of the film thickness of the interface layer and the composition ratio of glass and undoped ZnO of the BEMA model is not possible. Satisfying fit results are reached if the composition ratio is fixed. Since the interface layer does not improve the fit result of the lower doped samples, the spectroscopic data of these samples are modeled without the interface layer. However, the existence of the interface layer of these films is questionable and will be discussed in the next section. The modification factor κ of the Tanguy model which was introduced in Sec. 3.2.2 to take account of a Gaussian-like broadening of the band-gap transitions decreases with decreasing doping concentration and reaches zero for the films sputtered from the target with 0.2 wt.% Al₂O₃ (see Appendix 3). The reststrahlen peaks in the infrared reflectance spectrum are modeled with two Gaussian oscillators [106]. The parameters of the oscillators are fixed since a unique determination was not possible. The reason is that only reflectance data in this wavelength range are available for this thesis, which is not enough information, and additional ellipsometric data would be required for a unique determination of these parameters.

In Appendix 3, the fit parameters of characteristic films sputtered from the targets with different Al₂O₃ content are shown.

Effective mass

For the determination of the free-carrier density N_e and mobility μ_e , the effective mass has to be known. Therefore, Hall measurements are taken at samples deposited at substrate temperatures ranging from room temperature up to 300 °C. Assuming $N_e \approx N_{\text{Hall}}$, the effective mass is calculated from Eq. 3.20 using the fit results of the Drude parameter A_D . Figure 3.24 shows the effective mass as a function of free-carrier density for samples with different doping concentration. The effective mass increases almost linearly with increasing free-carrier density. Linear regression yields $m_e^*/m_0 = 0.24 + 0.0259 \cdot 10^{-20} \text{ cm}^3 \cdot N_e$. The intercept corresponds to the effective mass of electrons at the bottom of the conduction band with $m_0^* = 0.24m_0$. The Pisarkiewicz model (Eq. 2.13) is also fitted to the data. If both values, the effective mass m_0^* of electrons at the bottom of the conduction band and the non-parabolicity factor C are used as fit parameters, the results with $m_0^* = 0.16m_0$ and $C = 0.77 \text{ eV}^{-1}$ are not reliable in comparison to literature data [35, 80–82]. Therefore, m_0^* is fixed at $0.24m_0$ and only C is used as fit parameter, which results in $C = 0.39 \text{ eV}^{-1}$.

Optical band gap

In Fig. 3.25, the optical band-gap values of the films deposited at various substrate temperatures are presented in dependence of the free-carrier densities. Both quantities, the free-carrier density and the optical band gap are determined by SE analysis. For the determination of the optical band gap, the original and the modified Tanguy model

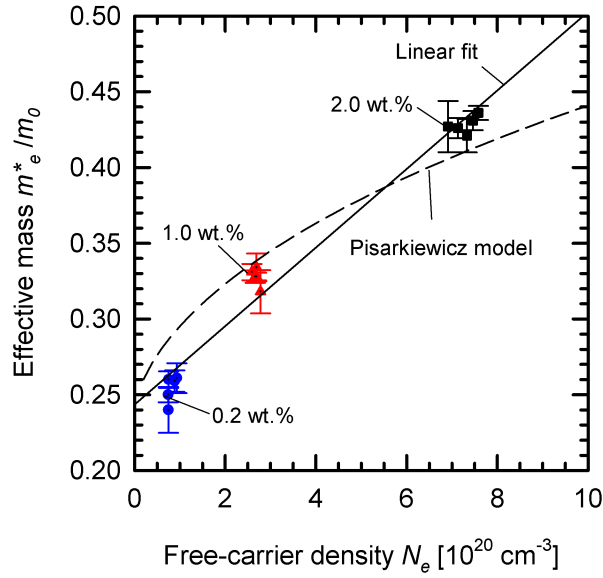


Figure 3.24: Effective mass of the free-carriers of ZnO:Al thin films with varying doping concentration determined by SE and Hall analysis. The solid black line depicts a linear fit of the effective mass data and the dashed black line is calculated with the effective mass model of Pisarkiewicz et al. [87].

are used, as shown by the open and filled symbols in Fig. 3.25. As mentioned already above, the modification factor κ which was introduced in Sec. 3.2.2 to take account of a Gaussian-like broadening of the band-gap transitions decreases with decreasing doping concentration and reaches zero for the films sputtered from the target with 0.2 wt.% Al_2O_3 . The optical band gap increases with increasing free-carrier density due to state filling and band-gap narrowing, as already described in Sec. 2.3.2 and schematically shown in Fig. 2.8. In order to characterize the dependency of the optical band gap on the free-carrier density, the experimental values determined by the optical analysis are compared to theoretical investigations. The theoretical band-gap widening is calculated by the Burstein-Moss model (Eqs. 2.10 and 2.11), which takes account of state filling of the conduction band. Another approach takes band-gap narrowing (BGN) due to many-body effects into account, besides the BM shift. The BGN is calculated with the Inkson model (Eqs. 2.14 and 2.15). For the calculation of the BM shift and the BGN, the effective mass of the free carriers at the Fermi level and of the holes in the valence band has to be known. As shown in Fig. 3.24, the effective mass of the free carriers is a function of free-carrier density due to the level of state filling and non-parabolicity of the conduction band. Therefore, the model of Pisarkiewicz is used for the determination of the effective mass at different free-carrier densities. The value of the effective mass of the light and heavy holes in the valence band is reported with $m_v^* = 0.59m_0$ [80].

The experimental optical band-gap values determined by the modified Tanguy model agree with the theoretical investigations while the experimental band-gap values determined by the original Tanguy model exhibit a larger deviation to the theoretical band

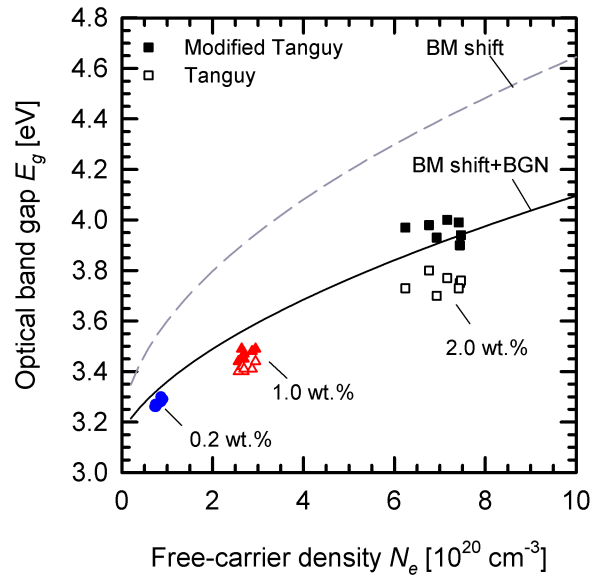


Figure 3.25: Optical band gap determined by SE analysis of ZnO:Al thin films with varying doping concentration deposited at different substrate temperatures. The optical band gap is determined using the original (open symbols) and the modified (filled symbols) Tanguy model. The dashed black line depicts the band-gap shift with respect to the Burstein Moss (BM) effect and the solid black line includes also band-gap narrowing (BGN) effects. The error of the optical band gap determined by the SE analysis is $\leq 1\%$.

gap.

Electronic properties

In the following, the experimental mean values of the effective mass of the samples of the temperature series for each doping concentration (see Fig. 3.24) are used to determine the free-carrier concentration and mobility as well as the resistivity from the Drude parameters of the MDF (Eqs. 3.20 and 3.21). Figure 3.26 shows the electronic properties of films, deposited at various substrate temperatures, determined by spectroscopic ellipsometry in comparison to the Hall measurements. Both characterization methods show the same trend of the electronic properties in dependence of the substrate temperature. The free-carrier concentration and the resistivity determined by SE analysis are in good agreement with the Hall measurements; however, there are differences in the mobility values. The films sputtered from the target with 2.0 wt.% Al_2O_3 show a maximum free-carrier density and a maximum mobility, which results in a minimum resistivity at a substrate temperature of 250 °C. In contrast, the films sputtered from the targets with 0.2 wt.% and 1.0 wt.% Al_2O_3 show a local maximum of the free-carrier density at 150 °C and a second increase of free-carrier density at temperatures higher than 350 °C. The mobility values are all small for samples deposited on unheated substrates. There is also a local maximum of mobility for samples sputtered from the targets with 0.2 wt.% and 1.0 wt.% Al_2O_3 at 150 °C. At higher

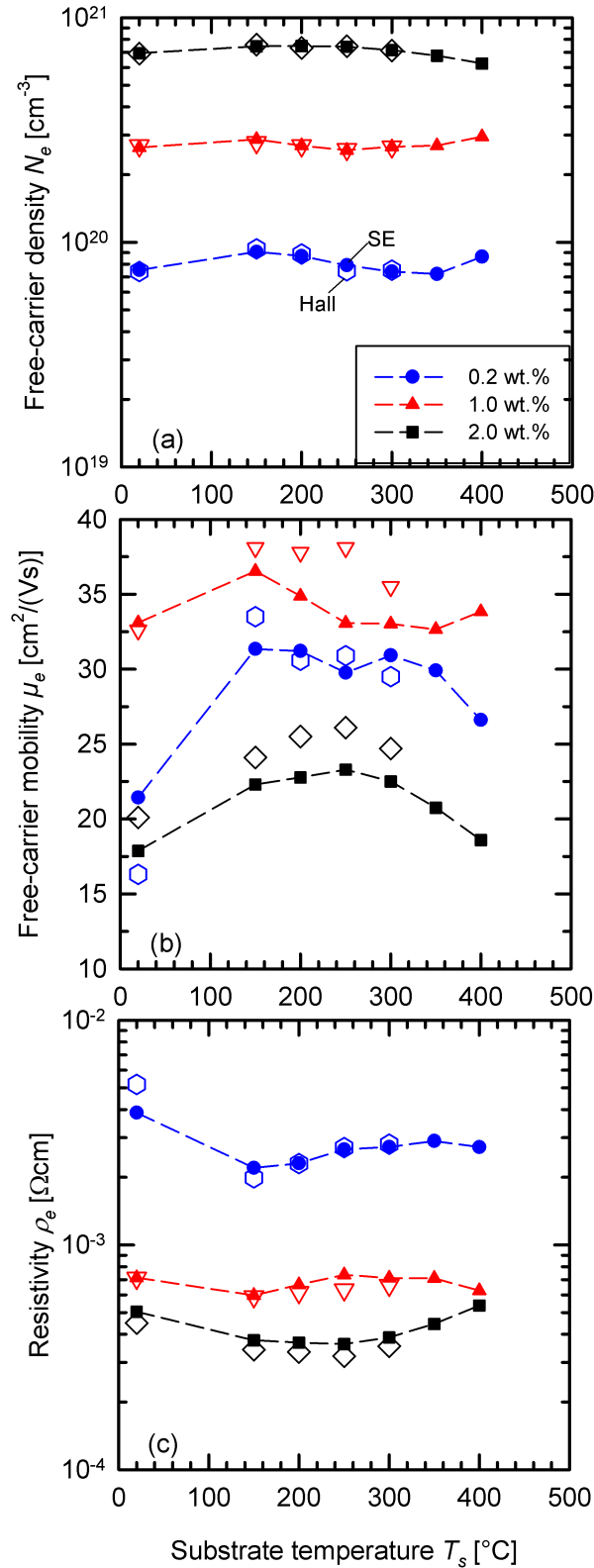


Figure 3.26: Free-carrier concentration (a) and mobility (b), as well as resistivity (c) determined by SE and Hall analysis of ZnO:Al thin films with varying doping concentration deposited at different substrate temperatures. Open and solid symbols depict the results of the Hall measurements and SE analysis, respectively. The error of the free-carrier properties determined by the SE and Hall analysis is $\leq 5\%$ and $\leq 2\%$, respectively.

substrate temperatures, there is no clear trend obvious. As a result, the resistivity of the samples sputtered from these targets exhibits a minimum at a substrate temperature of 150 °C and decreases again at substrate temperatures higher than 350 °C. Concerning the doping concentration of the targets, the films sputtered from the target with 0.2 wt.% Al₂O₃ exhibit the lowest and the films sputtered from the target with 2.0 wt.% Al₂O₃ show the highest free-carrier density. In contrast, the highest mobility values are reached by the films sputtered from the target with 1.0 wt.% Al₂O₃. The lowest resistivity values are reached by the films sputtered from the target with 2.0 wt.% Al₂O₃. The resistivity values of the films with the lowest doping concentration are one order of magnitude larger.

Figure 3.27 shows the electronic properties of samples with different doping concentration and varying film thickness values. The free-carrier concentration does not vary much with film thickness for all films. However, the films sputtered from the targets with 1.0 wt.% and 2.0 wt.% Al₂O₃ show a slight decrease in the free-carrier density with decreasing film thickness. The films with the lowest doping concentration show no clear trend. In contrast to the free-carrier density, the mobility is strongly influenced by the film thickness and decreases almost linearly with decreasing film thicknesses for all of the three doping concentrations but with different slopes. The slope of the films sputtered from the target with 2.0 wt.% Al₂O₃ is more flat than that for the other doping concentrations. As a result of the behavior of the free-carrier density and mobility, the resistivity of the films increases with decreasing film thickness.

Annealing

In a next step, the annealing behavior of films with different doping concentration is analyzed. Therefore, three films with a film thickness of approx. 400 nm (substrate temperature: 150 °C for the targets with 0.2 wt.% and 1.0 wt.% and 200 °C for the target with 2.0 wt.% Al₂O₃) are annealed at a hot plate in air with increasing temperature. The films are annealed for 30 min at every temperature step and then cooled down for the measurement of the sheet resistance by four-point probe measurements and the photometric data. Figure 3.28 shows the resistivity and the infrared emissivity of the three samples as a function of annealing temperature. The solar transmittance and reflectance are not shown since the change in these values is very small under temperature load. All samples show a small improvement of resistivity and emissivity at annealing temperatures lower than 300 °C. At higher temperatures, the resistivity increased drastically. In contrast, the emissivity values of all samples are similar after annealing at 400 °C.

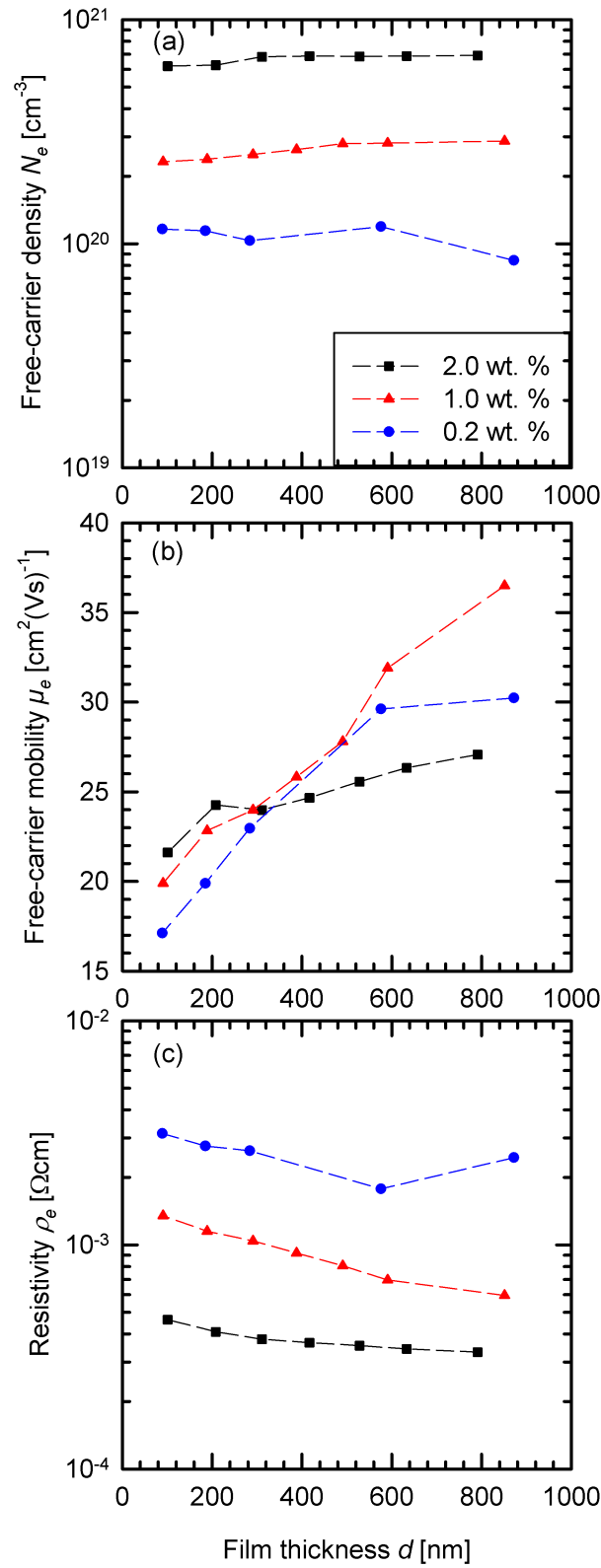


Figure 3.27: Free-carrier concentration (a) and mobility (b) as well as resistivity (c) determined by SE analysis of ZnO:Al thin films with varying doping concentration and film thickness. The error of the free-carrier properties determined by the SE analysis is $\leq 10\%$.

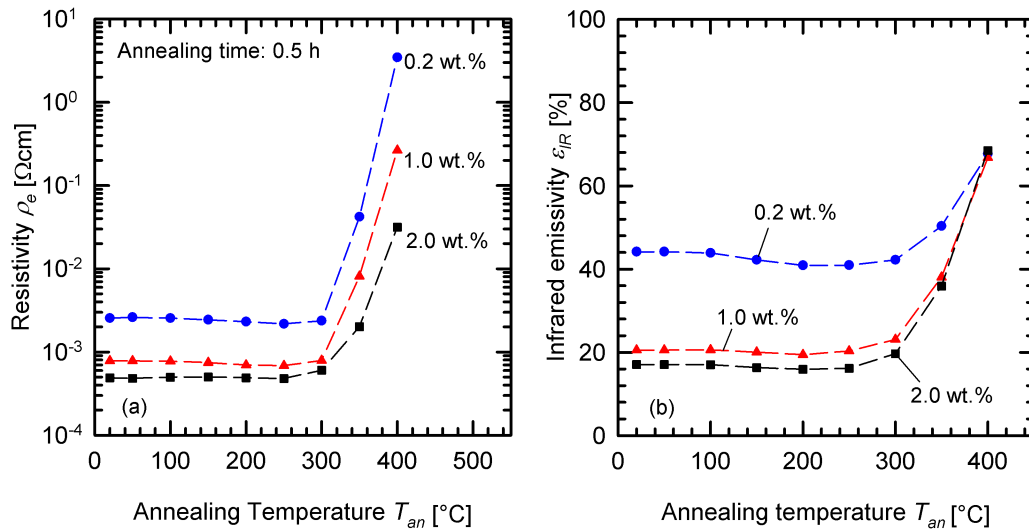


Figure 3.28: Development of (a) resistivity and (b) infrared emissivity of ZnO:Al thin films with varying doping concentration annealed in air.

3.3.6 Discussion of the results of the doping series

Morphology

The SEM top-view images in Fig. 3.22 show an increase of grain sizes with increasing substrate temperature up to 300 °C. The reason may be the higher thermal energy of the impinging sputtered particles, which enables a better migration on the substrate surface and, therefore, a better crystal growth. This trend is in accordance to the zone growth models developed by Thornton and Kluth [19, 131, 132], which predict an increase of film compactness with increasing substrate temperature. However, at higher substrate temperatures than 300 °C, the crystal structure of the samples presented in this thesis looks distorted, which may be caused by the influences of residual gas in the vacuum chamber or by evaporation of unbound zinc [161]. Also, film stress and strain are known to change the film structure due to different coefficients of thermal expansion of the substrate and film material [162]. Varying of the doping concentration also has a strong influence on crystal film growth. High number of impurities may disturb the crystal system, especially if the ion radius of zinc and the dopant atoms differ from each other. For very high doping concentrations of > 4 wt.%, a segregation and formation of clusters of Al_2O_3 at the grain boundaries were reported [18, 52]. Sieber et al. [59] showed that even at doping concentrations of 2.4 at.% a fine crystalline region at the substrate interface is formed before columnar film growth is reached. The fine crystalline region increases with increasing doping concentration until no columnar growth is observable any more at $C_{Al} = 8.6$ at.%.

Optical properties

The transmittance and reflectance spectra of the samples with different doping concentration show significant changes with the change in the free-carrier density, as shown in Fig. 3.23. The optical band gap is shifted to higher band-gap energies with increasing free-carrier density due to state filling and band-gap renormalization, as also shown in Fig. 3.25. The plasma wavelength of the free-carriers is shifted to lower wavelengths due to an increase of free-carrier concentration with increasing target doping concentration, as indicated in Fig. 3.23. In the infrared reflectance spectra of the lower doped samples in Fig. 3.23, characteristic peaks occur, which are caused by a coupling of the photons of the incident light with transversal optical phonons of the crystal [105]. The quanta of these photon-phonon couples are called polaritons. The dielectric function of the polaritons has a singularity at the lattice resonance frequency of the transverse optical phonons ω_{TO} and a zero point at the lattice resonance frequency of the the longitudinal optical phonons ω_{LO} [85]. Between these frequencies, the dielectric function is negative and the dispersion relation of the polaritons exhibits a region of forbidden light frequencies [105]. For this reason, total reflection occurs in this wavelength range and these bands are called “reststrahlen” bands [85, 105]. These bands only exist if the free-carrier density is low. In highly doped films, the optical phonon polaritons are effectively screened out by the free-carrier density [51]. Zinc oxide exhibits several phonon-mode frequencies [20]. However, in the reflectance spectra of the low-doping sample, only one peak is observable, which has a shoulder. This seems to be an indication of two peaks that are merged. Since the peaks could not be dissolved by decreasing the wavelength interval size of the reflectance measurements, this effect may be connected with a thermal broadening of the peaks at room temperature. The analysis of this effect requires measurements at cooled samples, favorable with spectroscopic ellipsometry since reflectance spectra do not provide enough information.

Interface layer

As mentioned in Sec. 3.3.5, the interface layer was not necessary to improve the optical modeling result of films sputtered from the targets with 0.2 wt.% and 1.0 wt.% Al_2O_3 . Since the existence of the interface layer was questionable, also HRTEM analysis was made at these samples in the same way as described in Sec. 3.1.2, which yield the same result as the HRTEM analysis of the sample sputtered from the target with 2.0 wt.% Al_2O_3 , as shown in Fig. 3.29. The HRTEM analysis indicates that a dilution of ZnO:Al into the glass substrate takes place independently of the doping concentration. The discrepancy between the SE and the HRTEM analysis may be caused by the similar refractive indices of the lowly doped ZnO films and the interface layer. In this case, there may arise numerical problems for the SE analysis which makes a unique determination of the film thickness of the interface layer and the composition ratio of the BEMA model of glass and diluted ZnO impossible.

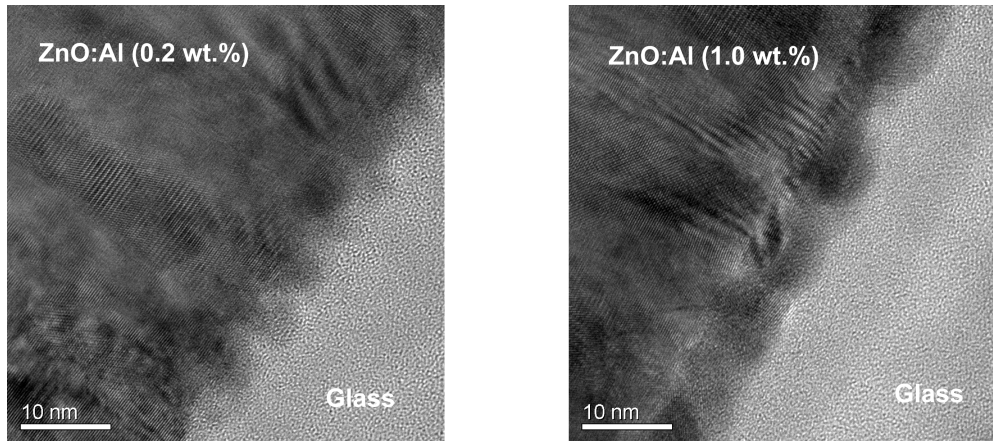


Figure 3.29: Cross-sectional HRTEM images of two 400-nm-thick ZnO:Al thin films on glass substrates (air side of float glass) sputtered from targets with 0.2 wt.% and 1.0 wt.% Al_2O_3 . The interface is presented diagonally due to a metrological caused image rotation.

Effective mass

The determination of the electron effective mass by SE and Hall analysis shows an increase with increasing free-carrier density due to band filling and non-parabolicity of the conduction band. The effective mass model developed by Pisarkiewicz was used by several authors [35, 78, 82] to describe the non-parabolicity of the conduction band. However, if the effective mass at the bottom of the conduction band and the non-parabolicity factor are both used as fit parameters, the result was implausible. Therefore, the effective mass at the bottom of the conduction band was fixed at $m_0^* = 0.24m_0$, a value which was reported by Pearton et al. [81] and Ruske et al. [82] and only the non-parabolicity factor C was fitted. However, there are some obvious differences between the Pisarkiewicz model and the measured data. The increase of the effective mass seems to be almost linear, which was also reported by Fujiwara et al. [35] and Ruske et al. [82], but with no physical motivation. The determination of the effective mass by SE and Hall measurements exhibits a high uncertainty. The reason is that the scattering parameter A_r of the Hall coefficient and the amount of non-parabolicity could not be determined by Hall measurements alone. It is, therefore, a common practice to set the scattering parameter to unity for Hall measurements of TCOs. Young et al. [159] measured the conductivity, the Hall, Seebeck, and Nernst coefficient by the method of four coefficients to obtain the density of states effective mass and the scattering parameter directly. For ZnO:Al, they showed that a first-order non-parabolicity approximation similar to the effective mass model of Pisarkiewicz is in agreement with the measured density of states effective masses by the method of four coefficients [21, 159].

Electronic properties

A high uncertainty in the effective mass causes a high uncertainty in the determination of the free-carrier concentration and mobility by the Drude parameters (Eqs. 3.20 and 3.20) of the SE analysis. This may be an explanation for the large deviation between the SE and Hall data of Fig. 3.26. Another explanation may be the different measurement techniques of AC and DC measurements. For DC measurements, grain boundary scattering may influence the measurements in contrast to the AC measurements. With this respect, it is expected that the SE analysis should provide higher mobility values than the Hall measurements, which was not observed in Fig. 3.26. For the samples sputtered from the targets with 0.2 wt.% and 1.0 wt.% Al₂O₃, the Drude parameters are also influenced by the phonon absorption of the reststrahlen bands. Since there are uncertainties of modeling the phonon absorption of reflectance measurements alone, uncertainties arise for the determination of the Drude parameters and the free-carrier properties. However, SE and Hall measurements show the same trend of the free-carrier properties in dependence of the substrate temperature and doping concentration. The temperature dependence of the samples with high doping concentration is in agreement with those mentioned in other publications [18, 157, 161, 163]. However, for the samples sputtered from the targets with 0.2 wt.% and 1.0 wt.% Al₂O₃, the lowest resistivities are reached with a substrate temperature of 150 °C. This is in contrast to observations made by Berginski [157] and Hüpkes [163], who analyzed the temperature dependence of ZnO:Al thin films with different doping concentrations deposited by RF magnetron sputtering and reactive mid-frequency sputtering, respectively. Both showed that there exist a maximal conductivity at a characteristic temperature for each Al content, which shifts to higher temperatures with decreasing Al content. The reason for the discrepancy may be the different plasma excitation such as DC, RF, and MF excitation or the target material. Especially, the target with 0.2 wt.% Al₂O₃ exhibits coarse grains, which may influence the homogeneity and reproducibility of the films. In literature [50, 157], an increase of free-carrier mobility with decreasing doping concentration is reported due to a decrease of the number of ionized impurities that act as scattering centers. The films sputtered from the target with 1.0 wt.% Al₂O₃ showed the highest mobility values of > 35 cm²/Vs. These values are slightly lower in comparison to RF sputtered films presented by Berginski [157]. The reason may be the lower ion bombardment of the growing film using RF plasma excitation [117]. As shown in Fig. 3.27, the films exhibit the same dependence of the electronic properties on film thickness nearly independent of the doping concentration. The decrease of the mobility with decreasing film thickness may be explained by the grain distribution. Thin films exhibit smaller grain sizes than thicker films which results in different grain boundary densities and defect levels. Fenske et al. [160] showed that ZnO has an anisotropic film growth with different growth rates perpendicular and parallel to the film plane. The dependence of the free-carrier mobility on the film thickness may

be, therefore, explained by the dependence on the crystalline structure which changes with the film thickness. The results presented in Fig. 3.27 are in agreement with observations made by Agashe et al. [52].

Although the electronic properties are determined by optical modeling in this thesis, the MDF does not implicitly take account of the thickness dependence of the electronic properties. For this reason, the MDF has to be determined for every individual sample with a certain film thickness. In the following simulations in Chapter 4 and 5, measured or modeled data with respect to the corresponding film thickness are, therefore, used.

Optical band gap

The optical band gap determined by SE analysis increases with increasing free-carrier concentration (see Fig. 3.25), independently of the band-gap model used. Using the modified Tanguy model yields band-gap values which are much more in agreement with the theoretical investigations on the band-gap shift than band-gap values determined without the modification, especially for highly doped films. The observation that the modification factor κ of the modified Tanguy model increases with increasing doping concentration is in agreement with the assumption that impurities cause the change from Lorentzian to Gaussian broadening of the band-gap transitions [33].

As shown in Fig. 3.25, considering only band-filling effects by the Burstein-Moss model [83, 84] (Eqs. 2.10 and 2.11) do not explain the experimental results, even if the non-parabolic form of the conduction band is taken into account by using the effective mass model developed by Pisarkiewicz [87] (Eq. 2.13). Therefore, band-gap renormalization due to many-body interactions have to be taken into account. In this thesis, the model developed by Inkson [90] (Eqs. 2.14 and 2.15) is used, which describes the observed band-gap shift. However, only the self-energy contributions to the conduction band are considered, which was also done by several other authors [164, 165]. If the self-energy contributions of the valence band are taken into account, the calculated BGN shift gets greater than the BM shift, which is in contrast with the experimental results. Small deviations between the Inkson model and the experimental data may be, therefore, caused by neglecting of self energy contributions of the valence band, the frequency dependence of the screening, or the polar character of ZnO [77].

Annealing

Minami et al. [67] showed that the thermal stability of undoped ZnO is poor, but can be increased by increasing doping concentration. However, Fig. 3.28 shows that the films presented in this thesis exhibit even a small decrease in resistivity and infrared emissivity after annealing in air at temperatures lower than 300 °C independent of the doping concentration. The reason for the decrease of resistivity and emissivity may be explained by a healing of defects and an improvement of crystalline quality, which

increases the mobility of the free carriers. Similar observations were made also by other authors [75, 157, 166]. There are several reasons possible, which may cause the increase of resistivity and emissivity of the annealed samples at higher temperatures. One reason may be the oxidization of the Al dopant due to adsorption and diffusion of ambient oxygen. Also, other atoms of the ambient atmosphere may be adsorbed. The increase of resistivity may be also the consequence of an out-diffusion of hydrogen, which acts as native donor. It is also reported that a diffusion of alkali atoms of the glass substrate into the film increases the resistivity, and in connection with humidity, corrosive processes may take place [10].

3.4 Summary

In this chapter, the deposition and characterization of ZnO:Al thin films with varying process parameters and doping concentrations were presented. This preliminary work was necessary for the development of AR coating systems and the simulation of the collector efficiency of the double-glazed collector, which will be shown in Chapter 4 and Chapter 5, respectively.

Special attention was paid to the simultaneous modeling of ellipsometric and photometric data of the films. The model dielectric function presented in this thesis enables the determination of physically credible parameters for the electronic, optical, and structural properties of the samples, which agree with the results of independent thin-film characterization methods such as four-point probe, Hall, XRD, AFM, and TEM measurements. The modeling was improved by dividing the ZnO:Al film into three model layers, i.e. the surface roughness layer, the ZnO:Al bulk layer, and an interface layer. Explanations for the interface layer were structural differences at the interface due to a dilution of ZnO:Al into the glass substrate referring to TEM analysis. Chemical reasons were not confirmed by SNMS.

The model dielectric function of the ZnO:Al bulk layer contained three oscillators to take account of high interband transitions, fundamental absorption, and free-carrier absorption. A pole oscillator was used for modeling high interband transitions. In this thesis, Tanguy's model [104], which explains the direct fundamental absorption including effects of excitonic interaction, was modified by using an energy-dependent damping term. Tanguy used Lorentzian broadening of the excitonic absorption lines in his model. But Lorentzian broadening causes extended absorption tails below the absorption threshold. For that reason, Gaussian broadening or intermediate types are more applicable and are explained by the influence of impurities, crystal strain, or alloys. Other types of broadening were achieved by using an energy-dependent broadening term developed by Kim et al. [153]. The modeling of the free-carrier absorption was improved by using a modified Drude formula with an energy-dependent damping term developed by Mergel et al. [94] The physical motivation for an energy-dependent

damping term of the Drude oscillator is the energy-dependent scattering of free carriers by ionized donors.

The model dielectric function presented in this thesis was used for the determination of the optical and electronic properties of ZnO:Al thin films deposited with varying deposition parameters and doping concentrations. For the films sputtered from the target with 2 wt.% Al₂O₃, the model yields good fit results for the ellipsometric and photometric spectra over the whole measured spectral range from 0.24 to 50 μm , which is the relevant spectral range for solar-thermal applications. However, the films sputtered from targets with lower doping concentrations exhibit infrared phonon absorption, so called “reststrahlen” bands, which were taken account of with two Gaussian oscillators with fixed parameters. To find an appropriate model for these phonon absorptions, additional ellipsometric measurements in the infrared wavelength range would be necessary since reflectance data do not provide enough information. The existence of the interface layer was also confirmed by HRTEM analysis for ZnO:Al films sputtered from targets with low doping concentrations while the interface layer was not necessary for the optical modeling, which might be explained by numerical problems of the modeling procedure. The modeling results of the samples with varying doping concentrations were also used to determine the effective mass of the free-carriers as well as the optical band-gap shift. Both quantities depend on the free-carrier density. The results of the effective mass were in agreement with the effective mass model developed by Pisarkiewicz et al. [87]. The band-gap shift determined by the optical modeling was compared to a band-gap model that takes account of a band-gap widening, the so called Burstein Moss shift [83, 84] due to band filling as well as of a band-gap narrowing due to many-body effects. The band-gap narrowing was calculated with a model developed by Inkson [90].

The results of the deposition parameter series showed that substrate heating during the deposition was necessary to improve the electronic and optical properties of the films. The temperature, which provided the lowest resistivity, varied with doping concentration. Also, the structural properties such as grain sizes depend strongly on the doping concentration as well as on the substrate temperature, as SEM analyses had shown. The influence of changing the argon pressure or the DC power was smaller in comparison to the substrate temperature. It was also found that the film properties change with their film thickness, which is related to an anisotropic film growth and the grain distribution. Independent of the doping concentration, the resistivity of the films increased with decreasing film thickness. Annealing in air at raising temperatures showed that the films were stable up to 300 °C, independent of the doping concentration.

4 Investigations of AR coating systems for collector covers

4.1 Simulations of AR coating systems

If an appropriate ZnO:Al coating is found, the solar reflectance has to be further reduced to increase the solar transmittance of the low-e coating on the inner glass pane of the collector. As already described in Sec. 2.4, the reflectance could be effectively reduced by adjusting the refractive indices and film thicknesses of additional layers with respect to the ZnO:Al layer to generate destructive interference of the reflected light. To reach an AR effect over a wide wavelength range, three-layer systems are favorable with the amplitude and phase requirements given in Eqs. 2.40 and 2.41. The additional AR coatings are usually dielectric materials, which provide very low absorption in the required wavelength range. Besides the optical properties of the materials, the applicability of sputter deposition techniques is essential for the choice of potential materials. The upper layer of the system should have a low refractive index to match the index mismatch between the ZnO:Al layer and the ambient. The lowest refractive index, 1.38, is reached by MgF_2 (the refractive indices in this section refer to a wavelength of $\lambda = 500 \text{ nm}$) [10]. However, the sputter deposition of MgF_2 is difficult. Another low-refractive index material is stoichiometric SiO_2 with $n = 1.46$, which is a standard material for sputter deposition. Lower refractive indices are reached with porous layers. Since the upper layer should additionally act as a protection layer, porous layers would not be favorable for the presented application. With Eq. 2.40, the refractive index of the inner layer between the glass substrate ($n = 1.52$) and the ZnO:Al layer ($n = 1.86$) should be in the range of 1.6 to 1.8. There are several materials that provide a refractive index in this range. In the following, Al_2O_3 and SiO_xN_y are investigated. Al_2O_3 and SiO_xN_y are applicable for reactive sputter deposition. Al_2O_3 has a refractive index of 1.77. The advantage of SiO_xN_y is that the refractive index is adjustable with respect to the oxygen and nitrogen contents between the refractive index of SiO_2 ($n = 1.46$) and Si_3N_4 ($n = 1.9$). Figure 4.1 depicts simulated transmittance and reflectance spectra of three-layer systems of different configurations. The optical constants used in the simulation are tabulated data [47, 167–169] for the dielectric materials and determined by SE analysis for the ZnO:Al layer (see Fig. 3.20). Layer thickness values are adjusted with respect to Eq. 2.41 for $\lambda = 570 \text{ nm}$. The glass absorption and glass phonon effects in the infrared region are neglected in this simulation for simplicity, which is acceptable since the TCO has only a low transmittance and a high reflectance in the infrared spectral range. In Fig. 4.1 (c), it becomes obvious, that the refractive index of the upper

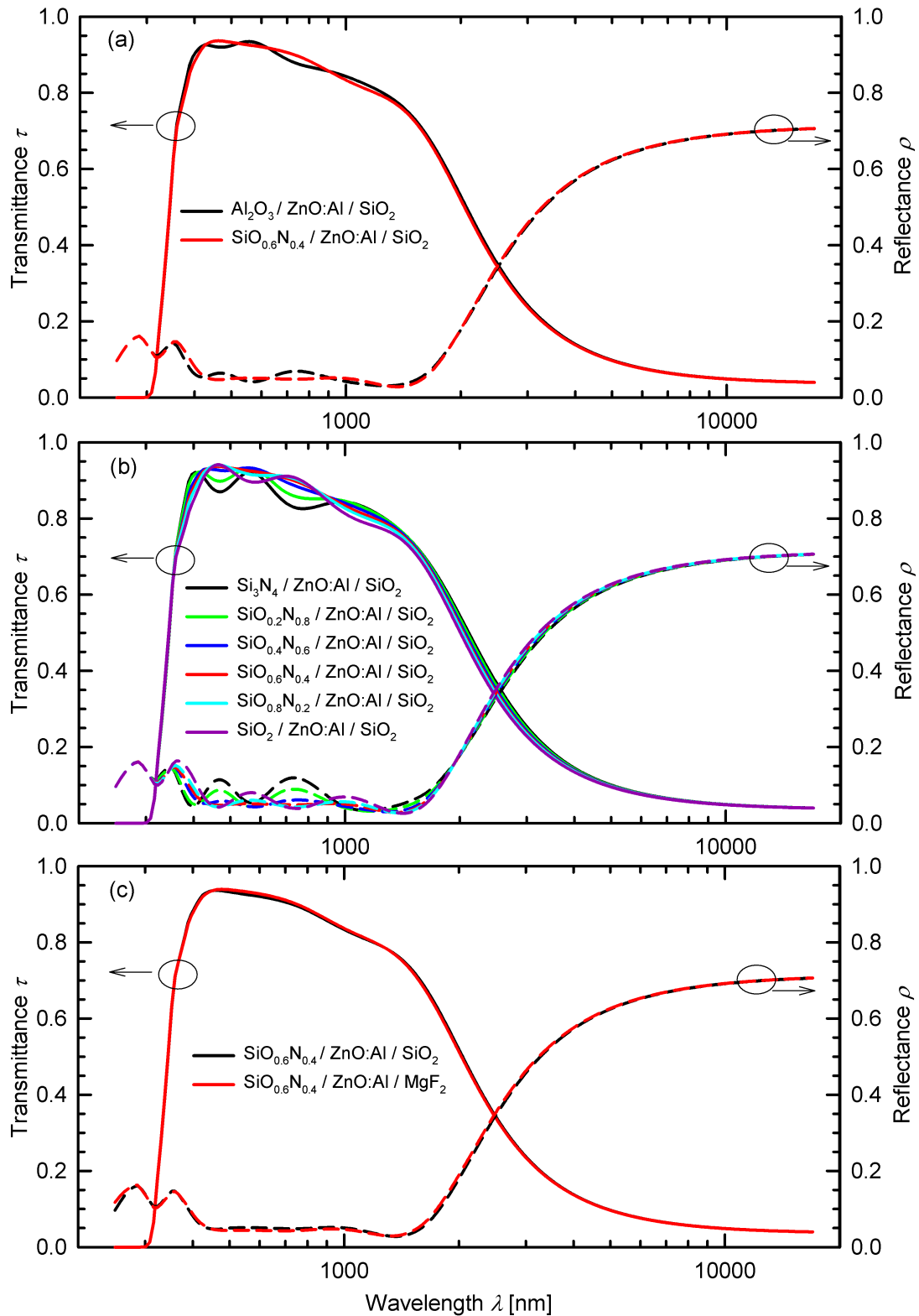


Figure 4.1: Simulated transmittance and reflectance spectra of antireflective coating systems with TCO layer. The subscripts of the silicon oxynitride films are the ratios of oxygen ($O/(O+N)$) and nitrogen ($N/(O+N)$) inside the compound.

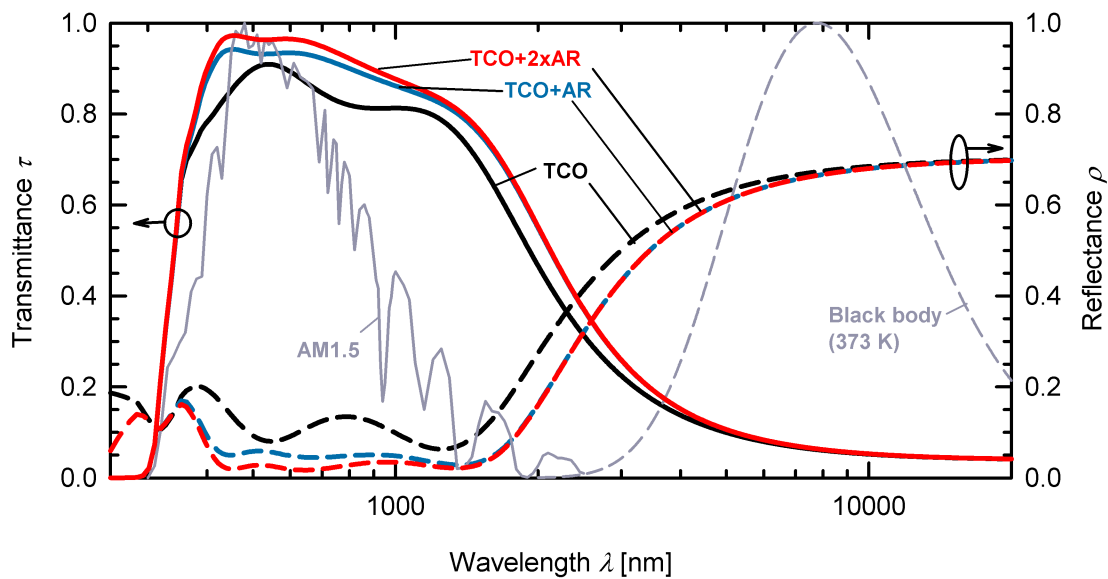


Figure 4.2: Simulated transmittance and reflectance spectra of a TCO single layer (TCO), of a three-layer AR system (TCO+AR) as well as of a three-layer AR system and an AR layer on the rear side of the substrate (TCO+2xAR).

layer has only little influence on the transmittance and reflectance spectra. Therefore, using SiO_2 is sufficient. Figure 4.1 (b) shows that a SiO_xN_y layer with an oxygen content ($\text{O}/(\text{O}+\text{N})$) in the range of 0.4 to 0.6 and a corresponding nitrogen content is favorable for the application as layer between the glass substrate and the ZnO:Al thin film since the interference oscillations and the solar reflectance are reduced for these coating systems. The corresponding refractive indices are in the range of 1.6 to 1.8, as tabulated [169].

Figure 4.2 shows simulated transmittance and reflectance spectra of a single ZnO:Al layer in comparison to a three-layer system consisting of two dielectric layers (with refractive indices of 1.65 and 1.46) and a ZnO:Al layer in the middle of the layer stack. It is obvious that AR coatings are necessary to increase the solar transmittance. In contrast, the AR coatings have no effect in the infrared region of the spectra. The transmittance could be further increased by introducing an additional AR layer on the rear side of the glass substrate, which should have a refractive index lower than glass. This can be realized with porous SiO_2 layers, which are commercially available (for instance HiT from Centrosolar [9]).

4.2 Experimental details

4.2.1 Film deposition

The SiO_xN_y and SiO_2 thin films are deposited by reactive pulsed DC bipolar magnetron sputtering in a batch coater (LS 900S from Von Ardenne Anlagentechnik). Figure 4.3 shows a schematic representation of the batch coater. The batch coater consists of a

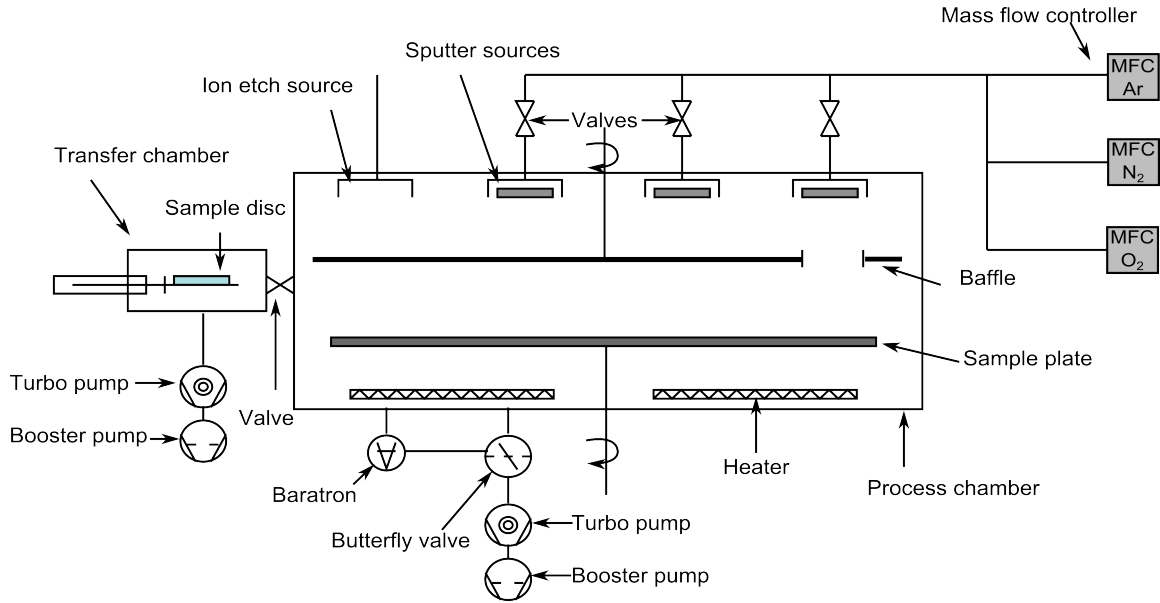


Figure 4.3: Schematic representation of the batch coater used for the deposition of antireflective coatings.

small transfer chamber and a process chamber, which houses one RF and two pulsed DC sputter sources as well as one ion beam etch source. The sputter sources are arranged at the cover of the chamber and the samples are located on a sample plate below the targets. The batch coater provides the possibility to rotate the sample plate. However, the samples presented in this thesis are deposited by static sputtering. One of the pulsed DC sputter source combines two concentric discharges on two separate silicon targets (6N, boron doped, 1 Ω cm from FHR Anlagenbau), which are formed as disc (diameter: 119 mm) and ring (inner diameter: 125 mm, outer diameter: 220 mm). The system's DC generator with double-cathode pulser (Pinnacle 6/6 kW and ASTRAL 20 from Advanced Energy) ensures the periodic variation of the targets as cathode and anode in bipolar mode. The parameters used for the deposition of the SiO_xN_y and SiO₂ thin films are shown in Table 4.1. The discharge power at each target is adjusted in such a way that both voltages and deposition rates are the same. Each deposition is carried out in compound mode to ensure stoichiometric and low-absorbing films. By varying the reactive gas content and composition, the refractive indices of the films are adjustable. The gas fluxes are controlled by mass flow meters.

The ZnO:Al thin films are deposited by DC magnetron sputtering in the in-line coater described already in Sec. 3.1.1 from ceramic targets made of ZnO and varying Al₂O₃ contents (from Avaluxe, diameter: 200 mm). The parameters used for the deposition of the ZnO:Al thin films are 0.5 Pa argon pressure, 500 W DC power and substrate temperatures of 150 °C and 200 °C for samples sputtered from the targets with 0.2 wt.% and 1.0 wt.% Al₂O₃ and for samples sputtered from the target with 2.0 wt.% Al₂O₃, respectively.

The optical path lengths $n \cdot d$ of the three coatings are adjusted with respect to Eq.

Table 4.1: Parameters for SiO_xN_y and SiO_2 deposition.

Parameter	SiO_xN_y	SiO_2
Target material	silicon	silicon
Target substrate distance	50 mm	50 mm
Substrate temperature	unheated	unheated
Discharge power ring-target	440 W	410 W
Discharge power disc-target	200 W	200 W
Pulse frequency	30 kHz	30 kHz
Duty cycle	50%	50%
Pressure before deposition	$< 5 \cdot 10^{-4}\text{Pa}$	$< 5 \cdot 10^{-4}\text{Pa}$
Pressure during deposition	0.5 Pa	0.5 Pa
Total gas flux	50 sccm	50 sccm
Flux fraction of argon	30%	40%
Flux fraction of nitrogen	varying	0%
Flux fraction of oxygen	varying	60%

2.41.

4.2.2 Film analysis and durability investigations

After deposition, the films are analyzed by spectroscopic ellipsometry and photometry as well as by SEM, as already described in Sec. 3.1.2. Since the refractive indices of the oxygen rich SiO_xN_y and SiO_2 films are very similar to that of the glass substrate, numerical problems may arise for the ellipsometric analysis. Therefore, silicon wafers (100) (boron doped with polished front and lapped rear side, from Wacker) are used as substrates for the determination of the refractive indices of these films.

A hot plate (Präzitherm PZ 28-3TD from Harry Gestigkeit) as well as a continuous furnace (RTC LA-310 from Radiant Technology Corporation) are used for heat tests, and for humidity and condensation tests, a climatic exposure test cabinet (MKF 240 from Binder) is applied. For the humidity tests, the sample temperature is 5 °C higher than the cabinet temperature of 60 °C. In the case of condensation tests, the sample temperature is 5 °C lower than the cabinet temperature of 45 °C. The relative humidity in the cabinet is fixed at 95% for both tests. The durability tests are performed for several periods with different lengths of time, and after each period, the samples are analyzed by spectroscopic photometry.

4.3 Results and Discussion

In the following, the results of the investigations on the SiO_xN_y and SiO_2 coatings as well as on the low-e coating system are presented. The first part is on the optical properties of the SiO_xN_y and SiO_2 coatings in dependence of the reactive gas composition, the second part deals with the structural and optical properties of the low-e coating system and the third part shows the results of the durability investigations.

4.3.1 Results of the AR coating deposition

In order to determine the optical constants and film thickness values of the SiO_xN_y and SiO_2 coatings, the measured SE data are modeled with a Bruggeman effective medium approximation (BEMA) (see Eq. 3.11) of a mixture of Si_3N_4 and SiO_2 , which was also reported by Xiong et al. [170]. The reason for using the BEMA model is that the BEMA model enables the determination of the volume fractions of SiO_2 and Si_3N_4 in the film. With this respect, an interpretation of the composition of the films is possible. For modeling, tabulated data [47, 167] of the optical constants of Si_3N_4 and SiO_2 are used. The fit parameters are the film thickness and the SiO_2 content. The results of the BEMA modeling are in agreement with the measured ellipsometric data, as shown in Fig. 4.4. During deposition, the reactive gas content is kept constant at 70% of the total gas flux of argon, oxygen, and nitrogen, but the oxygen and nitrogen contents are varied in such a way that the oxygen content of the reactive gas flux $f_{\text{O}_2}/(f_{\text{O}_2} + f_{\text{N}_2})$ is increased. Figure 4.5 depicts the BEMA SiO_2 contents of the films determined by SE analysis as a function of the oxygen gas flux content of the reactive gas flux. The BEMA SiO_2 content in the films raises in an s-like form with increasing oxygen gas content and saturated already for an oxygen content of the reactive gas flux of 40%. Figure 4.6 shows the corresponding refractive indices of the films. The values range between the refractive index of stoichiometric Si_3N_4 if the oxygen content of the reactive gas flux is zero and SiO_2 if the oxygen content is 100%. The extinction coefficients of the films are all zero in the considered wavelength range.

4.3.2 Discussion of the AR coating deposition

In Fig. 4.5, it becomes obvious that the BEMA SiO_2 content increases much faster than the oxygen content of the reactive gas flux and saturated already for an oxygen content of the reactive gas flux of 40%. The reason is that silicon has a higher affinity to oxygen than to nitrogen, which reflects the fact that the standard enthalpy of formation ΔH_f° of SiO_2 is much more negative with -910.9 kJ/Mol than that of Si_3N_4 with -744.8 kJ/Mol [74]. As a consequence, the oxygen content of the reactive gas flux has to be controlled carefully. Since the batch-coater does not provide a plasma monitoring system, the processes are very sensitive to gas flux and pressure fluctuations.

As shown in the simulated transmittance and reflectance spectra of Fig. 4.1 (b), the oxygen content of the SiO_xN_x layer between the glass substrate and the ZnO:Al thin film should be in the range of 0.4 to 0.6. These layers have tabulated refractive indices of 1.6 and 1.8 [169]. Films sputtered with an oxygen content of the reactive gas flux in the range of 25% to 30% fulfill this condition. However, the film sputtered with an oxygen content of the reactive gas flux of 30% exhibits a refractive index that is similar to that of the $\text{SiO}_{0.6}\text{N}_{0.4}$ layer in Fig. 4.1 (b), which provides the highest transmittance of the AR coating system.

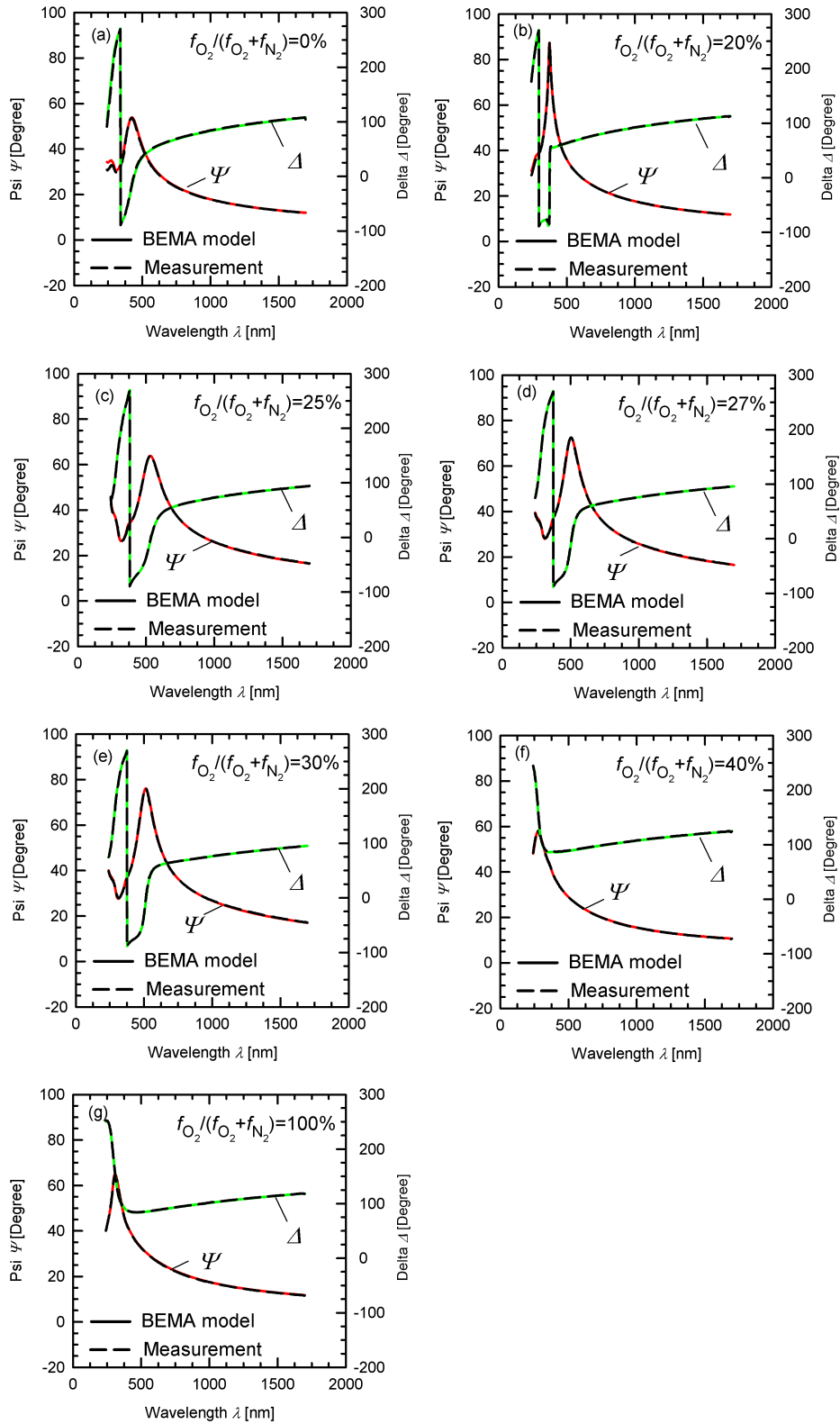


Figure 4.4: Overview of the BEMA modeling results of the measured ellipsometric spectra of the SiO_xN_y coatings for various oxygen contents of the reactive gas flux $f_{O_2}/(f_{O_2} + f_{N_2})$. The red and green solid lines represent the modeled Ψ and Δ spectra, respectively. The black dashed lines depict the measured data. The spectra of only one angle of incidence (70°) are shown for clarity.

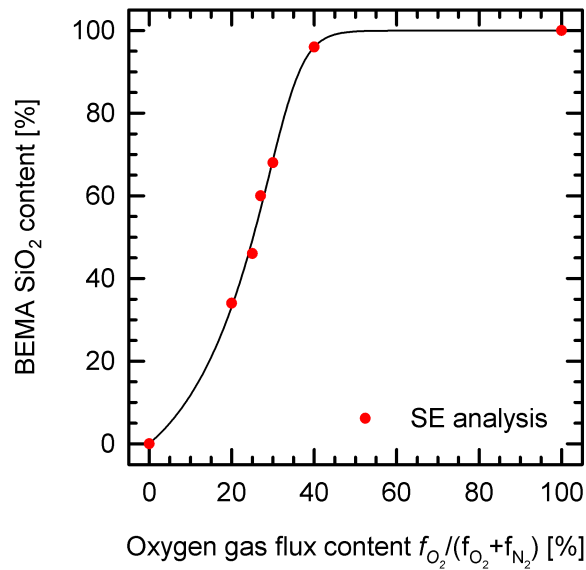


Figure 4.5: BEMA SiO₂ content determined by SE analysis as a function of oxygen reactive gas flux (red circles for SE analysis, black line to guide the eye).

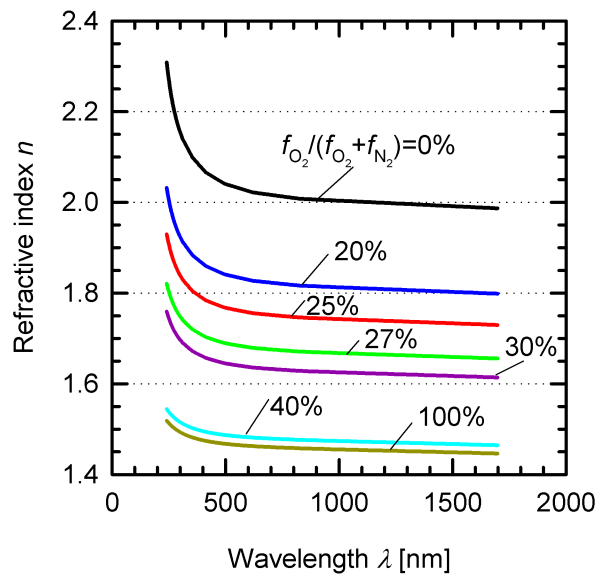


Figure 4.6: Spectral refractive index determined by SE analysis as a function of oxygen reactive gas flux.

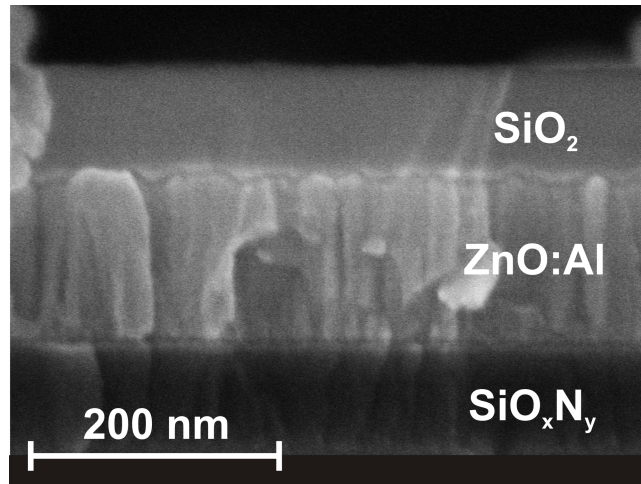


Figure 4.7: Cross-sectional scanning-electron microscope image of a three-layer antireflective coating system.

4.3.3 Results of the AR coating system

In the following, the structural and optical properties of low-e coating systems with varying doping concentrations of the ZnO:Al thin film will be presented. All the samples have the same AR coatings and only the doping concentration of the ZnO:Al layer is varied. The SiO_xN_y thin films are sputtered with the gas fluxes of 15 sccm argon, 24.5 sccm nitrogen, and 10.5 sccm oxygen, which corresponds to an oxygen content of the reactive gas flux of 30%. The other sputter parameters of the SiO_xN_y and SiO_2 depositions are shown in Table 4.1. In Sec. 4.2.1, the process parameters of the ZnO:Al depositions are presented.

In Fig. 4.7, an SEM cross-sectional image of the three-layer system is shown. The ZnO:Al thin film exhibits a columnar structure while the SiO_2 thin film is a smooth compact layer and protects the TCO film against ambient oxygen and humidity. Figure 4.8 depicts the measured transmittance and reflectance spectra of the three-layer systems with varying doping concentration. The spectra of the glass substrate are also shown. For the samples presented, non-low-iron glass was used. The effect of iron absorption in these glass substrates is, however, low since the thickness of the glass is only 1.1 mm. For the application as covering of a solar-thermal flat-plate collector, glass thicknesses of 3 to 4 mm are needed and then the use of low-iron glass is necessary to reach a high solar transmittance. Table 4.2 represents the corresponding solar transmittance and reflectance as well as the infrared emissivity data of the samples. The coating system with the highly doped ZnO:Al thin film provides a higher transmittance at short wavelengths in comparison to the lower doped samples. However, at long wavelengths, the transmittance of that sample decreases much faster. In the infrared wavelength range, the highly doped sample reaches the highest reflectance and therefore the lowest emissivity. All the reflectance spectra of the coating systems as well as of the glass substrate show characteristic peaks. The solar spectrum exhibits

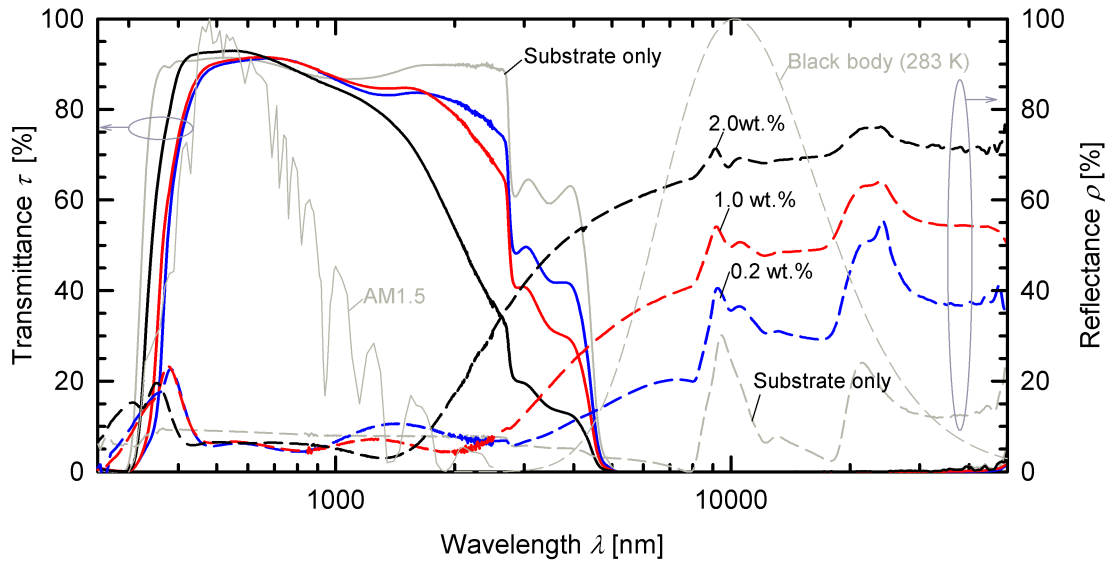


Figure 4.8: Measured transmittance and reflectance spectra of three-layer antireflective coating systems with ZnO:Al thin films with varying doping concentration.

Table 4.2: Measured solar transmittance and reflectance as well as infrared emissivity data of low-e coating systems with different doping concentrations.

Doping concentration [wt.%]	τ_{sol} [%]	ρ_{sol} [%]	ϵ_{IR} [%]
0.2	85.2	7.4	66.1
1.0	86.0	6.9	49.4
2.0	85.2	6.9	30.3

the most part of its intensity at wavelengths smaller than 1000 nm. The transmittance of the three samples is comparably high in this wavelength range, which results in similar solar transmittance and reflectance values. The main difference is found in the infrared reflectance values, which decrease with decreasing doping concentration. As a consequence, the infrared emissivity increases with decreasing doping concentration. Figure 4.9 shows the measured and modeled ellipsometric spectra of a low-e coating system with 2.0 wt.% doping concentration on a silicon wafer substrate. The silicon wafer is used as substrate for the SE analysis since the reflected light intensity of the low-e coating systems is very low in the measured wavelength range, and the ellipsometric data are determined by the polarization change of the reflected light waves. By using the silicon wafer, the reflected light intensity is increased and the signal-to-noise ratio at the detector is lowered. Another advantage is that the refractive index difference of the SiO_xN_y to the silicon wafer is higher in comparison to a glass substrate and the SE analysis becomes more precise. The film thicknesses and optical constants are determined after every deposition step. For modeling of the coating system on silicon substrates, no interface layers are needed.

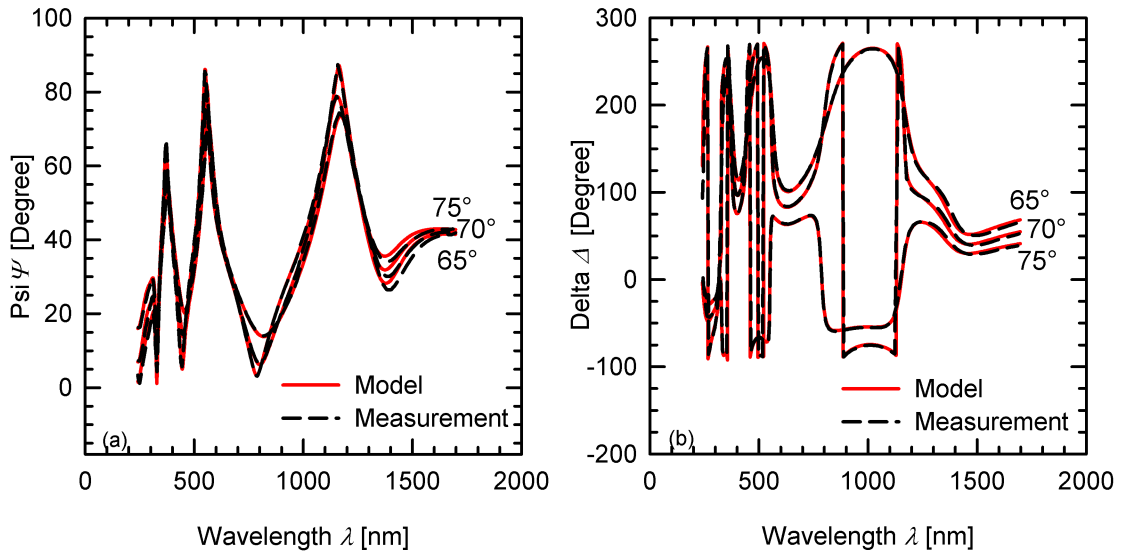


Figure 4.9: Measured and modeled ellipsometric spectra of a three-layer system consisting of $\text{SiO}_x\text{N}_y/\text{ZnO}:\text{Al}$ (2.0 wt.%) / SiO_2 deposited on a silicon wafer.

4.3.4 Discussion of the AR coating system

The optical band gap of the highly doped sample is shifted to shorter wavelengths due to band-filling and renormalization effects. The transmittance of the highly doped sample shows a stronger decrease in the near infrared wavelength range in comparison to the lower doped samples as a result of larger free-carrier absorption. The characteristic reflection peaks of the samples and the glass substrate are caused by phonon absorption. Lowly doped ZnO:Al thin films exhibit characteristic reststrahlen bands due to phonon-light interaction. However, the intensity of the reflection peaks becomes smaller with increasing doping concentration as a result of screening effects of the high free-carrier density. Since the film thicknesses of the samples are in the range of the penetration depth of the infrared light waves, the phonon absorption peaks of the glass substrate influence the reflectance spectra of the samples.

Since the transmittance and reflectance of the samples with varying doping concentration show no significant difference in their solar values, the infrared emissivity is the decisive parameter for the choice of the appropriate doping concentration. Therefore, the doping concentration that reaches the lowest emissivity is chosen for the application as selective coating of the collector cover.

As shown in Fig. 4.9, the model dielectric functions presented in Sec. 3.2 and 4.3.1 for the ZnO:Al layer and AR coatings are also applicable for modeling the whole low-e coating system. There are no significant differences in the modeling results of the single layers in comparison to the whole coating system, which is an indication that the reactive plasma during the SiO_2 deposition does not oxidize the Al dopant of the ZnO:Al layer.

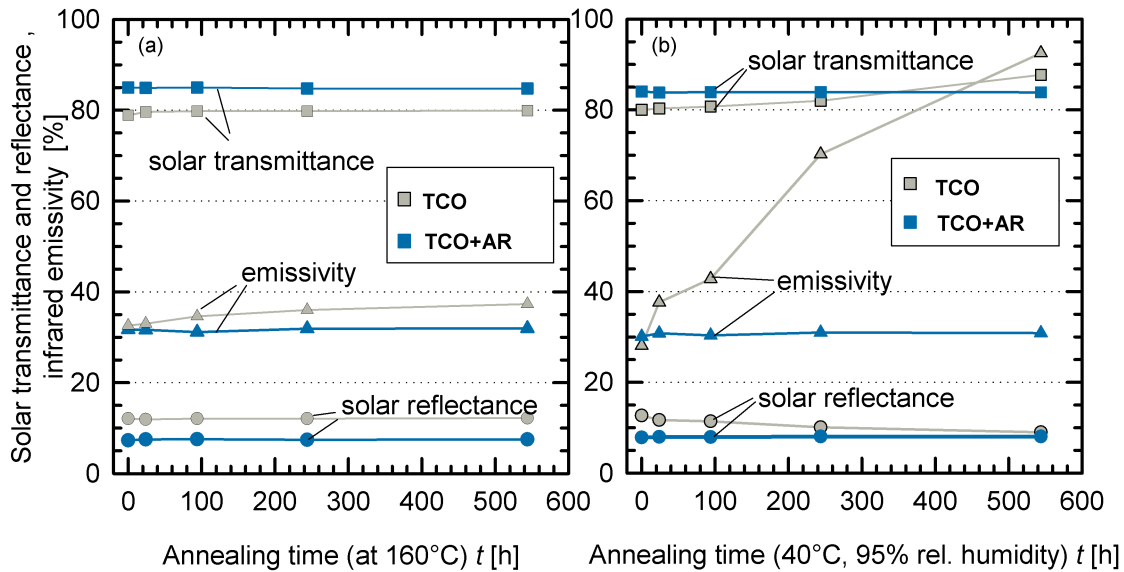


Figure 4.10: Development of the optical properties of a single ZnO:Al thin film (TCO) and of a three-layer system (TCO+AR) under (a) heat and (b) condensation load.

4.3.5 Results of the durability investigations

In the case of stagnation of the collector, which means that the collector fluid is evaporated and heat is not extracted any more, the low-e coated glass can reach high temperatures of up to 160 °C due to the higher heat performance of the absorber and the free-carrier absorption of the TCO-coating [171, 172]. If the edge bond of the double glazing is open and the gap is filled with air, the coating system is also in contact with ambient oxygen and humidity.

Therefore, durability tests are performed where some samples with the three-layer system containing ZnO:Al sputtered from a target with 2.0 wt.% Al₂O₃ are aged on a hot plate and in a climatic exposure test cabinet. The durability tests are also performed on single ZnO:Al coatings of the same film thickness. The humidity test is not shown, since the change in the optical properties of the three-layer system is smaller than 3%. Figure 4.10 shows the changes in the solar transmittance and reflectance as well as in the emissivity during (a) heat and (b) condensation load. The data of the coating system are mean values of two samples in the heat test and three samples in the condensation test, with all the samples demonstrating exactly the same behavior. There is no obvious change in the optical properties of the samples with the three-layer system under heat as well as under condensation load, while the samples with the single ZnO:Al coatings show changes especially in the infrared emissivity. Under condensation load, a drastic increase in the emissivity of the single ZnO:Al coatings occurred.

Due to high-temperature gradients across the glass panes in the collector, tempered safety glass is necessary to avoid breakage of the glass [172]. Therefore, the question

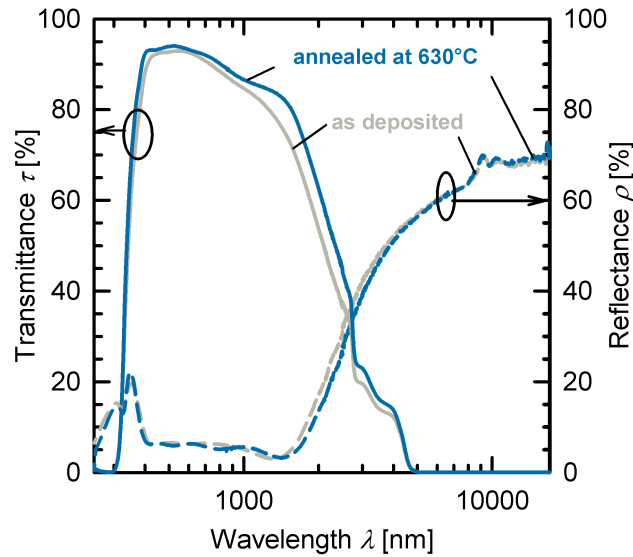


Figure 4.11: Measured transmittance and reflectance spectra of the three-layer system as deposited and after a high-temperature load of 630 °C for 3 min in air.

arises whether the thermal hardening of the glass can be performed after film deposition. For this purpose, a high-temperature test in a continuous furnace at 630 °C for 3 min is performed. Figure 4.11 depicts the measured transmittance and reflectance spectra before and after the high-temperature test. Due to the high temperature load, solar transmittance increases from 85% to 87.3%, solar reflectance decreases from 7.0% to 6.6%, and emissivity remains constant at 32%.

4.3.6 Discussion of the durability investigations

As shown in Fig. 4.10, single ZnO:Al coatings are not stable against long-term heat, humidity, and condensation loads. The change in emissivity is connected with the change in the conductivity of the films and may be caused by the oxidization of the aluminum dopant and other corrosive processes. In contrast, the low-e coating system, consisting of a ZnO:Al thin film sputtered from a target with 2.0 wt.% Al₂O₃ and sandwiched by two dielectric layers, shows a stable behavior during all the durability tests. This indicates that the SiO₂ top layer acts as an effective protection layer for the ZnO:Al coating against oxygen and humidity.

The change of the optical properties after the high-temperature test may be explained by an increase in the free-carrier mobility from 27.9 cm²/Vs to 30.1 cm²/Vs and a decrease in the free-carrier concentration from $6.0 \cdot 10^{20} \text{cm}^{-3}$ to $5.5 \cdot 10^{20} \text{cm}^{-3}$ of the ZnO:Al layer as determined by ellipsometric modeling, in such a way that the resistivity of the ZnO:Al layer stays constant at $3.7 \cdot 10^{-4} \Omega \text{cm}$. The observed increase of mobility after heat treatment of ZnO:Al thin films protected by a layer of SiO₂ is in accordance to investigations made by Berginski [157], who tested the heat stability of RF sputtered ZnO:Al thin films with and without a SiO₂ capping layer under vacuum and different

gases, as well as results made by Ruske et al. [173], who studied the heat stability of sputtered ZnO:Al thin films with a hydrogen-rich silicon capping layer. The increase of mobility may be caused by a healing of defects under heat treatment while the capping layer protects the aluminum dopant against oxygen of the ambient. The SiO_xN_y may also be a protection layer against diffusion of alkali atoms out of the glass substrate.

4.4 Summary

This chapter focused on the development of AR coating systems for the application to collector covers. For this purpose, simulations of transmittance and reflectance spectra of different coating systems were made. The simulations showed that a three-layer system was favorable to reduce reflective losses over a wide wavelength range. The additional AR coatings with the TCO reduced the reflectance in the solar spectral range while there was no effect in the infrared wavelength range so that the infrared emissivity remained at a low level. Appropriate coating materials with middle and low refractive indices were Al_2O_3 or SiO_xN_y and SiO_2 or MgF_2 . In this thesis, SiO_xN_y and SiO_2 were chosen as AR coating materials since both materials could be sputtered reactively from one silicon target. Only by changing the reactive gas composition, the refractive indices were varied between that of Si_3N_4 and that of SiO_2 . The SiO_xN_y coating composition was optimized for reaching a low solar reflectance. AR coating systems with varying doping concentration of the ZnO:Al thin films exhibited a high solar transmittance of 85%, independent of the doping concentration. The solar transmittance could be increased by 2–3% with an additional AR coating on the rear side of the glass substrate, as simulations have shown. The coating systems with a high doping concentration provided a higher UV transmittance while the films with lower doping concentration provided a higher NIR transmittance so that the solar transmittance of the coating systems was nearly independent of the doping concentration. However, the infrared emissivity increased with decreasing doping concentration. Therefore, a doping concentration of 2 wt.% would be favorable for the application in a solar-thermal flat-plate collector. The additional AR coatings with the TCO also acted as efficient protection layers, as durability tests have shown. The coating systems were stable over 540 h against temperature and condensation loads while single ZnO:Al layers were not. The results of first high-temperature tests were promising that a thermal hardening of the glass panes for the application in a flat-plate collector would be possible after film deposition, which would be favorable with respect to an industrial deposition of the films.

5 Modeling of collector efficiency

Since the size of the samples presented in this thesis is much smaller than typical collector sizes, and therefore, measurements of the coated samples in a collector are not accessibly, simulations with an appropriate collector model are necessary to evaluate the coating properties with respect to their influence on the collector efficiency.

It is a common practice to calculate the radiative transfer between the collector components in two different wavelength regimes, the solar and the infrared spectral range, with wavelength-averaged optical data such as the solar transmittance and reflectance as well as the infrared emissivity [37, 38, 174]. This is for practical reasons since usually only wavelength-averaged data are available in the data sheets instead of spectral data. Another assumption is that the infrared emissivity of the components is often used for a given temperature and not as a temperature dependent parameter [174]. The infrared transmittance of the glass panes is usually set to zero since glass has a high absorptance in the infrared spectral range [37, 38, 174]. As a consequence, the infrared radiative transfer inside a system consisting of two glass panes and an absorber reduces to the radiative transfer between only two neighboring opaque surfaces. These simplifying assumptions may be justified if materials used are not transparent in the infrared and if the coatings are not selective over the considered wavelength range. However, if selective coatings are used for the transparent cover as well as for the absorber or if infrared transparent media such as foils are applied instead of glass, these assumptions may no longer be valid. Additionally, the wavelength-averaged calculation requires the choice of a fixed temperature for the infrared emissivity (see Eq. 2.4) which leads to deviations from the spectral calculation.

Therefore, a collector model is developed here that calculates the spectral radiative transfer between the collector components over the wavelength range of 0.3 to 50 μm and takes account of multiple reflections inside the system even in the infrared spectral range if infrared transparent media are assumed. The model also includes the temperature dependence of the emitted radiation of the collector components. For the calculation of the conductive and convective thermal losses, common models are used [37, 175]. The following calculations of the radiative, conductive, and convective interactions in the collector are implemented into a Matlab program.

5.1 Collector model

5.1.1 Calculation of radiative transfer

The model used in this thesis is based on the radiation-balance method (RBM) developed by Rubin [174]. Originally, Rubin developed the RBM to calculate the energy performance of windows with wavelength-averaged radiation properties of the window

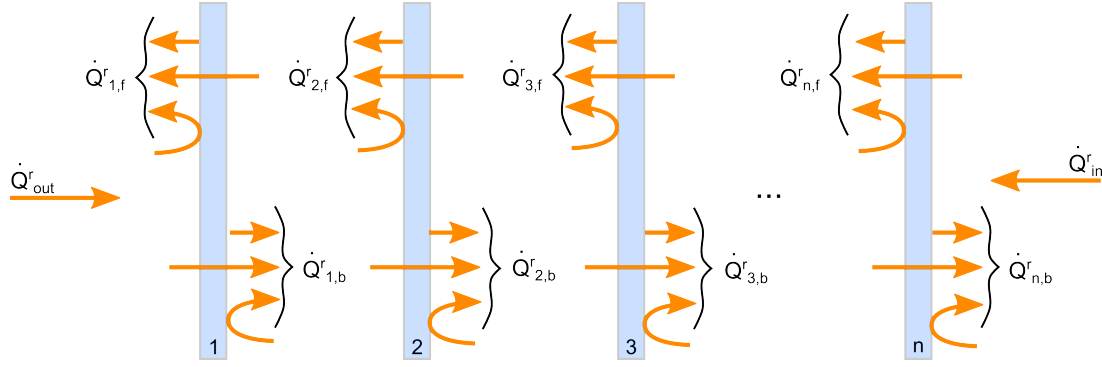


Figure 5.1: Radiation balance for a system of n solid layers by Rubin [174]. $Q_{i,f/b}$ are the energy flux densities from surface $i, f/b$, and Q_{out} and Q_{in} are the energy fluxes from the outside and inside environment.

materials. However, in this thesis the method is extended also to spectral data. In the case of the wavelength-averaged calculation, the solar and infrared wavelength range has to be treated separately. In that way, the infrared averaged glazing properties have to be weighted by the emissive power of a blackbody at a certain temperature. Rubin applied ambient temperature since the wavelength-averaged emissivity does not depend strongly on the choice of the source temperature in the temperature range of typical window materials. However, this will not be the case if collector components with a broad temperature range are considered. Applying spectral data to the RBM, no distinction of the wavelength range is necessary and the temperature dependence of the emitted radiation is taken into account. In the following, the extended RBM is presented.

The RBM allows the calculation of the radiative transfer inside a system of an arbitrary number of n components, which are bounded by $2n$ surfaces, as shown in Fig. 5.1. In the following, the surfaces of each component are distinguished by indices for front (f) and back (b). For the calculation of the steady-state energy balance of each collector component, the integrals over wavelength λ of the spectral radiant energy flux densities $\dot{q}_{i,f/b}^r(\lambda)$ are determined numerically by

$$\dot{Q}_{i,f/b}^r = \int \dot{q}_{i,f/b}^r(\lambda) d\lambda. \quad (5.1)$$

The spectral radiant energy flux density $\dot{q}_{i,f/b}^r(\lambda)$ of one surface of the i^{th} component is the sum of the spectral radiant emittance $s_{i,f/b}(\lambda)$ of the respective surface as well as the reflected energy flux density from the neighboring surface and the transmitted energy flux density through the i^{th} layer

$$\dot{q}_{i,b}^r(\lambda) = s_{i,b}(\lambda) + \rho_{i,b}(\lambda) \dot{q}_{i+1,f}^r(\lambda) + \tau_{i,b}(\lambda) \dot{q}_{i-1,b}^r(\lambda) \quad (5.2)$$

$$\dot{q}_{i,f}^r(\lambda) = s_{i,f}(\lambda) + \rho_{i,f}(\lambda) \dot{q}_{i-1,b}^r(\lambda) + \tau_{i,f}(\lambda) \dot{q}_{i+1,f}^r(\lambda), \quad (5.3)$$

where $\rho_{i,f/b}(\lambda)$ and $\tau_{i,f/b}(\lambda)$ are the spectral reflectance and transmittance of the respective surface. For asymmetric coated glass panes, the reflectance values are different for each side of the glass while the transmittance spectra are usually independent of the measurement direction if the surfaces are smooth and light scattering is negligible. The spectral radiant emittance $s_{i,f/b}(\lambda)$ of a surface at temperature T_{surf} is the product of the spectral emissivity $\epsilon_{i,f/b}(\lambda) = 1 - \rho_{i,f/b}(\lambda) - \tau_{i,f/b}(\lambda)$ and Planck's blackbody radiation $S_{P,T_{\text{surf}}}(\lambda)$ at wavelength λ and surface temperature T_{surf} . Usually, the optical constants of a medium are also temperature dependent. However, in this thesis, the spectral emissivity is determined from optical measurements at room temperature since a heatable sample holder for the spectrometers is not available yet. Since the emittance of sources of thermal radiation is of hemispherical nature (but not necessarily with Lambertian distribution), the hemispherical-averaged optical properties of the surfaces have to be used also for specularly reflecting surfaces [174]. However, for simplicity, only specular optical properties as well as an angle of incidence of 0° are considered here. This assumption is justified if the infrared radiative transfer takes place between two infinite parallel planes (according to Fig. 2.4). Then, all of the radiation emitted and reflected by one surface reaches the neighboring surface and vice versa and the radiation balance is independent of the spatial distribution of the emitted radiation [45]. This is approximately fulfilled by the double-glazed flat-plate collector since the glass panes are nearly opaque in the wavelength range of the emitted thermal radiation. As a result, the radiative transfer in this wavelength range takes place only between the two surfaces of each gap of the collector (gap between both glass panes and gap between the glass pane and the absorber).

For window calculations, the outdoor and indoor radiant energy flux densities have to be taken into account. However, in the case of a flat-plate collector, there is no radiant energy flux from indoor since the absorber plate is opaque. For the outdoor energy flux density, the sum of the spectral solar irradiance and the spectral infrared sky radiation $s_0(\lambda) = S_{\text{sol}} + S_{\text{IR,sky}}$ is used. For simplicity, the infrared sky radiation is assumed as the radiation of a blackbody at ambient temperature. However, this is a rough approximation and does not account for the absorption by clouds and moisture in the atmospheres. These effects are out of the scope of this thesis.

The Eqs. 5.2 and 5.3 of the $2n$ surfaces represent an inhomogeneous linear system of equations, which can be rearranged and written in matrix form

$$s_j(\lambda) = \sum_i M_{ji}(\lambda) \dot{q}_i^r(\lambda). \quad (5.4)$$

The spectral radiant energy flux densities $\dot{q}_i^r(\lambda)$ as functions of the radiation sources $s_i(\lambda)$ at surface temperature T_{surf} are calculated by inverting the matrix M_{ij}

$$\dot{q}_i^r(\lambda) = \sum_j M_{ij}^{-1}(\lambda) s_j(\lambda). \quad (5.5)$$

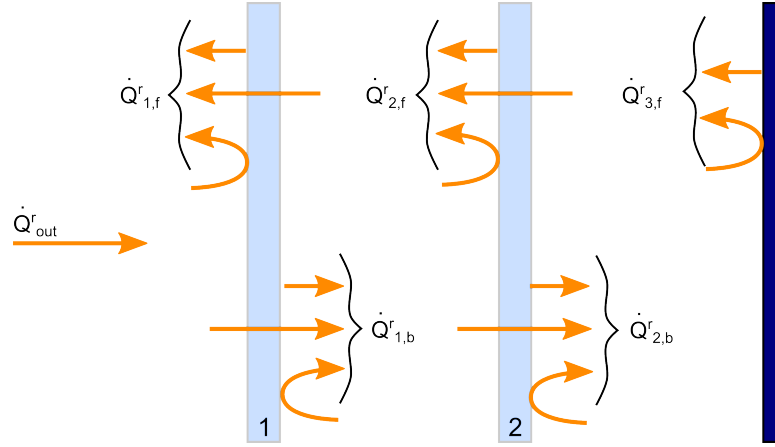


Figure 5.2: Radiation balance for a double-glazed collector if only radiative transfer is considered.

The inverted matrix includes all multiple reflections inside the system. If only radiative transfer is taken into account and convective and conductive thermal losses are neglected, the energy balance of each component i is determined by using the integral values for the spectral radiant energy flux density (see Eq. 5.1)

$$\Delta \dot{Q}_i^r = \dot{Q}_{i-1,b}^r + \dot{Q}_{i+1,f}^r - \dot{Q}_{i,f}^r - \dot{Q}_{i,b}^r. \quad (5.6)$$

In steady-state, the arriving and leaving energy fluxes of each component should balance each other. For a given configuration of a window or collector system, the inverse matrix can be determined analytically using variables. Only the determination of the steady-state energy balance and of the temperatures of the components requires a numerical iteration since the system of equations is nonlinear due to the nonlinear temperature dependence of the blackbody radiation. The calculation of the collector efficiency curves, including convective and conductive thermal losses, will be shown in Sec. 5.1.2.

In the following, the application of the spectral RBM to a double-glazed collector is presented. As shown in Fig. 5.2, the spectral radiant energy flux densities of the surfaces are

$$\dot{q}_0^r(\lambda) = s_0(\lambda) \quad (5.7)$$

$$\dot{q}_{1,f}^r(\lambda) = s_{1,f}(\lambda) + \rho_{1,f}(\lambda) \dot{q}_0^r(\lambda) + \tau_{1,f}(\lambda) \dot{q}_{2,f}^r(\lambda) \quad (5.8)$$

$$\dot{q}_{1,b}^r(\lambda) = s_{1,b}(\lambda) + \rho_{1,b}(\lambda) \dot{q}_{2,f}^r(\lambda) + \tau_{1,b}(\lambda) \dot{q}_0^r(\lambda) \quad (5.9)$$

$$\dot{q}_{2,f}^r(\lambda) = s_{2,f}(\lambda) + \rho_{2,f}(\lambda) \dot{q}_{1,b}^r(\lambda) + \tau_{2,f}(\lambda) \dot{q}_{3,f}^r(\lambda) \quad (5.10)$$

$$\dot{q}_{2,b}^r(\lambda) = s_{2,b}(\lambda) + \rho_{2,b}(\lambda) \dot{q}_{3,f}^r(\lambda) + \tau_{2,b}(\lambda) \dot{q}_{1,b}^r(\lambda) \quad (5.11)$$

$$\dot{q}_{3,f}^r(\lambda) = s_{3,f}(\lambda) + \rho_{3,f}(\lambda) \dot{q}_{2,b}^r(\lambda). \quad (5.12)$$

Rearranging of the system of equations and writing in matrix form yields $s_i(\lambda) =$

$\sum_j M_{ij}(\lambda) \dot{q}_j^r(\lambda)$ with

$$M_{ij}(\lambda) = \begin{pmatrix} 1 & 0 & 0 & 0 & 0 & 0 \\ -\rho_{1,f}(\lambda) & 1 & 0 & -\tau_{1,f}(\lambda) & 0 & 0 \\ -\tau_{1,b}(\lambda) & 0 & 1 & -\rho_{1,b}(\lambda) & 0 & 0 \\ 0 & 0 & -\rho_{2,f}(\lambda) & 1 & 0 & -\tau_{2,f}(\lambda) \\ 0 & 0 & -\tau_{2,b}(\lambda) & 0 & 1 & -\rho_{2,b}(\lambda) \\ 0 & 0 & 0 & 0 & -\rho_{3,f}(\lambda) & 1 \end{pmatrix}. \quad (5.13)$$

The inverse matrix is calculated with the symbolic toolbox of Matlab. The steady-state energy balance of the system components is then

$$\Delta \dot{Q}_1^r = \dot{Q}_0^r + \dot{Q}_{2,f}^r - \dot{Q}_{1,f}^r - \dot{Q}_{1,b}^r \quad (5.14)$$

$$\Delta \dot{Q}_2^r = \dot{Q}_{1,b}^r + \dot{Q}_{3,f}^r - \dot{Q}_{2,f}^r - \dot{Q}_{2,b}^r \quad (5.15)$$

$$\Delta \dot{Q}_3^r = \dot{Q}_{2,b}^r - \dot{Q}_{3,f}^r. \quad (5.16)$$

The component temperatures are the solutions of the system of equations with $\Delta \dot{Q}_i^r = 0$ ($i = 1, 2, 3$) and can be determined by Matlab with a numerical iteration.

To calculate the radiative transfer inside the system, measured transmittance and reflectance spectra, especially for the commercial products such as the first glass pane and the absorber, are used. To have more freedom in the evaluation of appropriate coating systems of the second glass pane for the application in the flat-plate collector, the transmittance and reflectance spectra are also simulated by the transfer-matrix method presented in Sec. 2.4 using optical constants of the coating materials. The optical constants are determined either by spectroscopic ellipsometry or from literature data [47, 167]. The transfer-matrix method treats the propagation of light coherent inside the system of thin layers and takes account of interference effects. However, the substrate is usually thick in comparison to the coherence length of light and has to be treated incoherent, as described in the publication of Harbecke [111]. To calculate the transmittance and reflectance spectra of the second glass pane of the collector, the transfer-matrix method with incoherent treatment of the substrate is applied to a Matlab program. Some assumptions are made for simplification, such as the angle of incidence is 0° , the surfaces are smooth and specular reflecting, gradients, and anisotropy of the thin films are neglected. Numerical problems may arise if the films or the substrate are highly absorbing. This is the case for a glass substrate in the infrared wavelength range. To avoid these problems, the reflectance spectra of each side of the sample are calculated by the product of the matrices of the coatings on each side and the propagation through the substrate is neglected. Figure 5.3 depicts simulated transmittance and reflectance spectra of the three-layer coating system presented in Sec. 4.3.3, which are calculated with Matlab and WVASE32, respectively. There are only very small deviations in the infrared wavelength range where the substrate is

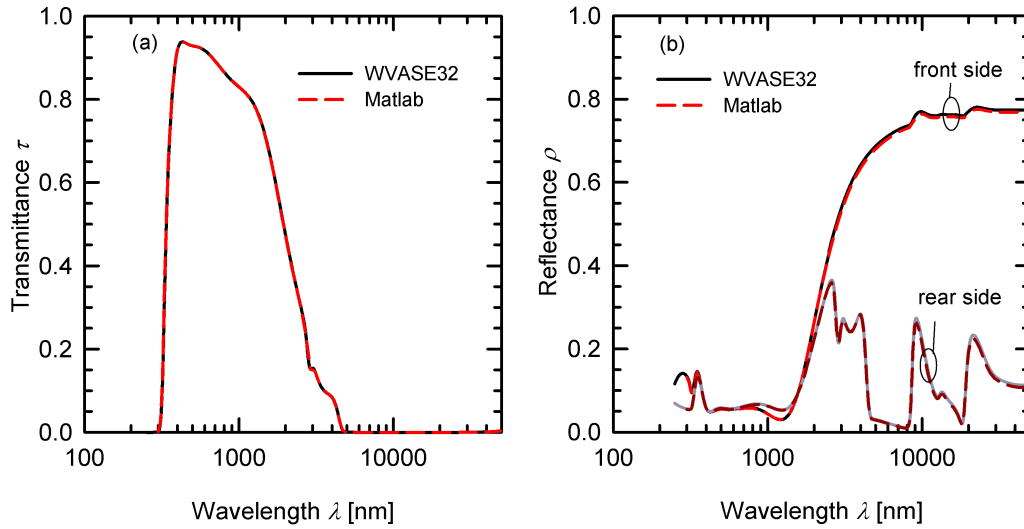


Figure 5.3: (a) Transmittance and (b) reflectance spectra of a three-layer system on glass consisting of $\text{SiO}_x\text{N}_y/\text{ZnO:Al}$ (2.0 wt.%) / SiO_2 modeled by the transfer-matrix method with Matlab as well as with the WVASE32 software.

highly absorbing. These deviations may be caused by numerical differences between Matlab and WVASE32.

5.1.2 Calculation of conductive and convective interchange

Besides radiative thermal losses, conductive and convective thermal losses occur, which reduce the collector efficiency at increasing temperatures. Usually, the convective losses are dominant in comparison to the radiative losses due to the low infrared emissivity of the glass and absorber coatings. To get a realistic representation of the component temperatures and the efficiency, these thermal losses should, therefore, be taken into account.

If the Rayleigh number Ra of a gas is lower than the critical Rayleigh number $Ra_{\text{crit}} = 1000$, the transfer of heat in a gas filled gap is dominated by thermal conduction. Then, the conductive energy flux density is determined by [37]

$$\dot{Q}_{ij}^{\text{cond}} = \frac{\lambda_c}{w} (T_i - T_j), \quad (5.17)$$

where λ_c is the thermal conductivity of the gas, w is the width of the gap and $\Delta T_{ij} = (T_i - T_j)$ is the temperature difference between the boundaries i and j of the gap. The Rayleigh number is the product of the Prandtl number Pr and the Grashoff number Gr

$$Ra = Pr \cdot Gr \quad (5.18)$$

with

$$Pr = \frac{c_p \mu_v}{\lambda_c} \quad \text{and} \quad Gr = \frac{g \beta \rho_g^2 w^3 \Delta T_{ij}}{\mu_v}, \quad (5.19)$$

where c_p is the specific heat, μ_v is the dynamic viscosity, β is the coefficient of thermal expansion, ρ_g is the density of the gas inside the gap. g denotes the gravitational acceleration. The material parameters of air and argon are, naturally, temperature dependent. For simplicity, this temperature dependence is neglected. Free convection occurs in a tilted gas filled gap if the critical Rayleigh number is exceeded. Then, the net energy flux density inside the gap between the boundaries i and j is described by [37]

$$\dot{Q}_{ij}^c = Nu \cdot \frac{\lambda_c}{w} (T_i - T_j), \quad (5.20)$$

with the Nusselt number Nu . The Nusselt number for an inclined gap with inclination angle θ can be calculated with the Hollands equation [176]

$$\begin{aligned} Nu = & 1 + 1.44 \cdot \left[1 - \frac{1708 \cdot \sin^{1.6}(1.8\theta)}{Ra \cos(\theta)} \right] \cdot \dots \\ & \cdot \frac{1}{2} \left[\left(1 - \frac{1708}{Ra \cos(\theta)} \right) + \left| 1 - \frac{1708}{Ra \cos(\theta)} \right| \right] + \dots \\ & + \frac{1}{2} \left[\left(\left(\frac{Ra \cos(\theta)}{5830} \right)^{1/3} - 1 \right) + \left| \left(\frac{Ra \cos(\theta)}{5830} \right)^{1/3} - 1 \right| \right], \end{aligned} \quad (5.21)$$

which is an empirical function and is only valid if the lower boundary has a higher temperature than the upper boundary of the gap and if the inclination angle is $0^\circ \leq \theta \leq 60^\circ$. The convective heat transfer calculated by the Hollands equation is usually underestimated [46]. Therefore, an amplification factor of $f_c = 1.2$ is introduced to Eq. 5.21. If the temperature of the upper boundary is higher than the temperature of the lower boundary of the gap, another definition of the Nusselt number has to be used which is given by the empirical function published by Arnold [177]

$$Nu = 1 + [Nu_{90^\circ} - 1] \sin(\theta + 90^\circ) \quad (5.22)$$

with the definition of the Nusselt number for vertical inclination found by Matuska [178]

$$Nu_{90^\circ} = \left(0.1464 - 2.602 \cdot 10^{-4} \cdot 90^\circ - 2.046 \cdot 10^{-6} \cdot (90^\circ)^2 \right) Ra^{0.29}. \quad (5.23)$$

This definition of the Nusselt number is valid for Rayleigh numbers of $Ra < 10^6$ and no amplification factor is used in this case.

The outside convective heat transfer depends on the wind speed v and is given by [37, 179]

$$\dot{Q}_{01}^c = \left(5.7 \frac{W}{m^2K} + 3.8 \frac{W_s}{m^3K} \cdot v \right) (T_{amb} - T_1). \quad (5.24)$$

Besides the heat transfer in the gaps of the glazing unit and the absorber, also conductive heat transfer through the glass panes and the insulation wool at the rear side of the

absorber occurs. Since the temperature difference between the two surfaces of one glass pane is small, the glass panes and the absorber are treated with a single temperature, and conductive heat transfer through them is not taken into account. The heat losses at the rear side of the collector are the radiative transfer between the rear side of the absorber and the insulation material, the conductive heat transfer from the absorber to and through the insulation material as well as the heat transfer from the insulation material to the ambient. The radiative transfer between the rear side of the absorber and the insulation material \dot{Q}_{rear}^r is calculated with wavelength-averaged data using Eq. 2.7. The conductive heat transfers from the absorber to $\dot{Q}_{\text{rear}}^{\text{cond}}$ and through $\dot{Q}_{\text{ins}}^{\text{cond}}$ the insulation material are calculated using Eq. 5.17, and the heat transfer between the insulation and the ambient \dot{Q}_{amb} is described by a constant heat transfer coefficient h_{amb} using $\dot{Q}_{\text{amb}} = h_{\text{amb}} (T_{\text{ins}} - T_{\text{amb}})$.

For the calculation of the collector efficiency curves, the connection from the absorber with the collector fluid has to be taken into account. The heat transfer from the absorber to the fluid \dot{Q}_{fluid} is described by an intern conductance value h_{int} using $\dot{Q}_{\text{fluid}} = h_{\text{int}} (T_{\text{abs}} - T_{\text{fluid}})$ [46]. Usually, the intern conductance value depends on the type of fluid flow such as laminar or turbulent flow. For simplicity, the fluid flow is not considered in this collector model and a constant value is used for h_{int} .

Another simplification of the model is that heat bridges of the collector sidewalls are neglected. The model and material parameters used for the calculation of the collector efficiency are tabulated in Appendix 4.

5.1.3 Calculation of collector efficiency

According to Fig. 5.4, the energy balance equations for the collector components including radiative, conductive, and convective heat transfer as well as the connection to the fluid are as follows:

$$\Delta\dot{Q}_1 = \dot{Q}_0^r + \dot{Q}_{2,f}^r - \dot{Q}_{1,f}^r - \dot{Q}_{1,b}^r + \dot{Q}_{01}^c - \dot{Q}_{12}^c \quad (5.25)$$

$$\Delta\dot{Q}_2 = \dot{Q}_{1,b}^r + \dot{Q}_{3,f}^r - \dot{Q}_{2,f}^r - \dot{Q}_{2,b}^r + \dot{Q}_{12}^c - \dot{Q}_{23}^c \quad (5.26)$$

$$\Delta\dot{Q}_3 = \dot{Q}_{2,b}^r - \dot{Q}_{3,f}^r - \dot{Q}_{\text{rear}}^r + \dot{Q}_{23}^c - \dot{Q}_{\text{rear}}^{\text{cond}} - \dot{Q}_{\text{fluid}} \quad (5.27)$$

$$\Delta\dot{Q}_4 = \dot{Q}_{\text{rear}}^r + \dot{Q}_{\text{rear}}^{\text{cond}} - \dot{Q}_{\text{ins}}^{\text{cond}} \quad (5.28)$$

$$\Delta\dot{Q}_5 = \dot{Q}_{\text{ins}}^{\text{cond}} - \dot{Q}_{\text{amb}} \quad (5.29)$$

The nonlinear system of equations is solved by the Matlab program with numerical iteration with the following conditions. The ambient temperature is treated constant at 20 °C and the initial temperatures for the collector components are set equal to the ambient temperature. The fluid temperature is increased in 20 K steps. For each step, the system of equations is solved iteratively with $\Delta\dot{Q}_i = 0$ ($i = 1, 2, 3, 4, 5$) and the component temperatures are determined as well as the thermal collector efficiency,

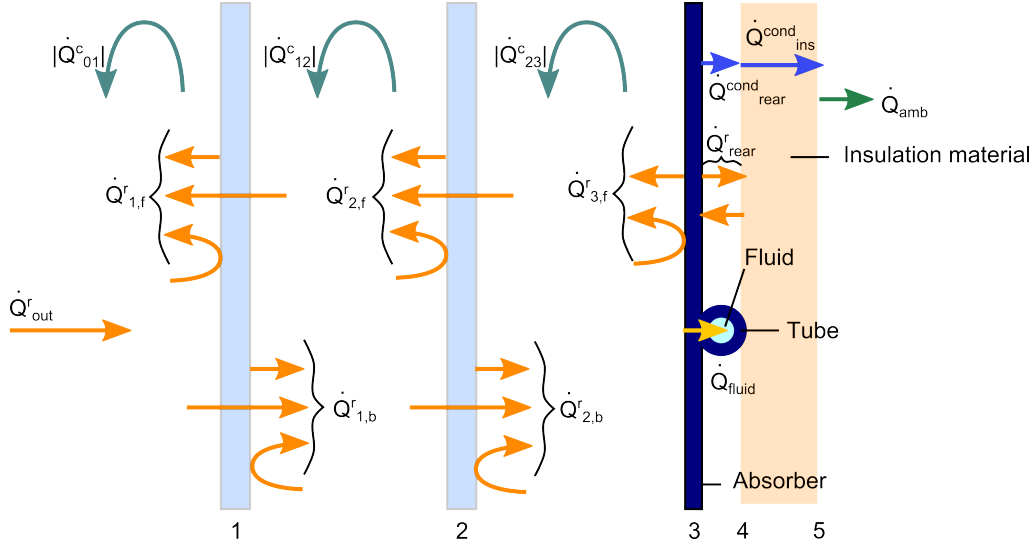


Figure 5.4: Radiation balance for a double-glazed collector taking radiative, conductive, and convective thermal losses as well as the connection to the collector fluid into account.

which is given by the following formula

$$\eta_{\text{col}} = \frac{\dot{Q}_{\text{fluid}}}{\int S_{\text{sol}}(\lambda) d\lambda}. \quad (5.30)$$

To evaluate the reliability of the results of the calculated efficiency curve using the RBM, a comparison with a calculated efficiency curve with our commonly used steady-state collector model (K-model) [46] is shown in Fig. 5.5. Since the calculation of the radiative transfer of the commonly used K-model is based on wavelength-averaged data, the integral RBM of Rubin is used for the comparison of both models instead of the extended spectral RBM developed in this thesis. To have a direct comparison between both models, the same wavelength-averaged input parameters for the solar and infrared spectral range are used in both simulations. The optical input quantities are the wavelength-averaged values of the measured transmittance and reflectance spectra of the first glass pane (HiT from Centrosolar) as well as of the measured reflectance spectra of the absorber (eta plus from Bluetec) and of the simulated transmittance and reflectance spectra of the coating system "AR/Glass/SiO_xN_y/ZnO:Al(2 wt.%) /SiO₂." The infrared transmittance of the glass panes is set to zero and the temperature dependence of the infrared emissivity is not taken into account. Rubin applied ambient temperature for the determination of the wavelength-averaged emissivity [174]. However, the temperature of the collector components is usually much higher, especially in the case of stagnation of the collector. Therefore, the wavelength-averaged emissivity is calculated (see Eq. 2.4) for the temperature of the components in the case of stagnation of the collector. These temperatures were previously determined by the spectral collector simulation. Conductive and convective thermal losses are considered while the commonly used K-model also takes account of the temperature dependence

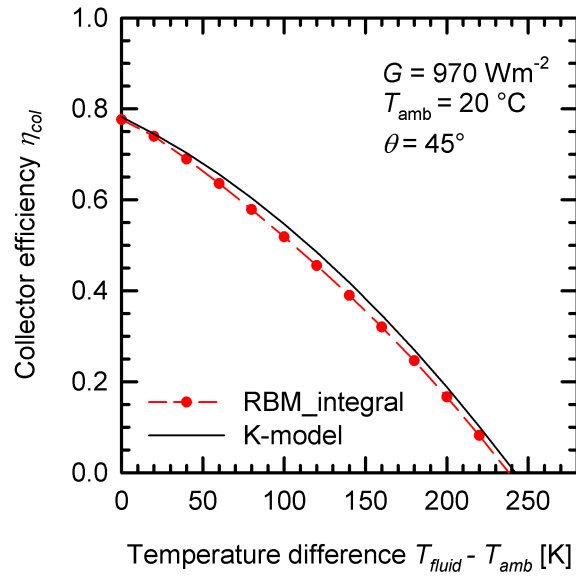


Figure 5.5: Efficiency curve of a double-glazed collector with low-e coating on the inner glass pane simulated by the RBM with wavelength-averaged optical properties (red line) taking conductive and convective losses into account in comparison to the result of the commonly used collector model (black line) [46].

of the material properties, which is not the case in the model presented in this thesis. The commonly used K-model takes also account of thermal bridges of the collector side walls as well as of the fluid flow. These differences between the models may be the reason for the small discrepancy between both the simulated efficiency curves (see Fig. 5.5).

Since the thermal interactions inside the collector are complex, the differences between the spectral and wavelength-averaged calculation with and without convective losses are studied. Figure 5.6 shows simulated efficiency curves using the extended spectral RBM developed in this thesis in comparison to the integral RBM of Rubin with wavelength-averaged values for the solar and infrared wavelength range. The optical input quantities are the spectral and wavelength-averaged data of the collector system considered already for the model comparison in Fig. 5.5. If only radiative thermal losses are taken into account, the difference between the spectral and integral calculation increases at higher temperatures. The reason is that the temperature dependence of the infrared wavelength-averaged values is not taken into account in the model of Rubin and the thermal losses are, therefore, underestimated. Considering convective and conductive losses inside the gap, the discrepancy between the spectral and wavelength-averaged calculation gets smaller, which is an indication that the thermal losses of the collector are dominated by the convective losses.

Finally, Fig. 5.7 shows the temperature development of the components with increasing fluid temperature taking convective and conductive thermal losses into account. At a fluid temperature of $T_{fluid} = 20$ °C the temperature of the second glass pane is

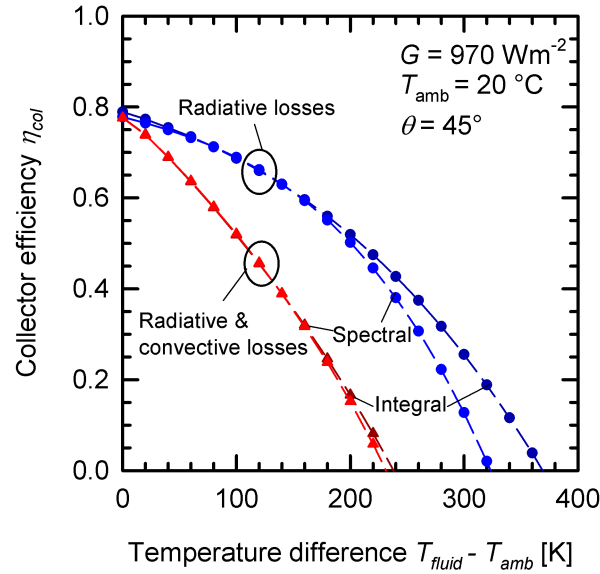


Figure 5.6: Efficiency curves simulated with the wavelength-averaged RBM of Rubin [174] in comparison to the results of the extended spectral radiation-balance method, with and without convective thermal losses.

even higher than the temperature of the absorber. The reason is that the absorption of the ZnO:Al coating causes a raise of temperature of the inner glass pane while the absorber is cooled by the fluid.

5.2 Decision criterion for applicability of coating systems for collector covers

In Fig. 5.8 are the schematic configurations of three different collector types shown. The first one is a single-glazed collector, the second one is a double-glazed collector without low-e coating, and the third one is a double-glazed collector with low-e coating on the inner glass pane. The glass panes without low-e coating are AR coated on each surface of the glass pane. Figure 5.9 shows the simulated efficiency curves of the three collector types. For comparison, there is also an efficiency curve of a vacuum tube collector (VTC) [180] shown. The first and second type of collectors provide higher efficiencies at low fluid temperatures. However, at higher temperatures, they exhibit higher thermal losses, which is the reason why their efficiency curves decrease much faster than the efficiency curves of the collector with low-e coating and the VTC. For the evaluation of the ability of a collector type for a certain application, the collector efficiency in the operating-temperature range of that application is, therefore, crucial. To find a more meaningful decision criterion of the applicability of a collector besides the thermal collector efficiency, another performance criterion P_C is used

$$P_C = \eta_{col} \cdot \eta_{carnot}, \quad (5.31)$$

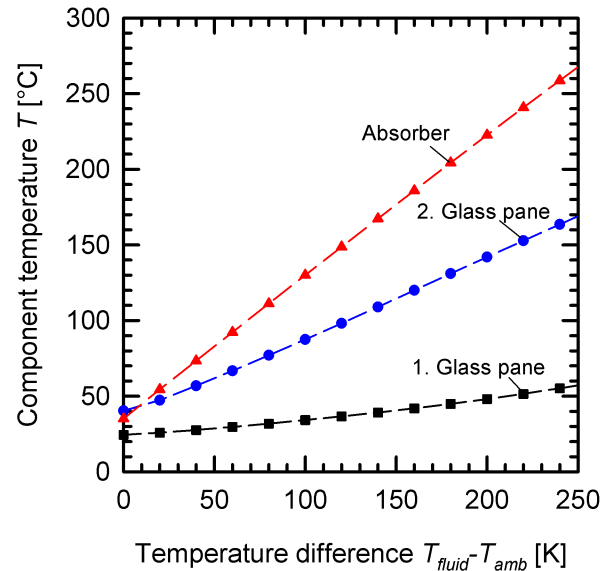


Figure 5.7: Simulated temperature development of the components of a double-glazed collector with low-e coating on the inner glass pane at different temperature differences between the fluid to the ambient. Conductive and convective thermal losses are taken into account.

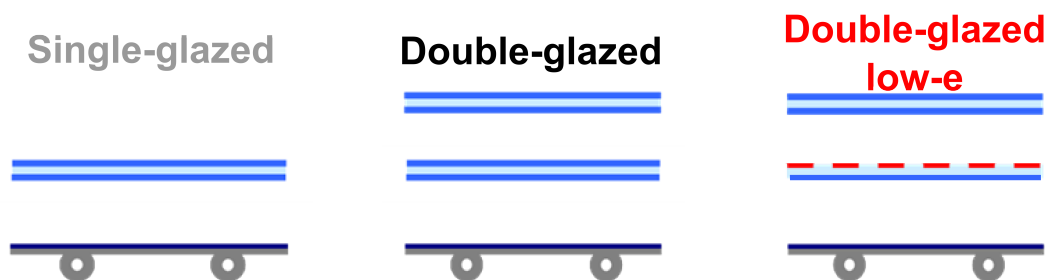


Figure 5.8: Schematic representation of three collector types. The first one is a single-glazed collector, the second one is a double-glazed collector without low-e coating and the third one is a double-glazed collector with low-e coating on the inner glass pane. The glass panes without low-e coating are AR coated on both surfaces.

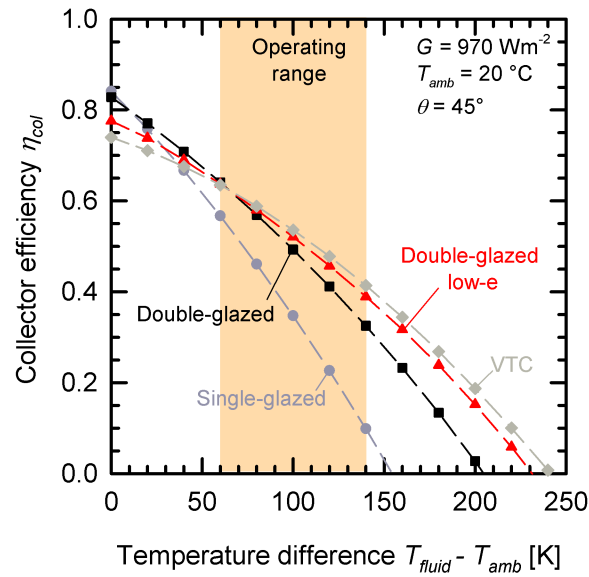


Figure 5.9: Simulated efficiency curves of a single-glazed collector (dark grey line), a double-glazed collector without low-e coating (black line), a double-glazed collector with low-e coating (red line), and a vacuum tube collector (light grey line).

which is the product of the thermal collector efficiency η_{col} and the Carnot efficiency $\eta_{carnot} = 1 - T_{amb}/T_{fluid}$ [181]. The Carnot efficiency describes the fraction of thermal energy, which is theoretically convertible to free energy. The fraction of usable energy is also called exergy. This performance criterion represents, therefore, the relation between the thermal collector efficiency and its thermodynamical usability at different process temperatures [181]. The P_C curve starts always at zero since the thermal energy at ambient temperature is useless. Collectors with higher conversion factors η_0 increase faster with increasing temperature. However with increasing temperature, the thermal losses of the collector start to dominate the increase of the Carnot-efficiency and a maximum is built before the P_C curve decreases to zero, as shown in Fig. 5.10. The level of the maximum of the P_C curves as well as the temperature at which the maximum occurs are used as an indication for the quality of a collector for a certain application. The larger the values of the maximum of the P_C curve the higher is the theoretically convertible amount of energy at the corresponding temperature. The single-glazed collector provides only a low maximum at low temperatures. The collector with low-e coating provides a higher maximum at higher temperatures. The maximum shifts to higher levels and to higher temperatures with the implementation of a second glass pane and a low-e coating. However, the vacuum tube collector provides still a better performance at higher temperatures. In the following, the level and temperature of the maximum is used as evaluation criterion for the low-e coatings with respect to the application to the collector cover.

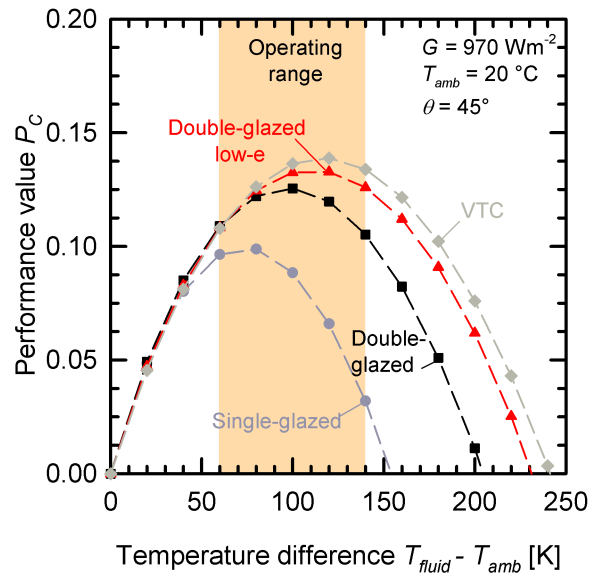


Figure 5.10: Simulated collector performance curves of a single-glazed collector (dark grey line), a double-glazed collector without low-e coating (black line), a double-glazed collector with low-e coating (red line), and a vacuum tube collector (light grey line).

5.3 Simulation of collector efficiencies for different coating configurations

In the following, the results of the parameter and doping variation studies as well as the usage of AR coatings with the ZnO:Al thin films of Sec. 3.3.3 and 4.3.3 are used for the simulation of collector efficiency curves to evaluate the ability of these coatings for the application to collector covers.

5.3.1 Collector simulation results of the deposition parameter studies

Since the deposition rate varies with the deposition parameters, as shown in Fig. 3.21, the film thickness values are different for different deposition parameters even if the sputtering time was the same. Therefore, the optical constants of the films deposited at different substrate temperatures, argon pressures, and DC powers determined in Sec. 3.3.3 are used to calculate the transmittance and reflectance spectra for a film thickness of 500 nm. A constant film thickness is chosen to make the simulation of the different samples comparable since the number of interference oscillations of the optical spectra, the absorption in the film, as well as the electronic film properties depend strongly on film thickness. Variation of the film thickness of films sputtered from the target with 2 wt.% Al₂O₃ have shown that the electronic properties are nearly the same for films thicker than 400 nm (see Fig. 3.15), which is the reason why 500 nm is chosen. The influence of the ZnO:Al film thickness on the collector efficiency will be shown in Sec. 5.3.4. With the simulated spectra for various deposition parameters, the efficiency and P_C curves are simulated. The curves of the substrate temperature

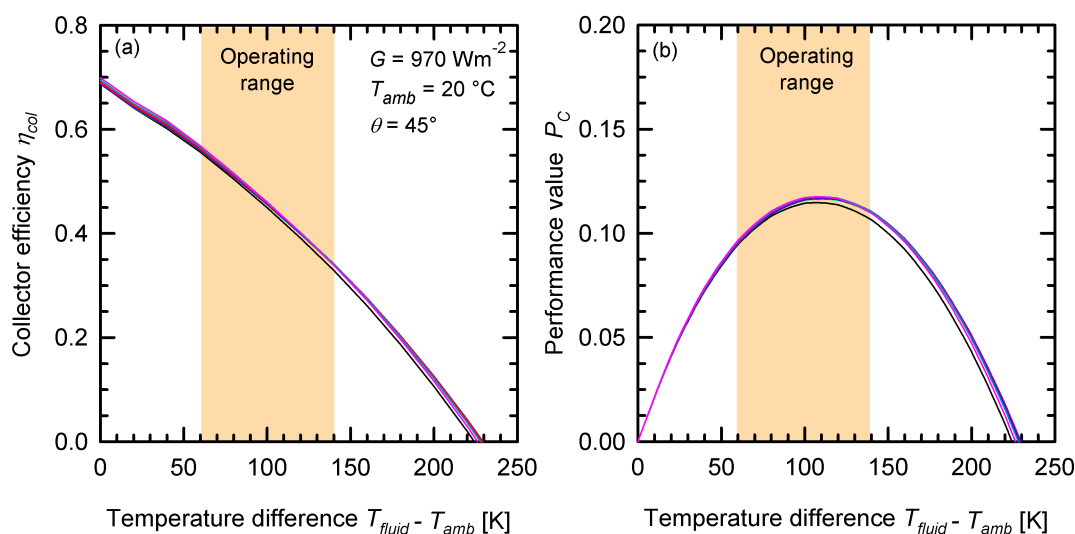


Figure 5.11: Simulated collector efficiency (a) and performance (b) curves of a double-glazed collector with ZnO:Al single layers of 500 nm thickness on the inner glass pane deposited at different substrate temperatures ranging from 20 °C to 400 °C. Figure 5.12 (a) shows the maximum of the performance value as a function of the substrate temperature.

series are representatively shown in Fig. 5.11. It becomes obvious that the difference between the efficiency and P_C curves for different substrate temperatures is very small. The simulated efficiency and P_C curves of the other parameter series also show small differences. Therefore, the maxima of the P_C curves are used for the comparison of the different samples, as shown in Fig. 5.12. The higher the maximum of the P_C curve the higher is the amount of convertible energy at the temperature level for the desired application of the collector. The highest P_C values are reached by the substrate heated to 400 °C. The reason is that the solar transmittance increases with increasing substrate temperature (see Fig. 3.21 (a)), which has an influence on the conversion factor of the collector. In addition, the infrared emissivity decreases with increasing substrate temperature up to 250 °C, which reduces the thermal radiative losses. The variation of the sputtering pressure shows that an argon pressure of 0.4 Pa would be favorable. This is caused by the low infrared emissivity and high solar transmittance of that film (see Fig. 3.21 (b)). The variation of the DC power shows an increase of the P_C value with increasing DC power, which is the result of the increasing solar transmittance and decreasing infrared emissivity with increasing DC power (see Fig. 3.21 (c)).

5.3.2 Collector simulation results of single ZnO:Al and AR-ZnO:Al coating systems

To evaluate the effect of additional AR coatings on the collector efficiency and P_C curves, three different coating configurations are compared such as (1) a single ZnO:Al thin film deposited from a target with 2 wt.% Al₂O₃, (2) the three-layer system of

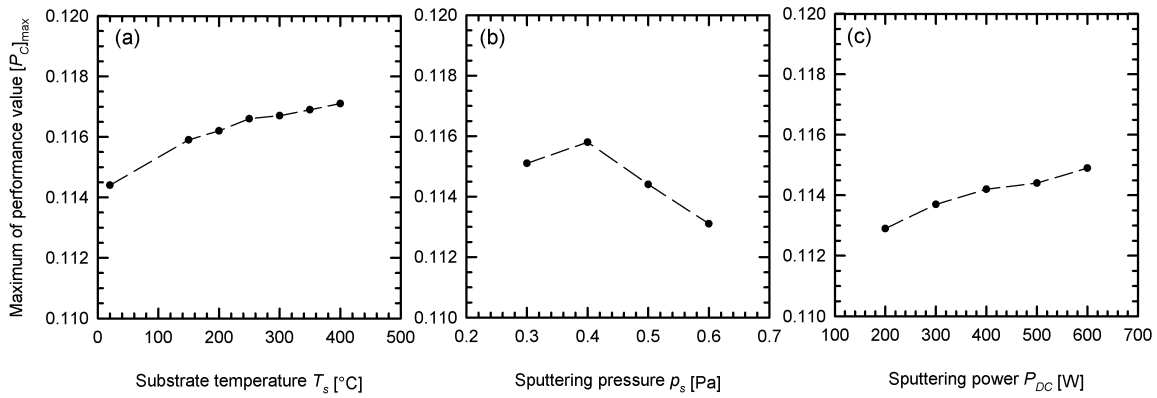


Figure 5.12: Maxima of the simulated collector performance value of a double-glazed collector with ZnO:Al single layers of 500 nm thickness on the inner glass pane in dependence of the deposition parameters such as (a) the substrate temperature, (b) the argon pressure, and (c) the DC power.

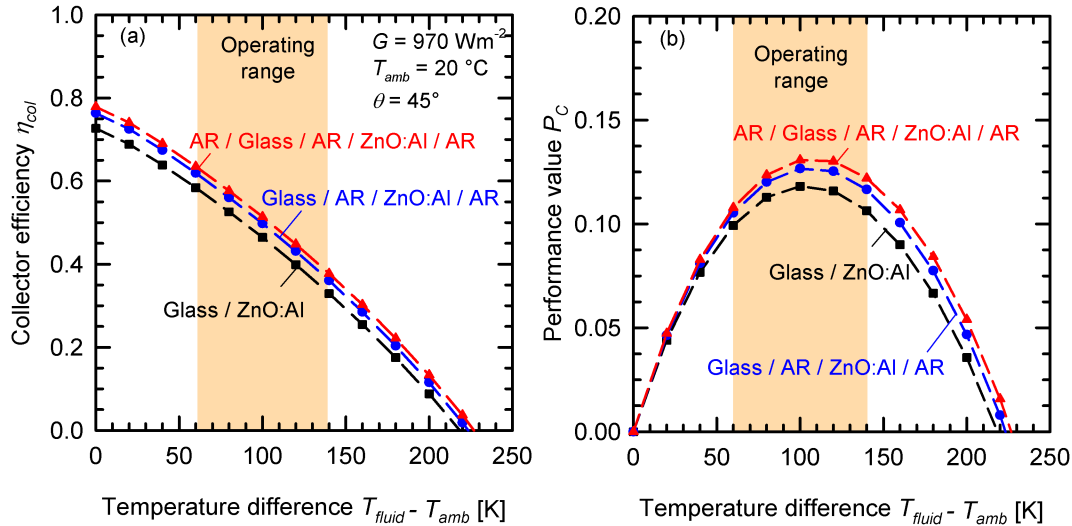


Figure 5.13: Simulated collector efficiency (a) and performance (b) curves of a double-glazed collector with different AR coating configurations on the inner glass pane.

Sec. 4.3.3 with ZnO:Al as middle layer and two additional AR coatings, and (3) the three-layer system in combination with an additional AR layer on the rear side of the glass substrate. In Fig. 5.13 (a), it becomes obvious that the three efficiency curves are parallel shifted, but they exhibit the same gradient. The reason is that the AR coatings have an effect in the solar and not in the infrared spectral range, as already shown in Fig. 4.2. The AR coatings reduce the solar reflective losses and therefore, influence mainly the conversion factor η_0 of the efficiency curve. In the infrared spectral range, the AR coatings have no effect on the emissivity of the coating system, and therefore, the thermal losses and the gradient of the efficiency curves are the same. Figure 5.13 (b) shows that the three-layer coating system with rear AR coating provides the highest P_C curve. The maxima of the three curves have all the same position at the temperature difference axis $T_{\text{fluid}} - T_{\text{amb}}$.

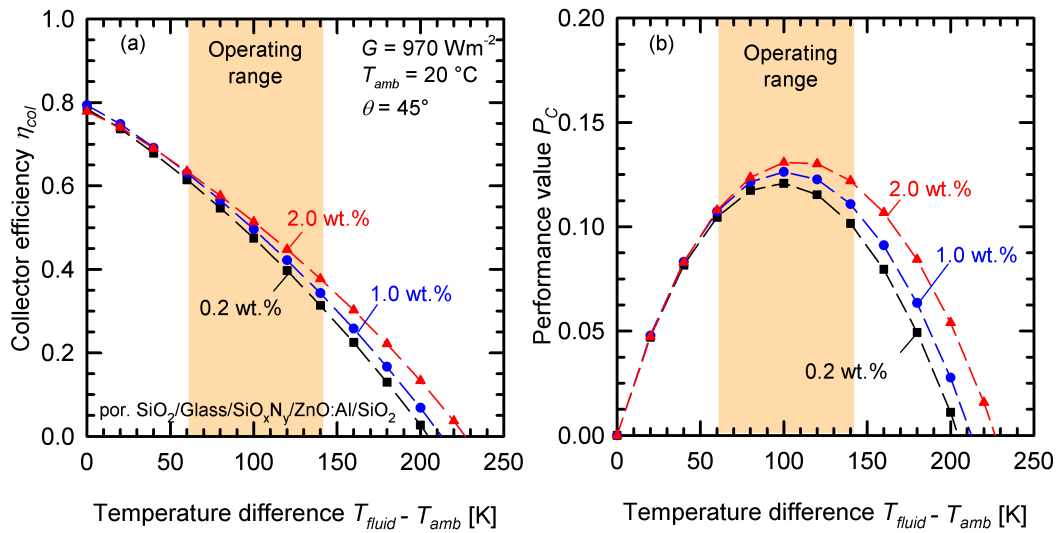


Figure 5.14: Simulated collector efficiency (a) and performance (b) curves of a double-glazed collector with different doping concentrations of the low-e coating on the inner glass pane.

5.3.3 Collector simulation results of coating systems with different doping concentration

Figure 5.14 shows simulated efficiency and P_C curves of collectors with AR coating systems with different doping concentrations of the ZnO:Al thin films. The conversion factors of the three efficiency curves vary little with varying doping concentration since the solar transmittance of the coating systems is nearly the same, as already shown in Table 4.2. However, the decrease of the efficiency curves becomes more flat for collectors with higher doping concentration. The reason is that the ZnO:Al thin films with higher doping concentration exhibit a lower infrared emissivity and, therefore, the thermal losses are less in comparison to the collectors with lower doping concentrations. Due to the reduced thermal losses with increasing doping concentration, the maxima of the P_C curves are shifted to higher values on the temperature difference axis as well as on the P_C axis.

5.3.4 Collector simulation results of coating systems with different ZnO:Al film thickness values

In Fig. 5.15 simulated efficiency and P_C curves of collectors with AR coating systems with different film thickness values of the ZnO:Al thin film are shown. It becomes obvious that the efficiency curves exhibit different conversion factors and gradients. The conversion factor decreases and the curves become more flat with increasing film thickness. The reason for the decreasing conversion factor is that with increasing film thickness the optical losses in the solar spectral range increase due to absorption in the film (according to the Lambert-Beer law [39]). In addition, the two AR coatings

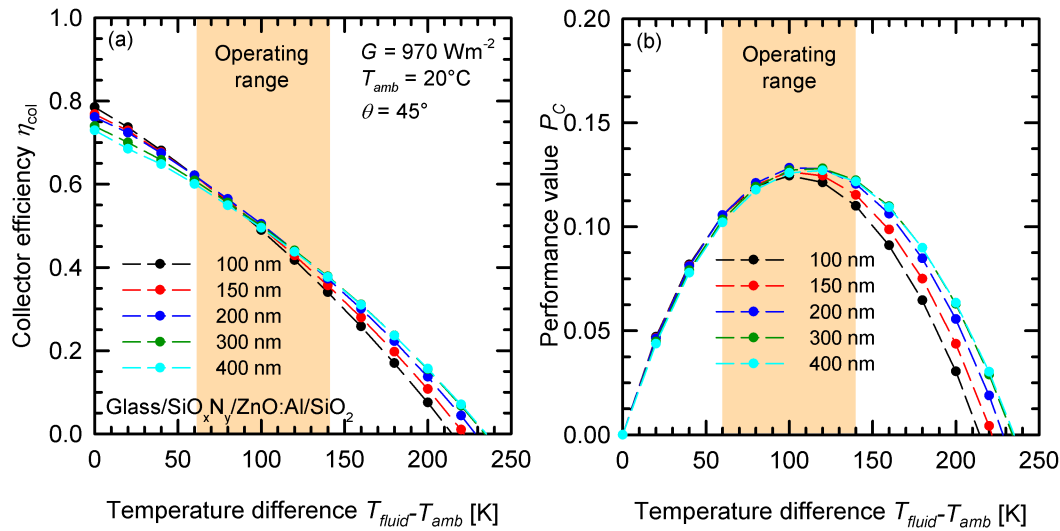


Figure 5.15: Simulated collector efficiency (a) and performance (b) curves of a double-glazed collector with different ZnO:Al film thickness values of the low-e coating on the inner glass pane.

cannot compensate all the interference oscillation since the optical path lengths of the films do not fulfill the “ $\lambda/4, \lambda/2, \lambda/4$ ” condition (see Eq. 2.41) if the ZnO:Al film thickness is changed. As a consequence, the reflective losses increase with increasing film thickness. The gradient of the efficiency curve depend on the infrared emissivity of the films. With increasing film thickness, the infrared emissivity decreases. One reason is the dependence of the electronic properties on film thickness (see Fig. 3.15). At a temperature difference between fluid and ambient of 100 K, the efficiency curves meet each other nearly at the same crosspoint.

Figure 5.16 shows the maximum values of the P_C curves as a function of film thickness. The AR coating system with a 200-nm-thick ZnO:Al thin film provides the highest value of the P_C curves and is, therefore, favorable for the collector application.

5.3.5 Discussion of the simulation results

As shown in Figs. 5.11 and 5.12, the variation of the deposition parameters such as substrate temperature, argon pressure, and DC power has little influence on the collector efficiency. The influence of small differences in the solar and infrared optical properties on the collector efficiency of films deposited with different parameters may be partly compensated by convective thermal losses. In Fig. 5.12 (a) it becomes obvious that increasing the substrate temperature higher than 400 °C may be favorable. However, with regard to the industrial practicability of the deposition process, much lower temperatures than 400 °C should be chosen. Therefore, a substrate temperature of 200 °C is used for the deposition of the ZnO:Al thin films. Since the difference of the collector efficiencies for different substrate temperatures is very small, films deposited on unheated substrates are also applicable which would be favorable for the industrial

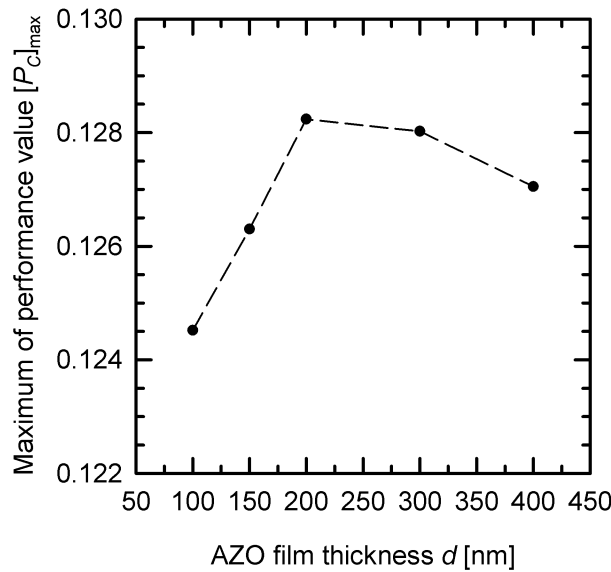


Figure 5.16: Maxima of the simulated collector performance value of a double-glazed collector with different ZnO:Al film thickness values of the low-e coating on the inner glass pane.

production. Figure 5.12 (c) demonstrates that an increase of the DC power slightly improves the collector performance. However, as already discussed in Sec. 3.3.4, the number of arcing events drastically increases with increasing DC power. Therefore, a DC power of 500 W is chosen. Higher DC power values are only possible if an effective arcing reduction would be available. To ensure the plasma stability during the deposition an argon pressure of 0.5 Pa is chosen although it is not the argon pressure with the highest P_C value.

In contrast, the addition of AR coatings, which increases the solar transmittance of the glazing, as well as the choice of the doping concentration, which reduces the infrared emissivity, are of much more importance for improving the collector performance (see Figs. 5.13 and 5.14) in comparison to the variation of the deposition parameters. The application of AR coatings, especially on the rear side of the inner glass pane, would be advantageous. The variation of the doping concentration has shown that a doping concentration even higher than 2 wt.% may be favorable. However, Jäger et al. [50] showed that the free-carrier concentration has a maximum for 2 wt.% and the resistivity increases with increasing doping concentration due to a decreasing mobility. The reason may be a segregation of Al_2O_3 so that an addition of Al_2O_3 does not cause an increase of free-carrier density but an increase of scattering centers. An increase of resistivity with increasing doping concentration causes an increase in infrared emissivity, which would be not favorable for the collector application.

The film thickness variation of the ZnO:Al thin films has shown (see Fig. 5.15) that the film thickness has a strong influence on the conversion factor and the gradient of the efficiency curves. However, the efficiency curves of the collectors with different ZnO:Al film thickness values meet each other at nearly the same crosspoint of 100 K tempera-

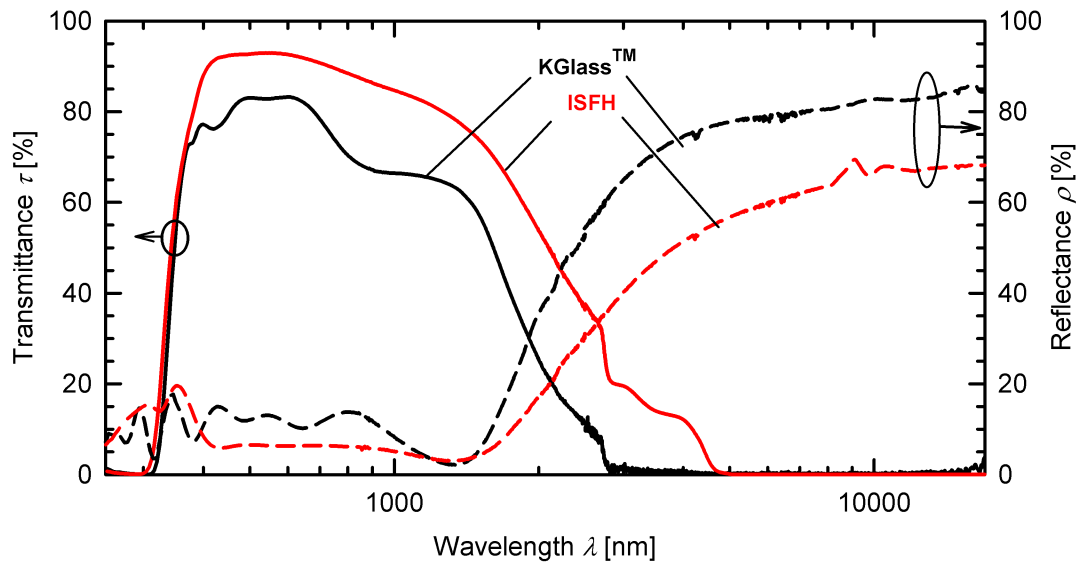


Figure 5.17: Measured transmittance and reflectance spectra of a three-layer system consisting of $\text{SiO}_x\text{N}_y/\text{ZnO:Al}$ (2.0 wt.)/ SiO_2 in comparison to $\text{KGlass}^{\text{TM}}$ from Pilkington.

ture difference between fluid and ambient. At this temperature difference, the collector with the 200-nm-thick ZnO:Al thin film provides a slightly higher collector efficiency and performance value in comparison to collectors with other film thickness values. The choice of an appropriate film thickness depends, however, on the temperature required for the desired application of the collector.

5.4 Comparison with commercially available low-e glass

Finally, Fig. 5.17 depicts the measured transmittance and reflectance spectra of the low-e coating system with 2.0 wt.% doping concentration of Sec. 4.3.3 in comparison to a commercially available low-e glass ($\text{KGlass}^{\text{TM}}$ from Pilkington), which is used in the HGlas project for first prototype collectors. The solar transmittance of the ZnO:Al based coating system is 85%, which is much higher than the solar transmittance of $\text{KGlass}^{\text{TM}}$, 71%. The infrared reflectance of the coating system is lower, and therefore, the emissivity is larger than that of $\text{KGlass}^{\text{TM}}$. The reason for the low solar transmittance of $\text{KGlass}^{\text{TM}}$ in comparison to the coating system presented in Fig. 5.17 is that $\text{KGlass}^{\text{TM}}$ is optimized for window applications. Therefore, $\text{KGlass}^{\text{TM}}$ provides only a sufficient visible transmittance, but over the whole solar spectral range, the transmittance is poor. The substrate has high iron content, which causes a considerably high absorption for glass thicknesses of 4 mm. The low-e coating is based on fluorine doped tin oxide. Additional AR coatings are missing, which becomes obvious by the high reflectance in the solar spectral range. For window applications, a low emissivity is needed, which may be reached by $\text{KGlass}^{\text{TM}}$ due to a larger film thickness. However, the increase of the film thickness would decrease the solar transmittance and, therefore,

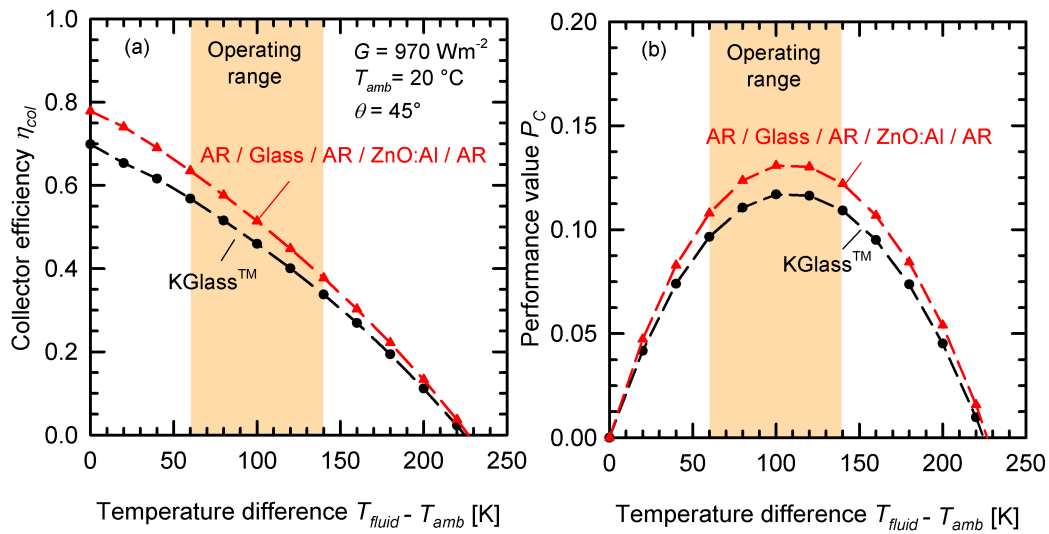


Figure 5.18: Simulated collector efficiency (a) and performance (b) curves a double-glazed collector with a three-layer system on the inner glass pane consisting of $\text{SiO}_x\text{N}_y/\text{ZnO:Al}$ (2.0 wt.%) / SiO_2 in comparison to a collector with KGlass™ from Pilkington.

would not be favorable.

However, the simulated efficiency curves shown in Fig. 5.18 demonstrate that the solar transmittance is of more importance than the infrared emissivity. The efficiency curve of the collector with the low-e coating system presented in Fig. 5.17 is higher than the efficiency curve of a collector with KGlass™ over the whole temperature range. In the desired operating temperature range, the collector with the low-e coating system presented in Fig. 5.17 provides higher P_C values, which means that more thermal energy is usable for other processes.

5.5 Summary

In this chapter, a collector model for a double-glazed collector was presented, which takes account of the spectral radiative transfer inside the collector. The RBM of Rubín [174] was extended in this thesis to a spectral calculation since a wavelength-averaged calculation and neglect of the temperature dependence of the component's emittance may lead to errors, especially if selective coatings are used for the collector cover and the absorber. The RBM enables the determination of the radiative transfer inside a system of infrared transparent media. The efficiency curves were determined using the RBM with and without taking convective and conductive thermal losses into account. The resulting efficiency curves of the wavelength-averaged calculation were in agreement with our commonly used collector model, which was an indication of the reliability of the model presented in this thesis. The comparison of the wavelength-averaged and the spectral calculation showed an increasing deviation of the efficiency curves at increasing temperatures, which were mainly caused by the neglect of the tem-

perature dependence of the infrared emittance. However, the convective heat transfer dominated the thermal losses. Besides the efficiency curves, another decision criterion was introduced to evaluate the ability of the coatings to the application as collector cover. The product of the collector efficiency with the Carnot efficiency is the fraction of the thermal energy, which is usable for exergy processes. The efficiency curves and the performance curves of ZnO:Al thin films deposited at different sputtering parameters and doping concentrations as well as different coating system configurations were analyzed. The analysis showed that the variation of the deposition parameters exhibited only small influences on the efficiency curves while the addition of AR coatings and the optimization of the doping concentration were necessary to improve the collector efficiency. The ZnO:Al film thickness had only a small influence on the collector performance in the desired temperature range. The application of a three-layer system with a ZnO:Al thin film with a doping concentration of 2 wt.% deposited on a heated substrate and an additional AR coating on the rear side of the substrate exceeded the efficiency and performance curves of a commercially available low-e glass, which was used for first prototype collectors.

6 Summary and outlook

In this thesis, the influence of the integration of double glazing with selective low-e coating into a flat-plate collector was theoretically studied. Due to an improvement in the insulation of the transparent cover, the efficiency of the flat-plate collector at high temperatures or at low solar irradiation was increased in comparison to a flat-plate collector without low-e coating. The application as a covering for flat-plate collectors requires a high solar transmittance to ensure high conversion factors as well as a low infrared emissivity. Therefore, glass substrates with low-iron content and AR coatings are essential for reducing absorption and reflection losses. TCO coatings are particularly suitable as low-e coatings due to their optical selectivity with high solar transmittance.

Material studies on DC magnetron sputter deposited ZnO:Al thin films were done with respect to varying deposition parameters and doping concentrations of the ceramic ZnO:Al₂O₃ targets. Aluminum-doped zinc oxide is a promising TCO material due to its good optical and electronic properties as well as the low material costs. Simultaneous modeling of ellipsometric and photometric data was an effective and non-destructive tool for the determination of the optical and electronic properties of the films. The model dielectric function presented in this thesis enabled the characterization of the films over a wide wavelength range of 0.3 to 50 μm , which is the relevant wavelength range of solar-thermal applications. The modeling results were compared to independent thin film characterization methods such as four-point probe, Hall, XRD and AFM, as well as SEM and TEM measurements to evaluate the reliability of the modeling results. The implementation of an interface layer between the glass substrate and the ZnO:Al bulk layer was necessary for modeling the ellipsometric data of films with high doping concentration. Explanations for the interface layer were structural differences at the interface due to a dilution of ZnO:Al into the glass substrate referring to TEM analysis. Chemical reasons were not confirmed by SNMS. At lower doping concentrations, the interface layer was found by the TEM analysis but not by the optical modeling, which might be explained by numerical problems of the modeling procedure. Special attention was paid to the modification of Tanguy's band-gap model, which explains the direct fundamental absorption including the effects of excitonic interaction. Tanguy used Lorentzian broadening, which produces extended absorption tails below the absorption threshold. However, Gaussian broadening or intermediate types are more applicable and are explained by the influence of impurities, crystal strain, or alloys. For that reason, an energy-dependent broadening term developed by Kim et al. [153] was introduced to the Tanguy model in this thesis. The effective mass as well as the band gap were determined by the optical modeling for films with varying doping concentration and the results were in agreement with theoretical investigations.

The increase of the effective mass with increasing free-carrier density was explained by the effective mass model of Pisarkiewicz [87], and the band-gap shift was explained by a band-gap widening due to band filling described by the Burstein Moss effect [83, 84] as well as by a band-gap narrowing due to many-body effects described by a model of Inkson [90].

The variation of the substrate temperature, the argon pressure and the DC power caused only slight changes in the optical and electronic properties in comparison to the variation of the doping concentration. By changing the doping concentration of the target, the free-carrier density, mobility, and effective mass as well as the band gap and the grain sizes were influenced. Every doping concentration exhibited a certain temperature at which the lowest resistivity was reached. However, the results presented in this thesis were different to results published by Hüpkes [18] and Berginski [157], who studied the substrate temperature dependence of reactive MF sputtered and RF sputtered ZnO:Al thin films with varying doping concentration, respectively. The reason for the discrepancy might be the different plasma excitation such as DC, RF, and MF excitation or the target material. Independent of the doping concentration, the resistivity of the films increased with decreasing film thickness. The films of the considered doping concentrations were stable up to 300 °C at the annealing in air with raising temperatures.

Simulations of transmittance and reflectance spectra had shown that additional AR coatings were necessary to reduce reflective losses in the solar spectral range while the AR coatings had no effect on the infrared emissivity. A three-layer system with two AR coatings and the ZnO:Al thin film as middle layer provided a reduction of reflective losses over a wide wavelength range. Appropriate coating materials would be dielectric materials such as Al_2O_3 , SiO_xN_y , SiO_2 , or MgF_2 . With respect to the associated deposition technique and the refractive indices of the films, SiO_xN_y and SiO_2 were chosen, which were reactively sputtered from a silicon target. The refractive indices were changed between that of Si_3N_4 and SiO_2 only by varying the reactive gas composition. The AR coating systems provided a high solar transmittance of 85% independent of the doping concentration of the ZnO:Al thin films, which might be further increased with an additional AR coating on the rear side of the glass substrate. However, the infrared emissivity of the coating systems with low doping concentration was too high for the application in a solar-thermal flat-plate collector. In contrast, the films sputtered from a target with 2 wt.% Al_2O_3 provide a low infrared emissivity of 31%, which would be favorable for the collector application. Durability tests had shown that the AR coatings acted as effective protection layers for the ZnO:Al coating. A high temperature test of the coating system showed an increase of the solar transmittance and no change in emissivity, which is advantageous with respect to the thermal hardening of the glass panes after film deposition.

To evaluate the film properties with respect to their influence on the collector effi-

ciency, a collector model was developed in this thesis, which enables the calculation of the radiative transfer even if infrared transparent media are used. Since selective coatings were used for the collector cover and the absorber, the calculation of the radiative transfer should take place with spectral data instead of wavelength-averaged data. The temperature dependence of the emitted thermal radiation should also be taken into account, which was not the case if the wavelength-averaged calculation was applied. As a consequence, the radiation-balance method developed by Rubin [174] was extended to a spectral calculation in this thesis. Another advantage of the spectral calculation was that the solar and infrared spectral range did not have to be treated separately. The comparison between the spectral and wavelength-averaged calculation of the efficiency curves yielded an increase in the differences between both models with increasing temperatures. The main reason was the neglect of the temperature dependence of the infrared emittance by the wavelength-averaged calculation. However, if convective thermal losses were also taken into account, the differences between both calculation methods decreased since the convective losses dominated the thermal losses. The collector model presented in this thesis, taking conductive and convective thermal losses into account, was in agreement with a commonly used collector model [46]. Another decision criterion, which is given by the product of the collector efficiency and the Carnot efficiency, was introduced to evaluate the ability of the coatings to the application as collector cover. The efficiency curves and the so called performance curves were calculated for ZnO:Al thin films deposited at different sputtering parameters, film thickness values, and doping concentrations, as well as different coating system configurations. As result, the dependence of the efficiency and performance curves on the variation of the deposition parameters and the ZnO:Al film thickness was only small while the addition of AR coatings and the optimization of the doping concentration had a greater influence. Therefore, a three-layer system with ZnO:Al sputtered from a target with 2 wt.% Al₂O₃ on a heated substrate and an additional AR coating on the rear side of the glass substrate improved the efficiency and performance curves in comparison to a commercially available low-e glass, which was used for first prototype collectors. The calculated collector efficiency of a double-glazed collector with the AR coating system developed in this thesis yielded 52% at a temperature difference between fluid and ambient of 100 K, which is much higher in comparison to a conventional single-glazed collector with only 35% and near to the efficiency of a vacuum tube collector of 54%.

The results presented in this thesis are promising for the development of highly efficient flat-plate collectors, which provide high efficiencies at temperatures above 100 °C as well as at low solar irradiation. With respect to the realization of the low-e coated covering for flat-plate collectors, the sputtering processes have to be scaled to collector sizes. Sputtering is an industrial applicable process. However, heating and sputtering on large substrates is still a challenge [10] since it takes longer to reach a good vacuum,

and the temperature distribution has to be homogeneous to avoid temperature gradients, which may influence the film properties or damage the glass substrate. Therefore, the results of the deposition parameter series were promising since the collector efficiency did not decrease much if the ZnO:Al thin films were deposited on unheated substrates. Another aspect is that it would be favorable if the thermal hardening of the glass substrates could take place after film deposition. As a consequence, it would be necessary to develop sputtering and post treatment processes, which enable the film deposition on unheated substrates and the activation of the free carriers of the ZnO:Al thin films within a post treatment process such as the thermal hardening process. Therefore, effective protection layers are essential for protecting the ZnO:Al thin films during the post treatment since ZnO:Al single layers are not stable at high temperatures if they are in contact with ambient oxygen and humidity. First high temperature tests had shown that the AR coating system developed in this thesis did not degrade at high temperatures since the AR coatings acted as effective protection layers for the ZnO:Al thin film. In the ongoing research, further tests have to be done with respect to the thermal hardening of the low-e coated glass and its durability after the hardening process to evaluate the applicability for the double-glazed flat-plate collector.

Appendix

1 Fit parameters of ZnO:Al thin films on different substrates

Best fit parameters are determined by ellipsometric studies of ZnO:Al thin films on glass and silicon substrates deposited at 250°C substrate temperature. The model dielectric function contains three and two layers. The ZnO:Al bulk layer is modeled using a pole oscillator for high interband transitions, a modified Tanguy model [104] for fundamental absorption using the formula developed by Kim et al. [153], and a modified Drude oscillator developed by Mergel et al. [94] for free-carrier absorption.

Table 1

Parameter	Glass / ZnO:Al	Silicon / ZnO:Al
MSE	9.17	11.13
d_s [nm]	6.23±0.03	6.64±0.02
d_b [nm]	714.3±0.2	701.9±0.5
d_i [nm]	13.84±0.07	-
A_p [eV]	134±1	166±2
E_p [eV]	10.11±0.04	10.94±0.04
A_g [eV ^{3/2}]	22.4±0.2	21.7±0.5
R [eV]	0.06 (fixed)	0.06 (fixed)
E_g [eV]	3.711±0.005	3.71±0.02
s	0.40±0.02	0.46±0.06
γ [eV]	0.075±0.001	0.088±0.003
κ	0.0150±0.0007	0.019±0.002
A_D [eV ²]	2.024±0.001	2.014±0.003
Γ_{low} [eV]	0.1348±0.0004	0.1316±0.0005
Γ_{high} [eV]	0.0262±0.0005	0.0428±0.0008
$\Gamma_{\text{changeover}}$ [eV]	1.127±0.003	1.110±0.003
Γ_{width} [eV]	0.260±0.004	0.232±0.005
dn	0.0166±0.0003	0.0172±0.0004

Most of the best fit parameters of the glass sample agree well with that of the silicon sample. The high-energy absorption positions E_p of both samples are in accordance to literature data [30, 34, 147]. The screening factor of the Tanguy model demonstrates with $s < 1$ that no bound state of the excitons exists. The reason may be the screening of the exciton interaction due to free carriers since the free-carrier density exceeds the Mott critical density of $N_{\text{crit}} \approx 10^{18} \text{ cm}^{-3}$. The band gap energies E_g are higher than that of undoped ZnO due to band-filling and renormalization effects. The κ values indicate that there is an intermediate type of broadening between Lorentzian and Gaussian form.

2 Electronic properties of ZnO:Al thin films with varying film thickness determined by SE and Hall analysis

Electronic parameters of the ZnO:Al samples on glass deposited at 200°C substrate temperature determined by Hall measurements and SE analysis. The measurement errors of the Hall parameters as obtained by repeated measurements on the same sample are for the electron concentration $\Delta N_{\text{Hall}} \leq 10\%$, the electron mobility $\Delta \mu_{\text{Hall}} \leq 1\%$, and the resistivity $\Delta \rho_{\text{Hall}} \leq 1\%$. The error of the results of the SE analysis as determined from the deviation of the fit parameters is $\Delta N_{\text{opt}} \leq 7\%$ for the electron concentration, $\Delta \mu_{\text{opt}} \leq 7\%$ for mobility, and $\Delta \rho_{\text{opt}} \leq 10\%$ for resistivity.

Table 2

d_{total}	A_D	N_{opt}	N_{Hall}	Γ_D	μ_{opt}	μ_{Hall}	ρ_{opt}	ρ_{Hall}
nm	eV ²	10 ²⁰ /cm ³	10 ²⁰ /cm ³	eV	cm ² /Vs	cm ² /Vs	10 ⁻⁴ Ωcm	10 ⁻⁴ Ωcm
791	2.383	6.91	6.99	0.1069	27.1	25.55	3.3	3.49
633	2.370	6.88	7.26	0.1099	26.3	25.48	3.4	3.43
528	2.383	6.84	7.22	0.1132	25.6	25.48	3.6	3.39
417	2.370	6.87	7.07	0.1173	24.7	25.47	3.7	3.47
311	2.348	6.81	6.91	0.1207	24.0	16.80	3.8	5.39
208	2.188	6.25	6.46	0.1193	24.3	19.93	4.1	4.85
101	2.135	6.19	5.63	0.1339	21.6	18.09	4.6	6.13

3 Fit parameters of ZnO:Al thin films with varying doping concentration

Best fit parameters are determined by ellipsometric and photometric studies of ZnO:Al thin films on glass substrates deposited from targets with different doping concentration at 150°C substrate temperature. The ZnO:Al bulk layer is modeled using a pole oscillator for high interband transitions, a modified Tanguy model [104] for fundamental absorption using the formula developed by Kim et al. [153], and a modified Drude oscillator developed by Mergel et al. [94] for free-carrier absorption. For the films sputtered from the targets with low doping concentration, phonon absorption in the infrared wavelength range occurs, which is modeled with two Gaussian oscillators.

It becomes obvious that the film thicknesses are different for the three targets although the deposition of the three samples took 620 s for each sample. Another difference is that the interface layer does not improve the fit result of the films sputtered from the targets with 0.2 wt.% and 1.0 wt.% Al₂O₃. Therefore, these samples are modeled without the interface layer. With increasing doping concentration, the Drude parameter A_D , which is related to the free-carrier concentration as well as the optical gap, increase. The parameter κ , which describes the type of broadening, changes with doping concentration. The films sputtered from the target with 0.2 wt.% Al₂O₃ show Lorentzian

Table 3

Parameter	0.2 wt.%	1.0 wt.%	2.0 wt.%
MSE	21.2	24.1	19.1
d_s [nm]	4.97±0.07	6.41±0.09	0.83±0.06
d_b [nm]	867.1±0.4	844.4±0.5	759.2±0.4
d_i [nm]	-	-	9.0±0.1
A_p [eV]	198±3	327±15	112±2
E_p [eV]	11.3±0.1	16.2±0.3	9.4±0.1
A_g [eV ^{3/2}]	17.7±0.2	24.2±0.8	23.1±0.4
R [eV]	0.06 (fixed)	0.06 (fixed)	0.06 (fixed)
E_g [eV]	3.290±0.005	3.48±0.01	3.90±0.02
s	0.45±0.03	0.31±0.05	0.9±0.2
γ [eV]	0.0268±0.0007	0.039±0.002	0.098±0.006
κ	0	0.0011±0.0003	0.023±0.003
A_D [eV ²]	0.4936±0.0007	1.208±0.002	2.3962±0.0007
Γ_{low} [eV]	0.2195±0.0008	0.0976±0.0007	0.1283±0.0003
Γ_{high} [eV]	0.0039±0.0007	0.047±0.001	0.027±0.001
$\Gamma_{\text{changeover}}$ [eV]	0.297±0.003	0.849±0.006	1.358±0.007
Γ_{width} [eV]	0.54±0.02	0.044±0.005	0.302±0.006
$A_{\text{Gaussian1}}$ [eV ²]	130.2 (fixed)	56.1 (fixed)	-
$E_{\text{Gaussian1}}$ [eV]	0.05044 (fixed)	0.05044 (fixed)	-
$B_{\text{Gaussian1}}$ [eV]	0.0035 (fixed)	0.00094 (fixed)	-
$A_{\text{Gaussian2}}$ [eV ²]	26.6 (fixed)	26.6 (fixed)	-
$E_{\text{Gaussian2}}$ [eV]	0.0542 (fixed)	0.0542 (fixed)	-
$B_{\text{Gaussian2}}$ [eV]	0.0139 (fixed)	0.01389 (fixed)	-
dn	0.0151±0.0005	0.0020±0.0006	0.0041±0.0004

broadening, while the other films exhibit an intermediate type of broadening between Lorentzian and Gaussian form. Since the free-carrier concentration even of the lowest doped samples exceeds the Mott critical density, no bound state of the excitons exists, as the screening parameter of the Tanguy model with $s < 1$ demonstrates. The phonon absorption in the infrared wavelength range of the samples sputtered from the targets with 0.2 wt.% and 1.0 wt.% Al₂O₃ is modeled with two Gaussian oscillators. However, since only reflectance data are available in this wavelength range, the fit of the oscillator parameters fails. Therefore, these parameters were fixed. The following figures show an overview of the measured and modeled ellipsometric and photometric data of the three samples.

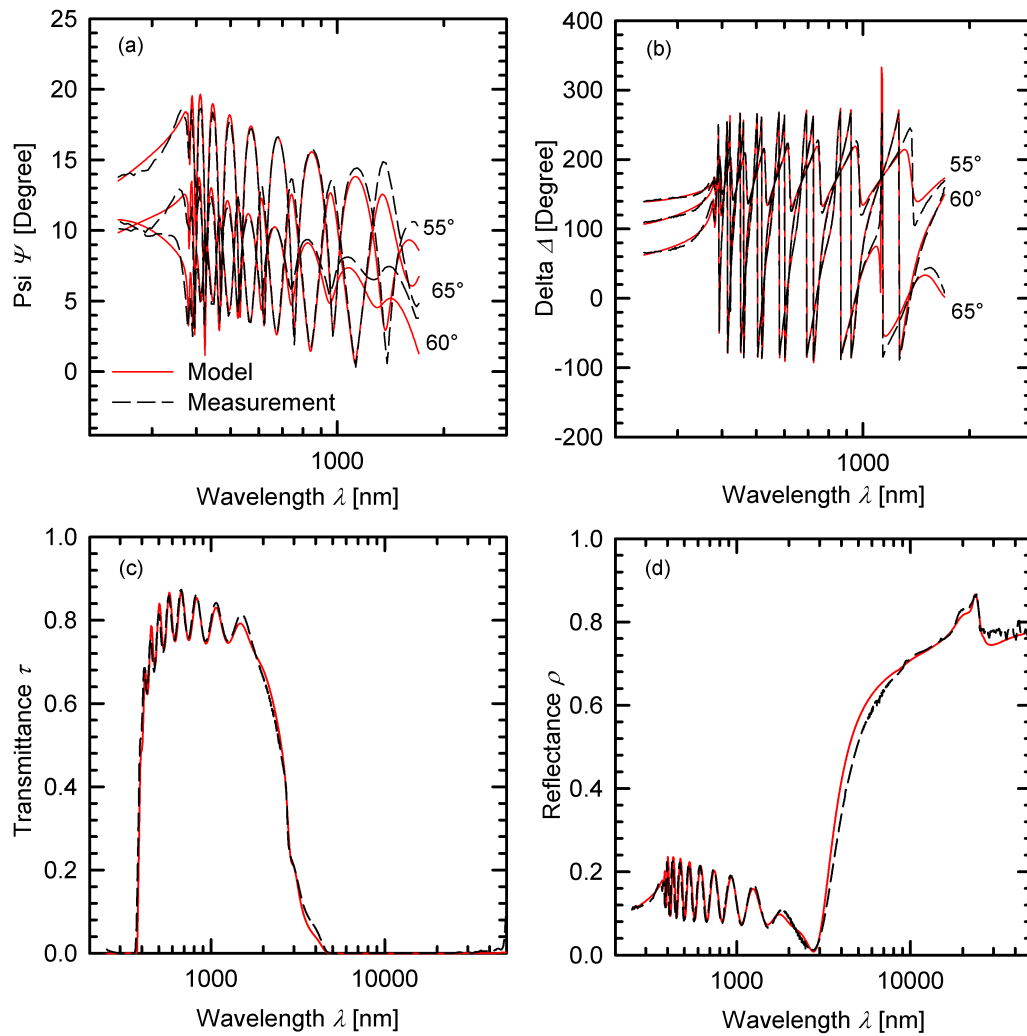


Figure 1: Measured (dashed black lines) and modeled (red solid lines) (a) Psi, (b) Delta, (c) transmittance, and (d) reflectance spectra of a ZnO:Al thin film on glass sputtered from a target with 0.2 wt.% Al_2O_3 at a substrate temperature of 150°C.

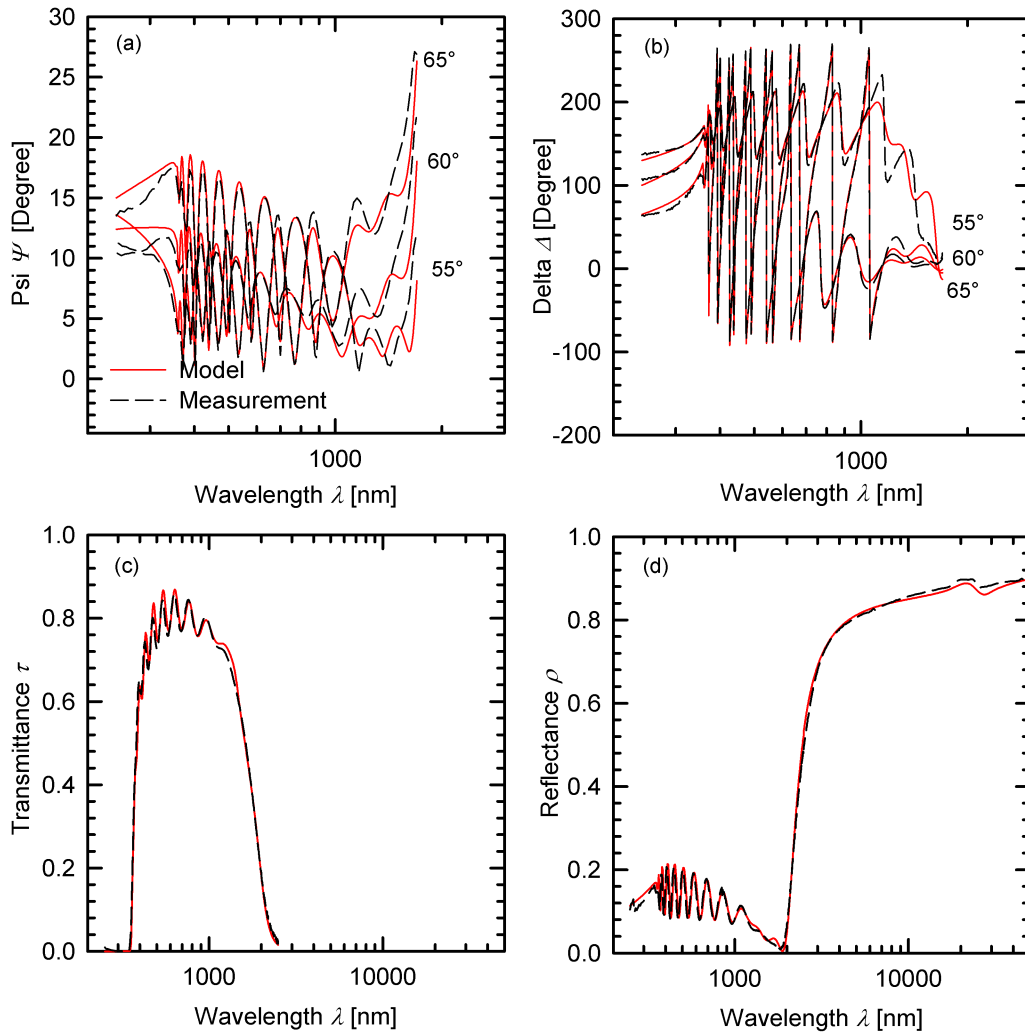


Figure 2: Measured (dashed black lines) and modeled (red solid lines) (a) Psi, (b) Delta, (c) transmittance, and (d) reflectance spectra of a ZnO:Al thin film on glass sputtered from a target with 1.0 wt.% Al_2O_3 at a substrate temperature of 150°C .

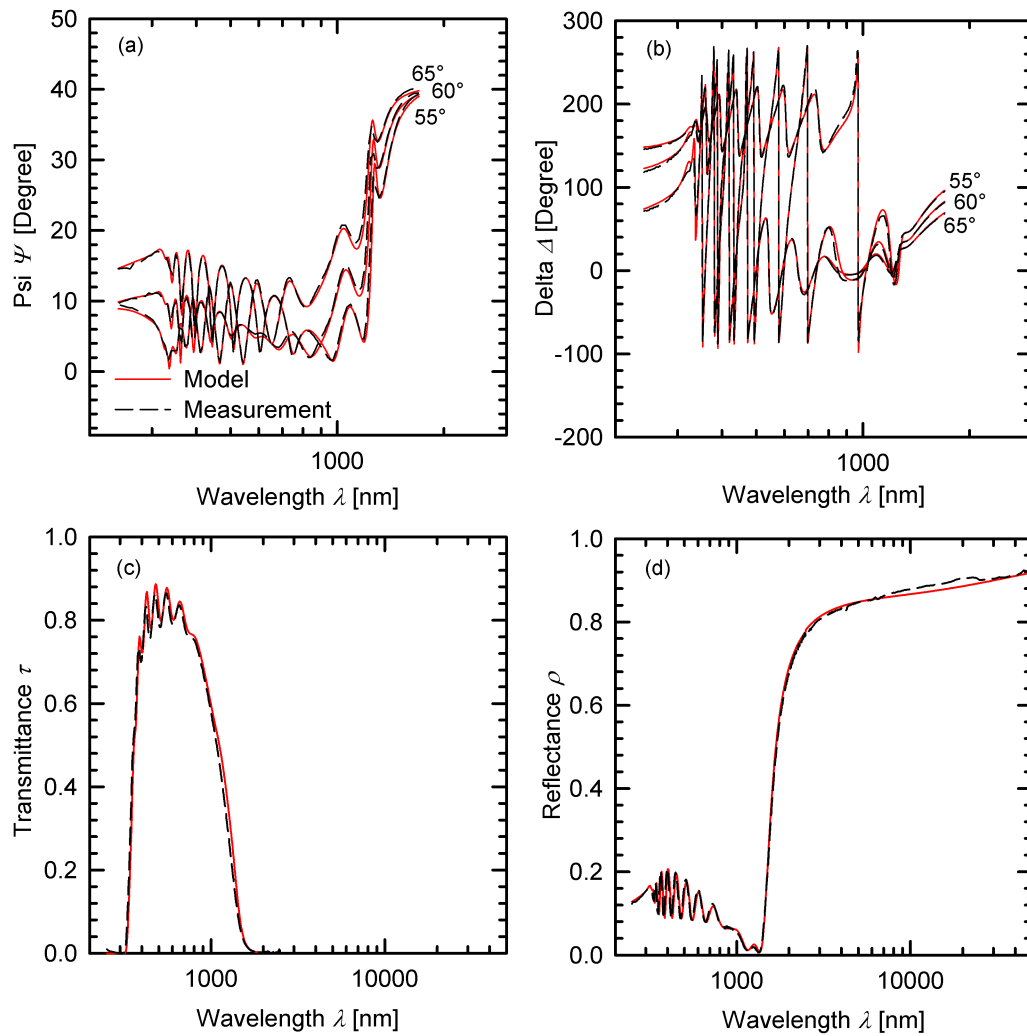


Figure 3: Measured (dashed black lines) and modeled (red solid lines) (a) Psi, (b) Delta, (c) transmittance and (d) reflectance spectra of a ZnO:Al thin film on glass sputtered from a target with 2.0 wt.% Al_2O_3 at a substrate temperature of 150°C.

4 Parameters for collector simulation

The following table contains the model and material parameters used for the calculation of the collector efficiency.

Table 4

Parameter	Value
λ_{Air} [W/mK]	0.03139
λ_{Ar} [W/mK]	0.0209
λ_{ins} [W/mK]	0.04
w_{12} [m]	0.008
w_{23} [m]	0.028
w_{34} [m]	0.005
w_{ins} [m]	0.10
Pr_{Air}	0.71
Pr_{Ar}	0.67
g [m/s ²]	9.812642
β_{Air} [1/K]	$3.67 \cdot 10^{-3}$
β_{Ar} [1/K]	$3.68 \cdot 10^{-3}$
$\nu_{\text{Air}} = \mu_v / \rho_g$ [m ² /s]	$2.351 \cdot 10^{-5}$
$\nu_{\text{Ar}} = \mu_v / \rho_g$ [m ² /s]	$2.069 \cdot 10^{-5}$
θ [°]	45
f_c	1.2
v [m/s]	3
σ [W/m ² K ⁴]	5.670400
ϵ_{abs}	0.06
ϵ_{ins}	0.85
h_{amb} [W/m ² K]	15
h_{int} [W/m ² K]	50

The following figure shows the measured transmittance and reflectance spectra used for the first glass pane and the absorber in the collector model. The AR glass HiT (from Centrosolar) is used as the first glass pane and the aluminum absorber eta plus (from Bluetec) is used as the absorber.

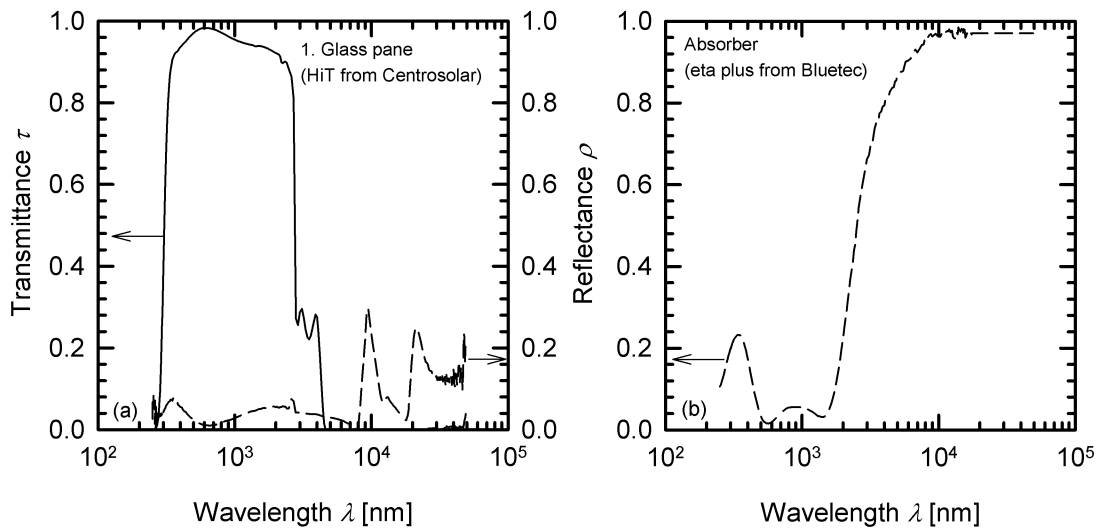


Figure 4: Measured transmittance (solid black line) and reflectance spectra (dashed black lines) used for the first glass pane (a) and the absorber (b).

Acronyms and symbols

List of acronyms

Acronym	Meaning
AC	Alternating current
AFM	Atomic force microscopy
Al ₂ O ₃	Aluminum oxide
AM	Air mass
AR	Antireflective
BEMA	Bruggeman effective medium approximation
BGN	Band-gap narrowing
BM	Burstein-Moss shift
BMU	German Federal Ministry for the Environment, Nature Conservation and Nuclear Safety
DC	Direct current
FOM	Figure of merit
FTIR	Fourier transform infrared
FTO, SnO ₂ :F	Fluorine doped tin oxide
FWHM	Full width at half maximum
HGlas	Project name for “Principles for selectively coated high-efficiency glazing to be applied in flat-plate collectors”
(HR)TEM	(High resolution) Transmission electron microscopy
TCO	Transparent conducting oxide
ISFH	Institute for Solar Energy Research Hamelin
ITO, In ₂ O ₃ :Sn	Tin doped indium oxide
KGlass TM	Commercial low-emissivity glass from Pilkington
Low-e	Low emissivity
MDF	Model dielectric function
MF	Mid-frequency
MgF ₂	Magnesium fluoride
MSE	Mean-squared error
N ₂	Nitrogen
O ₂	Oxygen
PEM	Plasma-emission monitoring
RBM	Radiation-balance method
RF	Radio frequency
SE	Spectroscopic ellipsometry
SEM	Scanning electron microscopy
SIMS	Secondary-ion-mass spectroscopy
SiO ₂	Silicon dioxide
SiO _x N _y	Silicon oxynitride
Si ₃ N ₄	Silicon nitride

Continued list of acronyms

Acronym	Meaning
SNMS	Secondary-neutral-mass spectroscopy
VTC	Vacuum tube collector
XRD	X-ray diffraction
ZnO:Al	Aluminum doped zinc oxide

List of symbols

Symbol	Meaning
a_B	Bohr radius
A_D	Strength of Drude oscillator
A_g	Strength of Tanguy oscillator
A_p	Strength of pole oscillator
A_r	Proportionality factor of Hall measurements
b_i ($i = 0, 1, 2, 3$)	Coefficients of regression analysis of collector efficiency
\vec{B}, B_0	Magnetic field vector and amplitude
B_m	Magnetic field intensity
c	Velocity of light
c_p	Specific heat
C	Non-parabolicity factor of Pisarkiewicz model
C_{Al}	Aluminum concentration
d	Film thickness
D	Electric displacement
D_m	Matrix for calculation of the propagation of light through a coating system
e	Elementary electric charge
E	Photon energy
\vec{E}, E_0	Electric field vector and amplitude
E_g	Band-gap energy
E_{g0}	Band-gap energy of undoped semiconductor
E_p	Pole position
$f_{a,b}$	Volume fraction of component a and b in the Bruggeman effective medium approximation
f_c	Amplification factor for the Hollands equation
g	Grain size determined by the Scherrer equation
g	Gravitational acceleration
G	Global irradiance
G_r	Grashoff number

Continued list of symbols

Symbol	Meaning
h_{amb}	Heat transfer coefficient for heat transfer to the ambient
h_{fluid}	Heat transfer coefficient for heat transfer to the fluid
i	Imaginary unit
I	Electric current
\vec{k}, k	Wave vector
k	Extinction coefficient
k_1, k_2	Heat loss coefficients of collector efficiency formula
k_F	Fermi wave vector
k_{TF}	Thomas-Fermi screening wave vector
l	Length of a conductor
l	Mean-free path of free carriers
m	Number of the layer of a coating system
m_0	Free-electron mass
m_0^*	Effective mass of free carriers at the bottom of the conduction band
m_e^*	Effective mass of free carriers in the conduction band
m_h^*	Effective mass of holes in the valence band
M_{ji}	Matrix for calculating the radiative interchange in the collector system
M_{ij}^{-1}	Inverse matrix for calculating the radiative interchange in the collector system
n	Refractive index
n_i	Refractive index of layer i in a layer system
N	Complex refractive index
N_{crit}	Mott's critical free-carrier density
N_e	Free-carrier density
N_{Hall}	Free-carrier concentration determined by Hall measurements
N_{SE}	Free-carrier concentration determined by spectroscopic ellipsometry
Nu	Nusselt number
Nu_{90°	Nusselt number for vertical collector inclination
p_s	Sputtering pressure
P	Dielectric polarization
P	Principal value of Kramer-Kronig relation
P_C	Performance value of collector
P_{DC}	Sputtering power

Continued list of symbols

Symbol	Meaning
P_m	Matrix for calculation of the propagation of light through a coating system
P_r	Prandtl number
\dot{q}	Heat flux density
$\dot{q}_{i,b}^r$	Spectral radiative heat flux density from rear surfaces
$\dot{q}_{i,f}^r$	Spectral radiative heat flux density from front surfaces
\dot{Q}_{amb}	Heat flux density from insulation material to the ambient
\dot{Q}_{fluid}	Heat flux density from the absorber to the fluid
\dot{Q}_i^r	Integral radiative heat flux density
\dot{Q}_{ij}^c	Convective heat flux density from surface i to j
\dot{Q}_{ij}^{cond}	Conductive heat flux density from surface i to j
\dot{Q}_{ins}^{cond}	Conductive heat flux density through the insulation material
\dot{Q}_{rear}^{cond}	Conductive heat flux density from the absorber to the insulation material
\dot{Q}_{rear}^r	Radiative heat flux density from the absorber to the insulation material
\vec{r}	position vector
r_p	Amplitude reflection coefficient for parallel polarization
r_s	Amplitude reflection coefficient for perpendicular polarization
R	Rydberg energy of unscreened exciton
R_a	Rayleigh number
R_H	Hall coefficient
R_{sheet}	Sheet resistance
s	Screening parameter of Tanguy model
$s_{i,b}, s_{i,f}$	Spectral emitted radiant energy density
$S_{IR,sky}$	Spectral infrared sky radiation
$S_{P,T}$	Planck's blackbody radiation
S_{sol}	Spectral solar irradiance
T_{amb}	Ambient temperature
T_{an}	Annealing temperature
T_{fluid}	Fluid temperature
T_i	Temperature of component i
T_{ij}	Transfer matrix for calculating the light propagation through a coating system
T_s	Substrate temperature
T_{surf}	Surface Temperature

Continued list of symbols

Symbol	Meaning
U	Voltage
v	Velocity of light in a medium
v	Wind speed
v_{Fermi}	Velocity of free carriers at the Fermi level
w	Width of a conductor
w	Width of the glazing gap
x	Depth during SNMS analysis
α	Absorptance
α_{sol}	Solar absorptance
β	Thermal expansion coefficient
γ	Broadening parameter of Tanguy model
Γ_D	Broadening parameter of Drude model
$\Gamma_{\text{low}}, \Gamma_{\text{high}}, \Gamma_{\text{changeover}}, \Gamma_{\text{width}}$	Parameters of modified Drude model
δ_m	Phase thickness
∂	Partial derivative
Δ	Ellipsometric magnitude
ΔE_{BM}	Burstein-Moss shift
ΔE_c^{ee}	Band-gap shift due to electron-electron interaction
ΔE_c^{ei}	Band-gap shift due to electron-ion interaction
$\Delta_f H_{\text{solid}}^\circ$	Standard enthalpy of formation
∇	Nabla operator
ϵ	Dielectric constant or function
ϵ	Emissivity
ϵ_{IR}	Infrared emissivity
ϵ_0	Permittivity of vacuum
ϵ_1, ϵ_2	Real and imaginary part of dielectric function
ϵ_∞	High-frequency dielectric constant
$\epsilon_{\text{band gap}}$	Dielectric function for band-gap transitions
$\epsilon_{a,b}$	Dielectric functions of the components a and b of a Bruggeman effective medium
$\epsilon_{\text{free carrier}}$	Dielectric function for free-carrier absorption
$\epsilon_{\text{high interband}}$	Dielectric function for high interband transitions
ϵ_s	Static dielectric constant
η_0	Conversion coefficient
η_{carnot}	Carnot efficiency
η_{col}	Collector efficiency

Continued list of symbols

Symbol	Meaning
θ	Angle of incidence
θ	Inclination angle of the collector
θ_{BR}	Angle, at which Bragg reflexes occurs
κ	Factor for modifying broadening of Tanguy model
λ	Wavelength of light
λ_c	Thermal conductivity
μ_e	Free-carrier mobility
μ_{Hall}	Free-carrier mobility determined by Hall measurements
$\rho_{i,f}$	Reflectance of front surfaces
μ_v	Dynamic viscosity
ρ	Reflectance
ρ_g	Gas density
ρ_e	Resistivity
$\rho_{i,b}$	Reflectance of rear surfaces
ρ_{ellips}	Ellipsometric magnitude
ρ_{sol}	Solar reflectance
σ	Conductivity
σ	Stefan-Boltzmann constant
τ	Transmittance
τ_e	Scattering time
τ_{sol}	Solar transmittance
ϕ_i	Angle of refraction in film i
χ	Dielectric susceptibility
ψ	Digamma function
Ψ	Ellipsometric magnitude
ω_D	Drude frequency
ω_{LO}	Resonance frequency of longitudinal optical phonons
ω_p	Plasma frequency
ω_{TO}	Resonance frequency of transversal optical phonons
\hbar	Reduced Planck's constant

Bibliography

- [1] G. Stryi-Hipp, H. Drück, V. Wittwer, W. Zörner, E. Bollin, B. Hafner, H.-M. Henning, U. Jordan, R. Köbbemann-Rengers, M. Köhl, K. Lambrecht, D. Mangold, C. Stadler, and K. Vajen. Forschungsstrategie Niedertemperatur-Solarthermie 2030 für eine nachhaltige Wärme- und Kälteversorgung Deutschlands. Technical report, Deutsche Solarthermie-Technologie Plattform (DSTTP), Berlin, 2010.
- [2] C.E. Kennedy. Review of Mid- to High-Temperature Solar Selective Absorber Materials. Technical report, National Renewable Energy Laboratory, Golden in Colorado, July 2002. NREL TP-520-31267.
- [3] A. Schäfer. Leistungsmessung eines Sonnenkollektors nach EN 12975-2:2006, Kollektorbezeichnung: Logasol SKS 4.0. Technical report, Fraunhofer-Institut für Solare Energiesysteme (ISE), Freiburg, November 2006. Prüfbericht: KTB Nr. 2006-30.
- [4] *Schüco Innovations 2010*. www.schueco.com, 2010. [accessed on 28 March 2011].
- [5] *Datenblatt für den Kollektor OekoTech HT*. www.oekotech.biz. [accessed on 28 March 2011].
- [6] Th. Beikircher. Hocheffizienter Flachkollektor mit Foliendämmung und Überhitzungsschutz für Betriebstemperaturen von 70-100°C. Technical report, Bavarian Center for Applied Energy Research (ZAE), Garching, April 2010. Project No. 0329280A.
- [7] *PtJ Forschungsjahrbuch 2009: Entwicklung eines Vakuum-Flachkollektors (Vacuplan)*. <http://www.forschungsjahrbuch.de>. [accessed on 28 March 2011].
- [8] W. Eisenmann, S. Jack, C. Lampe, F. Giovannetti, and R. Brendel. High-Efficiency Flat-Plate Solar Collectors Based on Selective Glazing. In *Proceedings of the 3rd European Solar Thermal Energy Conference (estec)*, pages 236–242, Freiburg, June 2007.
- [9] T. Hoffmann, M. Kursawe, A. Gombert, and W. Glaubitt. Entwicklung eines Verfahrens zur energieeffizienten Produktion von hochtransmissiven Gläsern für solare Anwendungen (HiT). Technical report, Centrosolar Glas GmbH & Co. KG, Fürth, April 2010. Project No. 0329800C.

-
- [10] H.J. Gläser. *Dünnschichttechnologie auf Flachglas*. Verlag Karl Hofmann, Schorn-dorf, 1999.
- [11] H.L. Hartnagel, A.L. Dawar, A.K. Jain, and C. Jagadish. *Semiconducting trans-parent thin films*. IOP Publishing, Bristol, 1995.
- [12] D. Song, P. Widenborg, W. Chin, and A.G. Aberle. Investigation of lateral parameter variations of Al-doped zinc oxide films prepared on glass substrates by RF magnetron sputtering. *Sol. Energy Mater. Sol Cells*, 73:1, 2002.
- [13] R.G. Gordon. Criteria for Choosing Transparent Conductors. *MRS Bulletin*, 25:52, 2000.
- [14] *Wärmedämmgläser - Technische Informationen*. www.pilkington.com. [accessed on 22 April 2008].
- [15] K. Ellmer, F. Kudella, R. Mientus, R. Schieck, and S. Fiechter. Influence of discharge parameters on the layer properties of reactive magnetron sputtered ZnO:Al films. *Thin Solid Films*, 247:15, 1994.
- [16] V. Sittinger, F. Ruske, W. Werner, C. Jacobs, B. Szyszka, and D.J. Christie. High power pulsed magnetron sputtering of transparent conducting oxides. *Thin Solid Films*, 516:5847, 2008.
- [17] E. Fortunato, D. Ginley, H. Hosono, and D.C. Paine. Transparent conducting oxides for photovoltaics. *MRS Bulletin*, 32:242, 2007.
- [18] J. Hüpkes, B. Rech, S. Calnan, O. Kluth, Z. Zastrow, H. Siekmann, and M. Wut-tig. Material study on reactively sputtered zinc oxide for thin film silicon solar cells. In *Proceedings of the 5th International Conference on Coatings on Glass and Plastics*, page 1, Saarbrücken, 2004.
- [19] O. Kluth, G. Schöpe, J. Hüpkes, C. Agashe, J. Müller, and B. Rech. Modified Thornton model for magnetron sputtered zinc oxide: film structure and etching behaviour. *Thin Solid Films*, 442:80, 2003. Figure 2.12 reprinted with permission from Elsevier.
- [20] K. Ellmer, A. Klein, and B. Rech, editors. *Transparent Conductive Zinc Oxide*, volume 104 of *Springer Series in Materials Science*. Springer, Berlin, 2008.
- [21] D.S. Ginley, H. Hosono, and D.C. Paine, editors. *Handbook of Transparent Con-ductors*. Springer, New York NY, 2010.
- [22] B. Szyszka. Transparent and conductive aluminum doped zinc oxide films prepared by mid-frequency reactive magnetron sputtering. *Thin Solid Films*, 351:164, 1999.

- [23] M. Rommel, C. Wittwer, and A. Gombert. Kollektorertragsverbesserungen durch die Antireflex-Beschichtung der Verglasung und der Einfluss ihrer Oberflächenstruktur. In *12. Symposium Thermische Solarenergie*, Bad Staffelstein, April 2002.
- [24] T. Minami, H. Sato, H. Imamoto, and S. Takata. Substrate temperature dependence of transparent conducting Al-doped ZnO thin films prepared by magnetron sputtering. *Jpn. J. Appl. Phys.*, 31:L257, 1992.
- [25] D. Herrmann, M. Oertel, R. Menner, and M. Powalla. Analysis of relevant plasma parameters for ZnO:Al film deposition based on data from reactive and non-reactive DC magnetron sputtering. *Surf. Coat. Technol.*, 174-175:229, 2003.
- [26] C. Goebbert, G. Gasparro, T. Schuler, T. Krajewski, and M.A. Aegerter. Influence of the layer morphology on the electrical properties of sol gel transparent conducting oxide coatings. *J. Sol Gel Sci. Technol.*, 19:435, 2000.
- [27] A.F. Aktaruzzaman, G.L. Sharma, and L.K. Malhotra. Electrical, optical and annealing characteristics of ZnO:Al films prepared by spray pyrolysis. *Thin Solid Films*, 198:67, 1991.
- [28] J. Hu and R.G. Gordon. Textured aluminum-doped zinc oxide thin films from atmospheric pressure chemical-vapor deposition. *J. Appl. Phys.*, 71:880, 1992.
- [29] S. Hayamizu, H. Tabata, H. Tanaka, and T. Kawai. Preparation of crystallized zinc oxide films on amorphous glass substrates by pulsed laser deposition. *J. Appl. Phys.*, 80:787, 2006.
- [30] Z. Qiao, C. Agashe, and D. Mergel. Dielectric modeling of transmittance spectra of thin ZnO:Al films. *Thin Solid Films*, 496:520, 2006.
- [31] H. Yoshikawa and S. Adachi. Optical constants of ZnO. *Jpn. J. Appl. Phys.*, 36:6237, 1997.
- [32] G.E. Jellison Jr. and L.A. Boatner. Optical functions of uniaxial ZnO determined by generalized ellipsometry. *Phys. Rev. B*, 58:3586, 1998.
- [33] A.B. Djurišić, Y. Chan, and E.H. Li. The optical dielectric function of ZnO. *Appl. Phys. A*, 76:37, 2003.
- [34] K. Postava, H. Sueki, M. Aoyama, T. Yamaguchi, K. Murakami, and Y. Igasaki. Doping effects on optical properties of epitaxial ZnO layers determined by spectroscopic ellipsometry. *Appl. Surf. Sci.*, 175-176:543, 2001.
- [35] H. Fujiwara and M. Kondo. Effects of carrier concentration on the dielectric function of ZnO:Ga and In₂O₃:Sn studied by spectroscopic ellipsometry: Analysis of free-carrier and band-edge absorption. *Phys. Rev. B*, 71:075109, 2005.

- [36] A. Pflug, V. Sittinger, F. Ruske, B. Szyszka, and G. Dittmar. Optical characterization of aluminum-doped zinc oxide films by advanced dispersion theories. *Thin Solid Films*, 455-456:201, 2004.
- [37] J.A. Duffie and W.A. Beckman. *Solar engineering of thermal processes*. John Wiley & Sons, New Jersey, 3rd edition, 2006.
- [38] M. Khoukhi, S. Maruyama, S. Sakai, and M. Behnia. Combined non-gray radiative and conductive heat transfer in solar collector glass cover. *Solar Energy*, 75:285, 2003.
- [39] E. Hecht. *Optik*. Oldenbourg Wissenschaftsverlag, München, 4th edition, 2005.
- [40] ISO 9050. Glass in building - Determination of light transmittance, solar direct transmittance, total solar energy transmittance, ultraviolet transmittance and related glazing factors. International Standard, August 2003. ISO 9050-2003(E).
- [41] DIN EN 410. Glas im Bauwesen - Bestimmung der lichttechnischen und strahlungsphysikalischen Kenngrößen von Verglasungen. Deutsche Norm, December 1998. DIN EN 410:1998-12.
- [42] R. Siegel, J.R. Howell, and J. Lohrengel. *Wärmeübertragung durch Strahlung*, volume 1. Springer-Verlag, Berlin, 1988.
- [43] A. Goetzenberger and V. Wittwer. *Sonnenenergie Thermische Nutzung*. B.G. Teubner, Stuttgart, 1999.
- [44] CEN: EN 12975-2. Thermische Solaranlagen und ihre Bauteile, Kollektoren - Teil 2 Prüfverfahren. Deutsche Norm, December 2002. CEN: EN 12975-2:2001.
- [45] R. Siegel, J.R. Howell, and J. Lohrengel. *Wärmeübertragung durch Strahlung*, volume 2. Springer-Verlag, Berlin, 1991.
- [46] S. Föste, N. Ehrmann, F. Giovannetti, G. Rockendorf, and R. Reineke-Koch. Grundlagen für selektiv beschichtete Hochleistungsverglasungen für Flachkollektoren. Technical report, Institute for Solar Energy Research Hamelin (ISFH), Hamelin, 2011. BMU contract no. 0329280D.
- [47] E.D. Palik, editor. *Handbook of Optical Constants of Solids*, volume 209. Academic Press, Inc., Orlando, 1985.
- [48] M. Meier. *Mikrostrukturierte Metallschichten auf Glas*. PhD thesis, Julius-Maximilians-Universität Würzburg, 2006.
- [49] Lawrence Berkeley National Laboratory: *International glazing database 2010*. <http://windows.lbl.gov/materials/IGDB/>. [accessed on 25 March 2011].

- [50] S. Jäger, B. Szyszka, J. Szczyrbowski, and G. Bräuer. Comparison of transparent conductive oxide thin films prepared by a.c. and d.c. reactive magnetron sputtering. *Surf. Coat. Technol.*, 98:1304, 1998.
- [51] I. Hamberg and C.G. Granqvist. Evaporated Sn-doped In_2O_3 films: Basic optical properties and applications to energy-efficient windows. *J. Appl. Phys.*, 60:R123, 1986.
- [52] C. Agashe, O. Kluth, G. Schöpe, H. Siekmann, J. Hüpkes, and B. Rech. Optimization of the electrical properties of magnetron sputtered aluminum-doped zinc oxide films for opto-electronic applications. *Thin Solid Films*, 442:167, 2003.
- [53] Y. Li, G.S. Tompa, S. Liang, C. Gorla, Y. Lu, and J. Doyle. Transparent and conductive Ga-doped ZnO films grown by low pressure metal organic chemical vapor deposition. *J. Vac. Sci. Technol. A*, 15:1063, 1997.
- [54] B. Rech and H. Wagner. Potential of amorphous silicon for solar cells. *Appl. Phys. A Mater. Sci. Process*, 69:155, 1999.
- [55] U. Rau, D. Braunger, and H.J. Schock. Air-Annealing Effects on Polycrystalline $\text{Cu}(\text{In,Ga})\text{Se}_2$ Heterojunctions. *Solid State Phenom.*, 67-68:409, 1999.
- [56] À. Németh, C.S. Major, M. Fried, Z. Lábadi, and I. Bársony. Spectroscopic ellipsometry study of transparent conductive ZnO layers for CIGS solar cell applications. *Thin Solid Films*, 516:7016, 2008.
- [57] S. Calnan and A.N. Tiwari. High mobility transparent conducting oxides for thin film solar cells. *Thin Solid Films*, 518:1839, 2010.
- [58] C. Agashe, O. Kluth, J. Hüpkes, U. Zastrow, and B. Rech. Efforts to improve carrier mobility in radio frequency sputtered aluminum doped zinc oxide films. *J. Appl. Phys.*, 95:1911, 2004.
- [59] I. Sieber, N. Wanderka, I. Urban, I. Dörfel, E. Schiehorn, F. Fenske, and W. Fuhs. Electron microscopic characterization of reactively sputtered ZnO films with different Al-doping levels. *Thin Solid Films*, 330:108, 1998.
- [60] Y. Yoshino, K. Inoue, M. Takeuchi, and K. Ohwada. Effects of interface micro structure in crystallization of ZnO thin films prepared by radio frequency sputtering. *Vacuum*, 51:601, 1998.
- [61] C. Li, M. Furuta, T. Matsuda, T. Hiramatsu, H. Furuta, and T. Hirao. Effects of substrate on the structural, electrical and optical properties of Al-doped ZnO films prepared by radio frequency magnetron sputtering. *Thin Solid Films*, 517:3265, 2009.

- [62] K. Ellmer. Resistivity of polycrystalline zinc oxide films: current status and physical limit. *J. Phys. D: Appl. Phys.*, 34:3097, 2001.
- [63] X.L. Guo, H. Tabata, and T. Kawai. p-type conduction in transparent semiconductor ZnO thin films induced by electron cyclotron resonance N₂O plasma. *Optical Materials*, 19:229, 2002.
- [64] K. Minegishi, Y. Koiwai, Y. Kikuchi, K. Yano, M. Kasuga, and A. Shimizu. Growth of p-type Zinc Oxide films by chemical vapor deposition. *Jpn. J. Appl. Phys.*, 36:L1453, 1997.
- [65] N. Nickel, editor. *Influence on Hydrogen Concentration on H Bonding in Zinc Oxide*. Zinc oxide - A material for Micro- and Optoelectronic Applications. Springer, Berlin, 2005.
- [66] T. Minami, H. Nanto, and S. Takata. Highly Conductive and Transparent Aluminum Doped Zinc Oxide Thin Films Prepared by RF Magnetron Sputtering. *Jpn. J. Appl. Phys.*, 23:L280, 1984.
- [67] T. Minami, H. Nanto, S. Shooji, and S. Takata. The stability of zinc oxide transparent electrodes fabricated by rf magnetron sputtering. *Thin Solid Films*, 111:167, 1984.
- [68] M. Bouderbala, S. Hamzaoui, M. Adnane, T. Sahraoui, and M. Zerdali. Annealing effect on properties of transparent conducting ZnO thin films. *Thin Solid Films*, 517:1572, 2009.
- [69] S.H. Lee, T.S. Lee, K.S. Lee, B. Cheong, Y.D. Kim, and W.M. Kim. Characteristics of hydrogen co-doped ZnO:Al thin films. *J. Phys. D: Appl. Phys.*, 41:095303, 2008.
- [70] K.C. Park, D.Y. Ma, and K.H. Kim. The physical properties of Al-doped zinc oxide films prepared by RF magnetron sputtering. *Thin Solid Films*, 305:201, 1997.
- [71] T. Minami, H. Nanto, and S. Takata. Group III Impurity Doped Zinc Oxide Thin Films Prepared by RF Magnetron Sputtering. *Jpn. J. Appl. Phys.*, 24:L781, 1985.
- [72] H. Sato, T. Minami, Y. Tamura, S. Takata, T. Mouri, and N. Ogawa. The stability of zinc oxide transparent electrodes fabricated by rf magnetron sputtering. *Thin Solid Films*, 246:86, 1994.
- [73] S. Brehme, F. Fenske, W. Fuhs, E. Neubauer, M. Poschenrieder, B. Selle, and I. Sieber. Free-carrier plasma resonance effects and electron transport in reactively sputtered degenerate ZnO:Al films. *Thin Solid Films*, 342:167, 1999.

- [74] R. Blachnik, editor. *D'Ans Lax: Taschenbuch für Chemiker und Physiker*, volume 3 of *Elemente, anorganische Verbindungen und Materialien, Minerale*. Springer, Berlin, 1998.
- [75] J.F. Chang, W.C. Lin, and M.H. Hon. Effects of post-annealing on the structure and properties of Al-doped zinc oxide films. *Appl. Surf. Sci.*, 183:18, 2001.
- [76] G.J. Fang, D. Li, and B.-L. Yao. Influence of post-deposition annealing on the properties of transparent conductive monocrystalline ZAO thin films prepared by RF magnetron sputtering with highly conductive ceramic target. *Thin Solid Films*, 418:156, 2002.
- [77] B.E. Sernelius, K.-F. Berggren, Z.-C. Jin, I. Hamberg, and C.G. Granqvist. Band-gap tailoring of ZnO by means of heavy Al doping. *Phys. Rev. B*, 37:10244, 1988.
- [78] J.G. Lu, S. Fujita, T. Kawaharamura, H. Nishinaka, Y. Kamada, T. Ohshima, Z.Z. Ye, Y.J. Zeng, Y.Z. Zhang, L.P. Zhu, H.P. He, and B.H. Zhao. Carrier concentration dependence of band gap shift in n-type ZnO:Al films. *J. Appl. Phys.*, 101:083705, 2007.
- [79] N.F. Mott. *Metal-Insulator Transitions*. Taylor & Francis Ltd, 1974.
- [80] A. Goldmann and E.-E. Koch, editors. *Landolt-Börnstein*, volume 23a of *Group III Condensed Matter*, page 74. Springer, Berlin, 1989.
- [81] S.J. Pearton, D.P. Norton, K. Ip, Y.W. Heo, and T. Steiner. Recent advances in processing of ZnO. *J. Vac. Sci. Technol. B*, 22:932, 2004.
- [82] F. Ruske, A. Pflug, V. Sittinger, B. Szyszka, D. Greiner, and B. Rech. Optical modeling of free electron behavior in highly doped ZnO films. *Thin Solid Films*, 518:1289, 2009.
- [83] E. Burstein. Anomalous Optical Absorption Limit in InSb. *Phys. Rev.*, 93:632, 1954.
- [84] T.S. Moss. The Interpretation of the Properties of Indium Antimonide. *Proc. Phys. Soc. London. Section B*, 67:775, 1954.
- [85] K. Kopitzki, editor. *Einführung in die Festkörperphysik*. Teubner Studienbücher Physik, Stuttgart, 3rd edition, 1993.
- [86] T.J. Coutts, D.L. Young, and X. Li. Characterization of Transparent Conducting Oxides. *MRS Bulletin*, 25:58, 2000.
- [87] T. Pisarkiewicz, K. Zakrzewska, and E. Leja. Scattering of charge carriers in transparent and conducting thin oxide films with a non-parabolic conduction band. *Thin Solid Films*, 174:217, 1989.

- [88] J.D. Ye, S.L. Gu, S.M. Zhu, S.M. Liu, Y.D. Zheng, R. Zhang, and Y. Shi. Fermi-level band filling and band-gap renormalization in Ga-doped ZnO. *Appl. Phys. Lett.*, 86:192111, 2005.
- [89] K.-F. Berggren and B.E. Sernelius. Band-gap narrowing in heavily doped many-valley semiconductors. *Phys. Rev. B*, 24:1971, 1981.
- [90] J.C. Inkson. Band-gap narrowing in heavily doped many-valley semiconductors. *J. Phys. C: Sol. State Phys.*, 9:1177, 1976.
- [91] P. Drude. Zur Elektronentheorie der Metalle. *Annalen der Physik*, 1:566, 1900.
- [92] E. Gerlach. Carrier scattering and transport in semiconductors treated by the energy-loss method. *J. Phys. C: Sol. State Phys.*, 19:4585, 1986.
- [93] I. Hamberg and C.G. Granqvist. Optical properties of transparent and heat-reflecting indium tin oxide films: Refinement of a model for ionized impurity scattering. *J. Appl. Phys.*, 56:2950, 1986.
- [94] D. Mergel and Z. Qiao. Dielectric modelling of optical spectra of thin $\text{In}_2\text{O}_3:\text{Sn}$ films. *J. Phys. D: Appl. Phys.*, 35:794, 2002.
- [95] H. Brooks. Theory of the Electrical Properties of Germanium and Silicon. *Adv. Electron. Electron Phys.*, 7:85, 1955.
- [96] H. Brooks. Scattering by Ionized Impurities in Semiconductors. *Phys. Rev.*, 83:879, 1951.
- [97] R.B. Dingle. Scattering of electrons and holes by charged donors and acceptors in semiconductors. *Phil. Mag.*, 46:831, 1955.
- [98] T. Minami. New N-Type Transparent Conducting Oxides. *MRS Bulletin*, 25:38, 2000.
- [99] V.A. Johnson and K. Lark-Horovitz. Transition from Classical to Quantum Statistics in Germanium Semiconductors at Low Temperature. *Phys. Rev.*, 71:374, 1947.
- [100] K. Ellmer and R. Mientus. Carrier transport in polycrystalline transparent conductive oxides: A comparative study of zinc oxide and indium oxide. *Thin Solid Films*, 516:4620, 2008.
- [101] K. Ellmer and R. Mientus. Carrier transport in polycrystalline ITO and ZnO:Al II: The influence of grain barriers and boundaries. *Thin Solid Films*, 516:5829, 2008.
- [102] J.Y.W. Seto. The electrical properties of polycrystalline silicon films. *J. Appl. Phys.*, 46:5247, 1975.

- [103] J.F. Muth, R.M. Colbas, A.K. Sharma, S. Oktyabarsky, and J. Narayam. Excitonic structure and absorption coefficient measurements of ZnO single crystal epitaxial films deposited by pulsed laser deposition. *J. Appl. Phys.*, 85:7884, 1999.
- [104] C. Tanguy. Analytical expression of the complex dielectric function for the Hulthén potential. *Phys. Rev. B*, 60:10660, 1999.
- [105] Ch. Kittel. *Einführung in die Festkörperphysik*, volume 11. R. Oldenbourg Verlag, München, 1996.
- [106] H. Fujiwara. *Spectroscopic Ellipsometry*. John Wiley & Sons, Chichester, 2007.
- [107] J.R. Bellingham, W.A. Phillips, and C.J. Adkins. Intrinsic performance limits in transparent conducting oxides. *J. Mat. Sci. Lett.*, 11:263, 1992.
- [108] O. Stenzel. *Das Dünnschichtspektrum*. Wiley-VCH Verlag, Berlin, 1996.
- [109] A. Thelen. *McGraw-Hill optical and electro-optical Engineering Series*. Design of optical interference coatings. Mc Graw-Hill, New York, 1989.
- [110] M. Rubin. Solar optical properties of windows. *Energy Research*, 6:123, 1982.
- [111] B. Harbecke. Coherent and Incoherent Reflection and Transmission of Multilayer Structures. *Appl. Phys. B*, 39:165, 1986.
- [112] C.C. Katsidis and D.I. Siapkas. General transfer-matrix method for optical multilayer systems with coherent, partially coherent, and incoherent interference. *Appl. Optics*, 41:3978, 2002.
- [113] N. Kaiser. Alte Faustregeln für das Design optischer Schichtsysteme. *Vakuum in Forschung und Praxis*, 19:17, 2007.
- [114] H. Frey and G. Kienel. *Dünnschichttechnologie*. VDI Verlag, Düsseldorf, 1987.
- [115] S. Jaeger and H.G. Schueller. Wärmedämmende Anti-Reflex-Beschichtung und deren Herstellung. EP Patent 0 814 351 A2, 1997.
- [116] B.N. Chapman. *Glow Discharge Processes: Sputtering and Plasma Etching*. John Wiley & Sons, New York, 1980.
- [117] K. Ellmer. Magnetron sputtering of transparent conductive zinc oxide: relation between the sputtering parameters and the electronic properties. *J. Phys. D: Appl. Phys.*, 33:R17, 2000.
- [118] U. Heister, J. Krempel-Hesse, J. Szczyrbowski, G. Teschner, J. Bruch, and G. Bräuer. TwinMagTMII: attempts to improve an excellent sputter tool. *Thin Solid Films*, 351:27, 1999.

- [119] W. de Boscher and H. Lievens. Advances in magnetron sputter sources. *Thin Solid Films*, 351:15, 1999.
- [120] H.E. McKelvey. Magnetron cathode sputtering apparatus. US Patent 4 356 073, 1982.
- [121] R.J. Hong, X. Jiang, V. Sittinger, B. Szyszka, T. Höng, G. Bräuer, G. Heide, and G.H. Frischat. Uniformity in large area ZnO:Al films prepared by reactive midfrequency magnetron sputtering. *J. Vac. Sci. Technol. A*, 20:900, 2002.
- [122] A.I. Ali, C.H. Kim, J.H. Cho, and B.G. Kim. Growth and characterization of ZnO:Al thin film using RF sputtering for transparent conducting oxide. *J. Korean Phys. Soc.*, 49:652, 2006.
- [123] T. Minami, T. Miyata, T. Yamamoto, and H. Toda. Origin of electrical property distribution on the surface of ZnO:Al films prepared by magnetron sputtering. *J. Vac. Sci. Technol. A*, 18:1584, 2000.
- [124] S. Berg and T. Nyberg. Fundamental understanding and modeling of reactive sputtering processes. *Thin Solid Films*, 476:215, 2005.
- [125] A. Pflug, B. Szyszka, and J. Niemann. Simulation of reactive sputtering kinetics in real in-line processing chambers. *Thin Solid Films*, 442:21, 2003.
- [126] B. Szyszka, V. Sittinger, X. Jiang, R.J. Hong, W. Werner, A. Pflug, M. Ruske, and A. Lopp. Transparent and conductive ZnO:Al films deposited by large area reactive magnetron sputtering. *Thin Solid Films*, 442:179, 2003.
- [127] C. May, R. Menner, J. Strümpfel, M. Oertel, and B. Sprecher. Deposition of TCO films by reactive magnetron sputtering from metallic Zn:Al alloy targets. *Surf. and Coat. Technol.*, 169-170:512, 2003.
- [128] S. Lange, H. Bartzsch, P. Frach, and K. Goedicke. Pulse magnetron sputtering in a reactive gas mixture of variable composition to manufacture multilayer and gradient optical coatings. *Thin Solid Films*, 502:29, 2006.
- [129] P. Frach, K. Goedicke, C. Gottfried, and H. Bartzsch. A versatile coating tool for reactive in-line sputtering in different pulse modes. *Surf. and Coat. Technol.*, 142-144:628, 2001.
- [130] H. Bartzsch, P. Frach, K. Goedicke, and C. Gottfried. Different pulse techniques for stationary reactive sputtering with double ring magnetron. *Surf. and Coat. Technol.*, 120-121:723, 1999.
- [131] J.A. Thornton. Influence of apparatus geometry and deposition conditions on the structure and topography of thick sputtered coatings. *J. Vac. Sci. Technol.*,

- 11:666, 1974. Figure 2.11 reprinted with permission from the American Institute of Physics.
- [132] J.A. Thornton. The microstructure of sputter-deposited coatings. *J. Vac. Sci. Technol. A*, 4:3059, 1986. Figure 2.11 reprinted with permission from the American Vacuum Society.
- [133] B. Movchan and A. Demchishin. Study on the structure and properties of thick vacuum condensates of Ni, Ti, W, Al₂O₃ and ZrO₂. *Fiz. Metal. Metalloved.*, 28:653, 1969.
- [134] J.A. Woollam Co., Inc. *Guide to Using WVase32*.
- [135] R.A. Synowicki, B.D. Johs, and A.C. Martin. Optical properties of soda-lime float glass from spectroscopic ellipsometry. *Thin Solid Films*, 519:2907, 2011.
- [136] L.J. van der Pauw. A method of measuring of specific resistivity and Hall effect of discs of arbitrary shape. *Philipps Res. Repts.*, 13:1–9, 1958.
- [137] L.J. van der Pauw. A method of measuring of the resistivity and Hall coefficient on lamellae of arbitrary shape. *Philipps Techn. Rev.*, 20:220–224, 1958/59.
- [138] L. Reimer. *Scanning electron microscopy : Physics of image formation and microanalysis*, volume 45 of *Springer series in optical sciences*. Springer, Berlin, 2nd edition, 1998.
- [139] M. Birkholz. *Thin Film Analysis by X-Ray Scattering*. Wiley-VCH Verlag, Weinheim, 2006.
- [140] R. Garcia, editor. *Amplitude Modulation Atomic Force Microscopy*. Wiley-VCH Verlag, Weinheim, 2010.
- [141] L. Reimer and H. Kohl, editors. *Transmission electron microscopy: Physics of Image Formation*. Springer Series in Optical Sciences 36. Springer, New York, 5th edition, 2008.
- [142] P. Scherrer. Bestimmung der Grösse und der inneren Struktur von Kolloidteilchen mittels Röntgenstrahlen. *Nachrichten der Gesellschaft der Wissenschaften zu Göttingen*, 2:98, 1918.
- [143] J.S. Becker and H.-J. Dietze. Inorganic mass spectrometric methods for trace, ultratrace, isotope, and surface analysis. *Int. J. Mass Spectrom.*, 197:1, 2000.
- [144] S. Shokhovets, L. Spie, and G. Gobsch. Spectroscopic ellipsometry of wurtzite ZnO and GaN: Examination of a special case. *J. Appl. Phys.*, 107:023509, 2010.

- [145] D. Fritsch, R. Schmidt-Grund, H. Schmidt, C.M. Herzinger, and M. Grundmann. Polarization-dependent optical transitions at the fundamental band gap and higher critical points of wurtzite ZnO. In *Proceedings of the 5th International Conference on Numerical Simulation of Optoelectronic Devices (NUSOD'05)*, page 69, Berlin, September 19-22 2005.
- [146] D.A.G. Bruggeman. Berechnung verschiedener physikalischer Konstanten von heterogenen Substanzen. *Ann. Phys. (Leipzig)*, 24:636, 1935.
- [147] K. Postava, H. Sueki, M. Aoyama, T. Yamaguchi, Ch. Ino, Y. Igasaki, and M. Horie. Spectroscopic ellipsometry of epitaxial ZnO layer on sapphire substrate. *J. Appl. Phys.*, 87:7820, 2000.
- [148] J. Koh, Y. Lu, C.R. Wronski, Y. Kuang, R.W. Collins, T.T. Tsong, and Y.E. Strausser. Correlation of real time spectroellipsometry and atomic force microscopy measurements of surface roughness on amorphous semiconductor thin films. *Appl. Phys. Lett.*, 69:1297, 1996.
- [149] T. Holdon, P. Ram, F.H. Pollak, J.L. Freeouf, B.X. Yang, and M.C. Tamargo. Spectral ellipsometry investigation of Zn_{0.53}Cd_{0.47}Se lattice matched to InP. *Phys. Rev. B*, 56:4037, 1997.
- [150] Jr. G.E. Jellison and F.A. Modine. Parameterization of the optical functions of amorphous materials in the interband region. *Appl. Phys. Lett.*, 69:371, 1996.
- [151] S.K. O'Leary, S.R. Johnson, and P.K. Lim. The relationship between the distribution of electronic states and the optical absorption spectrum of an amorphous semiconductor: An empirical analysis. *J. Appl. Phys.*, 82:3334, 1997.
- [152] L. Hulthén. *Ark. Mat. Atron. Fys. A*, 28:1, 1942.
- [153] C.C. Kim, J.W. Garland, H. Abad, and P.M. Raccah. Modeling the optical dielectric function of semiconductors: Extension of the critical-point parabolic-band approximation. *Phys. Rev. B*, 20:11749, 1992.
- [154] M. Schubert, J.A. Woollam, G. Leibiger, B. Rheinländer, I. Pietzonka, T. Sa, and V. Gottschalch. Isotropic dielectric functions of highly disordered Al_xGa_{1-x}InP ($0 \leq x \leq 1$) lattice matched to GaAs. *J. Appl. Phys.*, 86:2025, 1999.
- [155] M. Losurdo, D. Barreca, P. Capezzuto, G. Bruno, and E. Tondello. Interrelation between nanostructure and optical properties of oxide thin films by spectroscopic ellipsometry. *Surf. Coat. Technol.*, 151-152:2, 2002.
- [156] H. Haitjema, J.J.Ph. Elich, and C.J. Hoogendoorn. The optical, electrical and structural properties of fluorine-doped, pyrolytically sprayed tin dioxide coatings. *Sol. Energy Mater.*, 18:283, 1989.

- [157] M. Berginski. *Lichtstreuende Oberflächen, Schichten und Schichtsysteme zur Verbesserung der Lichteinkopplung in Silizium-Dünnschichtsolarzellen*. PhD thesis, Rheinisch Westfälische Technische Hochschule Aachen, 2007.
- [158] K. Wasa and S. Hayakawa. *Handbook of Sputter Deposition Technology: Principles, Technology and Applications*, page 138. Noyes Publications, Westwood, 1992.
- [159] D.L. Young, T.J. Coutts, V.I. Kaydanov, A.S. Gilmore, and W.P. Mulligan. Direct measurement of density-of-states effective mass and scattering parameter in transparent conducting oxides using second-order transport phenomena. *J. Vac. Sci. Technol. A*, 18:2978, 2000.
- [160] F. Fenske, B. Selle, and M. Birkholz. Preferred Orientation and Anisotropic Growth in Polycrystalline ZnO:Al Films Prepared by Magnetron Sputtering. *Jpn. J. Appl. Phys.*, 44:L662, 2005.
- [161] M. Vinnichenko, R. Gago, S. Cornelius, N. Shevchenko, A. Rogozin, A. Kolitsch, F. Munnik, and W. Möller. Establishing the mechanism of thermally induced degradation of ZnO:Al electrical properties using synchrotron radiation. *Appl. Phys. Lett.*, 96:141907, 2010.
- [162] F. Conchon, P.O. Renault, E. Le Bourhis, C. Krauss, P. Goudeau, E. Barthel, S. Yu. Grachev, E. Sondergard, V. Rondeau, R. Gy, R. Lazzari, J. Jupille, and N. Brun. X-ray diffraction study of thermal stress relaxation in ZnO films deposited by magnetron sputtering. *Thin Solid Films*, 519:1563, 2010.
- [163] J. Hüpkes. *Untersuchung des reaktiven Sputterprozesses zur Herstellung von aluminiumdotierten Zinkoxid-Schichten für Silizium-Dünnschichtsolarzellen*. PhD thesis, Rheinisch Westfälische Technische Hochschule Aachen, 2005.
- [164] J. Wu, W. Walukiewicz, W. Shan, K.M. Yu, J.W. Ager III, E.E. Haller, H. Lu, and W.J. Schaff. Effects of the narrow band gap on the properties of InN. *Phys. Rev. B*, 66:201403, 2002.
- [165] C. Bulutay, C.M. Turgut, and N.A. Zakhleniuk. Carrier-induced refractive index change and optical absorption in wurtzite InN and GaN: Fullband approach. *Cond. Mat. Mtrl. Sci. arXiv*, 0911:2312v2, 2010.
- [166] C. Guillén and J. Herrero. Optical, electrical and structural characteristics of Al:ZnO thin films with various thicknesses deposited by DC sputtering at room temperature and annealed in air or vacuum. *Vacuum*, 84:924, 2010.
- [167] C.M. Herzinger, B. Johs, W.A. McGahan, J.A. Woollam, and W. Paulson. Ellipsometric determination of optical constants for silicon and thermally grown

- silicon dioxide via a multi-sample, multi-wavelength, multi-angle investigation. *J. Appl. Phys.*, 83:3323, 1998.
- [168] T. Lichtenstein, editor. *Handbook of Thin Film Materials*. College of Engineering and Applied Science, University of Rochester, 1979.
- [169] M. Theiss: Hard- and Software for Optical Spectroscopy, Aachen. *Scout*.
- [170] Y.-M. Xiong, P.G. Snyder, J.A. Woollam, G.A. Al-Jumaily, F.J. Gagliardi, and E.R. Krosche. Controlled index of refraction silicon oxynitride films characterized by variable angle spectroscopic ellipsometry. *Thin Solid Films*, 206:248, 1991.
- [171] S. Föste, N. Ehrmann, P. Degenhardt, G. Rockendorf, and J. Scheuren. High efficiency flat plate solar collector based on a selective double-glazing. In *Proceedings of the ISES Solar World Congress*, page 797, Johannesburg, October 2009.
- [172] S. Föste, M. Kirchner, and G. Rockendorf. Experimentelle Untersuchungen an Flachkollektoren zur Temperaturverteilung an Absorber und Verglasung im Stagnationsfall. In *Tagungsband 19. Symposium Thermische Solarenergie*, page 340, Bad Staffelstein, May 2009.
- [173] F. Ruske, M. Roczen, K. Lee, M. Wimmer, S. Gall, J. Hüpkes, D. Hrunski, and B. Rech. Improved electrical transport in Al-doped zinc oxide by thermal treatment. *J. Appl. Phys.*, 107:013708, 2010.
- [174] M. Rubin. Calculating heat transfer through windows. *Energy Research*, 6:341, 1982.
- [175] ISO 15099. Thermal performance of windows, doors and shading devices - Detailed calculations. International Standard, 2003. ISO 15099-2003.
- [176] K.G.T. Hollands, T.E. Unny, G.D. Raithby, and L. Konicek. Free Convection Heat Transfer Across Inclined Air Layers. *Trans. ASME J. Heat Transfer*, 98:189, 1976.
- [177] J.N. Arnold, I. Catton, and D.K. Edwards. Experimental Investigation of Natural Convection in Inclined Rectangular Regions of Differing Aspect Ratios. *J. Heat Transfer*, 98:67, 1976.
- [178] T. Matuska and V. Zmrhal. *KOLEKTOR 2.2: A mathematical model and design tool. Reference handbook*. Czech Technical University Prague, 3rd edition, 2009.
- [179] W.H. McAdams. *Heat Transmission*. McGraw-Hill, New York, 3rd edition, 1954.
- [180] *Vitosol 200-T SDA2, Solarkeymark certificate No. 011-7S555R*. <http://www.estif.org/solarkeymark/>, 2008. [accessed on 27 June 2011].

-
- [181] S. Abrecht, C. Kettner, and R. Meiner. Über den Wert von Solarwärme: Wo sich Spreu und Weizen trennen, Teil 2. *Heizungsjournal*, 7-8:1, 2008.

List of Publications

Publications arising from the work in this thesis

Refereed journal papers

- N. Ehrmann and R. Reineke-Koch. Ellipsometric studies on ZnO:Al thin films: Refinement of dispersion theories. *Thin Solid Films*, 519:1475, 2010.
- N. Ehrmann and R. Reineke-Koch. Selectively coated high efficiency glazing for solar-thermal flat-plate collectors. *Thin Solid Films*, 520:4214, 2012.

Presentations at international and national conferences

- S. Föste, N. Ehrmann, P. Degenhardt and G. Rockendorf. High efficiency flat plate collector based on a selective double glazing. In *Proceedings of the ISES Solar World Congress 2009*, Johannesburg, South Africa, October 2009.
- N. Ehrmann and R. Reineke-Koch. Refinement of dispersion theories for ZnO:Al thin films. In *5th International Conference on Spectroscopic Ellipsometry (ICSE5)*, Albany, NY USA, May 2010.
- S. Föste and N. Ehrmann. Highly efficient flat plate collectors with low-e coated insulating glazings. In *Intersolar Europe Conference*, Munich, Germany, June 2010.
- N. Ehrmann and R. Reineke-Koch. Selectively-Coated High-Efficiency Glazing for Solar-Thermal Flat-Plate Collectors. In *Proceedings of the 8th International Conference on Coatings on Glass and Plastics (ICCG8)*, Brunswick, Germany, June 2010.
- S. Föste, N. Ehrmann, F. Giovannetti and G. Rockendorf. Grundlagen zur Entwicklung eines hocheffizienten Flachkollektors mit selektiv beschichteter Doppelverglasung. In *Tagungsband 21. Symposium Thermische Solarenergie*, Bad Staffelstein, Germany, May 2011.
- S. Föste, N. Ehrmann, F. Giovannetti and G. Rockendorf. Basics for the development of a high efficiency flat-plate collector with a selectively coated double glazing. In *Proceedings of the ISES Solar World Congress 2011*, Kassel, Germany, August 2011.
- F. Giovannetti, S. Föste, N. Ehrmann, C. Ebermann and G. Rockendorf. Anwendungspotential von spektral selektiven Gläsern in solarthermischen Flachkollektoren. In *Tagungsband 22. Symposium Thermische Solarenergie*, Bad Staffelstein, Germany, May 2012.

Danksagung

An dieser Stelle sei all denen herzlich gedankt, die mich bei der Anfertigung dieser Arbeit unterstützt und somit maßgeblich zu deren Gelingen beigetragen haben. Im Besonderen möchte ich danken:

Prof. Dr. Rolf Brendel für die Möglichkeit, die Promotionsarbeit am ISFH durchführen und eigene Ideen verfolgen zu dürfen, sowie für sein Interesse für den Verlauf der Arbeit und die wertvollen Diskussionen und Anregungen;

Prof. Dr. Gunther Seckmeyer für sein Interesse an der Arbeit und die freundliche Übernahme des Korreferats;

Dr. Rolf Reineke-Koch für die hervorragende wissenschaftliche Betreuung, die lehrreichen Diskussionen, das Korrekturlesen der Arbeit, sowie für das stets gute und angenehme Arbeitsklima in der AG Thermische Materialien;

Gunter Rockendorf, Sebastian Föste und *Dr. Federico Giovannetti* für die gute Zusammenarbeit im HGlas Projekt und die interessanten und lehrreichen Diskussionen über Flachkollektoren und die Solarthemie;

Dr. Mircea Turcu, Daniel Münster und *Christine Hein* für die gute Einarbeitung bei der Schichtherstellung und Charakterisierung und die gute Zusammenarbeit bei der Wartung und Instandhaltung der Beschichtungsanlagen;

Stefan Eidelloth und *Dr. Ulrich Eitner* für die vielen Tipps und Tricks bei der Matlab Programmierung;

Stefan Beisse, Willy Giesecke, Johannes Schlieker, Andreas Treder und *Michael Weiß*, sowie *Joachim Otto* und *Tobias Ziegner* für die stets hilfsbereite Unterstützung bei technischen Problemen und Fragestellungen.

Julia Nehmann, Dr. Verena Jung, sowie unserer netten Mittagsrunde und allen anderen Mitarbeitern des ISFH für die angenehme Arbeitsatmosphäre und die gute Zusammenarbeit.

Für die externen Messungen und die interessanten Diskussionen möchte ich danken:

Dr. Florian Ruske (Helmholtz-Zentrum Berlin) für die Hall-Messungen, *Dr. Thorsten Gesing* (Solid State Analytics) für die XRD Untersuchungen, *Prof. Dr. Pfnür* (ATMOS, Leibniz Universität Hannover) für die AFM Untersuchungen, *Dr. Armin Feldhoff* und *Frank Steinbach* (PCI, Leibniz Universität Hannover) für die TEM Untersuchungen, und *Thomas Peter* (Technische Universität Clausthal) für die SNMS Messungen,

sowie *Dr. Thomas Wagner* (L.O.T.-Oriol GmbH) und *Dr. Christian Tanguy* (France Telecom R&D RTA/CDP) für die wertvollen und lehrreichen Diskussionen zur Modellierung von dielektrischen Funktionen.

Besonderer Dank gilt meiner Familie, Martin und meinen Freunden, die mich immer unterstützen und ein offenes Ohr für mich haben.

Lebenslauf

Persönliche Daten

Name	Nicole Ehrmann
Geburtstag	8. Dezember 1982
Geburtsort	Kassel
Nationalität	deutsch
Familienstand	ledig

Schulbildung

1989 - 1993	Grundschule Niedervellmar
1993 - 1999	Gesamtschule Ahnatal, Realschulabschluss
1999 - 2002	Jacob-Grimm-Schule, Abitur

Hochschulausbildung

Oktober 2002 - Januar 2008	Universität Kassel Studium der Physik
September 2004	Vordiplom
Oktober 2006 - Oktober 2007	Max-Planck-Institut für biophysikalische Chemie Göttingen, Abteilung NanoBiophotonik Diplomarbeit zum Thema "Neue Methoden der multikonfokalen Mikroskopie"
Januar 2008	Abschluss: Diplom-Physikerin

Beschäftigung

seit Februar 2008	Institut für Solarenergieforschung Hameln (ISFH) Wissenschaftliche Mitarbeiterin Bereich Thermische Materialien
-------------------	---